Universitat Autònoma de Barcelona

Structure-processing-performance nexus of solution processed organic thin films

Rana Adel Abdelaleim Mohammed

Universitat Autònoma de Barcelona

Structure-processing-performance nexus of solution processed organic thin films

Rana Adel Abdelaleim Mohammed

PhD Thesis

PhD in Materials Science

Supervisors: Dr. Mariano Campoy Quiles, Dr. Eugenia Martinez Ferrero and Dr. Marco Stella

Tutor: Dr. Mariano Campoy Quiles

Department of Physics

Faculty of Science

June 2022

This project has received funding from the European Union's Horizon 2020 programme under the Marie Skłodowska-Curie. Grant agreement No 722651.

SEPOMO SPINS FOR EFFICIENT PHOTOVOLTAIC DEVICES BASED ON ORGANIC MOLECULES

ICMAB INSTITUT DE CIÈNCIA DE MATERIALS DE BARCELONA EXCELENCIA SEVERO OCHOA

eurecat Centre Tecnològic de Catalunya

The thesis was an outcome from SEPOMO project funded from Horizon 2020 Marie Sklodowska-Curie ITN Programme, Network of 15 high level fellowships most talented ESRs for joint research and training on efficient photovoltaic devices.

.

Contents

Acknowledgement

I am so grateful for having my supervisor Prof.dr. Mariano Campoy-Quiles for providing an amazing opportunity to be a part of this interesting SEPOMO project as well as his continuous support and guidance thoughts through this thesis. I would like to thank my supervisors Dr. Eugenia Martinez Ferrero and Dr. Marco Stella for their advice, help, and encouragement along this thesis.

It was such an honour to join the SEPOMO project under the umbrella of Horizon 2020 Marie Sklodowska-Curie ITN SEPOMO network for having excellent communication network building up my future career. I would like to thanks my supervisors through my stay in the University of Wurzburg Dr.Vladimir Dyakonov and Dr. Andreas Sperlich as well as all my colleagues Jeannine Grüne and Maria Kotova for their warm welcome and help through my stay.

It was pleasure to have an industrial stay through my thesis in Merk Ltd. So I would like to thank my supervisors Dr.Priti Tiwana, Dr.Graham Morse as well as Stephene Wider for supporting my stay in the hard times and setting up everything for me to be able to finish my experiments.

I am so pleasant for meeting all my SEPOMO colleagues, Francesco Silvestri, Pierluigi Mondelli, Pablo Simon Marques, José María, Andres Castan, Ivan Ramirez, Lukasz Baisinger , Rishat Dilimulati , Giacomo Londi , Maria Kotova , Liudmila Kudriashova , Maria Saladina , Alberto Privitera , Nong Hoang , and Benedito A.L. Raul and spending amazing time together along the SEPOMO meetings in many countries all over Europe.

I am extremely thankful to Dr. Mª Isabel Alonso Carmona, Dr. Sebastián Reparaz, and Dr. Alejandro Goñi for taking the time to teach me new experimental techniques and the in-depth discussions. I especially want to thank Bernhard for always making time to help and resolve any problem I faced in the lab.

I want to say thanks to Enrique for always showing the first steps in the lab and sharing knowledge along my thesis.

I would also like to express my gratitude to all Nanopto members, Dr. Mª Isabel Alonso Carmona, Dr. Sebastián Reparaz, and Dr. Alejandro Goñi, Jose, Marti, Miquel, Mayte, Pau, Camilla, Ossnat, Valentia, Alex, Adrian, Bernhard, Cristiano Luis, Albert, Leonardo, Xabier, Marta, Jinui, Minghua, Ylli, and Kai.

Special thanks to all my family members, Mama, Tharwa, Eman, Midoo, Ahmed and my friends Sara Mohammed, Sara Said, Mohamed Fathy, Ahmed Ramadan, Hisham Fadl and Hussien Kawar for always being there for me in hard times.

List of abbreviation

AFM	Atomic force microscopy
I_m	Maximum current
4PIPM	11,11',11'',11'''-methanetetrayltetrakis(2-(2-decyldetradecyl)-1H-pyrido[3'',4'',5'':6',7']phenaleno[1',2',3':5,6]acenaphtho[1,2-b]quinoxaline-1,3(2H)-dione)
Ag	Silver
AG	Absorption of glass coated ITO
$AgNO_3$	Silver nitrate
AM	Air mass
ANOVA	Analysis of variance
Ap	Optical absorption of PET coated IMI
APTMS	3-aminopropyltrimethoxysilane
AZO	Aluminum doped zinc oxide
BC	Blade coating
BDPA	1,3-bis(diphenylene)-2- phenylallyl
BHJ	Bulk heterojunction
C	Light speed
CB	Chlorobenzene
CCD	Charge-coupled device
CF	Chloroform
CNT	Carbon nanotubes
CS	Charge separation
Cs_2CO_3	Caesium carbonate
CT	Charge transfer
$CuCl_2$	Copper(II) chloride
CVD	Chemical vapor deposition
DCM	Dichloromethan
DFT	Discrete Fourier transform
DI	Diimide
EAA	electron affinity of the acceptor material
E_B	Binding energy
EG	Ethylene glycol
E_{HOMO}	Energy of HOMO level
E_{LUMO}	Energy of LUMO level
EPR	Electron paramagnetic resonance
EQE	External quantum efficiency
ETL	Electron transport layer
EVA	Ethylene vinyl acetate
EVOH	Ethylene vinyl alcohol copolymer
FA	Fullerene acceptor
$FeCl_3$	Iron(III) chloride
FF	Fill factor
FOM	Figure of merit
GFF	Geometrical fill factor
GH	Gigahertz
GIWAX	Grazing incident wide angle X-ray scattering
GO	Graphene oxide
h	Planck constant.

HOMO	Highest occupied molecular orbital
HOMOD	Highest occupied molecular orbital of donor material
HTL	Hole transport layer
I	Photo current source
I_0	Dark current
$IC_{60}BA$	Indene-C60 bisadduct
$IC_{70}BA$	Indene-C70 bisadduct
IMI	Insulator metal insulator
IP	In plane
IPA	Isopropanol
IPD	Ionization potential of the donor material
IQE	Internal quantum efficiency
IR	Infra-red
ISOS	International Standards Organization
ITO	Indium tin oxide
IV	Current - voltage
J_0	Reverse current
J_{sc}	Short circuit current
JV	Current density- voltage
KB	Boltzman constant
KBr	Potassium bromide
KPFM	Kelvin probe force microscopy
LBIC	Light beam induced current
LED	Light emitting diode
LUMO	Lowest unoccupied molecular orbital
LUMOA	Lowest unoccupied molecular orbital of acceptor material
MEA	2- [2- (2-Methoxyethoxy) ethoxy] acetic acid
MoO3	Molybdenum Oxide
MTP	Multiple twinned particle
MW	Molecular weight
NaOH	Sodium hydroxide
Nd: YVO_4	Neodymium-doped yttrium orthovanadate
NDI	Naphthalenetetracarboxylic diimide
N_e	Number of photoinduced charges
NFA	Non -fullerene acceptor
NMR	Nuclear magnetic resonance
NP	Nanoparticle
N_{ph}	Number of incident photons
NWs	Nanowires
o-IDTBR	(5Z,5'Z)-5,5'-((7,7'-(4,4,9,9-tetraoctyl-4,9-dihydro-s-indaceno[1,2-b:5,6-b']dithiophene-2,7-diyl)bis(benzo[c][1,2,5]thiadiazole-7,4-diyl))bis(methanylylidene))bis(3-ethyl-2-thioxothiazolidin-4-one)
OLED	Organic light emitting diode
OOP	Out-of-plane
OPV	Organic photovoltaic
OSC	Organic solar cell
P3HT	Poly(3-hexyl)thiophene
PAL	Photoactive layer
PBDBT	Poly[(2,6-(4,8-bis(5-(2-ethylhexyl)thiophen-2-yl)-benzo[1,2-b:4,5-b’]dithiophene))-alt-(5,5-(1’,3’-di-2-thienyl-5’,7’-bis(2-ethylhexyl)benzo[1’,2’-c:4’,5’-c’]dithiophene-4,8-

	dione)]
PBDTTPD	Poly[(5,6-dihydro-5-octyl-4,6-dioxo-4H-thieno[3,4-c]pyrrole-1,3-diyl)[4,8-bis[(2-ethylhexyl)oxy]benzo[1,2-b:4,5-b′]dithiophene-2,6-diyl]
PBTff4T-2OD	poly[(5,6-difluoro-2,1,3-benzothiadiazol-4,7-diyl)-alt-3,3'''-di(2-octyldodecyl)-2,2';5',2'';5'',2'''-quaterthiophene-5,5'''-diyl)]
PCBM	[6,6]-Phenyl-C61-butyric acid methyl ester
PCDTBT	Poly[N-9'-heptadecanyl-2,7-carbazole-alt-5,5-(4',7'-di-2-thienyl-2',1',3'-benzothiadiazole)]
PCDTBT	Poly[[9-(1-octylnonyl)-9H-carbazole-2,7-diyl]-2,5-thiophenediyl-2,1,3-benzothiadiazole-4,7-diyl-2,5-thiophenediyl]
PCE	Power conversion efficiency
PCPDTBT	Poly[2,6-(4,4-bis-(2-ethylhexyl)-4H-cyclopenta [2,1-b;3,4-b′]dithiophene)-alt-4,7(2,1,3-benzothiadiazole)]
PDI	perylenediimide
PEDOT	poly(3,4-ethylenedioxythiophene)
PEDOT:PSS	poly(3,4-ethylenedioxythiophene) polystyrene sulfonate
PEI	Polyethylenimine
PET	Polyethylene terephthalate
PFN	Poly [(9,9-bis(3'-(N,N-dimethylamino)propyl)-2,7-fluorene)-alt-2,7-(9,9–dioctylfluorene)]
PI	Pylene imide
PID	Perylenimide diketone
PIPB	2-(2-Decyltetradecyl)-1H-pyrido[3'',4'',5'':6',7']phenaleno[1',2',3':5,6]acenaphtho[1,2-b]quinoxaline-1,3(2H)-dione
PL	Photoluminescence
P_L	Incident radiation
P_{max}	Maximum electric power
PMW	Microwave power
PNT4T-2OD	Poly(Naphtho[1,2-c:5,6-c']bis[1,2,5]Thiadiazole-C20); Poly(NTz-C20)
PPV	polyphenylene vinylene
PSSN	poly(sodium-4-styrene sulfonate)
PTB7	Poly({4,8-bis[(2-ethylhexyl)oxy]benzo[1,2-b:4,5-b′]dithiophene-2,6-diyl}{3-fluoro-2-[(2-ethylhexyl)carbonyl]thieno[3,4-b]thiophenediyl})
PTB7-th	Poly([2,6′-4,8-di(5-ethylhexylthienyl)benzo[1,2-b;3,3-b]dithiophene]{3-fluoro-2[(2-ethylhexyl)carbonyl]thieno[3,4-b]thiophenediyl}), PCE-10
PVA	polyvinyl alcohol
PVB	Polyvinyl butyral
PVP	Vinyl pyrrolidone
q	Electron charge
RG	Reverse gravure
RH	Relative humidity
RL	infinite resistance
RMS	Root mean square
Rs	Series resistance
Rsh	Shunt resistance
RT	Room temperature
SEM	Scanning electron microscope
SFE	Surface free energy
SFT	Surface tension
Si-PCPDTBT	Poly(4,4-dioctyldithieno(3,2-b:2',3'-d)silole)-2,6-diyl-alt-(2,1,3-benzothiadiazole)-4,7-diyl)

T	Optical transmittance
TCE	Transparent conductive electrode
TEM	Transmission electron microscope
TPU	Thermoplastic polyurethane
TW	terawatt
UV	Ultraviolet
VIS	Visible
V_m	Maximum voltage
V_{oc}	Open circuit voltage
VR	Volume ratio
WF	Work function
WO_3	Tungsten trioxide
ZnO	Zinc oxide
α	Absorption coefficient
ξ	Ideality factor
σ	Electrical conductivity

List of publications

(I) E. Pascual-San-José, X. Rodríguez-Martínez, R. Adel-Abdelaleim, M. Stella, E. Martínez-Ferrero and M. Campoy-Quiles, Blade coated P3HT:non-fullerene acceptor solar cells: a high-throughput parameter study with a focus on up-scalability, *Journal of Materials Chemistry A*, 7, 20369–20382, 2019, doi:10.1039/c9ta90222h.

(II) Rana Adel , Elena Gala, Matías J. Alonso-Navarro, Edgar Gutierrez, Jaime Martin, Marco Stella, Eugenia Martinez-Ferrero, Alejandro de la Peña, Alexandra Harbuzaru, María del Mar Ramos, Rocio Ponce Ortiz, Jose Luis Segura and Mariano Campoy-Quiles, Comparing the microstructure and photovoltaic performance of 3 perylene imide acceptors with similar energy levels but different packing tendencies , Journal of Materials Chemistry C , 10, 1698-1710, 2022, doi: 10.1039/D1TC05037K.

(III) Rana Adel, Graham Morse, Francesco Silvestri, Esther Barrena, Eugenia Martinez-Ferrero, Mariano Campoy-Quiles, Priti Tiwana and Marco Stella, Understanding the blade coated to roll-to-roll coated performance gap in organic photovoltaics, accepted, *Solar Energy Materials and Solar Cells*, 2022

(IV) Rana Adel, Jeannine Grüne, Jannis Klotz, Maria Kotova, Marco Stella, Mariano Campoy-Quiles, Andreas Sperlich, and Eugenia Martinez-Ferrero Stability and Degradation of Organic Solar Modules: the influence of the encapsulant material, (in preparation)

List of tables

List of figures

Resumen

La eficiencia de la energía fotovoltaica orgánica está aumentando rápidamente, sin embargo, su rendimiento en dispositivos a gran escala y su estabilidad todavía suponen un reto. El desarrollo de la tecnología fotovoltaica ha sido intenso durante los últimos años, abordando problemas críticos a través del aumento del tamaño de los módulos OPV desde dispositivos a escala de laboratorio a módulos a escala industrial. El logro de procesos fiables de impresión y recubrimiento para módulos a gran escala ha sido un desafío hasta el momento y, por lo tanto, ha sido el tema de investigación de esta tesis.

La técnica de roll-to-roll es una técnica de procesamiento aplicada en esta tesis para lograr una solución de alto rendimiento para módulos OPV a gran escala. En este trabajo se ha demostrado la fabricación de módulos OPV basados en P3HT: PCBM y P3HT:o-IDTBR sobre un sustrato flexible, obtenidos a gran escala (Capítulo 3). La nueva metodología destaca los desafíos para escalar los pequeños dispositivos de laboratorio a módulos más grandes. Comprender los pasos críticos en el proceso de escalado es decisivo para abordar los esfuerzos de investigación y así disminuir la brecha antes mencionada. En el Capítulo 5, analizamos las pérdidas de eficiencia asociadas con varios de los pasos principales involucrados en el proceso de escalado de los dispositivos OPV, desde el recubrimiento por doctor blade a escala de laboratorio hasta el recubrimiento por roll-to-roll preindustrial. En el capítulo, demostramos que cuando se utilizan materiales en la capa activa cuyo rendimiento es tolerante con respecto a variaciones de espesor/microestructura, los pasos críticos están relacionados con las capas de bloqueo de portadores de carga, así como con las pérdidas potenciales debidas a la absorción parásita en los electrodos.

También investigamos el empaquetamiento molecular de las moléculas pequeñas y su correlación con el rendimiento del dispositivo en el Capítulo 4. Nuestros datos sugieren que la cristalinidad tanto del donante de electrones como del aceptor de electrones es una fuente de separación y recombinación de fases y, por lo tanto, además de la alineación del nivel de energía, se debe lograr una estructura de ordenamiento óptima entre el donante de electrones y el aceptor de electrones. Apoyamos nuestra investigación obteniendo los espectros de absorción óptica tanto en solución como en estado sólido, voltamperometría cíclica y GIWAXS para las películas en estado sólido.

No solo se ha investigado el procesamiento de los módulos sino también su geometría y los resultados se reportan en un tercer capítulo. Se optimizó la geometría de los electrodos impresos por la serigrafía para obtener un mejor rendimiento fotovoltaico de los módulos OPV. Además, se ha realizado un estudio comparativo de los diferentes materiales de electrodos serigrafiados. El módulo OPV más eficiente mostró un valor de PCE del 1% en condiciones AM 1.5.

La degradación de los módulos fotovoltaicos procesados en solución sigue siendo un problema crucial para poder cumplir con los requisitos industriales que hemos tratado en el Capítulo 6. Dado que la degradación de los módulos se correlaciona principalmente con los componentes de la capa activa, hemos investigado y comparado también la degradación de los módulos preparados por roll-to-roll basados en heterouniones formadas por aceptores de fullereno y no fullereno (P3HT: PCBM P3HT:o-IDTBR, respectivamente)para tener más información para mejorar la vida útil de los módulos OPV para la aplicación a escala industrial. Se utilizan dos tipos de sistemas de encapsulación (solo PET y lámina de barrera) para aislar los módulos de las condiciones ambientales, como la difusión de oxígeno y humedad en los módulos OPV. Los módulos basados en P3HT: PCBM y P3HT:o-IDTBR,

encapsulados con lámina de barrera, han mostrado actividad hasta 522 y 249 horas, respectivamente, mientras que los módulos encapsulados con lámina de PET mostraron actividad durante 21 horas. Además, se descubrió que no solo los componentes de la capa fotoactiva son responsables del proceso de degradación, sino que también la capa transportadora de huecos juega un papel en la estabilidad.

Resum

L'eficiència de la fotovoltaica orgànica està augmentant ràpidament, però el seu rendiment en dispositius a gran escala i la seva estabilitat són molt difícils d'aconseguir. El desenvolupament de la tecnologia fotovoltaica ha estat intens, abordant problemes crítics mitjançant l'augment d'escala dels mòduls OPV des de dispositius a escala de laboratori fins a mòduls a escala industrial. L'assoliment de processos d'impressió i recobriment fiables per a mòduls a gran escala ha estat un repte fins ara i, per tant, ha estat el tema de recerca d'aquesta tesi.

Roll-to-roll és una tècnica de processament aplicada en aquesta tesi per aconseguir una solució d'alt rendiment per a mòduls OPV a gran escala. En aquest treball s'han demostrat mòduls OPV basats en P3HT: PCBM i P3HT:o-IDTBR sobre un substrat flexible, obtinguts a gran escala. La nova metodologia destaca els reptes per ampliar els petits dispositius de laboratori a mòduls més grans. Entendre els passos crítics en el procés d'augment d'escala és decisiu per abordar els esforços de recerca per reduir la bretxa esmentada. En un capítol, analitzem les pèrdues d'eficiència associades a diversos dels passos principals implicats en la via d'augment d'escala dels dispositius OPV, des del recobriment per doctor blade a escala de laboratori fins al recobriment preindustrial fet per roll-to-roll. Mostrem que quan s'utilitzen materials a la capa activa per als quals el rendiment és tolerant a les variacions de gruix/microestructura, els passos crítics estan relacionats amb les capes de bloqueig dels portadors de càrrega, així com les pèrdues potencials degudes a l'absorció parasitària als elèctrodes.

També hem investigat l'empaquetament molecular de les molècules petites i la seva correlació amb el rendiment del dispositiu. Les nostres dades suggereixen que la cristalinitat tant del donant d'electrons com de l'acceptor d'electrons són una font de separació i recombinació de fases i, per tant, a més de l'alineació del nivell d'energia, s'ha d'aconseguir una estructura òptima d'ordenació entre el donant i l'acceptador d'electrons. Hem aconseguit la nostra investigació obtenint els espectres d'absorció òptica tant en estat sòlid com en solució, voltammetria cíclica i GIWAXS per a les pel·lícules en estat sòlid.

S'ha investigat no només el processament dels mòduls, sinó també la seva geometria i els resultats es reporten en un tercer capítol. La geometria de l'elèctrode impresa per la serigrafia es va optimitzar per obtenir un millor rendiment fotovoltaic dels mòduls OPV. A més, s'ha realitzat un estudi comparatiu dels diferents materials dels elèctrodes serigrafiats. El millor mòdul OPV va mostrar un valor PCE de l'1% en condicions AM 1.5.

La degradació dels mòduls fotovoltaics processats en solució segueix sent un problema dominant per a acomplir les exigències industrials. Atès que la degradació dels mòduls es correlaciona principalment amb els components de la capa activa, també hem investigat i comparat la degradació dels mòduls roll-to-roll basats en heterounions fetes amb acceptors de fullerè i no fullerè (P3HT: PCBM P3HT: o-IDTBR, respectivament). per tenir més coneixements per millorar la vida útil dels mòduls OPV per a l'aplicació a escala industrial. S'utilitzen dos tipus de sistemes d'encapsulació (només PET i làmina de barrera) per aïllar els mòduls de les condicions ambientals, com ara la difusió d'oxigen i humitat als mòduls OPV. Els mòduls basats en P3HT: PCBM i P3HT:o-IDTBR, encapsulats amb làmina de barrera han mostrat activitat fins a 522 i 249 hores, respectivament, mentre que els mòduls encapsulats amb làmina de PET van mostrar activitat durant 21 hores. A més, no només es va trobar que els components de la capa fotoactiva eren responsables del procés de degradació, sinó que també hi va tenir un paper la capa transportadora de buits.

Abstract

The efficiency of the organic photovoltaics is rapidly increasing. Their performance in large-scale devices and their stability is, however, still highly challenging. The development of photovoltaic technology has been intense, addressing critical issues through the upscaling of OPVs from lab scale devices to industrial scale modules. The achievement of reliable printing and coating processes for large-scale modules has been challenging thus far, and it has been therefore one of the main topics of research in this thesis.

Roll-to-roll is a processing technique applied in this thesis to achieve high throughput solution for large-scale OPV modules. OPV modules based on P3HT: PCBM and P3HT:o-IDTBR on a flexible substrate, obtained at large-scale, have been demonstrated in this work (Chapter 3). New methodology highlights the challenges to scale up the small lab devices to larger modules. Understanding the critical steps in the upscaling process is decisive to address the research efforts towards decreasing the aforementioned gap. In Chapter 5, we quantify the efficiency losses associated with several of the main steps involved in the up-scaling pathway of the OPV devices, from lab-scale blade coating to pre-industrial slot die roll-to-roll coating. We show that when using materials in the active layer for which the performance is tolerant to thickness/microstructure variations, the critical steps are related to the charge carrier blocking layers, as well as potential losses due to parasitic absorption in the electrodes.

We have also investigated the molecular packing of the small molecules and its correlation with the device's performance in Chapter 4. Our data suggest that the crystallinity tendency of both electron donor and electron acceptor are a source of phase separation and recombination, and thus besides energy level alignment, an optimum of ordering structure between the electron donor and the electron acceptor have to be achieved. We supported our investigation by obtaining the optical absorption spectra in both solution and solid states, cyclic voltammetry and GIWAXS for the solid-state films.

Not only the modules processing but also their geometry has been investigated and the results reported in the third chapter. The electrode geometry printed by the screen printer was optimized to obtain better photovoltaic performance of OPV modules. In addition, a comparative study of the different screen-printed electrode materials has been carried out. The fabricated OPV modules showed PCE values of ca 1% under AM 1.5 conditions.

The degradation of solution processed photovoltaic modules is still a dominant issue for the industrial requirement, and the topic of Chapter 6. Since the degradation of the modules is mainly correlated to the active layer components, we have investigated and compared as well the degradation of roll-to-roll modules based on fullerene and non-fullerene acceptors (P3HT: PCBM P3HT:o-IDTBR, respectively) heterojunctions to have more insights for improving the lifetime the OPV modules for the industrial scale application. Two types of encapsulation systems (PET only and barrier foil) were used to isolate the modules from the environmental conditions, minimizing diffusion of oxygen and humidity into OPV modules. Modules based on P3HT: PCBM and P3HT:o-IDTBR, encapsulated with barrier foil have shown activity up to 522 and 249 hours, respectively, while modules encapsulated with PET foil showed activity for 21 hours. In addition, not only the photoactive layer components were found to be responsible for the degradation process but also the HTL had a role in the resulting stability.

Chapter 1 Introduction

Abstract

OPV technology has the potential to offer many applications to the silicon PV dominated market, such as flexibility, semitransparency, integration within buildings exhibiting colourful appearance, and powering portable electronics. OPV needs to fulfil a good performance in terms of efficiency, lifetime, and production cost to be attractive for industry. The module efficiency needs to exceed the 10% with lifetime over 10 years accompanied with cost production of less than 1 euro per watt. However, while there has been a huge boost in the lab scale efficiency of OPV devices because of applying non-fullerene acceptors up to over 18%, processing OPV in large scale by roll-to-roll methods is still lacking the equivalent efficiency. Moreover, the stability of the organic components in BHJ currently limits device lifetime.

In this thesis we have investigated the challenging of upscaling processing from blade coating to roll-to-roll processing, implying novel non-fullerene acceptors and correlating their microstructure to the device's performance. In the first part of the thesis, we have been investigating silver nanowires to achieve semi-transparent OPV modules. Despite their roughness, silver electrode was screen printed in OPV modules. In addition, the electrode geometry has been optimized in the third chapter to obtain OPV module illustrated a power conversion efficiency of 1% under AM 1.5 conditions in chapter three.

Since Non-fullerene acceptors offer wide tunability of absorption spectra and less voltage losses due to the energy levels compared to fullerene acceptors, which results in higher PCEs. We have also investigated the molecular packing of the small molecules and its correlation with the device's performance by measuring solution and solid-state absorption, cyclic voltammetry as well as characterizing the films by grazing incident wide angle X-ray scattering (GIWAXS). We showed that the crystallinity of both electron donor and electron acceptor are a source of phase separation and recombination, and therefore not only the energy level alignment, but also the ordering tendencies of the donor and the acceptor.

To deepen the understanding of the efficiency lack between the lab-scale devices and the large-scale devices. We analysed the efficiency losses associated with several of the main steps involved in the up-scaling pathway of the OPV devices, from lab-scale blade coating to pre-industrial slot die roll-to-roll coating. We show that when using materials in the active layer for which the performance is tolerant to thickness/microstructure variations, the critical steps are related to the charge carrier blocking layers, as well as potential losses due to parasitic absorption in the electrodes. Hole transport layer was responsible of the major efficiency loss through the upscaling processing.

Finally, we have investigated and compared as well the degradation of roll-to-roll modules based on P3HT: PCBM and P3HT:o-IDTBR heterojunctions to have more insights for improving the lifetime the OPV modules for the industrial scale application. Two types of encapsulation systems (PET only and barrier foil) are used to isolate the modules from the environmental conditions such as the diffusion of oxygen and humidity into OPV modules. Modules based on P3HT: PCBM and P3HT:o-IDTBR, encapsulated with barrier foil have shown activity up to 522 and 249 hours, respectively, while modules encapsulated with PET foil showed activity for 21 hours. In addition, not only the photoactive layer components were found to be responsible for the degradation process but also the HTL had a role in it.

1.1 Solar energy

The solar irradiation is an extremely abundant and constant renewable energy source. The sun is the star of the Solar System, has a diameter of 1 392 684 km and is located 1.496×10^8 km far from the Earth[1]. It was formed 4.5 billion years ago, and it is calculated that it will last for another 5 billion of years. The sun irradiation has an average power density of 100 W/cm^2 [2] arriving to the earth daily. The solar spectrum has the range of wavelengths from 280 to 4000 nm. Since the earth is rotating, the sun intensity is varying along the day. The sun radiation reaches to the earth surface through the atmosphere and its optical path length is defined by the Air Mass coefficient "AM" that has the value 1 for normal incidence (see Figure 1.1), being that the reference is Air Mass 0, outside the atmosphere. The air mass is explained in figure 1.1(b). The standard air mass "AM 1.5" corresponds to a solar zenith angle of z=48.2°.

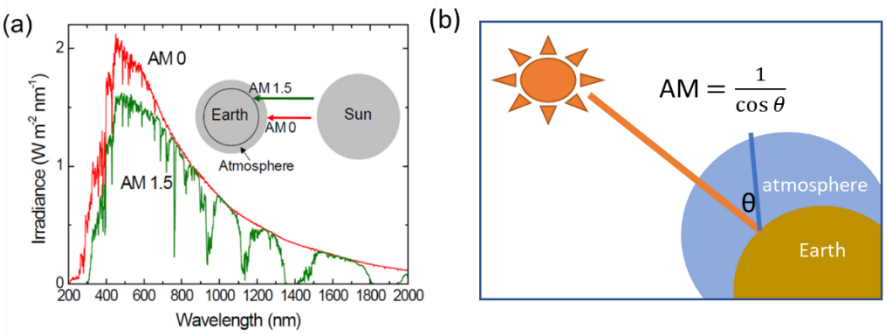

Figure 1.1 (a) The solar irradiance with air mass 0 (reference) in red and with air mass 1.5 in green and (b) an explanation of the air mass definition, pictures reproduced from references [3], [4].

The arriving energy to the surface of the earth every hour is found to be $4.39 \cdot 10^{20}$ Joule while the worldwide energy consumption in 2010 was $5.5 \cdot 10^{20}$ Joule[5]. This comparison shows the importance and the motivation of this renewable source of energy. The solar energy reaching to the surface of the earth every hour almost satisfies the global energy demand over the entire year [6]. The estimated energy hitting the earth in a year is 23,000 TW/year,13 times greater than the combined energy potential of coal, natural gas, petroleum, and uranium, along with wind and other types of renewable energy sources [7].

1.2 Scaling up the OPV devices

Yet, scaling up the OPV devices from lap-scale to large scale is complex due to several factors discussed as follows.

Electrical factors are including the electrode sheet resistance of the large area in OPV modules is higher than in case of the small area devices since it is proportional to the dimension of the area used. In addition, the flexible substrate (PET coated with ITO) has higher sheet resistance then the rigid substrates (glass coated ITO). The electrode material and the deposition technique affect the sheet resistance of the electrode. The investigation reported[8] that the graphene deposited by screen printing has the high sheet resistance and the metal nanowire deposited by screen printing has the lowest sheet resistance. Another factor is the geometrical design of the module in which the connecting parts (dead zones) between the cells in the module are considered in the area but not able to generate current. Both factors are increasing the series resistance of the produced modules. These factors result in reduction in the photogenerated current and the fill factor modules and therefore the efficiency of the produced. The solution for these challenge is; first, to apply highly conductive transparent electrodes to overcome the evolution of the sheet resistance with the large area. Second, is to minimize the length of the dead zone. Laser patterning is the reported technique to minimize the length of the dead zone to 80 μm, the minimum reported dead zone, by optimizing the duration and the wavelength of the laser pulse reaching maximum geometrical fill factor of 98%[9].

Optical factors are considering the more absorption of the incident light to the cell. The large area transparent electrode found to be less transparent than the transparent electrode at small area. In large scale modules the layers such as interfacial and photoactive layers are thicker than the small area devices resulting in more light absorption. Silver grid applied in modules as a top electrode has shads that reduce the incoming light to the photoactive layer. These factors related to the loss of the photogenerated current of the modules and the efficiency as well. The suggested solution is to apply transparent top electrode such as PEDOT: PSS[10].

Factors associated to the photoactive layer are considered challenging in the upscaling such as the dark current at the large area modules arising from increasing the defect numbers in the photoactive layer. In small area devices, the PAL has a 100 nm thickness unlike at large scale modules PAL should be thicker to overcome the defects. Thickness inhomogeneity is reported to hinder the modules performance. Furthermore, materials with less sensitivity to thickness variations have the potential to be applied at the large area modules. Forming thick PAL comes along with systems that have face-on ordering are desired for the vertical charge transport. Temperature dependant aggregation systems such as PBTff4T-2OD, PTB7-th, and PNT4T-2OD are reported to have the optimum morphology in the thick PAL and therefore high fill factor and efficiency. Fluorinated and chlorinated polymers reported to improve the charge mobility through the π-π stacking. Not only the materials but also the solvent used since halogenated solvents are used in small area devices should be replaced by the non-halogenated solvents at the large-scale modules which found to negatively affect the photovoltaic performance[11]. Hansen parameters were reported as a lead to the non-halogenated solvents selection for the materials.

1.3 Deposition techniques

Large scale production is carried out by considering different deposition technique with low-cost production.
No contact (coating) techniques in which the solution is conducted from the head to the substrate without contact such as blade coating, spin coating, slot-die roll-to-roll, and spray coating. While the contact method is two-dimension pattern printing in which the substrate has a contact with the solution such as flexographic printing, and screen printing, unlike the inkjet printing. The most applied methods in the large-scale processing are the slot die roll-to-roll and screen printing. Blade coating is a method that produce zero- dimension layer, slot die roll-to-roll can produce one -dimension strips and the ink jet is able to produce two-dimension different patterns. In this thesis we employed blade coating, screen printing and slot die roll-to-roll (see experimental chapter).

1.4 Basic working principles

Organic semiconductors are π-conjugated polymers consists of carbon and hydrogen atoms that combine the electrical conductivity of semiconductors and the flexibility of plastic. Organic semiconductors are amorphous or polycrystalline structures. The conjugation in these materials arises from the iteration between the single and double bonds between the carbon atoms. Molecular orbitals in these materials form two bonds, namely σ-bonds and π-bonds. σ-bonds resulted from the sp2 hybridization between the orbitals and π-bonds arises from the overlapping between the unhybridized p-orbitals. Organic semiconductors have low band gap of 1- 5 eV between the high occupied molecular orbitals (HOMO) and the low occupied molecular orbitals (LUMO). The charge carriers are localised to the HOMO and the LUMO and can move by hopping along the conjugation of the polymer backbone. When photon, with the same energy to the band gap of the polymer, is absorbed, electron moves to excited state forming exciton. Excitons are of two different types of singlet and triplet excitons. When the electron and the hole have the opposite spins, they form singlet exciton and in case of spinning at the same direction they from triplet exciton.

Organic semiconductors have desired properties for organic electronic devices such as light weight, low charge-carrier mobilities(10^{-3} $cm^2/V{\cdot}s$) [12], low dielectric constant (ε_r = 3 – 4) [13], [14], excitonic characteristics [15] which means that the photon absorption generates a coulombically bound (0.5–1.0 eV) electron-hole pair, low-cost manufacturing, and mechanical flexibility[16]. Organic semiconductors have the potential to be applied in organic electronics such as photovoltaic devices. The photovoltaic process gains differences based on the device type.

Single junction devices shown in Figure 1.2(a) have one organic photoactive layer between two electrodes[17]. Light absorption in organic layer induces the production of photo exciton (electron hole pair). The electric field lead to the HOMO and the LUMO bending, and to form the Schottky barrier between the electrode and the organic layer [18], [19]. This field is responsible for the charge dissociation of excitons to deliver free charges (electron and holes) collected at electrodes. Because of the short diffusion length in organic materials (5-100 nm)[20]–[22], all excitons formed beyond the depletion region recombine in addition to the fact that all charges are moving in the same phase / layer, so the probability to recombine is high.

Higher efficiencies of about 1% were obtained with the bilayer heterojunction devices (see Figure 1.2 (b)), demonstrated by C. Tang in 1986, due to the introduction of the

donor-acceptor heterojunction concept. In bilayer devices, the photoactive layer consists of two layers of electron donor (D) and electron acceptor (A) organic semiconductors. The photo-generated exciton moves to the donor/acceptor interfacial heterojunction by diffusion, the photo excited electrons transfer from the donor LUMO to the acceptor LUMO ($LUMO_A$), and the holes would stay in the donor HOMO ($HOMO_D$). The offset (LUMO of donor-LUMO of acceptor and HOMO of donor- HOMO of acceptor) is responsible for the charge separation through the charge-transfer (CT) process resulting in the diffusion of the electrons and holes to the electrodes (see Figure 1.2 (f)) [23]. In bilayer heterojunction OPV devices, the charge recombination is reduced due to the Frenkel exciton when electrons and holes diffuse to two phases. The limited PCE of the bilayer devices is due to the low donor/acceptor heterojunction interfacial area.

For improving the efficiency of the bilayer, heterojunction OPV devices can be obtained by maximizing the donor acceptor interface, combined with decreasing the exciton diffusion pathway to the interface. Therefore, bulk hetero junction (BHJ) photoactive layer is formed by blending the donor and acceptor materials together (Figure 1.2(c)). The principles of BHJ OPV devices based on fullerene acceptors consist of five steps: light absorption Figure 1.2(f)-(i) by the donor generating bounded excitons Figure 1.2(f)-(ii), exciton diffusion to the donor/acceptor interface, exciton dissociation into free-charges or charge separation (CS) Figure 1.2(f)-(iii), free-charges transport (CT) to the interface Figure 1.2(f)-(iv), free-charges collection at the electrodes[23]. The bounded exciton can recombine to the ground state or to the triplet state of the donor material (T) [24]. The efficiency enhancement in BHJ devices is due to the large donor/acceptor interface and the reduced domains of the donor and acceptor, which reflects the importance of the film morphology of the photoactive layer in OPV device. If the D/A blend domains are in the same range of the D and A exciton diffusion lengths, all excitons will reach the interface[25]. This helps to increase the thickness of the photoactive layer more than 100 nm[26] and hence improve the light harvesting although the non-geminate recombination is still limiting the BHJ devices efficiency. The optimal morphology is a fine intermix of donor and acceptor domains, with sizes that meet the donor and acceptor exciton diffusion lengths and a high donor/acceptor interface, through bi-continuous percolation pathways for charges transport to the electrodes[27].

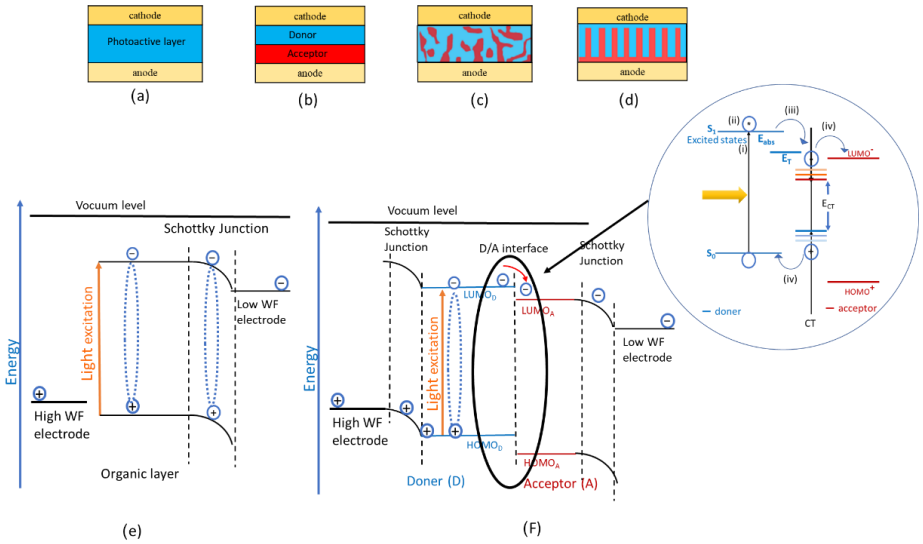

Figure 1.2 OPV devices: (a) single photoactive layer, (b) bilayer heterojunction photoactive layer, (c) bulk heterojunction photoactive layer, (d) interdigitated photoactive layer, (e) the photovoltaic process in single organic layer and (f) the photovoltaic process in organic heterojunction layer.

1.4.1 Exciton creation by light absorption

The incident photons to the photoactive layer are absorbed by the donor material with a certain efficiency. This optical absorption is affected by the optical absorption coefficient, molar extinction coefficient, their density in the photoactive material. The absorption of the donor material is limited by its bandgap, that is the difference between its LUMO and HOMO levels[28]. The absorption coefficient depends on the density of the electronic and vibrational states, the overlap of the wavefunction between the ground state and excited state, and molecular orientation in the organic material. Improving the absorption coefficient of organic materials can be obtained by tunning the molecular structure and their packing in the film. Second is the light pathway penetrating the photoactive layer that is dependent on the film thickness. The film thickness of the photoactive layer is limited by the low charge mobility that characterizes the organic semiconductors.

The light absorption happens in the photoactive layer and, as a consequence, an electron is promoted from the ground state to the excited state, to form a bounded exciton (Frenkel exciton) with the hole remaining in the HOMO. Dissociating the exciton into two free charges requires overcoming the coulombic energy (E_B) of the interaction still present between the electron-hole pair.

1.4.2 Exciton diffusion and charge separation

Normally, the exciton is formed and the charge transfer takes less than 100 fs to reach the interface [29] despite the geminate recombination, in which the electron and the hole of the same exciton recombine together. The domain size of the donor material needs to be in the range of the exciton diffusion length to overcome the recombination mechanisms. Exciton dissociation represented in equation 1.

$$IP_D - EA_A - E_B > 0 \qquad \text{Equation 1}$$

After the dissociation, the charges separate, with the hole staying in the donor material and the electron transferring to the acceptor one. However, the charges are still bounded by coulombic force so that the internal electric field, arising from the difference between the two electrodes, is needed to obtain free charges. If the built-in electric field is low the geminate recombination (occurring within micro- to milliseconds time ranges) is likely to happen[30].

In BHJ films, organic materials are amorphous or semicrystalline where the charge transport (or polaron diffusion) happens by the hopping mechanism[31]. Since in organic semiconductors the conductive electronic states are more localized, their charge mobility is low (usually lower than 10^{-2} $cm^2/V{\cdot}s$)[32], compared with other traditional semiconductors (10^3 $cm^2/V{\cdot}s$). The morphology of the photoactive layer is a limiting key factor since the intermixing phases between the donor and the acceptor should imply high interfacial area for efficient charge separation and overcoming recombination.

1.4.3 Charge extraction

The two electrodes should have different work functions; the work-function of the cathode should be lower than the LUMO of the acceptor and the one of the anodes should be higher than the HOMO of the donor. The position of the work function with respect to semiconductor levels defines the contact type either ohmic or blocking. In the non ohmic contact of the organic electrode interface there is an electrical loss while in case of the ohmic contact there is a high efficiency of the charge collection at the electrodes[33] Al, Ca, and Ag are the most common low work function electrode while Indium Tin Oxide (ITO) is common high work function electrode with transparency to visible light (90%) due to its high bandgap

(around 3.7 eV) for letting the light in the device[34]. The selective collection for the charges at the BHJ film/electrode interface implies less non geminate recombination of the charges. Therefore, buffer layers are applied into OPV devices[35]. Interfacial layers work as optical spacer and selectively exhibit ohmic contact to the electron donor or the electron acceptor. PEDOT: PSS, MoO_3 and V_2O_5 are the most common anode buffer layers and typical cathode buffer layers are LiF, TiO_2 and ZnO.

1.5 Equivalent circuit of BHJ solar cell

Figure 1.3 (a) shows an equivalent circuit of the OPV device[36]. By illuminating the cell, the short circuit current I_{sc} of the cell is defined when the circuit is closed, and the terminals are connected while the open circuit voltage V_{oc} is defined when the circuit is opened, and the terminals are separated by infinite resistance R_L. The current density J_{sc} is mostly employed instead of the current. $V = I*R_L$ is the voltage generated in the cell. The relation between the current and the voltage under the illumination of the cell as well as the power $P = I*V$ relation with the voltage is presented in Figure 1.3(b)

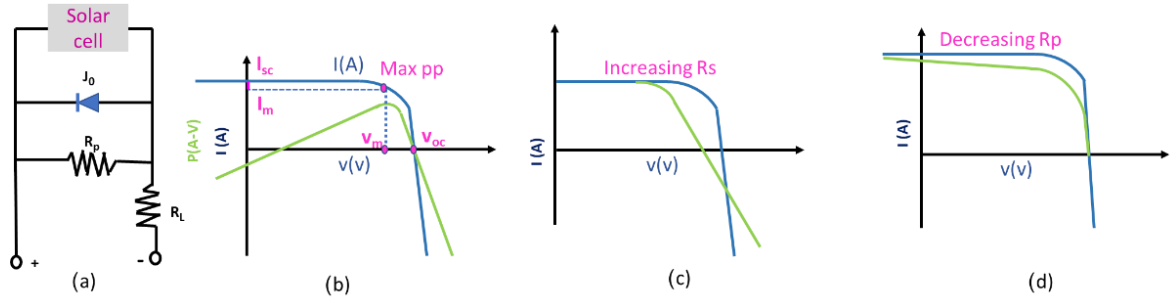

Figure 1.3 (a) The equivalent circuit of BHJ solar cell and (b) I-V and P-V curves of the corresponding cell with the photovoltaic parameters, (c) the I-V curves of the corresponding cell with increasingly high Rs and (d) the I-V curves of a solar cell with gradually lower Rp.

The dark current can be defined when the cell is not illuminated and the there is a potential difference between the circuit terminals, that generates a current that opposes the photo generated current under illumination resulting that the total current in the circuit has lower value than the short circuit value expressed in Equation 2 [36]

$$J = J_0\left(e^{\frac{q\,V}{K_B\,T}} - 1\right) \qquad \text{Equation 2}$$

The total current density in the solar cell is expressed by Equation 3:

$$J(V) = J_{sc} - J_{dark}(V) \qquad \text{Equation 3}$$

To be substituted in the ideal diode equation 4[37]

$$J = J_{sc} - J_0\left(e^{\frac{q\,V}{K_B\,T}} - 1\right) \qquad \text{Equation 4}$$

The ideality factor represents the deviation of the real diode respect to the ideal case, here introduced, leading to Equation 5:[38]

$$J = J_{sc} - J_0\left(e^{\frac{qV}{\xi K_B T}} - 1\right) \qquad \text{Equation 5}$$

By applying this to the BHJ device Equation 5 define the real BHJ OPV device (see Figure 1.3) which consists of (1) the photo current source I, (2) dark current I_0 at reverse bias, with

an ideality factor ξ, (3) parallel resistance R_p (to be infinite in ideal solar cell), which considers current leakage and (4) series resistance R_s (to be zero in ideal solar cell), that considers the resistivity of the semiconductors and electrodes as well as the ohmic resistance at interfaces[2]. This leads to Equation 6:

$$J = J_{sc} - J_0\left(e^{\frac{q(V-IR_s)}{\xi K_B T}} - 1\right) + \frac{V-IR_s}{R_p} \quad \text{Equation 6}$$

1.6 Photovoltaic parameters of solar cell

Figure 1.3(b) shows all the photovoltaic parameters of the solar cell. The open circuit voltage V_{oc} is defined as the voltage of the cell with no current flows, that is depends on the difference between $HOMO_D$ - $LUMO_A$. The photogenerated current density J_{sc} is the current of the cell when V =0.

The maximum electric power (P_{max}) produced under illumination is the product of the maximum current I_m and the maximum voltage of V_m. The ratio between the maximum power obtained by the cell ($I_m \cdot V_m$) and the obtained power from the cell ($I_{sc} \cdot V_{oc}$) is called the fill factor FF and be calculated as in Equation 7:

$$FF = \frac{P_{max}}{I_{sc} \cdot V_{oc}} \quad \text{Equation 7}$$

The FF indicates the quality of a photovoltaic cell. FF depends on the recombination in the solar cell, the buffer layers, the shunt, and series resistance.

The power conversion efficiency (PCE, in W/m^2) is defined in Equation 8:

$$PCE = \frac{P_m}{P_L} = \frac{J_{sc} \cdot V_{oc} \cdot FF}{P_L} \quad \text{Equation 8}$$

P_m is the output power of the cell and P_L is the incident power of light.

The PCE measured in standard temperature (25°C) and illumination conditions (incident radiation P_L = 100 mW/cm^2 and AM1.5 spectral shape) is the conventional efficiency (η) value given for any solar cell.

The External Quantum Efficiency (EQE) is defined by Equation 9

$$EQE = \frac{N_e}{N_{ph}} \quad \text{Equation 9}$$

The EQE(λ) can be obtained from the short-circuit current $I_{sc}(\lambda)$ of the cell illuminated at each wavelength λ and the incident light intensity Ji(λ) at the same wavelengths (see Equation 10):

$$EQE(\lambda) = \frac{N_e}{N_{ph}} = \frac{I_{sc}(\lambda)}{J_i(\lambda)} \cdot \frac{hc}{q\lambda} \quad \text{Equation 10}$$

where c is the light speed and h is the Planck constant.

The internal quantum efficiency (IQE) represents the conversion of absorbed photons into charges within the cell, because in EQE the light absorption capability of the active layer and the possible losses due to reflection and scattering are considered.

1.7 OPV device architecture: conventional and inverted structure

Different device structures have been investigated for seeking better efficiency and stability. The expression of conventional configuration refers to the structure where electrons are collected at the opaque electrode. The opposite occurs in the case of the inverted configuration, where the opaque electrode acts as the anode (see figure 1.4). The inverted configuration is more stable than the conventional structure because of the high work function electrode that is more resist to oxidation [2].

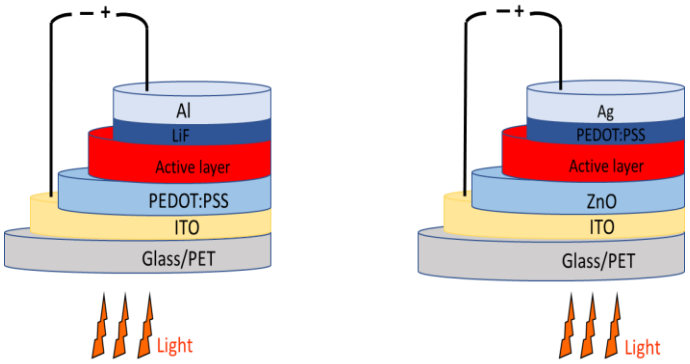

Figure 1.4 (a)Scheme of the conventional configuration of the OPV device and (b) the inverted configuration of the OPV device.

1.8 Active layer materials: fullerene- and non-fullerene-conjugated polymers blends

Different material combinations have been used for the photoactive layer in BHJs with the purpose of obtaining efficient charge transfer, such as blends of polymers, and blends of polymer and small molecules. Poly(3-hexylthiophene):[6,6]-phenyl C61-butyric acid methyl ester (P3HT:PCBM) has been applied extensively [39] in BHJ OPV cells due to the ultrafast electron transfer from P3HT to PCBM, due to their low cost that makes them very attractive for high throughput application. Although, fullerene acceptor has a deep LUMO level providing good electron conductivity, their absorption is limiting the light-harvesting.

Fullerene derivatives form favourable morphology with polymer donors. C_{60} and C_{70} eventually applied in vacuum deposited OPVs and their soluble derivatives $PC_{61}BM$ and $PC_{71}BM$ have been applied in solution processed OPVs. The spherical shape of C_{60}, discovered by Kroto, provides a good acceptor character due to its isotropic microstructure and its alignment to the donor p-system and the delocalization of LUMO level over the whole surface of the molecule. $PC_{61}BM$, synthesized by Hummelen, is more soluble in organic solvents than C_{60}. The bulk hetero junction has introduced by with the soluble $PC_{61}BM$ acceptor and the polymer donor. The main advantages of the fullerene acceptors are the high electron mobilities, and the ability to form both pure and mixed domains for the appropriate charge transfer. However, the main drawback of $PC_{61}BM$ is its narrow absorption in the visible region, because of the C_{60} symmetry so that Wienk synthesized the $PC_{71}BM$.The efficiency of devices based on $PC_{61}BM$ or $PC_{71}BM$ is over 7.7%.
In addition to the deep LUMO levels of the $PC_{61}BM$ that result in V_{OC} loss in OPV devices, so that bis$PC_{61}BM$, C_{60} bisadduct $IC_{60}BA$, and indene-C_{70} bisadduct $IC_{70}BA$ which exhibited 0.1, 0.17 and 0.19 eV LUMO level shifted up, respectively. For further improvement in the device's efficiency, non-fullerene acceptors have been introduced to the application in the OPV devices.

Non fullerene acceptor (NFA) has a high potential for their strong absorption and tunability[39], [40]. The efficiency of OPV devices based on the non-fullerene acceptor has exceeded 18% in single-junction OSCs[41], [42]. NFA has the advantages of enhanced processability and solubility, efficient charge transfer, and ease of synthesis.
NF acceptors are either fused aromatic diimides acceptors, or push–pull strong intramolecular acceptors. Their interesting features presented in Figure1.5 such as (i) conjugated backbones with π-conjugated functional carbonyl groups (oxygen) and/or nitrogen cyano group(nitrogen) that provides strong electron-accepting ability. (ii) these π-electrons are well delocalized into the backbones that ensures the electron transportation without being trapped.

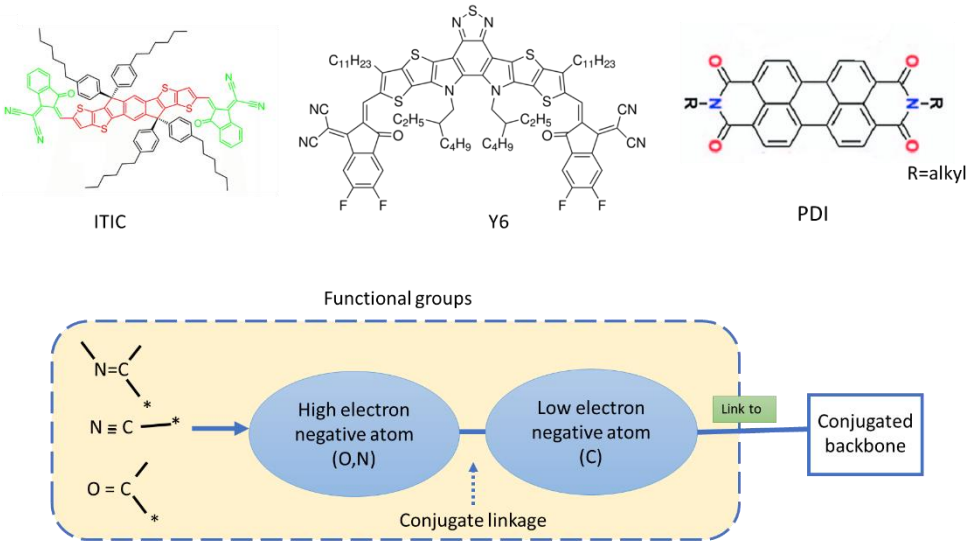

Figure 1.5 The molecular structure of most common NFA applied in OPV devices.

DI molecule was implemented in bilayer OPV device in 1986[43],[44] Eventually, the efficiency of OPV device based on the perylene diimide (PDI) acceptors exceeded 12%[45], [46]. Among the fused aromatic diimides, PDI derivatives are one of the most intensively studied molecules due to their high photo stability, their optical absorption in the visible spectrum, electron mobility due to the intermolecular coupling arises from the planar structure, high electron affinity (3.9 eV)[47] and crucially their cost is lower than fullerenes. Moreover they offer multiple sites for structural modification to tune their absorption and imide group that has high electron affinity[48]. Their properties can be tailored by the substitution of the imide nitrogen atoms or on the rylene core (see small molecule chapter) in addition to the π−π stacking that form crystal motifs proper for charge transport[32]. PDIs have planar backbone molecular structure so that in solid state they make large crystals, which hinder the charge transport, that makes the main consideration of PDI molecules to control their solubility and hence their aggregation. Side chained PDI derivatives can twist which hinder their aggregation and provide low bandgap as reported in spirobifluorene PDI, N-alkyl-substituted PDIs and naphthalenetetracarboxylic diimide (NDI) that used as effective electron acceptors in OPV devices[49]–[52]. More detailed information about the effect of the molecular packing on the performance of OPV devices is elaborated in chapter five.

1.9 Degradation of BHJ OPV devices

Improving the lifetime of OPV device is challenging since the degradation mechanisms [53], [54] such as oxygen and water diffusion [66], electro-migration, electrode oxidation [55], [56] [67], diffusion of In to PEDOT:PSS[57], bleaching and intrinsic degradation of organic materials in PAL [58]. Degradation factors can be categorized into intrinsic or extrinsic. Table1.1 summarizes the degradation factors that stand against the device stability.

Table1.1 Summary of the degradation sources for the organic solar cell.

	Stress	Mechanism	Solution
Extrinsic degradation	Water and oxygen	Water reacts with low work function electrode Oxygen produces unintentional doping	Encapsulation
	Photo induced degradation	Organic materials bleaching by photooxidation	Encapsulation associated with UV filters
		Photo induced traps on non-fullerene materials enhancing the density of states	Enhance the order of crystallinity in materials
		Dimerization of PCBM	NFA
Intrinsic degradation	Thermal degradation in darkness	Phase separation in BHJ	Crosslinking, vitrification
		Forming blocking layer at the electrode interface	Use of alternative materials

1.9.1 Intrinsic degradation

Losses in OPVs by time are divided into three regimes: “burn in” in which the performance deteriorate by 10–50% in hundred or thousand hours, “stabilized” long-term rate, a period of constant degradation in which the performance reduced by extra 20% in thousands of hours, and device failure (Figure 1.6).

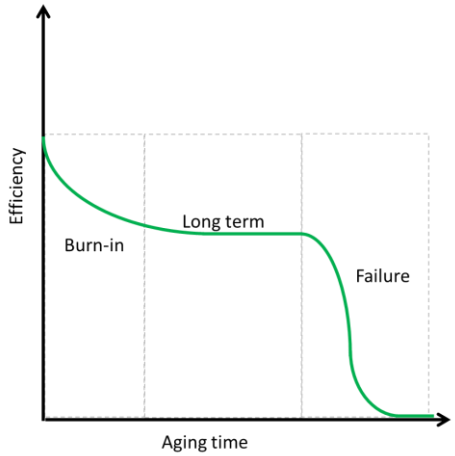

Figure 1.6 OPV degradation over time.

The intrinsic degradation in dark in the photoactive layer and or in the buffer layers happens due to the thermally induced molecular rearrangement that can hinder charge extraction. Organic materials phase separate over long times, fact that deteriorate free

carriers generation[59]. This is a critical intrinsic degradation pathway that it cannot be avoided by the encapsulation of the devices.

In the photoactive layer, phase separation improved by applying high boiling solvents, although the additive inhibits the device stability[60], [61]. Some of these additives affect the polymer conjugation, introduce traps, and introduce the oxidation in the PAL[62], [63].

Dark degradation could be identified when the OPV devices are heated in dark, and the corresponding performance is measured. Rapid degradation of devices aging in dark ambient at room temperature was reported to expose two stages of degradation, the first stage had a rapid degradation between the cathode and the PAL due to the exposure to O_2 and H_2O during the manufacturing followed by the second phase in which the degradation is slower.

1.9.2 Extrinsic degradation

Extrinsic factors require an external stimulus, such as oxygen and water for chemical degradation, bending for mechanical degradation, light for photoinduced degradation or heat for thermal degradation. Encapsulation slows down the extrinsic degradation rate.

1.9.3 Electrode Degradation

The degradation of the metal electrode result in deteriorating the device performance[64]. Two different mechanisms can lead to the electrode degradation; first is the electrode oxidation by the diffusion of oxygen[65] and the second is the reaction of the electrode with the active layer or charge transport layers [65]. When the metal oxidizes, the series resistance of the cell increases, and the charge selectivity of the electrode is hindered. Low work function metal electrode oxidizes by the diffusion of water through the pores in the metal layer and create a barrier for the charge transport [66].Al interacts with C_{60}, forming Al-C_{60}bonds that cause reduced charge transport and device performance[67]. Silver electrodes is more stable than the aluminium electrode to be oxidized[64]. Therefore, in order to improve the stability of the devices, it is advisable to use high work function metals in the inverted structure[65],[68].

1.9.4 Degradation of the hole transport material

The most applied HTL in OPV devices is poly (ethylenedioxythiophene) poly (styrene sulfonic acid) (PEDOT: PSS), although PEDOT: PSS deteriorate the device stability. PEDOT: PSS is highly hygroscopic, and that the absorption of water leads to a reduction of its conductivity and the device stability. PEDOT:PSS accelerate the degradation since water can diffuse through it reaching the cathode[69]. Furthermore, the absorption of water by the PEDOT: PSS increase the resistance at the interface [71] and introduce the degradation in the PAL, forming aggregation and decreasing the absorption[70]. Different alternatives have been reported for the PEDOT:PSS of better stability such as vacuum deposited MoO_3[71], sputtered chromium oxide-chromium nitride[72], sputtered nickel oxide (NiO) [72], copper oxide (CuOx)[73], lithium benzoate[74], the phosphine oxide 2,7-bis (diphenyl phosphoryl)-9, 9-spirobi [fluorene][75], cesium carbonate [76], LiF and Cs_2CO_3[77] or cadmium selenide (CdSe) [71].

1.9.5 Photo-oxidation of the active layer P3HT: PCBM

The Photo-oxidation in organic films lead to optical bleaching that imply the loss in their optical density via a free-radical reaction[78]. It is reported in many polymers such as PPV[79], [80], P3HT[81]–[83], PCDTBT[84], [85], PTB7[86], PBDTTPD[86], Si-PCPDTBT[86] and others[86],the reaction of polymers with oxygen indicated by the loss of conjugated bonds and a growth of carbonyl, ester, and alkoxy bonds, indicating that the materials have reacted with oxygen. The photo oxidation process consists of initiation, propagation, and termination. The initiation is when a bond breaks and a free radical is formed and this is normally seen when a hydrogen atom is introduced in the polymer side chain, then propagation occurs, when this free radical propagates via diffusion, in which the conjugated bonds break that is the main reason for the optical bleaching. The Propagation is accelerated by the oxygen diffusion. When the two free radicals combine the termination happens as elaborated in the following equations.

(1) $initiation \quad r^{\cdot} + PH \rightarrow P^{\cdot} + rH$
(2) $propagation\, P^{\cdot} + O_2 \rightarrow PO_2^{\cdot}$
(3) $PO_2^{\cdot} + PH \rightarrow PO_2H + P^{\cdot}$
(4) $termination\, PO_2^{\cdot} + PO_2^{\cdot} \rightarrow inactibe\, products + O_2$
(5) $branching\, PO_2H \xrightarrow[h\upsilon,\Delta]{} PO^{\cdot} + HO^{\cdot}$

Photochemical degradation mechanisms of the conjugated polymers can be summarised as follows: photo bleaching(perturbation of the π-conjugation), photo-doping (charge transfer D + A = [Dδ+ Aδ−]), and free radical initiated that is followed by secession and cross-linking[87].

Removing the polymer side chain, the initiation point, is a way to enhance the stability of the solution-processed polymers[88]. Both factors the film morphology and the film density are correlated to the stability since crystalline films have been found to be more stable[81], [89] and dense films tend to be more stable since the oxygen cannot diffuse easily to reaction sites[90].

1.9.6 Degradation of the electron transport layer (ETL)

ETL was reported to increase the lifetime of the OPV devices to be longer than devices without ETL kept in dark. Zinc oxide (ZnO) is the most common ETL used in inverted structure solution processed OPV devices[91]. The conductivity of ZnO is affected by the dopant materials, Aluminium doped ZnO was reported to be more stable and efficient in OPV device[92].The conductivity of ZnO enhances by exposure to UV-irradiation through the direct bandgap excitation[87]. Under the UV radiation, the oxygen de-dopes as shown in figure 1.7 and the conductivity improves. after the gradual de-doping of oxygen, the oxygen is re adsorb again on the surface of ZnO nanoparticles and re-doped the ZnO nanoparticles. The stability of the devices with radiated ETL was enhanced to over 500 h.

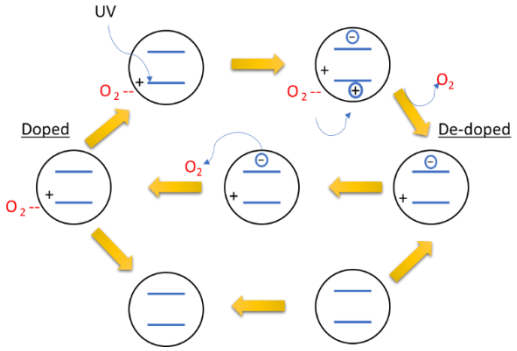

Figure 1.7 The conductivity enhancement process of the ZnO particles by UV radiation.

1.9.7 Degradation effect on the photovoltaic parameters

The degradation mechanisms have the following effects on the photovoltaic parameters:

- The fill factor FF is affected by the efficiency of the interfacial charge transfer between layers therefore the degradation of the PAL/electrode interface has a major influence on the F value, mobility, and thus to the degree of phase separation (thermal degradation).
- The variation of the serial resistance, is related to the resistivity of the whole stack in the OPV device such as the metal busbar and specially the contact resistance between the photoactive layer (PAL) and the electrode
- The shunt resistance can vary due to changes in the leakage current through the whole device and the presence of shunts and shorts.
- The open circuit voltage is affected by several parameters such as the variation in the interface of the PAL and electrode, change of the effective band gap of the PAL, electrode work function change, and increase in recombination due to increase in phase separation upon thermal stress.
- The short circuit current is proportional to the light absorption efficiency so it is highly influenced by the loss of polymer conjugation, the molecular architecture of the polymer, the thickness of the PAL, the loss in the degree of transparency of the stack, the exciton dissociation efficiency, the change in donor/acceptor morphology, the decrease in the interfacial area between the donor and the acceptor , the increase of the blend domains, the loss of percolating paths, the degradation of the electrode/PAL interface.

1.10 Motivation

OPV has reported high efficiencies of 18% in lab scale devices that assure that the OPV technology has a high potential not only for the outdoor application but also the indoor application. These efficiency values are far from the produce large scale devices. The reported efficiency for large scale modules is 11.7%[93]. Several factors are considered quite challenging while upscaling processing in each layer. First Deposition method is required for depositing homogenous photoactive layer since the thickness variation is reported to affect the photovoltaic performance. The photoactive layer in large scale OPV modules should have thickness less than 300 nm due to the short diffusion length and the limited charge mobility. Complexity of modules manufacturing is related to the implementation of green solvents instead of the halogenated solvents.

Second factor limiting the upscaling is the monolithically connection between the series connected cells resulting in losses in the photogenerated current and the FF of the produced modules.

Third, is the electrical conductivity of the transparent electrode. Although ITO is the most applied transparent electrode in OPV devices, its conductivity stands against the generated current in large scale devices. Not only its conductivity but also its rigidity limits the flexibility of the OPV devices

Fourth, the top electrode in OPV devices usually is evaporated which increase the cost of the large-scale production, therefore the boost of the solution processed electrodes is required in the high throughput production.

Finally, the stability of the OPV modules is still far from the required market need of 10 years lifetime. Therefore, new encapsulation mechanisms are needed.

The main investigation carried out in this thesis was about the challenges that OPV device face through the upscaling processing from blade coating to roll-to-roll deposition technique. In addition to synthesize and apply new materials seeking highly efficient devices and correlated their photovoltaic performance to the molecular structure of the BHJ in the photoactive layer. Furthermore, deepen the understanding of the degradation sources in OPV devices and their effect on the device's lifetime.

1.11 References of Chapter 1

[1] J. Schindler and Werner Zittel, “Crude oil- the supply out look,” *Ludwig-Boelkow-Foundation*, no. February, 2008.

[2] Jenny Nelson, *The physics of solar cells*. Imperial College, 2002.

[3] R. A. Voloshin, M. V. Rodionova, S. K. Zharmukhamedov, H. J. M. Hou, J.-R. Shen, and S. I. Allakhverdiev, “Components of Natural Photosynthetic Apparatus in Solar Cells,” *Appl. Photosynth. - New Prog.*, 2016, doi: 10.5772/62238.

[4] K. W. Böer, *The physics of solar cells*, vol. 50, no. 8. 1979.

[5] “Mini-Modules and Tandem Organic Solar Cells : Strategies to improve device efficiency Mini-Modules and Tandem Organic Solar Cells : Strategies to improve device efficiency,” 2014.

[6] M. A. Fusella, Y. L. Lin, and B. P. Rand, *20 - Organic photovoltaics (OPVs): Device physics*, 2nd ed. Elsevier Ltd., 2019.

[7] R. Perez and M. Perez, “A Fundamental Look At Supply Side Energy Reserves For The Planet,” *Int. Energy Agency SHC Program. Sol. Updat.*, vol. 62, no. April 2009, pp. 4–6, 2015, [Online]. Available: http://www.iea-shc.org/data/sites/1/publications/2015-11-A-Fundamental-Look-at-Supply-Side-Energy-Reserves-for-the-Planet.pdf.

[8] D. Li, W. Y. Lai, Y. Z. Zhang, and W. Huang, “Printable Transparent Conductive Films for Flexible Electronics,” *Adv. Mater.*, vol. 30, no. 10, pp. 1–24, 2018, doi: 10.1002/adma.201704738.

[9] L. Lucera *et al.*, “Highly efficient, large area, roll coated flexible and rigid OPV modules with geometric fill factors up to 98.5% processed with commercially available materials,” *Energy Environ. Sci.*, vol. 9, no. 1, pp. 89–94, Jan. 2016, doi: 10.1039/C5EE03315B.

[10] N. Kim, H. Kang, J. H. Lee, S. Kee, S. H. Lee, and K. Lee, “Highly conductive all-plastic electrodes fabricated using a novel chemically controlled transfer-printing method,” *Adv. Mater.*, vol. 27, no. 14, pp. 2317–2323, 2015, doi: 10.1002/adma.201500078.

[11] M. Schr *et al.*, “Reel-to-reel wet coating by variation of solvents and compounds of photoactive inks for polymer solar cell production,” *Sol. Energy Mater. Sol. Cells*, vol. 107, pp. 283–291, 2012, doi: 10.1016/j.solmat.2012.06.048.

[12] M. S. White *et al.*, “Ultrathin, highly flexible and stretchable PLEDs,” *Nat. Photonics*, vol. 7, no. 10, pp. 811–816, 2013, doi: 10.1038/nphoton.2013.188.

[13] O. Par *et al.*, “The Binding Energy of Charge-Transfer Excitons Localized at Polymeric Semiconductor Heterojunctions,” pp. 7114–7119, 2011.

[14] T. M. Clarke and J. R. Durrant, “Charge photogeneration in organic solar cells,” *Chem. Rev.*, vol. 110, no. 11, pp. 6736–6767, 2010, doi: 10.1021/cr900271s.

[15] J. Frenkel, “On the transformation of light into heat in solids. i,” *Phys. Rev.*, vol. 37, no. 1, pp. 17–44, Jan. 1931, doi: 10.1103/PhysRev.37.17.

[16] R. Fu *et al.*, “U.S. Solar Photovoltaic System and Energy Storage Cost Benchmark: Q1 2020,” *Natl. Renew. Energy Lab.*, no. September, pp. 1–120, 2021, [Online]. Available: https://www.nrel.gov/docs/fy21osti/77324.pdf.

[17] S. R. Scully and M. D. McGehee, “Effects of optical interference and energy transfer on exciton diffusion length measurements in organic semiconductors,” *J. Appl. Phys.*, vol. 100, no. 3, p. 034907, Aug. 2006, doi: 10.1063/1.2226687.

[18] C. W. Tang and A. C. Albrecht, “cells *,” vol. 62, no. 6, pp. 2139–2149, 1975.

[19] D. Keaens and M. Calvin, “Photovoltaic effect and photoconductivity in laminated organic systems,” *J. Chem. Phys.*, vol. 29, no. 4, pp. 950–951, 1958, doi: 10.1063/1.1744619.

[20] P. Peumans, A. Yakimov, and S. R. Forrest, “Small molecular weight organic thin-film photodetectors and solar cells,” *J. Appl. Phys.*, vol. 93, no. 7, p. 3693, Mar. 2003, doi: 10.1063/1.1534621.

[21] Y. Terao, H. Sasabe, and C. Adachi, “Correlation of hole mobility, exciton diffusion length, and solar cell characteristics in phthalocyanine/fullerene organic solar cells,” *Appl. Phys. Lett.*, vol. 90, no. 10, p. 103515, Mar. 2007, doi: 10.1063/1.2711525.
[22] R. R. Lunt, N. C. Giebink, A. A. Belak, J. B. Benziger, and S. R. Forrest, “Exciton diffusion lengths of organic semiconductor thin films measured by spectrally resolved photoluminescence quenching,” *J. Appl. Phys.*, vol. 105, no. 5, p. 053711, Mar. 2009, doi: 10.1063/1.3079797.
[23] R. Kroon, M. Lenes, J. C. Hummelen, P. W. M. Blom, and B. De Boer, “Small bandgap polymers for organic solar cells (polymer material development in the last 5 years),” *Polym. Rev.*, vol. 48, no. 3, pp. 531–582, Jul. 2008, doi: 10.1080/15583720802231833.
[24] C. Deibe, T. Strobe, and V. Dyakonov, “Role of the charge transfer state in organic donor-acceptor solar cells,” *Adv. Mater.*, vol. 22, no. 37, pp. 4097–4111, 2010, doi: 10.1002/adma.201000376.
[25] X. Liu, B. P. Rand, and S. R. Forrest, “Engineering Charge-Transfer States for Efficient, Low-Energy-Loss Organic Photovoltaics,” *Trends Chem.*, vol. 1, no. 9, pp. 815–829, 2019, doi: 10.1016/j.trechm.2019.08.001.
[26] M. P. De Jong, L. J. Van Ijzendoorn, and M. J. A. De Voigt, “Stability of the interface between indium-tin-oxide and poly(3,4-ethylenedioxythiophene)/poly(styrenesulfonate) in polymer light-emitting diodes,” *Appl. Phys. Lett.*, vol. 77, no. 14, p. 2255, Sep. 2000, doi: 10.1063/1.1315344.
[27] B. Kannan, K. Castelino, and A. Majumdar, “Design of Nanostructured Heterojunction Polymer Photovoltaic Devices,” *Nano Lett.*, vol. 3, no. 12, pp. 1729–1733, Dec. 2003, doi: 10.1021/NL034810V.
[28] M. C. Scharber *et al.*, “Design Rules for Donors in Bulk-Heterojunction Solar Cells—Towards 10 % Energy-Conversion Efficiency,” *Adv. Mater.*, vol. 18, no. 6, pp. 789–794, Mar. 2006, doi: 10.1002/ADMA.200501717.
[29] N. S. Sariciftci, L. Smilowitz, A. J. Heeger, and F. Wudl, “Photoinduced electron transfer from a conducting polymer to buckminsterfullerene,” *Science*, vol. 258, no. 5087, pp. 1474–1476, 1992, doi: 10.1126/SCIENCE.258.5087.1474.
[30] P. Peumans and S. R. Forrest, “Separation of geminate charge-pairs at donor–acceptor interfaces in disordered solids,” *Chem. Phys. Lett.*, vol. 398, no. 1–3, pp. 27–31, Nov. 2004, doi: 10.1016/J.CPLETT.2004.09.030.
[31] E. A. Silinsh and V. Cápek, “Organic molecular crystals: interaction, localization, and transport phenomena,” *Choice Rev. Online*, vol. 32, no. 10, pp. 32-5670-32–5670, Jun. 1995, doi: 10.5860/choice.32-5670.
[32] C. Guo, W. Hong, H. Aziz, and Y. Li, “Recent Progress in High Mobility Polymer Semiconductors for Organic Thin Film Transistors,” *Rev. Adv. Sci. Eng.*, vol. 1, no. 3, pp. 200–224, Sep. 2012, doi: 10.1166/rase.2012.1014.
[33] S. S. Sun and L. R. Dalton, “Introduction to organic electronic and optoelectronic materials and devices: Second edition,” *Introd. to Org. Electron. Optoelectron. Mater. Devices Second Ed.*, pp. 1–1069, Oct. 2016, doi: 10.1201/9781315374185.
[34] A. Andersson, N. Johansson, P. Bröms, N. Yu, D. Lupo, and W. R. Salaneck, “Fluorine Tin Oxide as an Alternative to Indium Tin Oxide in Polymer LEDs,” *Adv. Mater.*, vol. 10, no. 11, pp. 859–863, 1998, doi: 10.1002/(sici)1521-4095(199808)10:11<859::aid-adma859>3.3.co;2-t.
[35] R. Steim, F. R. Kogler, and C. J. Brabec, “Interface materials for organic solar cells,” *J. Mater. Chem.*, vol. 20, no. 13, pp. 2499–2512, Mar. 2010, doi: 10.1039/B921624C.
[36] A. McEvoy, T. Markvart, and L. Castañer, *Solar Cells*. Elsevier Ltd, 2013.
[37] W. Shockley, “The Theory of p-n Junctions in Semiconductors and p-n Junction Transistors,” *Bell Syst. Tech. J.*, vol. 28, no. 3, pp. 435–489, Jul. 1949, doi: 10.1002/j.1538-7305.1949.tb03645.x.
[38] W. Shockley and W. T. Read, “Statistics of the recombinations of holes and electrons,” *Phys. Rev.*, vol. 87, no. 5, pp. 835–842, Sep. 1952, doi: 10.1103/PhysRev.87.835.

[39] C. J. Brabec, S. Gowrisanker, J. J. M. Halls, D. Laird, S. Jia, and S. P. Williams, “Polymer-fullerene bulk-heterojunction solar cells,” *Adv. Mater.*, vol. 22, no. 34, pp. 3839–3856, Sep. 2010, doi: 10.1002/adma.200903697.

[40] P. Cheng, G. Li, X. Zhan, and Y. Yang, “Next-generation organic photovoltaics based on non-fullerene acceptors /639/301/299/946 /639/624/399 review-article,” *Nature Photonics*, vol. 12, no. 3. Nature Publishing Group, pp. 131–142, Mar. 01, 2018, doi: 10.1038/s41566-018-0104-9.

[41] Y. Cui *et al.*, “Single-Junction Organic Photovoltaic Cells with Approaching 18% Efficiency,” *Adv. Mater.*, vol. 32, no. 19, p. 1908205, May 2020, doi: 10.1002/adma.201908205.

[42] L. Meng *et al.*, “Organic and solution-processed tandem solar cells with 17.3% efficiency.,” *Science*, vol. 361, no. 6407, pp. 1094–1098, Aug. 2018, doi: 10.1126/SCIENCE.ACSAMI2612.

[43] T. Y. Li *et al.*, “Small molecule near-infrared boron dipyrromethene donors for organic tandem solar cells,” *J. Am. Chem. Soc.*, vol. 139, no. 39, pp. 13636–13639, Oct. 2017, doi: 10.1021/JACS.7B07887/SUPPL_FILE/JA7B07887_SI_004.CIF.

[44] J. Hou, O. Inganas, R. H. Friend, and F. Gao, “Organic solar cells based on non-fullerene acceptors,” *Nat. Mater.*, vol. 17, no. 2, pp. 119–128, 2018, doi: 10.1038/NMAT5063.

[45] H. Hu *et al.*, “Effect of Ring-Fusion on Miscibility and Domain Purity: Key Factors Determining the Performance of PDI-Based Nonfullerene Organic Solar Cells,” *Adv. Energy Mater.*, vol. 8, no. 26, Sep. 2018, doi: 10.1002/AENM.201800234.

[46] A. D. Hendsbee *et al.*, “Synthesis, self-assembly, and solar cell performance of N-annulated perylene diimide non-fullerene acceptors,” *Chem. Mater.*, vol. 28, no. 19, pp. 7098–7109, Oct. 2016, doi: 10.1021/ACS.CHEMMATER.6B03292/SUPPL_FILE/CM6B03292_SI_001.PDF.

[47] C. B. Nielsen, S. Holliday, H. Y. Chen, S. J. Cryer, and I. McCulloch, “Non-Fullerene Electron Acceptors for Use in Organic Solar Cells,” *Acc. Chem. Res.*, vol. 48, no. 11, pp. 2803–2812, 2015, doi: 10.1021/acs.accounts.5b00199.

[48] V. Sharma, J. D. B. Koenig, and G. C. Welch, “Perylene diimide based non-fullerene acceptors: top performers and an emerging class featuring N-annulation,” *J. Mater. Chem. A*, vol. 9, no. 11, pp. 6775–6789, 2021, doi: 10.1039/d0ta11197j.

[49] L. Gao *et al.*, “All-Polymer Solar Cells Based on Absorption-Complementary Polymer Donor and Acceptor with High Power Conversion Efficiency of 8.27%,” *Adv. Mater.*, vol. 28, no. 9, pp. 1884–1890, Mar. 2016, doi: 10.1002/ADMA.201504629.

[50] S. Li *et al.*, “Green-Solvent-Processed All-Polymer Solar Cells Containing a Perylene Diimide-Based Acceptor with an Efficiency over 6.5%,” *Adv. Energy Mater.*, vol. 6, no. 5, p. 1501991, Mar. 2016, doi: 10.1002/AENM.201501991.

[51] D. Mori, H. Benten, I. Okada, H. Ohkita, and S. Ito, “Highly efficient charge-carrier generation and collection in polymer/polymer blend solar cells with a power conversion efficiency of 5.7%,” *undefined*, vol. 7, no. 9, pp. 2939–2943, 2014, doi: 10.1039/C4EE01326C.

[52] Y. Guo *et al.*, “Improved Performance of All-Polymer Solar Cells Enabled by Naphthodiperylenetetraimide-Based Polymer Acceptor,” *Adv. Mater.*, vol. 29, no. 26, Jul. 2017, doi: 10.1002/ADMA.201700309.

[53] H. J. Kim, H. H. Lee, and J. J. Kim, “Real Time Investigation of the Interface between a P3HT:PCBM Layer and an Al Electrode during Thermal Annealing,” *Macromol. Rapid Commun.*, vol. 30, no. 14, pp. 1269–1273, Jul. 2009, doi: 10.1002/MARC.200900224.

[54] A. Guerrero, P. P. Boix, L. F. Marchesi, T. Ripolles-Sanchis, E. C. Pereira, and G. Garcia-Belmonte, “Oxygen doping-induced photogeneration loss in P3HT:PCBM solar cells,” *Sol. Energy Mater. Sol. Cells*, vol. Complete, no. 100, pp. 185–191, May 2012, doi: 10.1016/J.SOLMAT.2012.01.012.

[55] M. Jørgensen, K. Norrman, and F. C. Krebs, “Stability/degradation of polymer solar

cells," *Sol. Energy Mater. Sol. Cells*, vol. 92, no. 7, pp. 686–714, Jul. 2008, doi: 10.1016/J.SOLMAT.2008.01.005.
[56] T. S. Glen *et al.*, "Grain size dependence of degradation of aluminium/calcium cathodes in organic solar cells following exposure to humid air," *Sol. Energy Mater. Sol. Cells*, vol. C, no. 140, pp. 25–32, Sep. 2015, doi: 10.1016/J.SOLMAT.2015.03.015.
[57] B. Ecker *et al.*, "Degradation Effects Related to the Hole Transport Layer in Organic Solar Cells," *Adv. Funct. Mater.*, vol. 21, no. 14, pp. 2705–2711, Jul. 2011, doi: 10.1002/ADFM.201100429.
[58] G. E. Morse *et al.*, "The effect of polymer solubilizing side-chains on solar cell stability," *Phys. Chem. Chem. Phys.*, vol. 17, no. 17, pp. 11884–11897, May 2015, doi: 10.1039/C5CP01158B.
[59] J. Kesters *et al.*, "Enhanced organic solar cell stability by polymer (PCPDTBT) side chain functionalization," *Chem. Mater.*, vol. 27, no. 4, pp. 1332–1341, Feb. 2015, doi: 10.1021/CM504391K.
[60] X. Wang *et al.*, "Morphology related photodegradation of low-band-gap polymer blends," *Adv. Energy Mater.*, vol. 4, no. 17, Dec. 2014, doi: 10.1002/AENM.201400497.
[61] N. K. Zawacka *et al.*, "The influence of additives on the morphology and stability of roll-to-roll processed polymer solar cells studied through ex situ and in situ X-ray scattering," *J. Mater. Chem. A*, vol. 2, no. 43, pp. 18644–18654, Oct. 2014, doi: 10.1039/C4TA03484H.
[62] W. Kim, J. K. Kim, E. Kim, T. K. Ahn, D. H. Wang, and J. H. Park, "Conflicted effects of a solvent additive on PTB7:PC71BM bulk heterojunction solar cells," *J. Phys. Chem. C*, vol. 119, no. 11, pp. 5954–5961, Mar. 2015, doi: 10.1021/JP510996W/SUPPL_FILE/JP510996W_SI_001.PDF.
[63] A. Tournebize, A. Rivaton, H. Peisert, and T. Chassé, "The crucial role of confined residual additives on the photostability of P3HT:PCBM active layers," *J. Phys. Chem. C*, vol. 119, no. 17, pp. 9142–9148, Apr. 2015, doi: 10.1021/ACS.JPCC.5B01733/SUPPL_FILE/JP5B01733_SI_001.PDF.
[64] L. Zhao and T. C. W. Mak, "Silver(I)-thiophene π interaction in the assembly of coordination networks with the supramolecular synthons R-C≡C⊃Agn (R = 2- Or 3-thienyl; n = 4)," *Organometallics*, vol. 26, no. 18, pp. 4439–4448, Aug. 2007, doi: 10.1021/om700370p.
[65] M. T. Lloyd *et al.*, "Impact of contact evolution on the shelf life of organic solar cells," *J. Mater. Chem.*, vol. 19, no. 41, pp. 7638–7642, Oct. 2009, doi: 10.1039/B910213B.
[66] M. Jørgensen *et al.*, "Stability of Polymer Solar Cells," *Adv. Mater.*, vol. 24, no. 5, pp. 580–612, Feb. 2012, doi: 10.1002/ADMA.201104187.
[67] J. Nishinaga, T. Aihara, H. Yamagata, and Y. Horikoshi, "Mechanical and optical characteristics of Al-doped C60 films," *J. Cryst. Growth*, vol. 278, no. 1–4, pp. 633–637, May 2005, doi: 10.1016/J.JCRYSGRO.2004.12.083.
[68] E. Voroshazi, B. Verreet, A. Buri, R. Müller, D. Di Nuzzo, and P. Heremans, "Influence of cathode oxidation via the hole extraction layer in polymer:fullerene solar cells," *Org. Electron.*, vol. 12, no. 5, pp. 736–744, May 2011, doi: 10.1016/J.ORGEL.2011.01.025.
[69] H. Jin, M. Tuomikoski, J. Hiltunen, P. Kopola, A. Maaninen, and F. Pino, "Polymer−Electrode Interfacial Effect on Photovoltaic Performances in Poly(3-hexylthiophene):Phenyl-C61-butyric Acid Methyl Ester Based Solar Cells," *J. Phys. Chem. C*, vol. 113, no. 38, pp. 16807–16810, Sep. 2009, doi: 10.1021/JP906277K.
[70] M. Manceau, A. Rivaton, J. L. Gardette, S. Guillerez, and N. Lemaître, "Light-induced degradation of the P3HT-based solar cells active layer," *Sol. Energy Mater. Sol. Cells*, vol. 95, no. 5, pp. 1315–1325, May 2011, doi: 10.1016/J.SOLMAT.2010.09.021.
[71] R. Betancur, Maymóc, X. Elias, L. T. Vuong, and J. Martorell, "Sputtered NiO as electron blocking layer in P3HT:PCBM solar cells fabricated in ambient air," *Sol. Energy Mater. Sol. Cells*, vol. 95, no. 2, pp. 735–739, Feb. 2011, doi: 10.1016/J.SOLMAT.2010.10.014.

[72] P. Qin *et al.*, “Nitrogen doped amorphous chromium oxide: Stability improvement and application for the hole-transporting layer of organic solar cells,” *Sol. Energy Mater. Sol. Cells*, vol. 95, no. 3, pp. 1005–1010, Mar. 2011, doi: 10.1016/J.SOLMAT.2010.12.015.
[73] M. Wang *et al.*, “Device lifetime improvement of polymer-based bulk heterojunction solar cells by incorporating copper oxide layer at Al cathode,” *Appl. Phys. Lett.*, vol. 98, no. 18, p. 183304, May 2011, doi: 10.1063/1.3580629.
[74] Y. Wang, L. Yang, C. Yao, W. Qin, S. Yin, and F. Zhang, “Enhanced performance and stability in polymer photovoltaic cells using lithium benzoate as cathode interfacial layer,” *Sol. Energy Mater. Sol. Cells*, vol. 95, no. 4, pp. 1243–1247, Apr. 2011, doi: 10.1016/J.SOLMAT.2011.01.012.
[75] S. O. Jeon and J. Y. Lee, “Improved high temperature stability of organic solar cells using a phosphine oxide type cathode modification layer,” *Sol. Energy Mater. Sol. Cells*, vol. 95, no. 4, pp. 1102–1106, Apr. 2011, doi: 10.1016/J.SOLMAT.2010.12.022.
[76] F. C. Chen, J. L. Wu, S. S. Yang, K. H. Hsieh, and W. C. Chen, “Cesium carbonate as a functional interlayer for polymer photovoltaic devices,” *J. Appl. Phys.*, vol. 103, no. 10, p. 103721, May 2008, doi: 10.1063/1.2937202.
[77] L. Yang, H. Xu, H. Tian, S. Yin, and F. Zhang, “Effect of cathode buffer layer on the stability of polymer bulk heterojunction solar cells,” *Sol. Energy Mater. Sol. Cells*, vol. 94, no. 10, pp. 1831–1834, Oct. 2010, doi: 10.1016/J.SOLMAT.2010.05.043.
[78] A. Rivaton, A. Tournebize, J. Gaume, P. O. Bussière, J. L. Gardette, and S. Therias, “Photostability of organic materials used in polymer solar cells,” *Polym. Int.*, vol. 63, no. 8, pp. 1335–1345, Aug. 2014, doi: 10.1002/PI.4656.
[79] S. Chambon, A. Rivaton, J. L. Gardette, M. Firon, and L. Lutsen, “Aging of a donor conjugated polymer: Photochemical studies of the degradation of poly[2-methoxy-5-(3′,7′-dimethyloctyloxy)-1,4-phenylenevinylene],” *J. Polym. Sci. Part A Polym. Chem.*, vol. 45, no. 2, pp. 317–331, Jan. 2007, doi: 10.1002/POLA.21815.
[80] S. Chambon, A. Rivaton, J. L. Gardette, and M. Firon, “Reactive intermediates in the initiation step of the photo-oxidation of MDMO-PPV,” *J. Polym. Sci. Part A Polym. Chem.*, vol. 47, no. 22, pp. 6044–6052, Nov. 2009, doi: 10.1002/POLA.23628.
[81] A. Dupuis, P. Wong-Wah-Chung, A. Rivaton, and J. L. Gardette, “Influence of the microstructure on the photooxidative degradation of poly(3-hexylthiophene),” *Polym. Degrad. Stab.*, vol. 97, no. 3, pp. 366–374, Mar. 2012, doi: 10.1016/J.POLYMDEGRADSTAB.2011.12.012.
[82] N. Sai, K. Leung, J. Zádor, and G. Henkelman, “First principles study of photo-oxidation degradation mechanisms in P3HT for organic solar cells,” *Phys. Chem. Chem. Phys.*, vol. 16, no. 17, pp. 8092–8099, Apr. 2014, doi: 10.1039/C4CP00146J.
[83] M. Manceau, A. Rivaton, J. L. Gardette, S. Guillerez, and N. Lemaître, “The mechanism of photo- and thermooxidation of poly(3-hexylthiophene) (P3HT) reconsidered,” *Polym. Degrad. Stab.*, vol. 94, no. 6, pp. 898–907, Jun. 2009, doi: 10.1016/J.POLYMDEGRADSTAB.2009.03.005.
[84] A. Tournebize *et al.*, “Impact of UV-Visible Light on the Morphological and Photochemical Behavior of a Low-Bandgap Poly(2,7-Carbazole) Derivative for Use in High-Performance Solar Cells,” *Adv. Energy Mater.*, vol. 3, no. 4, pp. 478–487, Apr. 2013, doi: 10.1002/AENM.201200662.
[85] P. O. Bussière, A. Rivaton, S. Thérias, and J. L. Gardette, “Multiscale Investigation of the Poly(N-vinylcarbazole) Photoageing Mechanism,” *J. Phys. Chem. B*, vol. 116, no. 2, pp. 803–812, Jan. 2012, doi: 10.1021/JP211358Q.
[86] J. Razzell-Hollis, J. Wade, W. C. Tsoi, Y. Soon, J. Durrant, and J. S. Kim, “Photochemical stability of high efficiency PTB7:PC 70 BM solar cell blends,” *J. Mater. Chem. A*, vol. 2, no. 47, pp. 20189–20195, Nov. 2014, doi: 10.1039/C4TA05641H.
[87] M. R. Lilliedal, A. J. Medford, M. V. Madsen, K. Norrman, and F. C. Krebs, “The effect of post-processing treatments on inflection points in current–voltage curves of roll-to-roll processed polymer photovoltaics,” *Sol. Energy Mater. Sol. Cells*, vol. 94, no. 12, pp. 2018–2031, Dec. 2010, doi: 10.1016/J.SOLMAT.2010.06.007.

[88] M. Manceau, M. Helgesen, and F. C. Krebs, “Thermo-cleavable polymers: Materials with enhanced photochemical stability,” *Polym. Degrad. Stab.*, vol. 95, no. 12, pp. 2666–2669, Dec. 2010, doi: 10.1016/j.polymdegradstab.2010.08.004.

[89] Y. W. Soon *et al.*, “Material Crystallinity as a Determinant of Triplet Dynamics and Oxygen Quenching in Donor Polymers for Organic Photovoltaic Devices,” *Adv. Funct. Mater.*, vol. 24, no. 10, pp. 1474–1482, Mar. 2014, doi: 10.1002/ADFM.201302612.

[90] W. R. Mateker *et al.*, “Molecular Packing and Arrangement Govern the Photo-Oxidative Stability of Organic Photovoltaic Materials,” *Chem. Mater.*, vol. 27, no. 18, pp. 6345–6353,Sep.2015,doi:10.1021/ACS.CHEMMATER.5B02341/SUPPL_FILE/CM5B02341_SI_001.

[91] M. S. White, D. C. Olson, S. E. Shaheen, N. Kopidakis, and D. S. Ginley, “Inverted bulk-heterojunction organic photovoltaic device using a solution-derived ZnO underlayer,” *Appl. Phys. Lett.*, vol. 89, no. 14, p. 143517, Oct. 2006, doi: 10.1063/1.2359579.

[92] M. H. Chen, Y. C. Kuo, H. H. Lin, Y. P. Chao, and M. S. Wong, “Highly stable inverted organic photovoltaics using aluminum-doped zinc oxide as electron transport layers,” *J. Power Sources*, vol. 275, pp. 274–278, 2015, doi: 10.1016/j.jpowsour.2014.11.011.

[93] Y. Yan *et al.*, “Best Research-Cell Efficiency Chart | Photovoltaic Research | NREL,” *Journal of the American Chemical Society*, vol. 5, no. 5. pp. 1–8, 2020, Accessed: Mar. 28, 2022. [Online]. Available: https://www.nrel.gov/pv/cell-efficiency.html.

Chapter 2 Experimental work

Abstract

In this chapter, the materials used in the different processing techniques applied to prepare the OPV devices were presented. Solution processing techniques were pointed out as the main coating techniques like blade coating, slot die roll-to-roll and screen printing. Insights about not only lab-scale devices preparation of semitransparent devices and ITO free OPV devices but also large-scale OPV modules preparation were shown. Coating recipe of preparing the lab-scale devices and printing conditions of the roll-to-rolled modules were listed as well.

Furthermore, towards the cost reduction a modification of the slot die head has been carried out giving the ability to fit the use of small amount of the inks will be explained.

Characterization protocol of the applied inks to test their printing reliability according to the applied printing techniques were employed. After the inks revealed the printing ability, thin layers are printed and then characterized. Preparing OPV devices or modules of different printed layers in the inverted structure. Characterization of the prepared devices and modules was elaborated. Further experiments to study the degradation of the prepared OPV modules were illustrated.

This work has been done in different labs, most of the experiments were carried out in Eurecat and in ICMAB. Under SEPOMO umbrella of the ITN network framework, two entities were involved in this thesis through two secondments one in Merck Ltd. (chapter five) and second in the University of Wurzburg (chapter six).

2.1 Materials

Since most of the OPV devices in this thesis were realized with the inverted structure of substrate/bottom electrode/ ETL/PAL/HTL/top electrode, the materials will be listed following the same order.

2.1.1 Substrates and bottom electrodes

In case of the substrate with the bottom electrode, different types have been used, depending on the experiment.

For lab scale devices prepared by blade coating, patterned substrates were used as following:

1- (In Eurecat) Patterned 25 x 25 mm ITO-coated glass slides were purchased from PsiOTec Ltd. The pattern consisted of a central strip (19 x 25 mm) with sheet resistance 24 Ω/□.
2- (In ICMAB) Patterned ITO coated glass (25x75 mm) provided from Ossila with sheet resistance 20 Ω/□ and thickness of 100 nm.
3- (In Merck) Patterned 5x5 cm ITO coated glass slides provided by Merck with a sheet resistance of 5 Ω/□

In case of the devices prepared by roll-to-roll methods, the substrates that have been used are the following ones:

1- (In Eurecat) ITO strip coated PET with 50 Ω/□ and 150 nm thickness, provided by Technifilm.
2- (In Merck) IMI (Insultor-Metal-Insultor) patterned PET with sheet resistance 7 Ω/□. The IMI substrates rolls had dimensions 165 mm ×150 m and were laser patterned with a Rofin1064 nm Nd: YVO_4 laser.

2.1.2 Electron transport layer

Both ZnO and AZO have been used for the electron transport layer. In the early work of this thesis Zinc Oxide (ZnO), used for the ETL for both lab-scale devices and modules printed by roll-to-roll, however AZO supplied form Avantma N-21X replaced the ZnO due to the better process ability and the more conductivity. ZnO was prepared in the lab in Eurecat by sol gel method as shown in Figure 2.1.

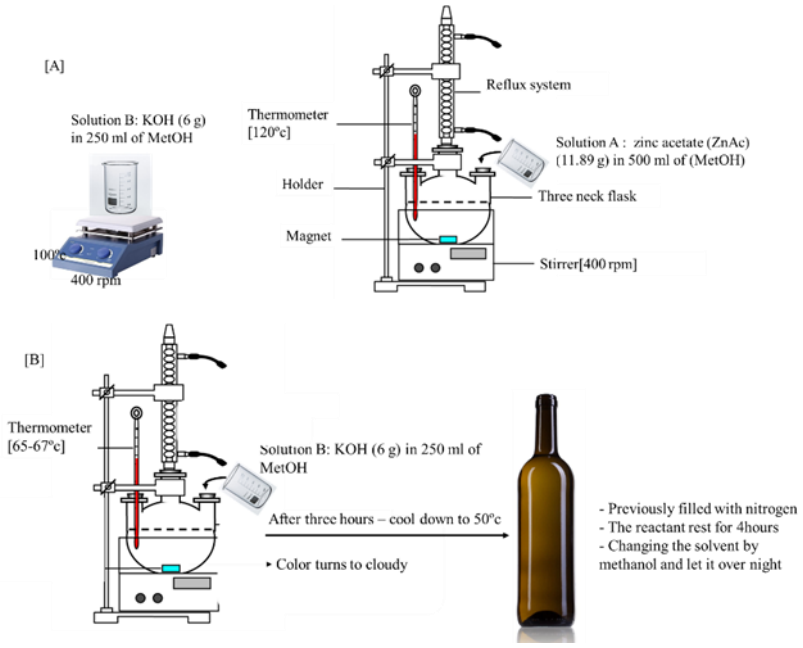

Figure 2.1 the procedure to prepare ZnO by sol gel.

1. Preparing two solutions: one solution of zinc acetate (ZnAc) (11.89 g) in 500 ml of methanol (MetOH) and the second solution of KOH (6 g) in 250 ml of MetOH.

2. Placing the first solution in three neck flask connected to a reflux system and surrounded with aluminum foil to keep the temperature homogenous on a hot plate at T = 120 ° C and adjust the magnetic stirrer at 400 rpm. A thermometer was place inside the flask to indicate the reaction temperature. The KOH solution in a beaker covered with the large watch glass on another plate at T = 100 ° C and 400 rpm.

3. When the thermometer indicates T> 60 ° C, the KOH solution was added to the flask.

4. The mixture should become cloudy and become transparent in a few moments. The reaction should be with reflux for 3 hours.

Controlling the temperature in the flask, and keep the T stablilzed between 65 and 67 °C.

5. After 3 hours, the plate turned off and the solution cooled down to 50 ° C. Then, the dispersion transferred to a previously filled bottle of N2 in the glove-box and rest for 4 hours.

6. After 4 hours, the solvent changed by methanol by delicate pouring of the supernatant into another container and new methanol was added.

7. Next day, all of the supernatant removed with a syringe and the remaining volume of ink was weighted and calculated it in the excel sheet. A 16% by weight of dispersant, of 2-[2- (2-Methoxyethoxy) ethoxy] acetic acid (MEA) was added. In the excel sheet prepared for dilution calculations enter the total volume of ink, sum of the volume prior to the addition of MEA, plus that of MEA added. Finally, the required ZnO concentration was adjusted by adding the corresponding amount of methanol and the whole dispersion was filtered with a 0.2 µm PTFE filter.

ZnO was applied as an ETL since it is the most common metal oxide ETL used in OPV devices due to its relatively high electron mobility, transparency, wide direct bandgap [3.2

eV] and solution process ability[1]. However later on in this studies it has been replaced with Aluminum doped Zinc oxide [AZO]. The replacement was due to processing issues raised while printing by roll-to-roll technique, whitish color and less adhesion to the ITO layer even after applying corona to PET coated ITO surface. The printed ZnO was easy to be removed by rolling the whole web. The performance of the OPV devices with ZnO as ETL was pretty close to OPV devices with AZO as ETL on the average performance despite the best cell performance [see Figure 2.2] was pretty higher PCE 2.4% with AZO than in case of the ZnO of PCE 1.8% as shown in Table 2.1. The reproducibility problems of ZnO has been reported[2,3] since ZnO tends to form trap states associated with defects. In AZO the doping of the ZnO with Al improving the wettability of the ETL on top of the P3HT: PSS layer as it introduces electrical polarization into the ZnO lattice as reported[4,5]. SEM images of both ETLs deposited by blade coating on glass were shown in Figure 2.3. Moreover, the AZO has been used as it is more conductive and as a result of the band gap shift the depletion region on both sides of the ETL has reduced than in case of ZnO which cause more charge carriers to tunnel the barrier.

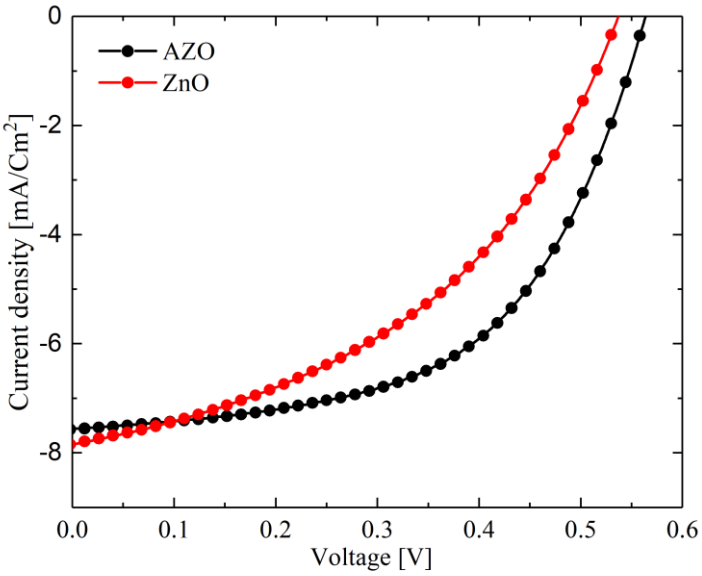

Figure 2.2 The JV curves of the best modules with different ETL AZO in black color and ZnO in red color.

Table 2.1 The photovoltaic performance of devices OPV modules with AZO and ZnO as ETL

.

ETL	V_{oc}[V]	J_{sc}[mA/Cm^2]	FF[%]	PCE[%]
ZnO	0.55±0.02	-6± -1	42±3	1.3±0.3
Best Cell	0.54	-7.8	44	1.8
AZO	0.52±0.07	-6.2± - 0.8	46±9	1.5±0.4
Best Cell	0.56	-7.6	56	2.4

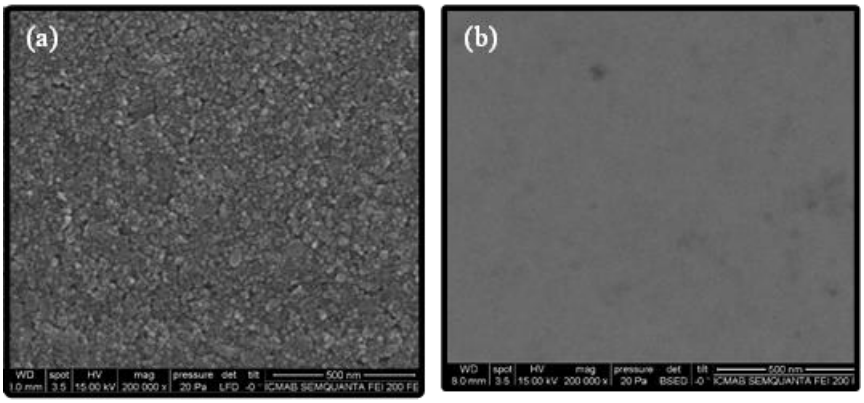

Figure 2. 3 SEM images of (a) AZO layer on glass and (b) ZnO layer on glass.

2.1.3 Photoactive layer

Both lab-scale devices and large-scale modules were constructed with inverted bulk heterojunction structure. The photo active layer (PAL) was a blend of electron donor material and electron acceptor material and also in this case, depending on the experiment, the materials for these components have been changed. The chemical structures of the Photoactive materials are shown in Figure 2.4.

The donor materials were as follows(see Figure2.4):

(A)91-94%, Mw =50-70 kDa regioregular P3HT purchased from Rieke Metals, (B) PBDB-T and (C)PCDTBT were purchased from Ossila. The photoactive layer of the roll to roll devices prepared in Merck was based on the blue donor (d)PBTZT-stat-BDTT-8, however the acceptor was not declared from Merck.

The acceptor materials were as follows (see Figure2.4):

In the framework of the collaboration with the Universidad Complutense, three small molecules were synthesized as acceptors (e) 3PIPT, (f)4PIPM, (h)PIPB; and [g] $PC_{60}BM$ > 99% purity purchased from Solenne BV.

Alll the solvents were used as delivered from Sigma-Aldrich: chlorobenzene, Chloroform, acetone, isopropanol, ethanol or methanol.

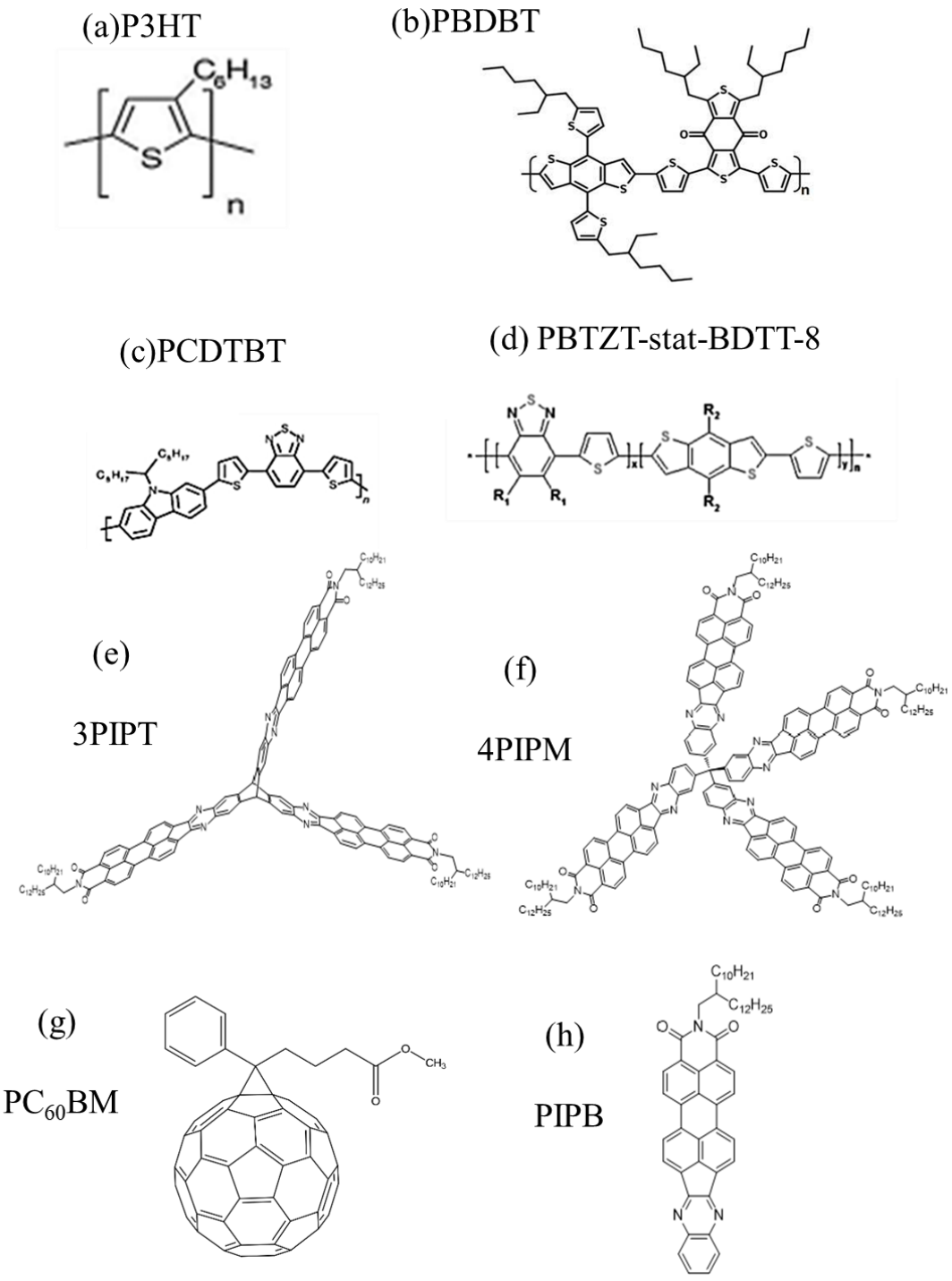

Figure 2. 4 The chemical structure of the Photo active materials in the OPV devices (a) P3HT, (b) PBDBT, (c) PBTBT, (d) PBTZT-stat-BDTT-8, (e)3PIPT, (f)4PIPM, (g) $PC_{60}BM$ and (h)PIPB.

2.1.4 Hole transport layer

For the lab scale devices (MoO_3) was thermally evaporated and the pellets were provided by Alfa Aesar.

For preparing lab scale devices in Merck (chapter two) PEDOT: PSS P VP AL 4083, Clevios solar 388 and Clevios solar 434 were applied as HTL and were provided by Heraeus.

For the roll-to-roll experiments FHC Solar PEDOT: PSS provided from Heraeus.

2.1.5 Top electrode

Silver top electrode was thermally evaporated in the lab scale devices. The silver pellets were provided from Kurt J. Lesker. However, in the large-scale modules prepared by roll-to-roll the top electrode was silver paste DuPont 5000 and was screen printed.

In either ITO-free or semitransparent lab-scale devices Poly bio wire silver nanowires (AgNWs) provided from poly ink and Clevios HYE provided from Hareous were applied as electrodes.

2.2 Processing techniques

In this section the printing techniques used for our research are introduced, with a description of the working mechanisms. The used techniques are blade coating for preparing the lab scale devices, slot die roll-to-roll and screen printing for preparing the large-scale modules.

2.2.1 Substrates cleaning

Depending on the type of substrate and the lab where the experiment was performed, differences were introduced in the process employed for cleaning the substrates(see Table 2.2).

Table 2.2 the cleaning protocol followed in each lab

Lab	Cleaning protocol
Eurecat	1. Sonication bath in acetone (5 minutes) 2. Sonication bath in isopropanol (5 minutes) 3. Sonication bath in ethanol (5 minutes) 4. Drying by nitrogen gun
Merck	1. Sonication bath in acetone (5 minutes) 2. Sonication bath in isopropanol (5 minutes) 3. Sonication bath in ethanol (5 minutes) 4. Rinsing in distilled water 5. Drying the substrates on a hot plate in air for 30 minutes
ICMAB	1. Sonication bath in acetone (5 minutes) 2. Sonication bath in10% vol. Helmanex in H2O solution (5 minutes) 3. Sonication bath in isopropanol (5 minutes) 4. Sonication bath in acetone (5 minutes) 5. Sonication bath in 10% w/v NaOH in water solution (20 minutes) 6. Drying by compressed air gun

2.2.2 Blade coating technique

Doctor blade is a non-contact solution deposition technique while applying temperature to the platform. Furthermore, this technique could be integrated to the roll-to-roll printing line. A sketch of the working principle of such technique is presented in Figure 2.5.

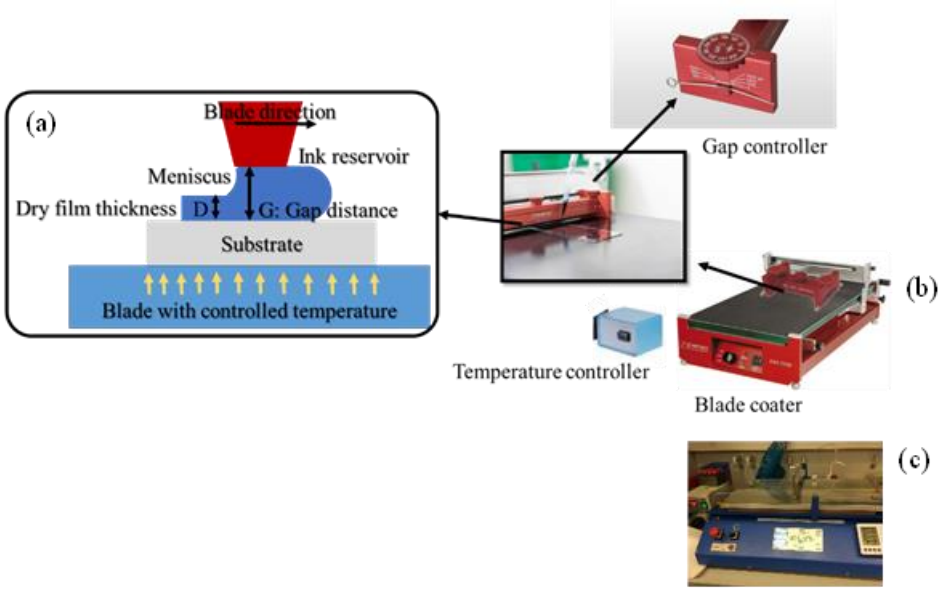

Figure 2. 5 (a) Illustration of the doctor blade process coater, (b)the blade coater at ICMAB and Eurecat and (c) the blade coater in Merck.

The deposition process starts by applying a certain ink volume, V, by the pipette in the gap height, G, between the substrate and the blade. The blade moves, accordingly with the adjusted speed, spreading the ink over the substrate, with the effect of producing a wet film on it. Adjusting the platform temperature is often useful in order to control the drying dynamics, which on its turn, has effects on the film morphology. Fast drying is preferred, in case of using high boiling point solvents, to eliminate the material inhomogeneity and, for example, to decrease the phase separation between donor and acceptor, in the case of the active layer. The temperature of the plate controls the drying dynamics and affecting the morphology of the resulted film. The maximum achieved thickness is approximately 50% of the gap height as reported[6].Towards the upscaling doctor blade is mainly applied to optimize the layer thicknesses and to allow further study over the wide range of thickness in the small scale before transmit it to the roll to roll printing technique. The blade coater used in Eurecat and in ICMAB was of model (ZUA 2300, Zehntner), however in Merck the blade coater was provided from Zhnite. The blade coater in ICMAB was modified by a home-made electronic board to allow the coating using variable blade speed, which results in a thickness gradient within the same substrate. This enables the thickness optimization within a single substrate, which has the advantage of using less material.

The resulting thickness of the dried film depends on different parameters

1- Ink properties such as rheological properties, viscosity, concentration and solvent boiling point.

2- The processing parameters such as blade speed [the faster the blade the thicker the film produced], blade height, ink volume and plate temperature.

The optimized depositing conditions of lab-scale devices in chapter two, ITO free devices and the semitransparent devices are summarized in Table 2.3.

Table 2.3 the inks formulations and the printing conditions of all the lab devices.

Printing conditions of the ITO free devices		
Ink	Formulation	Printing parameters Ink volume[µl], blade speed[mm/s],Blade gap[µm] & plate temperature [ºc]
ZnO	15 mg/ml prepared in Eurecat	40 µl, 40 mm/s,100 µm &45ºc
P3HT:PC60BM	[30:24] wt% in CB	40 µl, 5 mm/s,100 µm &45ºc
PolyBio wire	Commercial	100 µl, 40 mm/s,100 µm &80ºc
HYE	Commercial ink provided by Heraeus	60 µl, 5 mm/s,100 µm &80ºc
Semitransparent devices with AgNWs as a top electrode		
AZO	Avantama N21X	30ml, 5mm/s, 150mm, 45ºC
P3HT:PC_{60}BM	(30:24) wt % in CB	40ml, 40mm/s, 200um, 100ºC
PEDOT:PSS (FHC)	PEDOT:H2O(80:20)wt% with 0.5% Capstone	30ml, 3 mm/s, 250mm, 80ºC
PolyBio wire	Commercial	40ml, 90mm/s, 250mm, 65ºC
HYE	Commercial ink provided by Heraeus	40ml, 10mm/s, 250mm, 65ºC
AgNW	In ethanol 6mg/ml	40ml, 45mm/s, 250mm, 65ºC
OPV devices optimized based on blue ink		
AZO	Avantama N21 X	50 µl, 5 mm/s,50 µm &40ºC
Blue ink	Formulated by Merck	80 µl, 6 mm/s,100 µm &60ºC
P VP AL 4083	Commercial ink provided by Heraeus	180 µl, 5 mm/s,575 µm &65ºC
Clevios 388 & Clevios 434	Commercial inks provided by Heraeus	100 µl, 4 mm/s,200 µm &65ºC

All lab-scale devices were completed with the thermal evaporation of MoO_3, for the HTL, and silver, as the top electrode. For this step, equipment by Kurt J. Lesker is employed (Figure 2.6).

The evaporation is performed by using a shadow mask to define the shape of the top electrode, which determined the active area of the device. where six substrates, each substrate contain six devices, were placed [in Eurecat] or six substrates, each substrate contains 24 devices, were placed [in ICMAB] at high vacuum [10^{-6} mbar]. A thermal evaporator provided from Kurt J. Lesker [in Eurecat] and provided from ECOVap, MBraun [in ICMAB] attached to a glovebox where the samples were placed into the shadow mask. The thickness as well as the rate of evaporation was monitored by using an oscillating quartz crystal. The thickness of silver electrode was100 nm and the one of MoO_3 was 10 nm. The evaporation rate in case of Ag 3Å/m and in case of MoO3 was 1 Å/m. The active area was set to 25 mm^2 in [Eurecat] and 5mm^2 [in ICMAB]. In all cases, a high substrate rotation speed was set in order to minimize border shadowing effects.

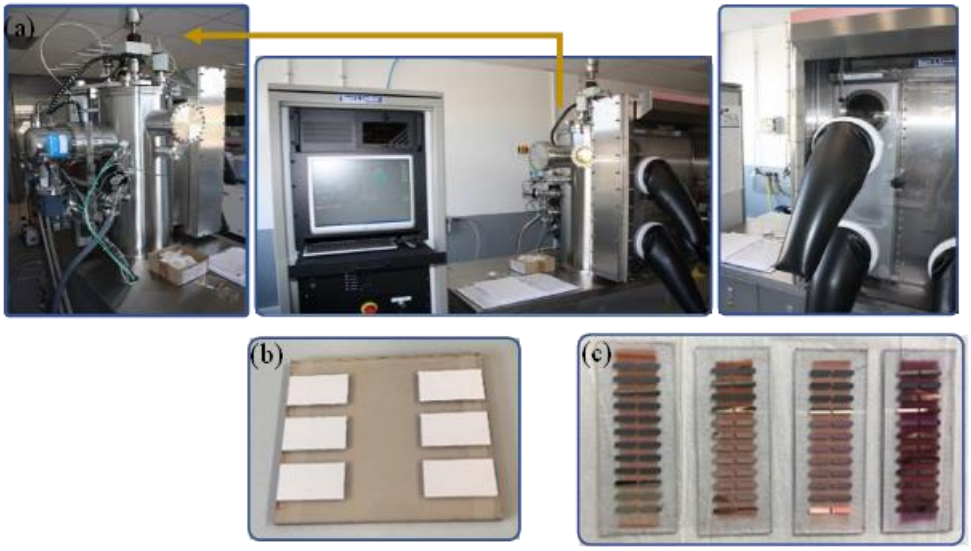

Figure 2. 6 (a) The thermal evaporator equipment in Eurecat, (b) substrate out of the thermal evaporator with 6 OPV devices[in Eurecat] and (c) the substrate after the evaporation of the MoO_3 and the silver top electrode, 24 OPV devices in each substrate, [at ICMAB].

2.2.3 Roll-to-roll technique

Devices up-scaling was performed by using roll-to-roll technology that allows high throughput processing. Slot-die and mini roll-to-roll, shown in Figure 2.7 and Figure 2.8, are the machines used in this work. Coating by the slot die takes place through moving a web of flexible substrate aligned along the whole machine. The head is continuously filled with the ink by a syringe pump as showed in Figure 2.7 c). A wide range of inks viscosity [0.1-1000 Pa·s] is compatible with slot-die technique. The wet thickness is controlled by different factors, mostly the pumping rate and the web speed. The web moves in a wide range of speed: 1-600 m/min. The dried film thickness could be between 50 nm up to 2 dimensions. The dired film thickness can be determined from Equation 2.1[7]:

$$t = \frac{Q}{V.W}\frac{C}{\rho}$$ Equation 2.1

Where t is the produced dry film thickness, Q is the flow rate (cm^3/min), V is the coating speed (cm/min), w is the coating width(cm), c is the ink concentration (gm/cm^3) and ρ is the material density (g/cm^3).

An internal mask with a thickness of 50 µm, made of stainless steel, enables the controlled ink flow to the web and enables the printing of well defined stripes. A second internal mask, provided with meniscus helps guiding the ink to the substrate in the form imposed by the previous one. The width of the so-generated meniscus defines the width of the printed stripes, which, in Eurecat, can be equal to 4, 5.5 or 6.7 mm, depending of the ink to be printed. The choice of the width to be used depends on factors like ink wettability and layer. Inks with low surface tension and, hence, good wettability behaviour, could require a smaller width in order not to exceed the stripe nominal width. In terms of layer, on the other side, the last layer is required to be sharper in order to avoid unwanted contact with the other stripes.

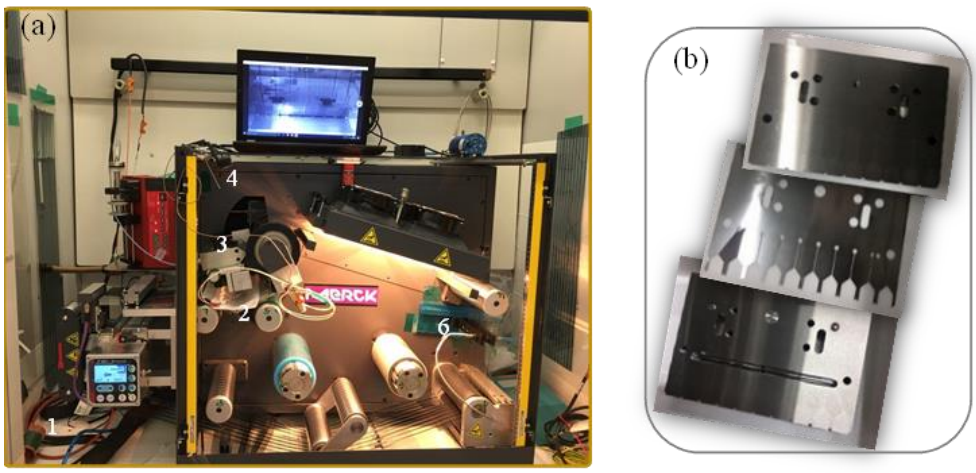

Figure 2. 7 (a) The real image of the roll to roll machine with clarification of the web alignment in blue, (b) illustration of the slot die head components, (c)the substrate roll of the three layers printed ETL,PAL and HTL by the modified mask and (d) the process of the slot die printing.

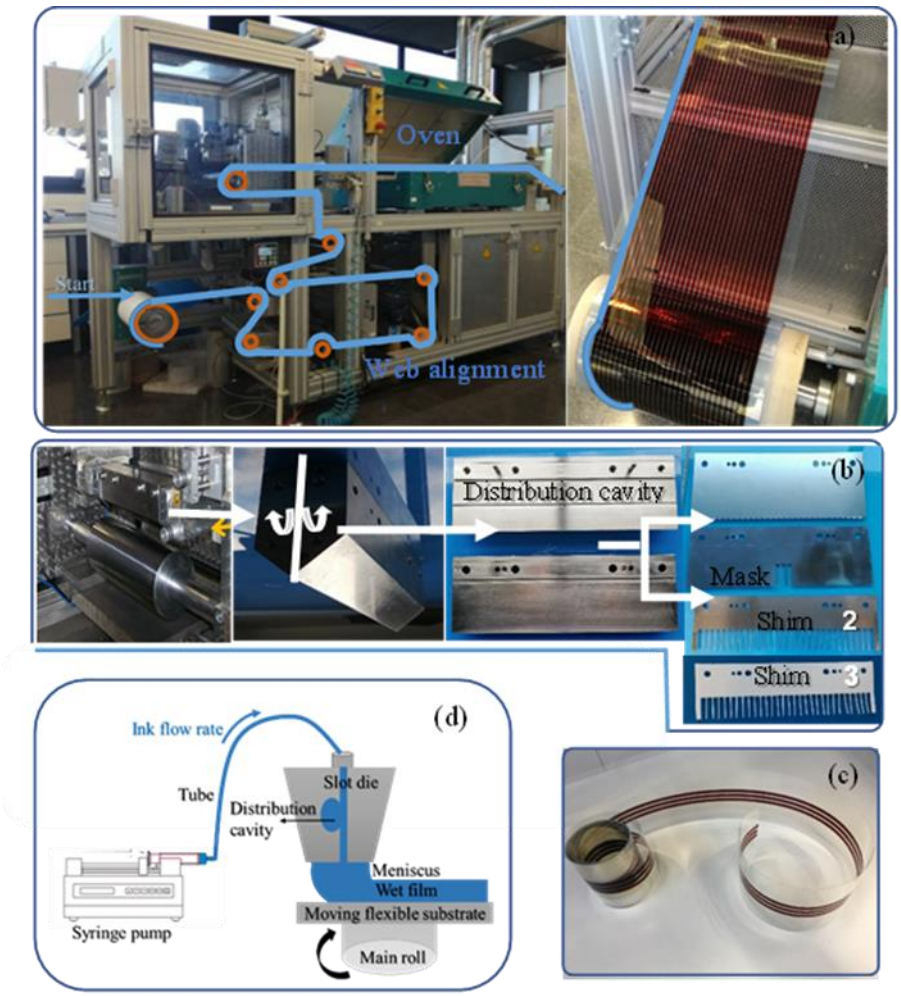

Figure 2.8 (a)Real image of the mini roll to roll in the loop printing mode since(1)is the heating syringe unit, (2) the heating rode used to heat the slot die head, (3) the slot die head with holes to enable heating the inks while printing, (4) camera to monitor the printing process, (5)IR heating unit to dry the printed layers and (6) . UV-VIS spectroscopy to determine the printed layers thicknesses by the optical density measurement and (b) Slot die head components

The choice of shim thickness - in our case always 50 µm – could depend on ink viscosity, being that a more viscous ink could require a higher thickness in order to flow properly through the system.

A modification of the internal shim has been carried out to help printing only three and six strips instead of thirty stripe that allows less materials consume and reduce the coast of the produced modules. That is not only because of the less materials consumption but also because of the less substrate used since, by that way, the main substrate roll could be cut into three sharper rolls, obtaining the triple the initial amount. That leaded to reduce the tension the machine applied to the substrate to the third [see Figure 2.9]. The tension reduction was motivated by the appearance of cracks in the ITO layer [Figure 2.10]. That is consequently reduce the performance of the OPV modules dramatically since longitudinal conductivity was [290±50Ω] and the transversal conductivity [55±20Ω] conductivity was

measured. Most of the layers have been printed by the roll to roll such as ETL, PAL and HTL. The recipe for the coating process is listed in Table 2.4.

During the secondment in Merck mini roll to roll machine used Figure 2.8. Such equipment is provided with heating accessories that have the aim to guarantees that the ink is maintained at a constant temperature, that is higher than room temperature: the syringe and the tube are surrounded by a heating foil, while, the main roll and the slot-die head are heated by a heating rode. These heating units allow the exposure of the ink to a homogeneous temperature through all the path from the source to the printing head. The recipe of the printing conditions of the different layers by the mini roll to roll are presented in Table 2.5.

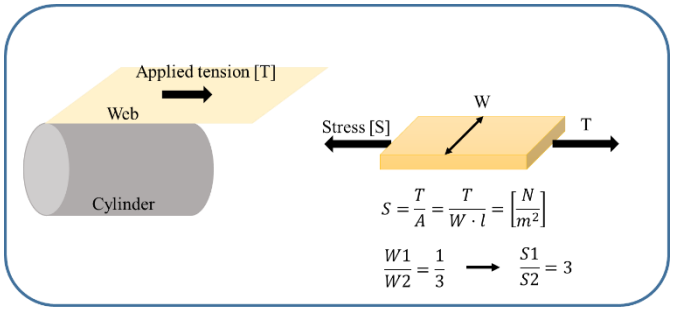

Figure 2.9 Relation between the web width and the applied tension producing more stress on the ITO layer.

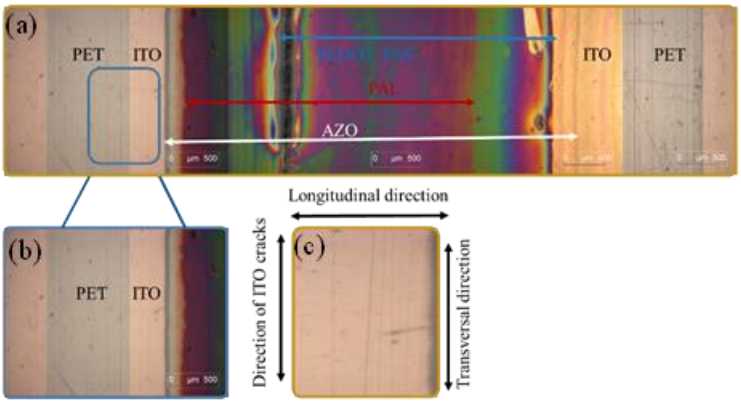

Figure 2. 10 (a) The microscopic image of the substrate and the three layers ETL,PAL and HTL printed on top, (b) the microscopic image of PET with ITO on top and (c) the microscopic image of the cracks presented in the ITO layer because of the extra stress applied to it.

Table 2. 4 The printing recipe for printing ETL,PAL and HTL by roll-to-roll machine.

	Printing conditions	ZnO	P_3HT: PCBM	PEDOT: PSS
Pump	Flow [ml/minute]	1.2	3	6.5
	Tube [internal diameter ,mm,]	1.45	2.06	2.54
Ink	Solvent	Methane	CB	Water
	Concentration [mg/ml]	50	30:24 MW	20% , 0.54 capstone
Substrate	Speed[m/minute]	1.2	1.4	0.8
	Tension[N]	30	30	30
Curing Temperature	Oven temperature [ºC]	140	140	140

Table 2. 5 The printing recipe followed to print ETL, PAL and HTL by the mini roll-to-roll coater.

Ink	Roll-to-roll printing parameters Back roll temperature[ºC], web speed [m/mint], ink flow[ml/mint], syringe temperature[ºC], Tube temperature[ºC], slot die head temperature[ºC] and curing temperature [ºC]
AZO	45ºC, 1m/min, 0.6 ml/min, RT, RT, RT & 110ºC
Blue ink	60ºC, 1m/min, 0.9 ml/min,60ºC, 60ºC, 60ºC &120ºC
P VP AL 4083	Not printable
Clevios 388 & Clevios 434	55ºC, 1m/min, 0.8 ml/min, RT, RT, RT & 120ºC

2.2.4 Screen-printing technique

The screen-printing techniques used to print the fingers pattern of the top electrode since its characteristic of printing thick layer. The screen-printing technique has two possible configurations as shown in Figure 2.11. To finish printing the OPV module Figure 2.12, the silver top electrode grid [that will be treated in chapter 3] was printed by flatbed screen printing technique, of model AT-60PD by ATMA shown in Figure 2.13. Screen printing is a contact printing technique where the ink is released to the substrate through the textured [mesh]screen. The mesh is placed over the substrate. The printing of the silver top electrode started when the squeegee moves over the screen. The moving squeegee forces the ink to filter through the screen texture to the substrate once the force is applied. Therefore, high viscous and low volatile inks are required for this technique in order to prevent too quick evaporation, screen clogging and resolution loss. The equipment used at Eurecat is semi-automatic because after each printing the following substrate must be placed manually.

The wet layer thicknesses of the layers printed by screen printers are of range from less than 10 µm up to more than 500 µm[7]. The dried thickness is calculated from the equation 2.2

$$t = V_{screen}.K_p.\frac{c}{\rho}$$ Equation 2.2

Where V_{screen} is the screen volume, c is the material concentration, ρ is the material viscosity and K_p is the pick out ratio that depends on the processing parameters such as squeegee force, printing speed, snap-off distance, snap-off angle and the ink rheology.

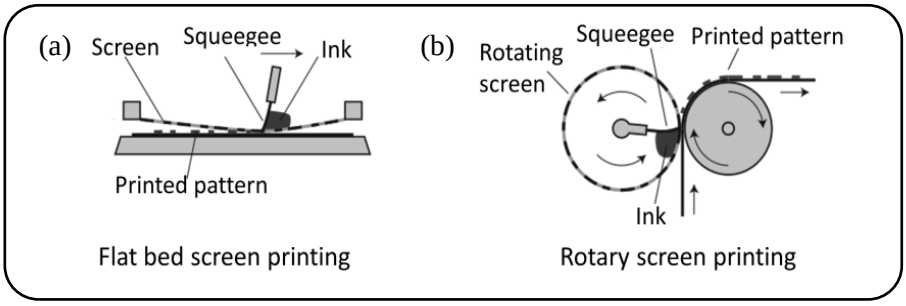

Figure 2. 11 The screen-printing technique (a) flatbed screen and (b) rotary screen printed.

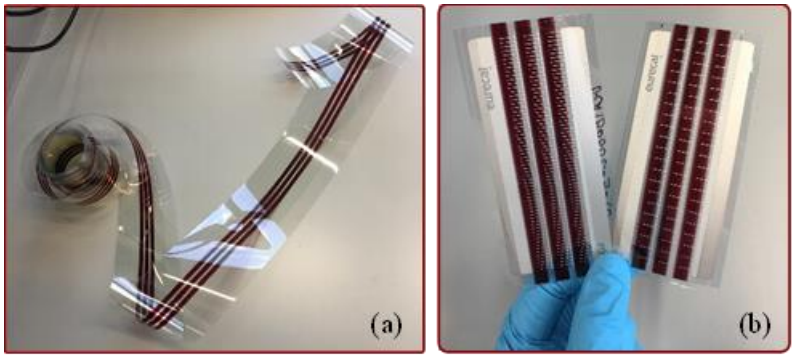

Figure 2. 12 (a)The roll of three printed layers ETL, PAL and PAL by roll-to-roll and (b) image of two OPV modules with printed silver top electrode with different finger spacing 1mm and 4mm.

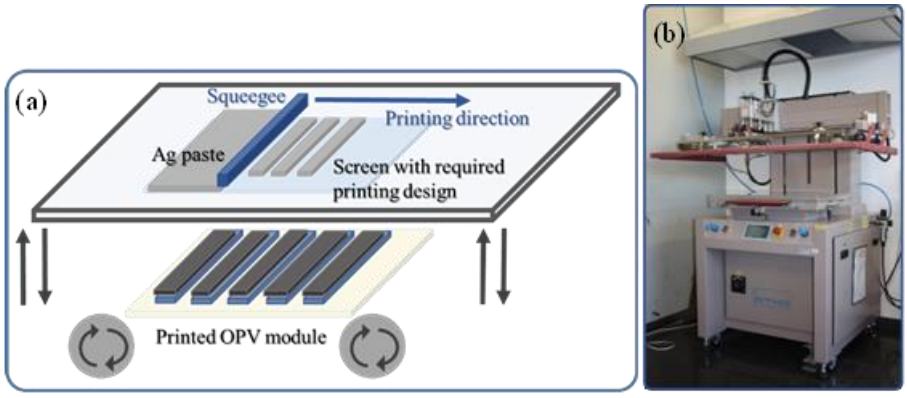

Figure 2. 13 (a) Scheme of the screen-printing technique, (b) the real image of the semi-automatic AT-60PD model by ATMA screen printer.

2.2.5 Encapsulation

The encapsulation is the step that completes module preparation. All the modules were laminated in the laminating machine shown in Figure 2.14 by introducing the solar module between two PET foils. The lamination is done by melting A4 size PET at 80ºC on top and below of solar module.Although it is not the ideal encapsulation, it is cheap and easy to process and offer the stability of the modules for days that is enough for the characterization and for more long living time the modules were usually kept in vaccum.

Figure 2. 14 The laminating equipment.

2.3 Degradation of modules prepared by slot-die roll-to-roll

Modules based on P3HT:PCBM and P3HT:o-IDTBR were employed for degradation experiment(chapter six). All the modules were differentiated by their encapsulation labelled, only PET and barrier. Only PET will mark modules encapsulated by thin PET foils. Encapsulation took place by sandwiching the modules between two PET foils to be inserted into the laminator at 80ºC. Barrier will mark modules with extra encapsulation that performed by gluing barrier foils to the OPV modules. The modules used have three devices connected in series, each of 0.001485 m^2. A picture of an encapsulated devices is presented in Figure 2.15. The degradation of modules implied by placing all modules in the climatic chamber to be degraded under illumination of power 474 mW/m^2, humidity of 40% and temperature of 30ºC. This work will focus on understanding the photodegradation of the OPV modules in general.

Different characterizations techniques were employed not only for the modules such as electrical, spectroscopic, and thermal characterization but also for the inks and the deposited layers as explained in the following section.

Figure 2.15 (a) modules are placed in the climatic chamber with the conditions written and (b) the four set of modules included in the study; P3HT:PCBM module (barrier) in dark red, P3HT:PCBM module (PET) in red, P3HT:o-IDTBR module (barrier) in dark blue and P3HT:o-IDTBR module (PET) in blue.

2.4 Charachterization techniques

In this section, the different characterization techniques were described. Primarily, several characterizations have been performed to the inks either commercially or lab prepared. Further characterizations are required after preparing the solar modules.

2.4.1 Characterization of inks

In solution printing technology the addressing of proper inks is mandatory to achieve a reliable process. The inks properties must be selected for compatibility requirements with the equipment itself, but also to assure the quality in the coated layers.

Rheology and wetting properties

Viscosity and surface tension are intrinsic ink properties that can be assessed by using rheometer and contact angle equipment, respectively. Surface tension of liquids, surface free energy of substrates and contact angle of inks on top of substrates were measured by a Drop Shape Analysis System DSA100 from Kruss. Table 2.6 shows the measured rheological properties of the inks used in the OPV devices. Measuring viscosities were applied by using HAAKE RheoStress 6000 universal rheometer (from Thermo Scientific). A data base was held to record the measured properties for the inks used in the solution

processed printing techniques to question their fitting to the process ability of the coating method.

Table 2. 6 Database of the rheological properties of the inks and resulting films used in preparing the OPV devices.

		FILM					INK		
Device component	Material	Coating technique	d [nm]	SFE [mN·m^{-1}]	□ [S·cm^{-1}]	R_s [Ω/□]	ρ [g·ml^{-1}]	SFT [mN·m^{-1}]	η@100s^{-1} [mPa·s]
Substrate	Glass PET Melinex	-	-	52 ± 2	-	-	-	-	-
Transparent electrode	ITO Technifilm+FOMTech.	-	120	50 ± 3	1678	50 ± 1	-	-	-
	Agnw PolyBioWire	Dr Blade		68 ± 6			1.01 ± 0.02	65.2 ± 0.4	41 ± 4
	HY E	Dr Blade					1.02 ± 0.01	25.8 ± 0.1	14.3 ± 0.2
ETL	ZnO Eurecat (30mg·ml^{-1})	Roll-to-Roll					~0.8	22.7 ± 0.2	0.49 ± 0.01
	AZO Nanograde (N-21X - Flex)	Roll-to-Roll	137± 22	79 ± 1			0.98 ± 0.03	27 ± 1	3.5
Active layer	P3HT:PCBM=30:24 in CB	Roll-to-Roll		38.41 ±1.07	-	-		33.03+-4.3	
	Merck blue ink								
HTL	Clevios FHC+20%w H_2O+0.5% Capstone	Roll-to-Roll	69 ± 12	45.05 ±3.49	734 ± 43	198 ± 3		17.9 ± 0.7	54 ± 6

2.4.2 Characterization of the layers

Layers characterization was the following step to have the insights into physical properties that influence the performance of the OPV devices. The layers' thickness was determined by Veeco Dektak 150 Profilometer [Figure 2.16]. Transmission of the transparent electrode has been measured by Perkin-Elmer Lambda 950 UV-Vis spectrophotometer. AFM was used to have insights into the layers' topology and roughness of the different HTLs applied in OPV devices in chapter two. TEM used to check the formation of the silver nanowires and to measure their diameters. For measuring the electrical conductivity of the printed or deposited films by doctor blade technique a four-probe technique.

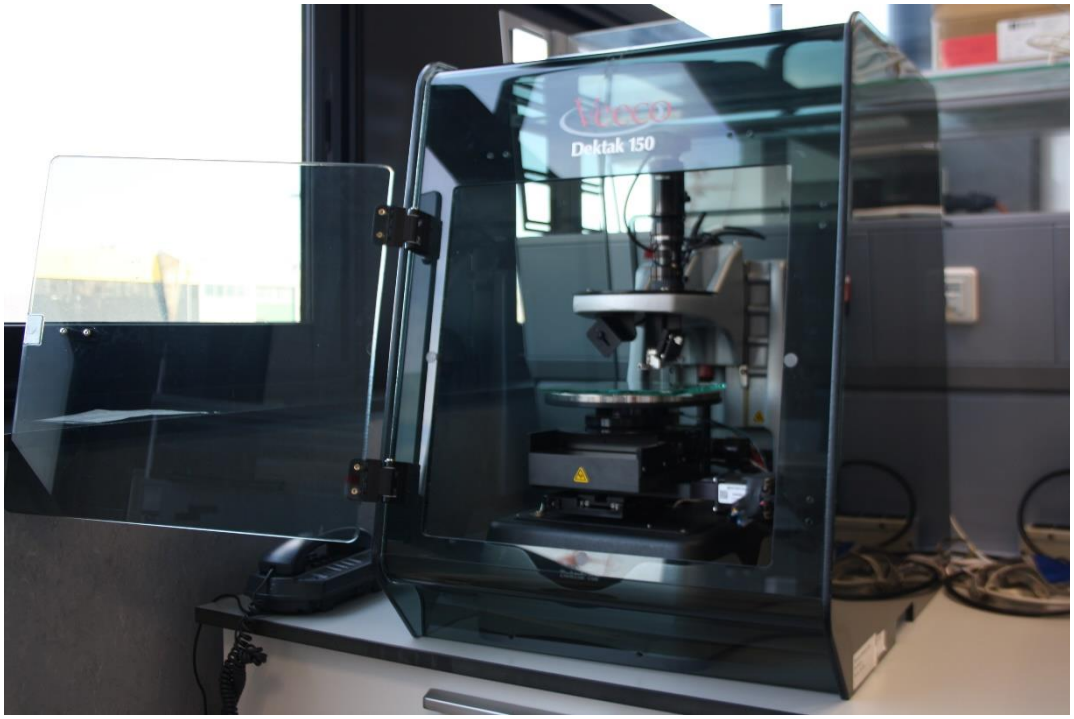

Figure 2. 16 Dektak 150 profilometer.

2.4.3 Module characterization

2.4.3.1 JV characterization

The JV characteristics of the solar cells or modules were measured under AM 1.5G [Air Mass 1.5 Global] illumination, 100 mW.cm^{-2}. The device characterization is performed using a solar simulator Atlas, model SolarTest 1200, regulated on 1000 W·m^{-2} power density [A]- Figure 2.17. The power density is calibrated by means of a pyranometer KippZonen, model CMP 6 [B]- Figure 2.17. The I-V curves of the devices is performed by using a source/meter Keithley, model 2602A [C]- Figure 2.17Figure 2.. Another JV characterization was applied for the small molecule devices (chapter four) in ICMAB using a Keithley 4200 power source meter under AM 1.5G illumination at an intensity of 100 mW cm^{-2}. The solar simulator was calibrated with a certified silicon solar cell (Oriel, Newport).

2.4.3.2 LBIC

Light beam induced current [LBIC] see Figure 2.18 used to have more insights regarding the best electrode ink and their compatibility with the layers beneath. LBIC was measured adapting the WITec alpha 300 RA+ microscope equipment Figure 2.18. The sample was illuminated locally by a monochromatic nm laser. The Raman signal was recorded with a spectrometer (CCD camera) and co-locally the photocurrent response (LBIC) with a source meter. This co-local technique refers to RamBIC (Raman and LBIC).

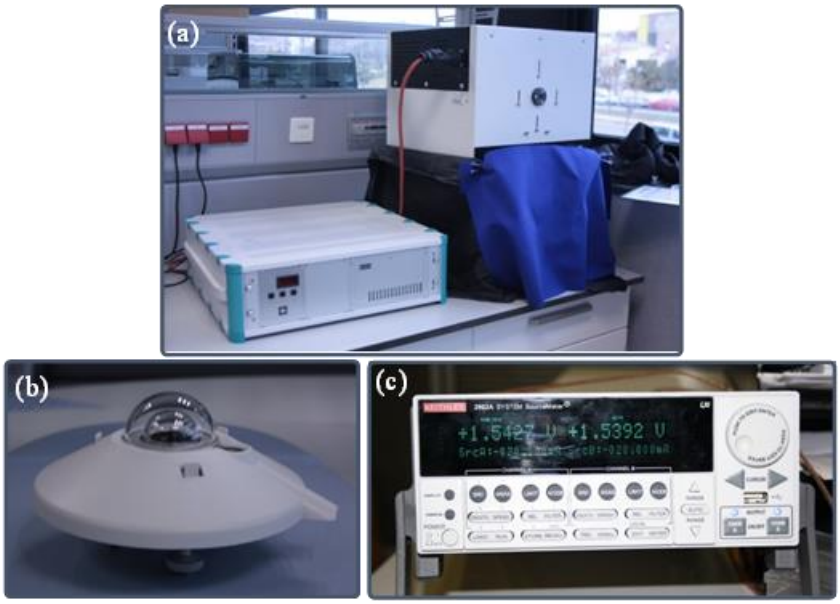

Figure 2.17 (a) Solar simulator, (b) pyrometer and (c) source meter by Keithey.

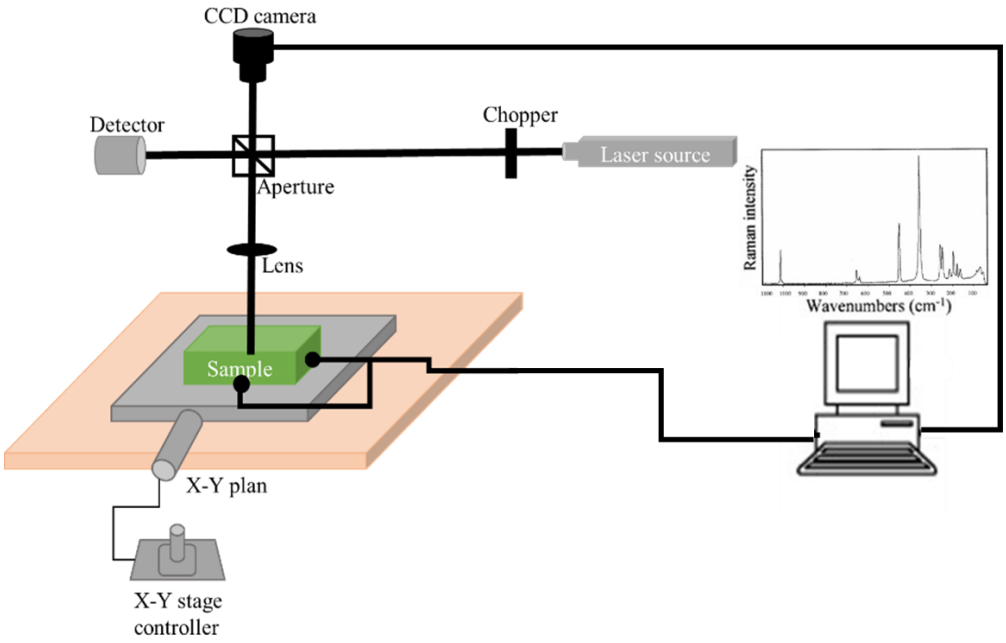

Figure 2.18 The LBIC equipment illustration.

2.4.3.3 EPR spectroscopy

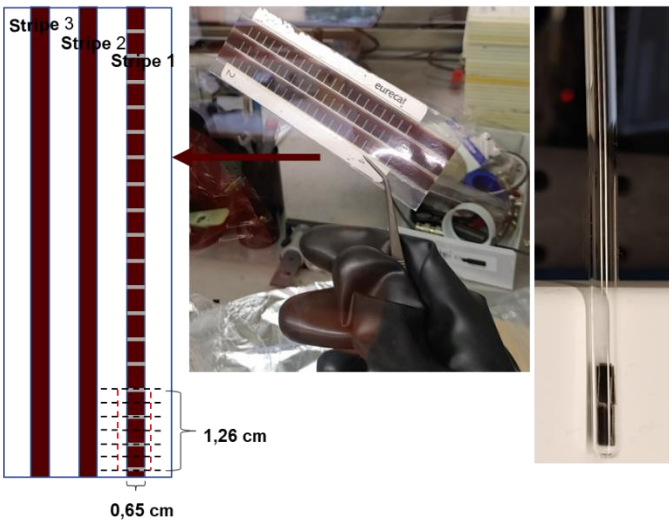

Figure 2.19 Schematic illustration of preparing the modules to be measured by the EPR spectroscopy since pieces of the stripes in the same module were cut and put into an EPR tube.

The modules were running the degradation experiments in chapter six, were stored and cut in the glovebox and, in order to obtain the EPR spectra of the modules, samples were prepared as followed (see Figure 2.19); the modules were cut into stripes of 5.5 mm (length) x 1.4 mm (width), while 6 stripes were placed in an EPR quartz tube (Wilmad) in a nitrogen-filled glovebox. EPR experiments were carried out with an X-band spectrometer (Magnettech MS-5000) with a resonance frequency of 9.42 GHz and a quality factor of Q ~ 1500 – 3000. The experimental settings were optimized to a modulation frequency of Bmod = 0.2 mT and microwave power of PMW = 1 mW at room temperature. For quantitative EPR, a reference sample of the molecular radical 1,3-bis(diphenylene)-2- phenylallyl (BDPA) with a known spin number of NBDPA = 3.6 x 1017 was used. By comparing the double integral (DI) of the reference EPR signal with the EPR signals of the modules (both measured with same settings) the spin number is given by (s = ½):

$$N_{modules} = N_{ref} \times \frac{DI_{ref}}{DI_{modules}} \times \frac{Q_{modules}}{Q_{ref}}$$ Equation 2.3

2.5 References of Chapter 2

[1] S. Chen, J.R. Manders, S.W. Tsang, F. So, Metal oxides for interface engineering in polymer solar cells, J. Mater. Chem. 22 (2012) 24202–24212. https://doi.org/10.1039/c2jm33838f.

[2] T. Hu, F. Li, K. Yuan, Y. Chen, Efficiency and air-stability improvement of flexible inverted polymer solar cells using ZnO/poly(ethylene glycol) hybrids as cathode buffer layers, ACS Appl. Mater. Interfaces. 5 (2013) 5763–5770. https://doi.org/10.1021/am4013038.

[3] A.E. Grigorescu, C.W. Hagen, ZResists for sub-20-nm electron beam lithography with a focus on HSQ: State of the art, Nanotechnology. 20 (2009). https://doi.org/10.1088/0957-4484/20/29/292001.

[4] Z. Jiang, S. Soltanian, B. Gholamkhass, A. Aljaafari, P. Servati, Light-soaking free organic photovoltaic devices with sol–gel deposited ZnO and AZO electron transport layers, RSC Adv. 8 (2018) 36542–36548. https://doi.org/10.1039/C8RA07071G.

[5] L.K. Jagadamma, M. Al-Senani, A. El-Labban, I. Gereige, G.O. Ngongang Ndjawa, J.C.D. Faria, T. Kim, K. Zhao, F. Cruciani, D.H. Anjum, M.A. McLachlan, P.M. Beaujuge, A. Amassian, Polymer Solar Cells with Efficiency >10% Enabled via a Facile Solution-Processed Al-Doped ZnO Electron Transporting Layer, Adv. Energy Mater. 5 (2015) 1500204. https://doi.org/10.1002/AENM.201500204.

[6] L. Wengeler, M. Schmitt, K. Peters, P. Scharfer, W. Schabel, Comparison of large scale coating techniques for organic and hybrid films in polymer based solar cells, Chem. Eng. Process. Process Intensif. 68 (2013) 38–44. https://doi.org/10.1016/j.cep.2012.03.004.

[7] Q. Huang, Y. Zhu, Printing Conductive Nanomaterials for Flexible and Stretchable Electronics: A Review of Materials, Processes, and Applications, Adv. Mater. Technol. 4 (2019) 1–41. https://doi.org/10.1002/admt.201800546.

Chapter 3 Solution processed semitransparent electrodes

Abstract

In the present chapter, we describe two different approaches for solution processed semitransparent electrodes. First, we report the synthesis and optimization of silver nanowire dispersions with controlled dimensions. We investigate their solution processing into films with varying transparency and electrical conductivity and demonstrate their use for electrodes in organic solar cells. On the other hand, semitransparent electrodes based on screen printed silver grids are designed and fabricated. A comparative study of the different screen-printed electrode materials is carried out and the printed electrode geometry is optimized to obtain an efficient photovoltaic performance of our photovoltaic modules.

3.1 Why are transparent electrodes so challenging for upscaling the OPV printing process?

Transparent conductive electrodes have a great importance in optoelectronic devices, such as photovoltaic cells and light-emitting diodes. Figure 3.1 shows that two electrodes are required in organic optoelectronic devices such as OPV and OLED[1] in order to collect or inject charges, respectively. One of the electrodes needs to be transparent so light can pass through; while the other electrode is normally opaque and reflects light back to the device. Lately, research has been done to obtain semitransparent devices because of potential applications in architecture, such as semitransparent windows. To meet the industrial challenges, materials, cost and processing are key factors.

Indium-tin oxide (ITO) is the most commonly used transparent electrode in OPV. This is due to its low sheet resistance (10-20 Ω/□) for films of thickness 100 to 300 nm corresponding to electrical conductivity in the order of 10^3 S/cm and high optical transmission (>80%) in the visible range. Despite of this attractive traits, ITO´s manufacturing complexity and high-cost production limit mass production of the up scaled OPV devices. ITO brittleness is an obstacle in the application of the flexible OPV devices. Cracks can appear under mechanical stress, which would be a source of dramatic decrease of the electrical conductivity. Commercial ITO electrodes are fabricated by sputtering, and thermal evaporation. Sputtering requires high- temperature treatment (400 to 500°C) and high-vacuum that increases the cost and processing complexity. Moreover, the fabrication of ITO on polyethylene terephthalate (PET), the most popular material employed for flexible substrates, consumes 87% of the energy and over 30% of the material cost.[1] Indium is a scarce element on the Earth´s crust, and as such, will never be cheap, particularly in applications for which one needs very large areas, such as sun light to electricity energy conversion. These conditions remark the importance of the simple processing and the need for solution processed transparent electrodes.

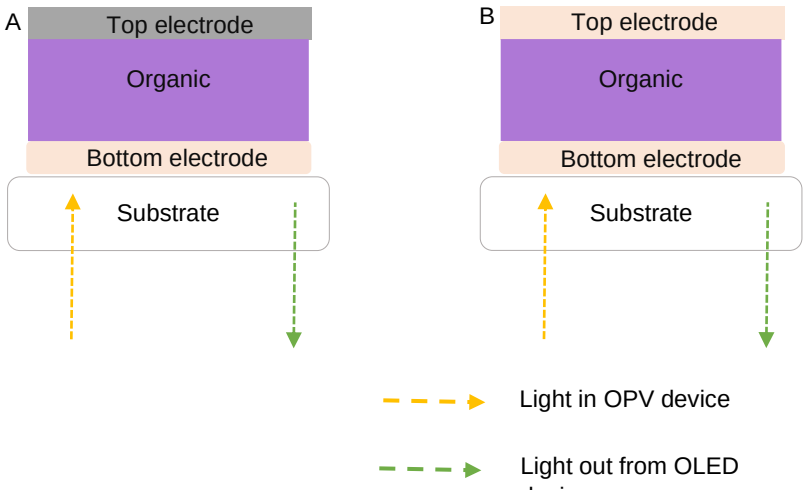

Figure 3.1 Optoelectronic device's structure a) OPV and bottom emitting OLED and b) transparent OPV and OLED.

Unlike sputtering and other vacuum complex processing techniques, solution processed printing techniques employ relatively simpler technologies, scale up at industrial level with a

lower cost and can open the possibility to more applications arising from having flexible devices [2–17]. Printing techniques have, therefore, a high potential to prepare transparent conducting electrodes at the industrial scale [18].

Different materials have been investigated for transparent conductive electrodes (TCE), including graphene, CNTs, conducting polymers and metal nanowires[19–23]. First, Carbon materials have low-cost and high stability[24,25]. Graphene has been investigated as TCEs due to its high transparency and conductivity[26–28]. Graphene sheet was calculated to have 97.7% transmittance and 6 Ω/□ sheet resistance[29,30]. However, processing is done by chemical vapor deposition which is against the low cost perspectives[26,28,31]. Graphene oxide (GO) has been used as a TCE because it is solution-processable[31,32]. The sheet resistance of GO electrode is 200-1000 Ω/□ and its transmission is lower than 90%[23]. Single carbon nanotubes (CNTs) films have high conductivity to be applied as TCE. However, the performance of solution processed CNT films is still limited due to its challenging purification, dispersion and stabilization[24,33]. A single CNT has high conductivity (3 $x10^6$ S m^{-1}) and mobility of 100000 cm^2/V s, which is not the case for the CNTs due to the resistance between the connections [34,35]. The sheet resistance of CNT is 10^2-10^4 Ω/□ and transmission of ~80% at 550 nm[36].

Second, conducting polymers are privileged for their ability of tuning their band gap by chemical modification and doping. Transporting electrons through delocalized π bonds is the main reason of the conductivity of the conducting polymers. The most widely used polymer is PEDOT:PSS, which has conductivity values between (100-1000 S cm^{-1}), however its sheet resistance (102-103 Ω/□) is still significantly higher than that of ITO, which limits its use as electrode in OPV devices [37].

Third, metals are favorable as they exhibit the highest electrical conductivity. Solution-based metal deposition technologies rely on dispersions of metal nanoparticles/nanowires in a given solvent[38–41]. Recently, silver nanowires (Ag NWs) have emerged as a promising candidate due to their high electrical conductivity, high optical transmission, excellent flexibility [38], their solution processing and are being applied in the large-scale production[42–44]. The wires aspect ratio is important since the percolation between the long wires have a huge influence in the electrical conductivity and the diameters of the wires highly influence the optical transmittance. The reported transmittance value is 80-90%, with sheet resistance of 1-100 Ω/□.

Silver nanowires (AgNWs) have 10–200 nm and lengths of 5–100 µm[45–49]. The aspect ratio, length over diameter, should be greater than 10 unlike the case of silver nanorods [47]. Enormous efforts are advocated obtaining high quality, uniformity and yields by high throughput techniques[50].

Methods for the synthesis of the AgNWs have been reported in the literature, such as electrochemical synthesis, template synthesis, and polyol synthesis [51,52]. Electrochemical method produce AgNWs based on single crystal, whereas the wet chemistry method produce AgNWs based on a multiply twinned crystal[53]. However, the advantage of the template method is the well-controlled manner of growth. Hard templates explored by Charles R. Martin's[54] produce highly ordered structure despite the removal of these templates that might damage the nanowires. In contrast, polymers as soft templates can be dissolved easily in solution, which is of high potential application in industry. Finally, Polyol method is defined as the soft chemical method for the preparation of nanowires.

Furthermore, composite materials have been investigated as TCE aiming at overcoming the disadvantages of single materials. One particularly used option is the combination of printed metal grids with EDOT: PSS underneath. The resulting composed electrode helps with the large sheet resistance (R_s) of to the conducting polymer alone and increases the collection of charges, when compared with the Ag grid alone[56–58].

The electrical sheet resistance and the optical transmittance are the most important parameters that characterize a semitransparent electrode film. Roughness, work function,

processability, and mechanical properties, are considered for electrode materials. A required compromise between transmittance and sheet resistance are considered for the adequate electrodes. The intrinsic limit of the conductivity is defined by electron–acoustic phonon scattering in the layer at room temperature[59].

The electrode sheet resistance, R_S, as displayed in equation 4.1.

$$R_S = (\sigma t)^{-1} \qquad \text{Equation 4. 1}$$

Whereas the optical transparency, T, follows, in a first approximation, an exponential decay behavior with *t* as given by the Beer-Lambert law shown in equation 4.2

$$T = \frac{I}{I_0} = e^{-\alpha t} \qquad \text{Equation 4. 2}$$

Where I_0 is the incident light intensity, and I is the transmitted light intensity. Table 3.1 presents the optical transmittance at wavelength 550 nm and the sheet resistance of solution processed TCEs reported in literature[60]. But what is the best way of comparing TCEs?

Table 3.1 Properties of solution processed TCEs.

Substrate	T	Rs (Ω/□)	Ref
ITO/glass	0.83	3.1	[61]
AgNW/PET	0.947	20.2	[62]
AZO/AgNW/AZO/ZnO/glass	0.934	11.3	[63]
PEDOT:PSS/glass	0.97	240	[64]
PEDOT:PSS/PET	0.86	24	[65]
PEDOT:PSS/Ag gird/PET	0.73	0.62	[66]
graphene/PET	0.90	41	[67]
graphene/glass	0.9	100	[68]

Researchers introduced the concept of figure of merit (FOM), $[\emptyset_{TC}]$, to evaluate specifically the performance of TCEs in order to incorporate both relevant parameters (light transparency and electrical conductivity). There have been different FOM proposed.
Fraser and Cook defined the FOM as a function of thickness through the following equation 4.3[69].

$$FOM[\emptyset_{TC}] = \frac{T}{R_s} \qquad \textit{Equation 4. 3}$$

By combining equation 4.1, 4.2 and 4.3 we get

$$FOM\ [\emptyset_{TC}] = \sigma t e^{-\alpha t} \qquad \textit{Equation 4. 4}$$

By solving this equation $\frac{\partial \emptyset_{TC}}{\partial t} = 0$, to obtain minimum thickness T = 1/e = 0.37.

Optimum FOM obtained at transmission of 0.37 which is not desired for the properties of TCEs. Therefore, Haacke[69,70] proposed FOM given by equation 4.5

$$FOM = \frac{T^x}{R_S} \qquad \textit{Equation 4. 5}$$

$$t = \frac{1}{\alpha x} \qquad \textit{Equation 4. 6}$$

$$x = \frac{-1}{lnT} \qquad \textit{Equation 4. 7}$$

Where x is an exponent. Minimum T is essential for maximum $\emptyset_{TC}$, and the value of x = 10 is associated to T = 90% [69].

Selecting a proper material is crucial for designing the device electrode. FOM is the dominant protocol for comparing the solution processed AgNWs and the commercial electrode materials synthetization of AgNWs based on Polyol method are presented as following.

By choosing the FOM as a criteria to qualify the electrode films we need to prepare and optimize the AgNWs, then prepare films of AgNWs and calculate the FOM of the prepared AgNWs films, before applying them in the OPV devices. For preparing the AgNWs, we chose polyol method for specific reasons, as it will be explained in the following section.

3.2 Synthesis of AgNW by the polyol method

In this work, we have selected the polyol method because it has been introduced as one of the most successful methods for preparing high quality AgNWs in large scale. Xia's group prepare AgNWs by the polyol method[42] in which Pt nanoparticles used as seeds. However, a self- seeding process that does not need any exotic seeds was later reported[71].

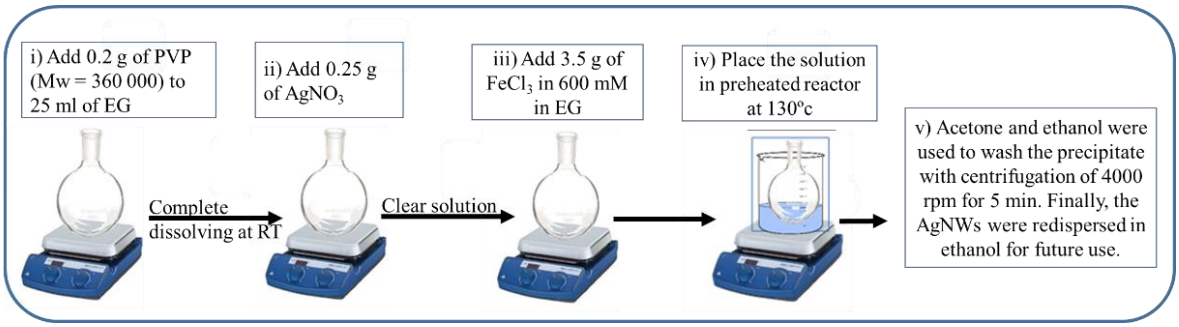

Figure 3. 2 Steps for preparing AgNWs by Polyol method.

The steps followed for the preparation are sketched in Figure 3.2. In brief, the steps are (i) PVP is added into a vessel with ethylene glycol and let to dissolve at RT; (ii) $AgNO_3$ is added to clear solution; (iii) prepare 600mM of $FeCl_3$ in ethylene glycol and add 3.5g to the previous solution;(iv) adjust the temperature of oil path to 130ºC or adjust the temperature of oven to be 130ºc and transfer the whole vessel after complete dissolving for 5 hours; (v) use acetone and ethanol to wash the precipitate with centrifugation at 4000rpm for 5minutes. All the synthesized AgNWs were eventually suspended in ethanol. The $AgNO_3$ happens when the concentration of silver atoms reaches a super saturation, nucleation and growth of nanoparticles begins. Both twinned and single-crystal seeds of silver are formed through homogeneous nucleation. The twinned particles, of low surface energy, happens by the nucleation [72]. The poly (vinyl pyrrolidone) (PVP) has two functions, first as a capping agent that adsorbs onto the surfaces of the particles and second as solvent to reduce the aggregation [73].

Figure 3.3 illustrates the growth mechanism of AgNWs by one pot approach in which the additives stirred at room temperature. AgNWs formation pass by three stages. First, the AgCl nano cubes formation at 100 ºC. Second, these cubes grown to multiply twinned particles. The third stage is similar to the syringe pump method.

3.2.1The role of multiple twinned particles

Murphy has reported that the multiple twinned particles (MTPs) act as seeds for nanorods and nanowires [75] and Gai et al.[76] reported the process in which nanorods formed from MTP seeds[77]. The MTP extended outwardly in a fivefold symmetry, and the MTP's surface consisted of ten {111} facets. In the Ostwald ripening process[74], the twin boundary of the highest surface energy is what makes silver atoms grow only at the twin boundaries producing the MTP and then extended in one dimension to be nanorods and nanowires.

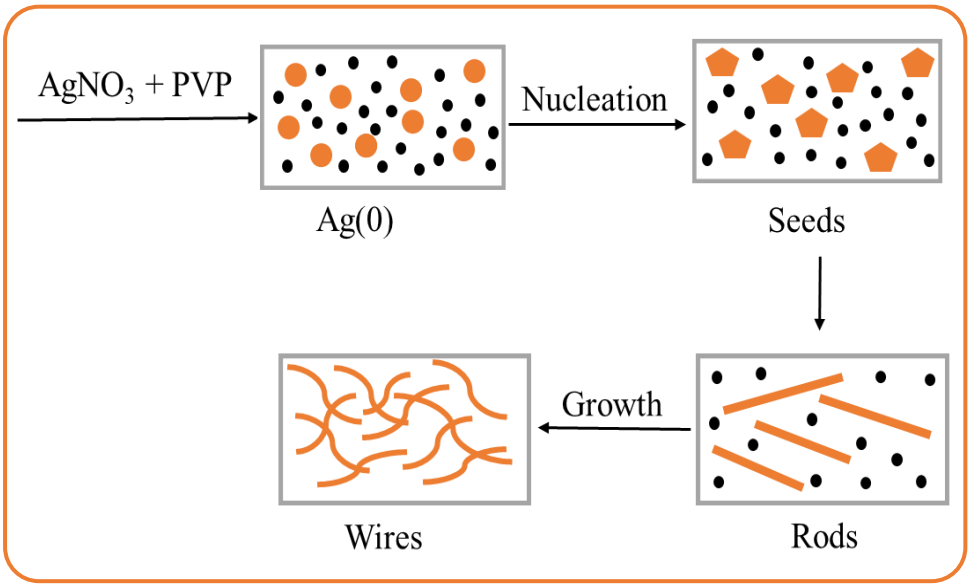

Figure 3. 3 The growth mechanism of AgNWs.

3.2.2 The role of PVP

The formed nanowires have {111} facets at their ends and {100} facets on their sides between the two ends. The PVP macromolecules interact with the {100} facets stronger than with the {111} facets because of their highest interaction energies between PVP and crystal facets {100}[78]. Therefore, the {111} facets have only sites for the growth and continued in one-dimension. The growth mechanism is shown in Figure 3.4 [37].

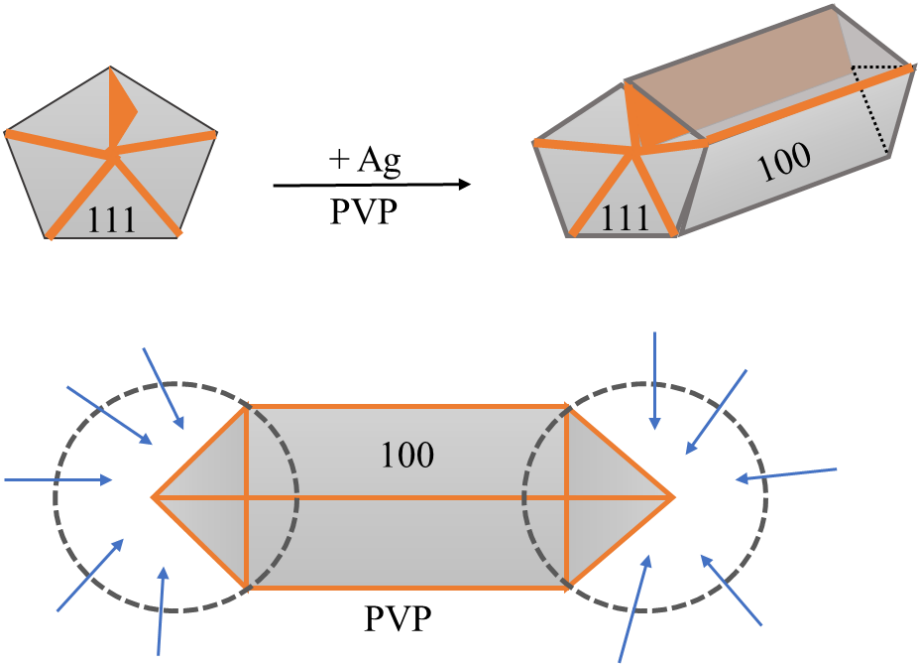

Figure 3. 4 The multiple twinned particles growth into nanowires mechanism.

The importance of adding NaCl to the reaction lies in the resulting better quality of Ag NWs since Cl^- ions coordinates to Ag^+ ions result in AgCl, which enables the silver nanoparticles to grow as MTPs[79]. Other additives such as KBr [80], $CuCl_2$ [80–82] and $FeCl_3$ [71] have been reported. Different parameters such as molecular weight of PVP[44,73], reaction temperature[83] and the stirring speed [84] have been investigated to optimize the size of Ag NWs.

3.3 Optimization of silver nanowires

Our goal is to obtain the maximum of the AgNWs aspect ratio since this affects the electrical and optical properties of the AgNWs as a TCE. The ratio of the length over the diameter is very important since it affects the optical and the electrical properties of the electrode. The nanowires diameter is important for the optical properties: the thinner the nanowires, the less light scattering is observed. The length is more related to the electrical properties as the longer the nanowires, the more interconnections between the wires and the more percolation in the network, with a consequent improvement in electrical conductivity of the film. Consequently, we explore the properties of the synthesized AgNWs by systematically investigating the chemical elements in the reaction.

3.3.1 The effect of the molar ratio between PVP: $AgNO_3$

Since the PVP plays an important role in the chemical reaction as explained before, we explored the changes of the molar ratio between PVP and $AgNO_3$ to study the resulting variations in the geometry of the AgNWs. Figure 3. 5 shows the TEM images of the AgNWs under the effect of the different molar ratios between PVP and $AgNO_3$. It was not possible to estimate the average length of the nanowires, since they are longer than the image scale and it was hard to track each single wire in the TEM pictures with different entanglements.

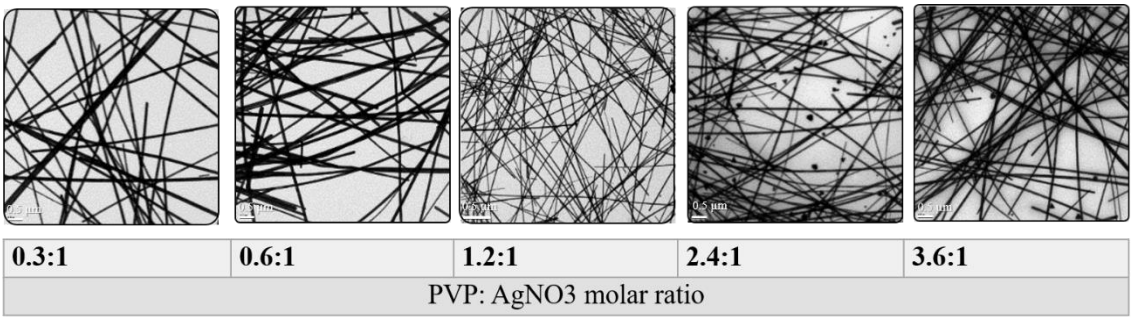

Figure 3.5 TEM images of the nanowires prepared with different molar ratios between PVP and AgNO3.

The effect of changing the molar ratio between PVP and $AgNO_3$ on the nanowires diameters is shown in Figure 3. 6(a). The results showed that the diameter of the nanowires is inversely proportional to the molar ratio of PVP: $AgNO_3$. This is understandable since the PVP is used as a capping agent that surrounds the nanowires in the reaction, limiting the diameter of the nanowires. Since by decreasing the molar ratio between PVP and $AgNO_3$ the silver growth of happens on both {111} and {100} faces resulting in wires with large diameter. Therefore, increasing the molar ration of PVP: $AgNO_3$ decreases the diameter of the nanowires.

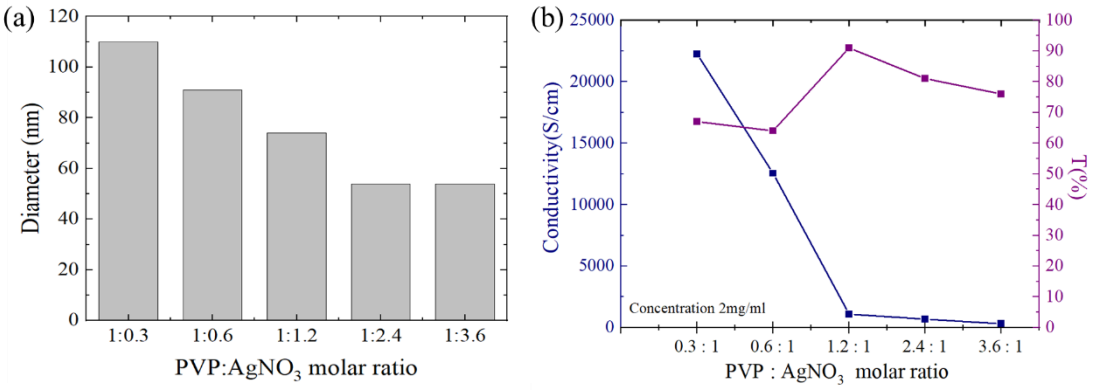

Figure 3. 6 (a) relationship between the PVP: $AgNO_3$ molar ration and the mean value of the nanowires diameter and (b) the electrical conductivity and the optical transmittance (at 550 nm) of AgNWs, as a function of the molar ratios between PVP: $AgNO_3$ films deposited by blade coating on glass.

Conductivity and optical measurements have also been conducted. The absorption spectrum of AgNWs is shown in Figure 3.6(b). To investigate the conductivity and the optical properties of the prepared AgNWs, different solutions of AgNWs in ethanol at the concentration of 2mg/ml were deposited on glass substrates by blade coating. Figure 3. 6(c) shows the conductivity measured by the four-probe technique and the transmittance of the films at 550 nm, a wavelength of the maximum power delivered by the sun. On one side, the electrical conductivity decreases with increasing the molar ratio PVP: $AgNO_3$. That is agreed with the results reported since increasing PVP:$AgNO_3$ molar ratio, PVP molecules block anisotropic growth the nanowires and the length of the nanowires decreases[85]. Furthermore, since the total weight is fixed so the amount of silver is decreased that leads to less conductivity. On the other side, the optical transmittance has a trend, it is not monotonous though. The highest transmittance observed is 91%, corresponding to the ratio PVP: $AgNO_3$ = 1.2:1. Since we seek the transparent conductive electrodes applications, 1.2:1 is the chosen optimized molar ratio between of PVP: $AgNO_3$ to be followed by the next optimization factor.

Applying silver nanowires in the organic solar cells gains many benefits related to their optical and electrical properties. When AgNWs applied in solar cells as a top transparent conductive electrode, it is reported that their plasmonic effect enhances the photovoltaic performance such as increasing the J_{sc} of the devices[86]. Also when AgNWs are used as bottom electrode in the inverted solar cells, the photovoltaic performance enhances by reducing the length for the holes to be collected[87]. AgNWs also exhibit the solar cells a transparency in the visible range since they absorb in the IR range of light spectrum[88]. A flexible solution processed solar cell by roll-to-roll has been reported by implementing AgNWs as a top electrode[89]. AgNWs offer better stability to the OPV devices by 1000%[89].

Haze, an observed phenomena of the AgNWs films, is related with the scattered light to the photoactive layer. Haze benefits the optical path in the photoactive layer improving the J_{sc} of the cell[87]. Haze is controlled by the diameter and the density of the NWs. A linear relation between the haze and the mass density of the nanowires, how many wires per area, has been reported[90]. Since haze reduces the transmission, its optimization is reported to be in the range 8% - 15% for transparent electrodes in solar cells]

3.3.2 The effect of the stirring speed

The stirring speed applied during the synthesis process is the next factor to be optimized as it is reported that the stirring speed plays an important role in the chemical reaction[85]. Four different stirring speeds 0, 300, 750 and 1000 rpm were tested while the PVP:$AgNo_3$ molar ratio kept fixed the optimized ratio. Figure 3.7 presents the TEM images of the nanowires prepared at different speeds of 0, 300, 750 and 1000 rpm since the stirring speed affects the concentration of the Ag^+ ions in the solution during the growth process. No stirring helps the silver nanowires to grow, as shown in the TEM images; however the stirring did not help the growth process as in case of 300 rpm short wires and silver spheres are formed. In the case of 750 and 1000 rpm, the nanowires are still shorter than in the case of no stirring.

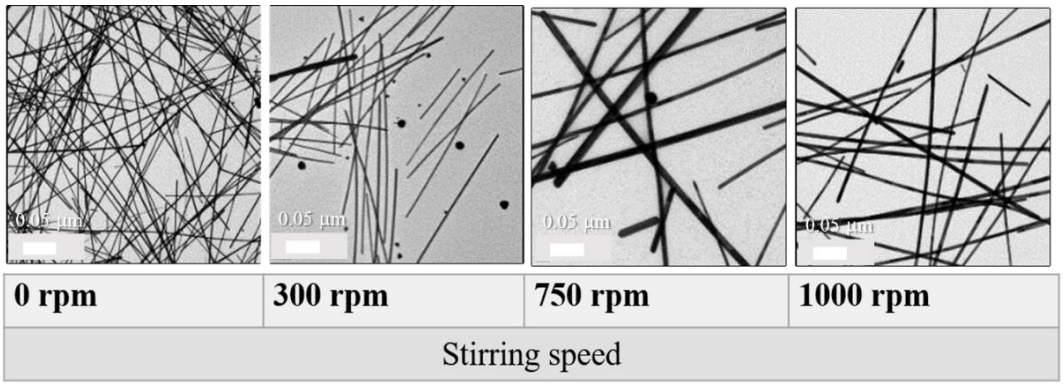

Figure 3.7 TEM images of AgNWs synthesized at different stirring speeds.

The diameter distribution over the stirring speed is shown in Figure 3.8.The electrical conductivity and the optical transmittance of the AgNW films of 6mg/ml concentration deposited by blade coating on glass have also been characterized, as shown in Figure 3.8(b). The AgNWs synthesized without stirring have the highest electrical conductivity since they have the longest wires that provide more percolation network while the highest transmittance, 83%, was observed for a stirring speed of 200 rpm. Therefore, the optimum condition seem to be 0 rpm since the stirring seems to break down the nanowires and decrease the conductivity.

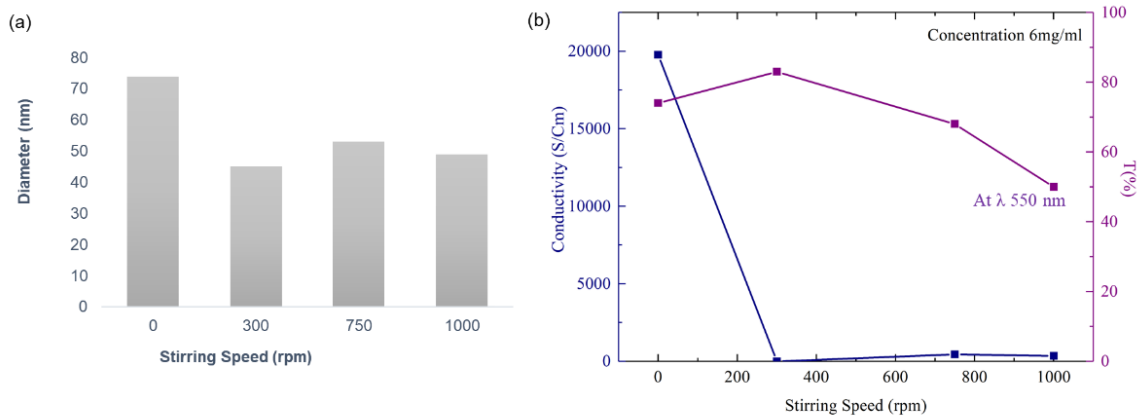

Figure 3.8 (a) AgNWs diameter synthesized at different stirring speeds and (b) electrical conductivity (left side) and optical transmittance (right) at wavelength 550 nm of the AgNWs, as a function of the stirring speed during the synthesis. The films were deposited by blade coating on glass.

3.3.3 The effect of the reaction temperature

The reaction temperature is another critical factor for AgNWs formation, since below a certain threshold temperature, Ag nanowires with a high aspect ratio cannot be formed. As the reaction temperature increases, the anisotropic growth is achieved. Figure 3.9 shows the TEM images of the AgNW prepared at different reaction temperatures at the optimum molar ratio between PVP: $AgNO_3$ 1.2:1 due to its desired properties (see the effect of the molar ratio between PVP: $AgNO_3$ section) and without stirring. Figure 3.9 shows the effect of the temperature reaction on the diameter of the AgNWs where the smallest diameters come with 130ºC. From the results, it seems that the higher temperature leads to higher diameter,

which agrees with a lower transmission that we observed. The electrical conductivity and the optical transmittance of the films are shown in Figure 3.10. It can be seen that the larger the diameter, the more scattered light within the Ag wire film resulting in more haze or whitish color of the deposited films of AgNW which, in turns, reduces the normal incidence transmittance of the resulting films (note that an integrated sphere has not been used in these experiments). Since we seek the application of semitransparent electrodes, we will choose the 130ºC as an optimum condition for the reaction temperature.

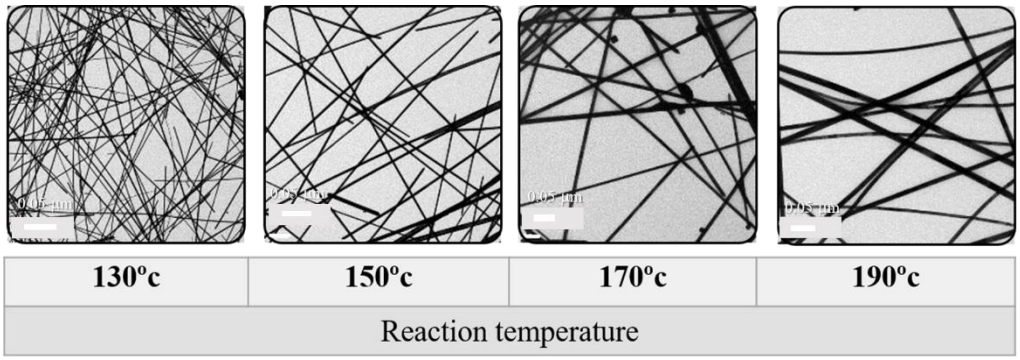

Figure 3.9 TEM images of AgNWs prepared at different reaction temperatures

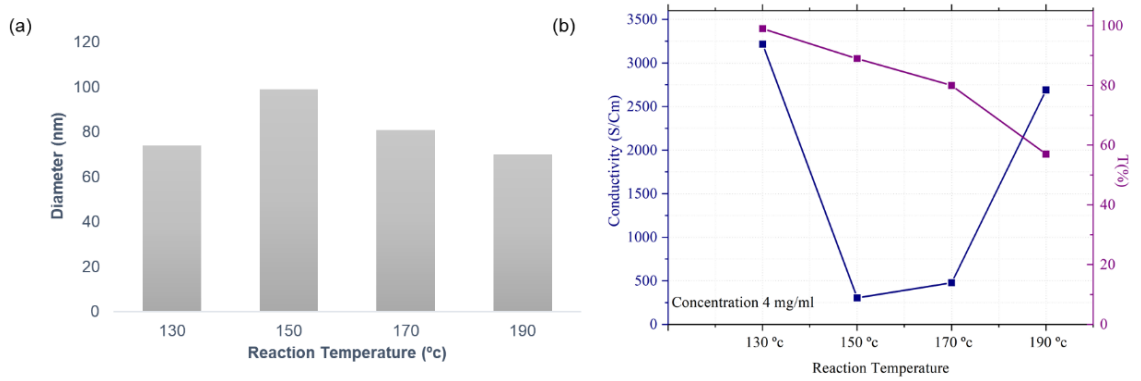

Figure 3.10 (a)The average values of the AgNWs diameter as a function of the reaction temperatures and (b) the optical transmittance at wavelength 550 nm and electrical conductivity of the AgNWs, as a function of the reaction temperatures, the films were deposited by blade coating on glass.

3.3.4 The effect of the concentration of ethylene glycol

Ethylene glycol (EG) is not only a solvent, but also a reducing agent. Therefore, we seek on optimizing the amount of the EG used in the reaction. Figure 3.11 shows the TEM images of the different AgNWs prepared by adding different volumes of ethylene glycol. The volume fraction of ethylene glycol can affect the reduction rate of the $AgNo_3$ and, consequently, the nanowires properties. The diameter of the resulted nanowires at different EG amounts are shown in Figure 3.12[a].

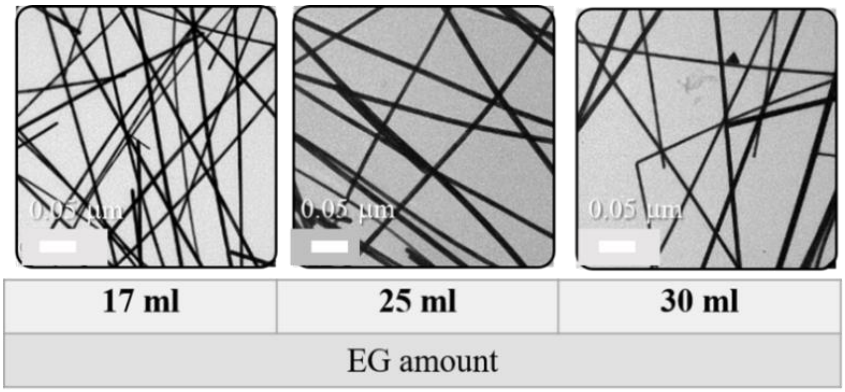

Figure 3.11 TEM images of different AgNWs prepared with different concentrations of EG.

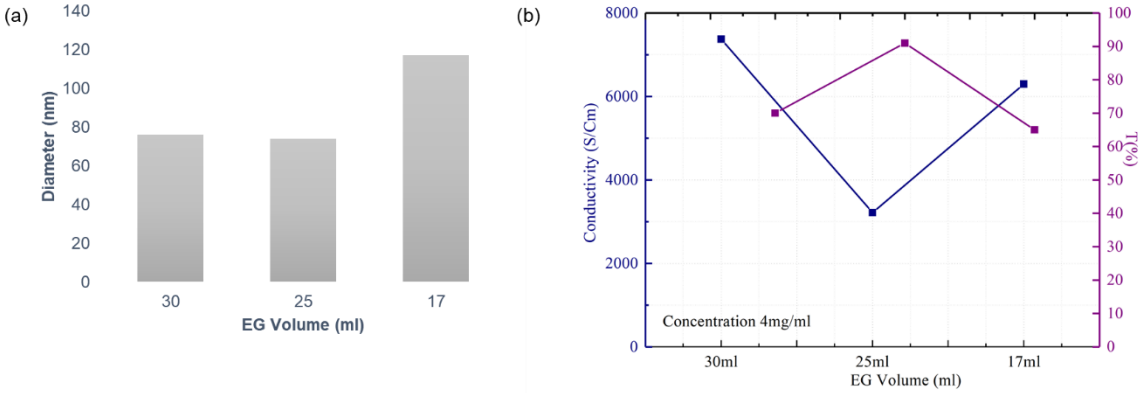

Figure 3.12 (a)Histogram of the AgNWs diameter synthesized with different EG volumes and (b) Optical (left side) and electrical (right) properties of AgNWs prepared with different added volumes of Ethylene glycol.

To examine the properties of the produced nanowires, AgNWs films are prepared by blade coating on glass. The results showed that by the EG amount influences the reduction rate and hence the nanowires characteristics. Therefore, the chosen optimum amount for EG is 25 ml since it resulted in the highest transmittance that will fulfil out desired requirement for the semitransparent electrode application.

3.3.5 Annealing temperature and anisotropy

The annealing treatment is another factor that demonstrated to have some effect on AgNW films conductivity. In order to observe this effect, we compared the conductivity of films not exposed to annealing with films exposed to 130°C for 30 minutes. The conductivity of the annealed films was higher (45.245 S/cm) compared to the non-annealed films (20.075 S/cm). The annealing helps the nanowires to sold and diffuse together helping the connections between the wires to be welded reducing the interfacial resistance between NWs, which in consequence increases the conductivity of the deposited films.

In addition, the conductivity of the printed silver nano wires films comes from the connection between the wires so that the conductivity might be anisotropic depending on the printing direction. Therefore, we have tested the anisotropic conductivity of the AgNWs films. We have followed two different ways for observing the anisotropic electrical conductivity of the films. The first one, as clarified in Figure 3. 13(a), is achieved by printing two layers either parallel to each other or perpendicular to each other. The conductivity measured by four-probe of these two layer on top of each other in the parallel case was of 28.590 S/cm and in case of the perpendicular direction was 23.310 S/cm. The second way consists of applying the electrodes either parallel to the printed layers or perpendicular to the printed layers, as it is shown in Figure 3.13(b). The corresponding conductivity has been calculated by equation 4.1 and it was 45.245 S/cm in the perpendicular direction and in case of the parallel direction it was 38.469 S/cm. The conductivity was higher in the perpendicular direction than the perpendicular one. This might reflect the anisotropic characteristic of the AgNWs conductivity.

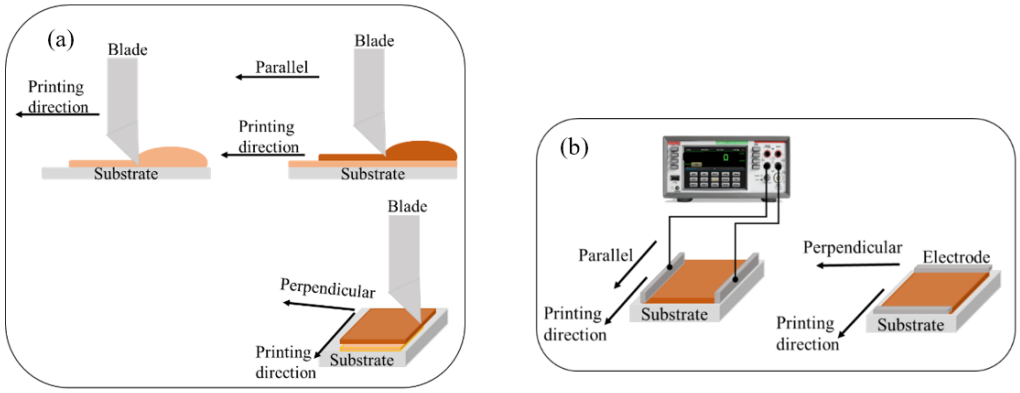

Figure 3.13 (a) Schematic illustration of printing two layers of AgNWs and (b) the direction of the applied electrodes.

3.4 Resume on the optimization of AgNWs

We have investigated in detail the synthesis and the optimization of AgNW for their application as a semitransparent electrode. The optimum conditions that we have found are no stirring for molar ration 1:1.2 between PVP and $AgNO_3$, at 130ºC and 25 ml of EG, which result in AgNW of lengths greater than 23 microns, and diameters of 74 nm. Films of different inks such as commercial AgNWs from PolyBio and the commercial PEDOT: PSS were blade coated on glass substrates and their electrical and optical properties were measured. FOM were calculated for these films based on Haacke relation discussed in section 1.2. Figure 3.14 represents the FOM of the optimized AgNW at concentration of 6 mg/ml in comparison to the commercial ITO, PolyBio and the PEDOT: PSS.

The synthesized AgNWs were of the highest FOM of 7.86E-02 Ω^{-1} while the rest of the materials exhibited FOM of 1.75E-02 Ω^{-1}, 7.05E-03 Ω^{-1} and 1.54E-03 Ω^{-1} for ITO, PolyBio wires and PEDOT: PSS, respectively. These findings showed the high potential for the synthesized AgNWs to be used as TCEs in OPV devices.

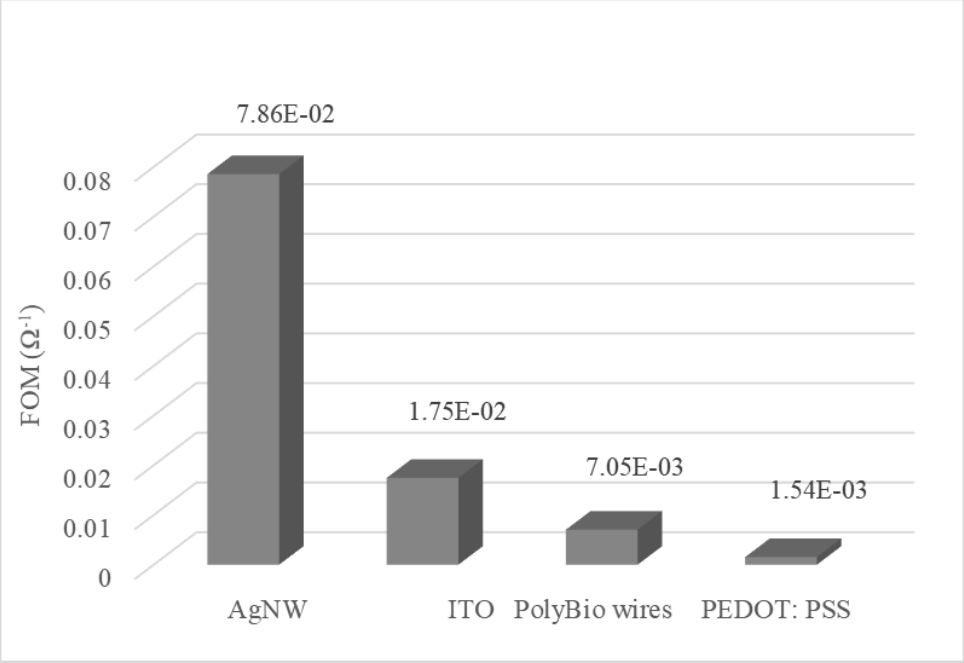

Figure 3.14 FOM of the optimized AgNWs compared to other promising commercial materials as TCEs.

3.5 Applying AgNWs in OPV devices

3.5.1 AgNW films as ITO replacement

We first attempted to use AgNW as an ITO replacement. For this, the deposition of AgNW electrode was made by blade coating in devices with the following structure: glass/AgNW/ZnO/P3HT: PCBM/MoO_3/Ag. AgNW, ZnO and PAL were also deposited blade coating, while MoO_3 and Ag were thermally evaporated. Table 3.2 lists the inks chosen based on their availability in our lab and the respective optimum deposition conditions after several trials to reach the optimum.

The average performance of the OPV devices, however they have poor performance, (12 device for each), is shown in Table 3.3. The values, however, they are not shown in the table, indicate that several devices are short circuited (3 out of 6) when applying AgNW, independently whether the ink is prepared in the lab or commercial. The JV curves for the champion cells are presented in Figure 3.15. The poor performance resulted from applying the nanowires in devices could be due to excessive roughness caused by the wires themselves. As a trial to overcome this issue, we applied the PEDOT: PSS as a matrix to embed the nanowires. PEDOT:PSS containing samples gave better photocurrent than those with the bare AgNW. The devices with electrode two layers of PEDOT: PSS and AgNWs give a lower photo-generated current and in turn lower efficiency than the devices with electrode of one layer of the nanowires mixed with PEDOT: PSS. That shows the better mixing between the polymer and the nanowires in which the PEDOT: PSS helps to fill the gaps between the wires and improves the conductivity. On the other hand, for devices based only on AgNW, both commercial and our formulations give similar efficiencies. For PEDOT:PSS containing electrodes, our formulation is the one that produces the best ITO-free cells of the considered electrodes. The final efficiency is, however, still, half of that obtained when using ITO. Further optimization would need to be undertaken in order to reduce the gap between ITO containing and ITO free cells.

Table 3.2 The deposition conditions of different inks by blade coatings in the inverted solar cells

Ink	Formulation	Printing parameters Ink volume[µl], blade speed[mm/s], blade gap[µm] & plate temperature [ºC]
ZnO	15 mg/ml prepared at Eurecat	40 µl, 40 mm/s,100 µm & 45 ºC
P3HT:PC_{60}BM	[30:24] wt% in CB	40 µl, 5 mm/s,100 µm & 45 ºC
PolyBio wire	Commercial	100 µl, 40 mm/s,100 µm & 80 ºC
HYE	Commercial	60 µl, 5 mm/s,100 µm & 80 ºC
AgNW mixed with PEDOT: PSS / PEDOT:PSS	Commercial	30µl, 3 mm/s,100 µm, 80 ºC
AgNW	In ethanol 6mg/ml	40µl, 45mm/s,100 µm, 65 ºC

Table 3. 3 The average values of the photovoltaic parameters ± the standard deviation values [the best cell performance] of ITO free solar cells prepared with different bottom electrodes. An ITO-containing device has been included for comparison purposes

Electrode	V_{oc}[V]	J_{sc}[mA/cm^2]	FF[%]	PCE[%]
AgNW	0.39±0.08[0.39]	1.05±0.68[1.53]	25.7±6.10[34.2]	0.18±0.08[0.2]
AgNW with PEDOT [Two layers]	0.48±0.03[0.5]	1.40±0.59[1.82]	37.9±3.6[40.5]	0.26±0.14[0.36]
HYE	0.35±0.32[0.45]	0.78±0.16[1]	25.5±42.3[36]	0.15±0.02[0.16]
Poly BIO Wires	0.30±0.05[0.36]	0.30±0.10[0.35]	25.6±3.1[25.1]	0.02±0.01[0.03]
ITO	0.55±0.01[0.55]	6.28±1.08[7.36]	49.72±3.55[44.7]	1.69±0.25[1.94]
AgNW mixed with PEDOT:PSS [one layer]	0.29±0.15[0.44]	5.13±0.61[5.74]	35.3±11.7[47]	0.62±0.49[1.11]

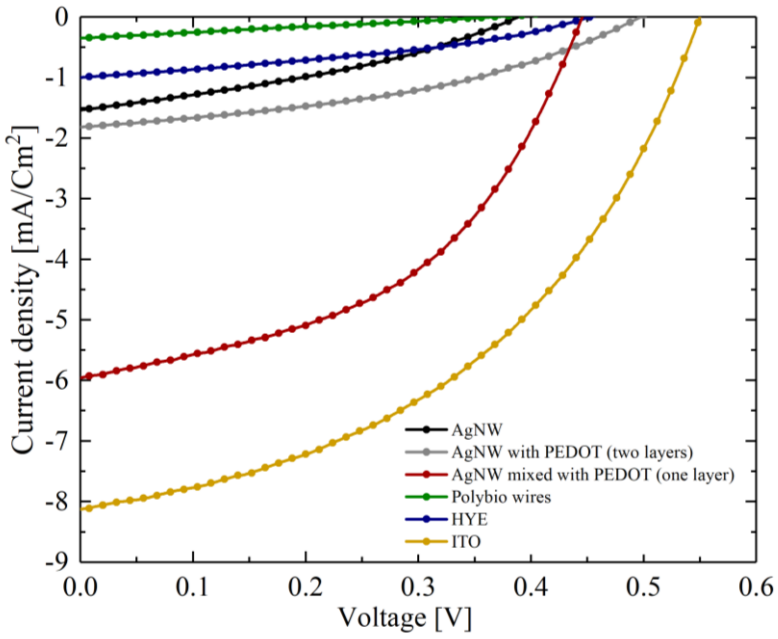

Figure 3.15 The best devices JV curves of ITO free solar cells prepared with different bottom electrode materials. ITO-containing device is shown for comparison purposes.

The synthesized AgNW showed high roughness (RMS)of 68±6 nm as measured by profilometer, for a layer with an as-deposited thickness of 108±18 nm. In order to flatten these films and to increase the conductivity between the wires, one solution was to deposit PEDOT: PSS (Clevios FHC Solar) layer on top (labelled as AgNWs mixed with PEDOT: PSS- two layers). Alternatively, we mix the two components together and print it as one layer (labelled as AgNWs mixed (1:1 VR) with PEDOT: PSS- one layer). Moreover, we compared our materials with two commercial inks: one only based on nanowires (Polybio wires), the other one based on a mixture of nanowires combined with PEDOT: PSS (HYE).

Different solution processed films were deposited by blade coating on PET substrate to test the potential of these materials to be applied as electrodes in OPV devices. The electric conductivity of the films measured by the four-probe technique showed values of 4.8 x10^4 S/cm, 2.4x10^3 S/cm, 2.1x10^2 S/cm and 2.6 x10^2 S/cm for the Ag Dupont 5000, PolyBio wires, PEDOT: PSS, PolyBio wires and PEDOT: PSS on top (two layers), respectively. The

deposited films were of thicknesses 7.46 µm, 0.075 µm, 0.511 µm and 0.208 µm, respectively. The Ag Dupont 5000 was totally opaque. However, the optical transmissions (at wavelength, λ = 550 nm) of the PolyBio wires, PEDOT: PSS, PolyBio wires and PEDOT: PSS on top (two layers) were 87%, 75% and 81%, respectively.

These findings revealed the ease solution synthetization and optimization of the silver nano wires as a high potential material to replace indium tin oxide for the application of semitransparent electrode in OPV devices due to their remarkable FOM, solution-processing, flexibility and cost wise. The disadvantages of AgNWs are high roughness, low adhesion to substrates and high resistance at the wires junction. Yet, AgNWs still have the potential as a TCEs and it has reported a new generation of the silver nano rings with their outstanding properties for more potentials due to the high transmittance, high conductivity, easy processing, and notable flexibility[91].

As reported in the literature the main challenge stands against the application of silver nanowires in OPV devices is the roughness and the reported solution are by embedding the AgNW into the substrate [either by contact transfer method or by applied pressure method] or by addition of another layer over the AgNWs. The reported solutions for the future work [86] of AgNWs as TCE are listed in the Table 3.4.

Table 3.4 solution for the reported challenges of applying AgNWs in solar cells.

High Roughness	Two solutions (a)Embedding AgNWs into substrates either by contact transfer methos or by applied pressure (b) Coating overcoat layer on AgNWs network
Low Adhesion on substrate	Heating of AgNWs, Coating overcoat layer on AgNWs network and Substrate, Embedding AgNWs into polymer substrates, Substrate surface modification and Using Adhesion Promoter
High Wire-Wire Junction resistance Physically welding methods	Physically welding methods, Chemically Welding methods, and Coating overcoat layer (Nano soldering)
Atmospheric corrosion Embedding AgNWs into polymer substrates	AgNWs into polymer substrates, Coating overcoat layer on AgNWs network and Chemical treatment

3.5.2 Evaporation free semitransparent solar cells

The importance of AgNWS as TCE can come along with their application as top electrode as well as discussed in in section 3.2. Applying AgNWs as a top electrode in solar cells allows the complete coating of all device layers without decreasing the transparency compared to the evaporated electrodes. Different silver nano wires (AgNWs, polybio wires and HYE) have been tested as top electrode, in devices with structure glass/ITO/AZO/PAL/PEDOT: PSS/Top electrode. We shifted from using the ZnO to the AZO as a ETL since we found some problems while coating the ZnO by roll-to-roll and also when AZO used the modules performance do not vary critically on the variation of the coated layer thickness. The printing parameters employed for these experiments are listed in Table 3.5. Table 3.6 shows the photovoltaic parameters of semitransparent devices with three blade speeds for the deposition optimization of the top electrode. The IV curves of the champion cells are shown in Figure 3.16.

Table 3.5 The printing parameters of the semitransparent devices.

Ink	Formulation	Printing parameters [Ink volume , blade speed, blade Gap, plat temperature]
AZO	AVANTAMA	30 µl, 5mm/s, 150 µm, 45ºC
P3HT:$PC_{60}BM$	[30:24] wt % in CB	40 µl, 40mm/s, 200 µm, 100ºC
PEDOT:PSS	PEDOT:H_2O[80:20]wt% with 0.5% Capstone [Eurecat R2R recipe]	30 µl, 3 mm/s, 250 µm, 80ºC
PolyBio wire	Commercial 10% DAPRO W-77	40 µl, 90mm/s, 250 µm, 65ºC
HYE	Commercial	40 µl, 10mm/s, 250 µm, 65ºC
AgNW	In ethanol 6mg/ml	40 µl, 45mm/s, 250 µm, 65ºC

Table 3.6 Photovoltaic parameters of the semitransparent devices.

Blade Speed [mm/s]	Electrode	V_{oc} [V]	J_{sc} [mA/cm^2]	FF[%]	PCE[%]
45 mm/s	**AgNW**	0.44±0.06[0.48]	2.13±0.42[2.21]	32.31±2.87[35.43]	0.31±0.10[0.37]
	Polybio wires	0.36±0.12[0.44]	2.29±0.06[2.29]	35.13±7.14[40.41]	0.31±0.15[0.46]
	HYE	0.50±0.01[0.51]	2.90±0.19[3.03]	42.37±0.47[42.03]	0.62±0.05[0.67]
10 mm/s	**AgNW**	0.22±0.07[0.29]	2.27±0.42[2.57]	28.92±2.72[31.85]	0.16±0.08[0.24]
	Polybio wires	0.47±0.04[0.47]	4.63±0.43[4.71]	38.47±2.41[39.11]	0.83±0.18[0.86]
	HYE	0.43±0.10[0.44]	5.04±1.23[6.07]	33.04±6.30[35.32]	0.71±0.26[0.97]
90 mm/s	**AgNW**	0.30±0.12[0.4]	2.42±0.88[3.2]	32.32±5.55[33.08]	0.26±0.18[0.42]
	Polybio wires	0.47±0.01[0.47]	3.40±0.62[4.12]	40.73±3.16[37.52]	0.65±0.10[0.75]
	HYE	0.47±0.06[0.52]	4.59±1.76[5.66]	39.02±6.63[44.81]	0.82±0.35[1.17]

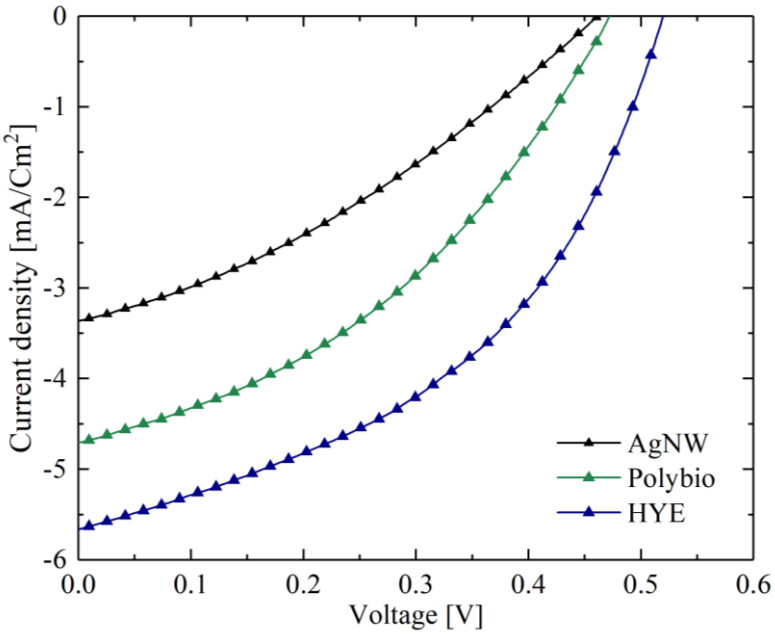

Figure 3. 16 The JV curves of the best semitransparent devices.

The devices with optimized Polybio wires and HYE have the better photocurrent and hence better efficiency than the devices with the synthesized AgNWs. The modules with the synthesized AgNWs as an electrode have the lowest current between the three modules due to the low adhesion of the AgNWs layer to the beneath layers that lead to low ability of charge collection. The V_{oc} values of the modules found to be low compared to the performance of the solar cells with evaporated silver electrode that could be due to the change of the electrode work function by introducing the PEDOT:PSS as it is mentioned in the literature that the work function is related to the type of PEDOT:PSS used based on ink

formation PH that changes the work function of the electrode and hence as a consequence the device performance[92].

The prepared AgNWs ink formulation was not adequate for its processing by roll to roll. The printed layers were not homogeneous in case of the synthesized AgNWs. Moreover, the adhesion to the substrate and or to the PEDOT: PSS layer of AgNWs layer is too poor that stands against their application in the OPV devices. We found that the adhesion problem of AgNWs film weather to the substrate or to the layer beneath was reported[86]. It was found that the thermal treatment of the AgNWs and intense light pulse light enhances the adhesion for the small-scale devices and for the large-scale the use of binder polymer, coating extra layer of metal oxides and embedding the silver nanowires in polymer substrates reported to improve the adhesion issues this problem has been reported in the literature [86].

As we did not succeed to formulate the ink for the synthesized silver nanowires, thus we shifted to apply solution processed silver electrode by screen printed technique and for further optimization for the electrode geometry as follows in the next section.

3.6 Applying solution processed electrodes in OPV devices

3.6.1 30 cells module: Importance of the silver fingers

We shifted from the roll-to-rolled slot die silver nano wires to screen printed silver grid electrodes. The metal grid has economic advantages by allowing thick metal layer with minimum cost. We chose Ag Dupont 5000 from the reported inks for its roll-to-roll compatible processability and its conductivity[93]. In addition, the grid geometry improves the transparency of the OPV modules. The grid design needs to be optimized for a good charge carrier collection and avoid damaging the underneath layers due to its ink solvents. The whole modules design has been led by the previous work presented in the literature[94,95]. For this reason, the top electrode is printed in form of fingers, minimizing the contact between silver paste and the other layers, taking advantage from the presence of the conductive PEDOT: PSS

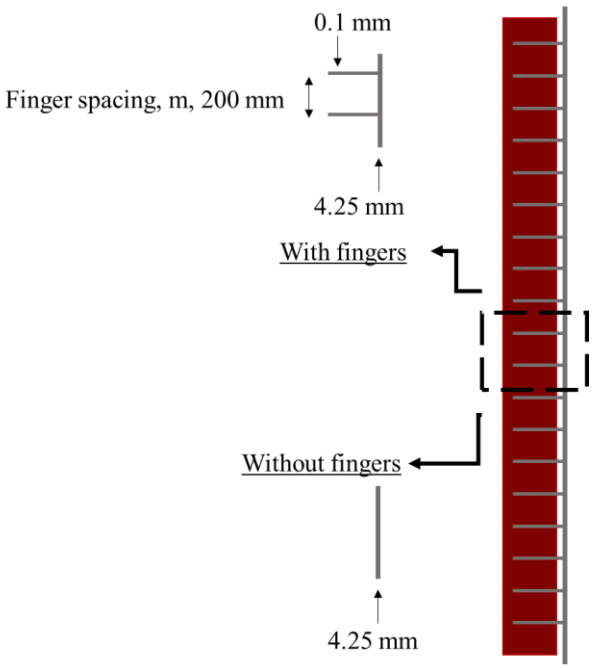

Figure 3.17 The geometry of the screen-printed silver electrode.

Figure 3.17 shows the design of the screen-printed silver electrode that contains two parts, one with fingers and the other without fingers. The geometry of the OPV modules of 30 cells are shown in Figure 3.18 showing the inverted structure of the solo devices of PET/ITO/ETL/PAL/HTL/Ag. ETL, PAL and HTL are slot die coated whereas the top silver electrode was screen printed where the stripes are of active area 11.2 cm^2. The schematic illustration of the series interconnection between 30 cells in one module is shown in Figure 3.18 [a]. This reflects the advantage of this printing technique providing the less coasty efficient compared to the laser patterning way to introduce the monolithic interconnection between the 30 cells in one module. The resolution of the printing technique affects the active and the dead areas in the module and in consequence the geometrical fill factor of the module. Printing the HTL is playing an important role in the monolithically inter connection, so its printing is slightly shifted on purpose as shown in Figure 3.18 [a] to connect the bottom electrode, ITO, with the top electrode, Ag.

The geometric fill factor (GFF), described in equation 4.8, is the active area over the total area of module connected monolithically where the dimensions are shown in Figure 3.18 [b], The parameters are: n is the cells number, L is the length of the module, W is the width of the module, and the w is the width of the single cell.

$$GFF = \frac{Active\ area}{Total\ area} = \frac{n \times L \times w}{n \times L \times W} \qquad \text{Equation 4. 8}$$

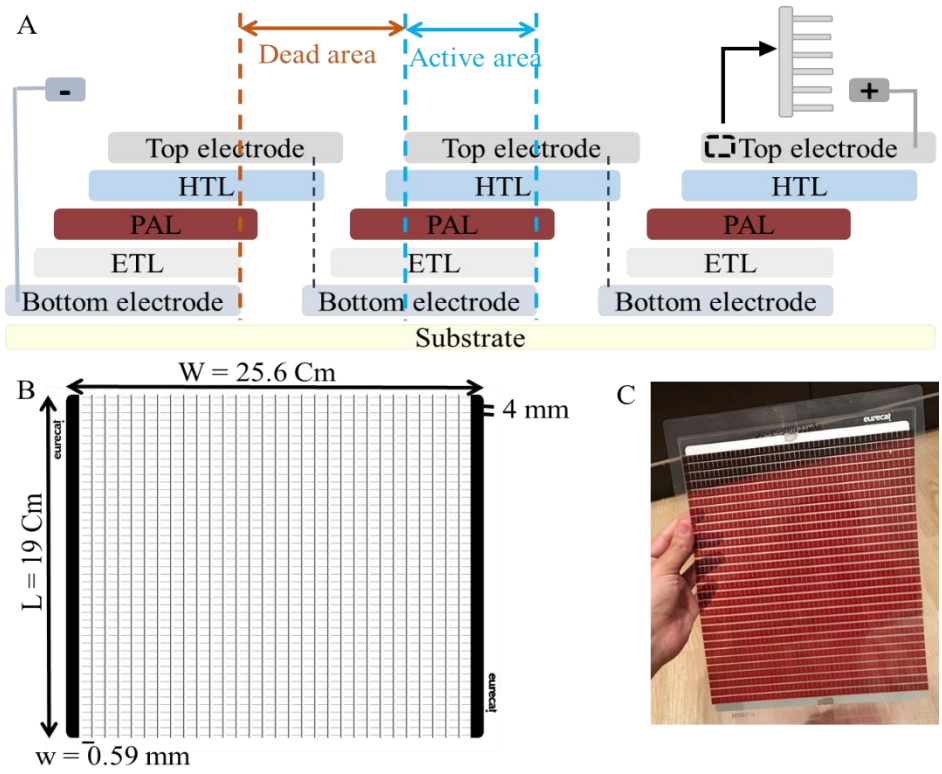

Figure 3.18 (A) The module design,(B) the top electrode geometry and (C)real image of the fully solution processed module of 30 cells.

The coating parameters of the roll-to-roll processed layers are tabulated in Table 3.7. Silver conductor Dupont 5000 ink was printed by screen printing technique. The blade pressure was set to the minimum to ensure printing all thin fingers throughout the mask. This fact is very relevant because some damage was inferred in the layer's underneath like PEDOT: PSS and active layer while printing silver with serigraphy.

Two designs of silver electrode were performed. The first one is the traditional with contacts at the edges of the module, bus bar and fingers. Furthermore, we tested the performance of the solar cell without grid fingers and bus bars, in other words, only silver contacts in the edges were printed, which served to evaluate any lack of compatibility between the screen-printed ink and the layers underneath. After silver printing, modules were cured in the oven at 120ºC for 20 minutes. The lamination step was carried out with the laminating machine by introducing the solar module between PET foils. The lamination is done by melting A4 size

PET at 80ºC on top and below of solar module. Figure 3.19 shows the best JV curves of the modules with two different designs of top electrode. The photovoltaic parameters are presented in Table 3.7, which shows the importance of the fingers in the charge collection.

Table 3.7 The printing conditions of the slot die roll to rolled OPV module.

	Printing conditions	ZnO	P3HT: PCBM	PEDOT: PSS
Pump	Flow [mL/minute]	1.2	3	6.5
	Tube [internal diameter, mm]	1.45	2.06	2.54
Ink	Solvent	Methanol	CB	Water
	Concentration[mg/mL]	50	30:24 MW	20% , 0.54 capstone
Substrate	Speed[m/minute]	1.2	1.4	0.8
	Tension[N]	30	30	30
Curing Temperature	Oven temperature [ºC]	140	140	140

Table 3.8 The average photovoltaic parameters of the modules with different top electrodes

Modules	V_{oc} [V]	J_{sc} [mA.cm^{-2}]	FF [%]	PCE [%]
Without fingers	14±0.4	3±0.3	33±2	0.40±0.05
With fingers	8±5	3±1	30±6	0.3±0.2

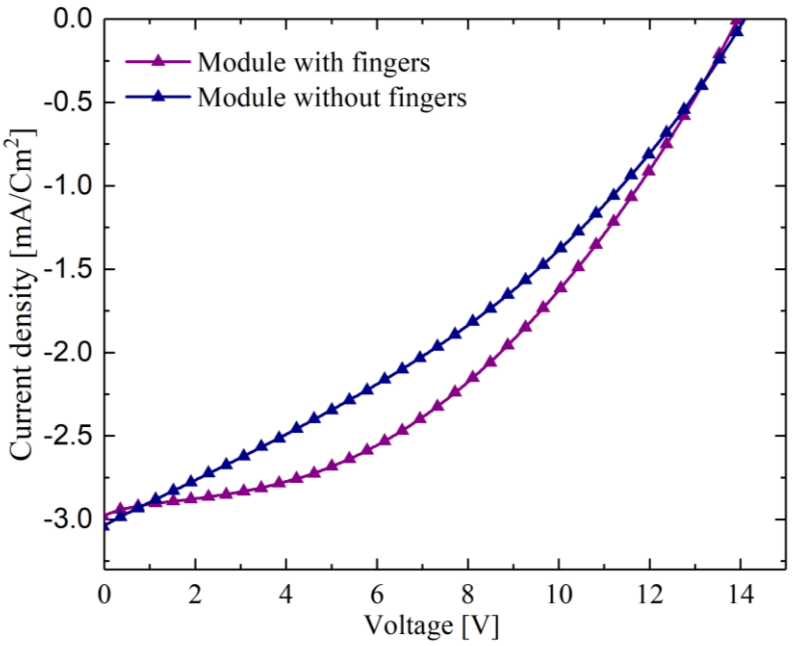

Figure 3.19 The best JV curves of modules with two silver top electrode with fingers (purple color) and without fingers (blue color).

The results shown in the figure showed that the photovoltaic performance is better when the electrode design is with fingers because the V_{oc} and J_{sc} are similar, but the FF is better. The average performance of modules presented in table 3.8 showed that, however being in

principle good, having electrode design with fingers leads to larger spread of values in the performance. However, the concept of the fingers was to enhance the charge extraction and to reduce the distances that the charge carriers need to travel through the PEDOT: PSS to reach the electrode. In order to have a deeper understanding of this result we carried out an additional characterization of the modules.

Light Beam Induced Current, LBIC, measurement was carried out to understand if the fingers are chemically damaging the layers beneath or they are participating in collecting the charge carriers: LBIC was measured on a 4-stripe module, together with simultaneous Raman measurement of the same area. The module illuminated by a 532 nm laser source and the corresponding Raman spectra obtained by WITec alpha 300 RA.

Figure 3.20 revealed that areas covered with silver grid fingers are the areas with lowest photocurrent. However, active areas between fingertips and bus bar are the areas with the higher photocurrent. The Raman signal of the P3HT placed under the silver fingers has less intensity than the area of P3HT placed between the silver fingers suggesting the interaction of the solvents of the silver paste with the active layer beneath.

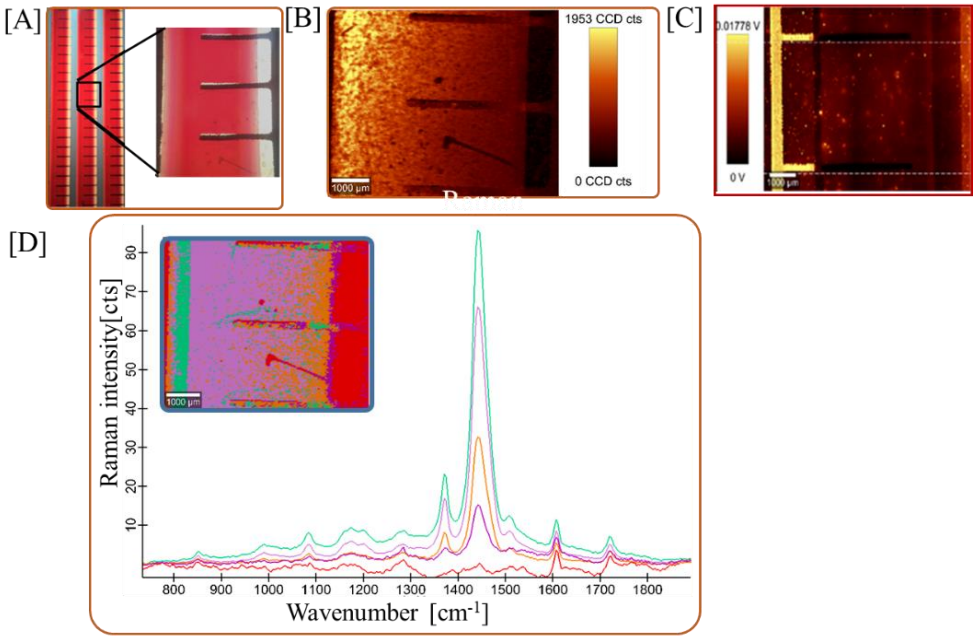

Figure 3.20 [A] Photo of the measured module,[B] the integrated Raman intensity for P3HT, [C] the LBIC measured for the module and [D] a cluster analysis of the Raman signal, which we used to quantify the amount of P3HT in the different regions. The color code is the same that different areas in the module; dark purple is for the area beneath the silver.

3.6.2 3&6 cells module: Optimization of the finger spacing

In the silver grid, the PEDOT: PSS layers plays two roles, first as a hole transport layer (electron blocking layer) and second as part of the electrode, as it has to transport the charges laterally towards the silver electrode fingers. The distance between silver fingers is, thus, an important parameter when working with such a configuration that needs to be optimized according to the PEDOT conductivity[96,97]. In this section, we thus investigate finger interspacing. Moreover, the study has been designed to also test if important differences can be observed when changing the number of cells forming a module: 3 and 6 series-connected cells have been tested.

Different modules were tested for two reasons the first is to optimize the spacing between the electrode fingers 1mm, 2mm, 4mm and 8mm, and the second is the optimize the number of cells per modules [either 3 or 6 cells] as shown in Figure 3.21 of device structure employed in this case was PET/ITO/AZO/P3HT:PC_{60}BM/PEDOT: PSS/Ag.

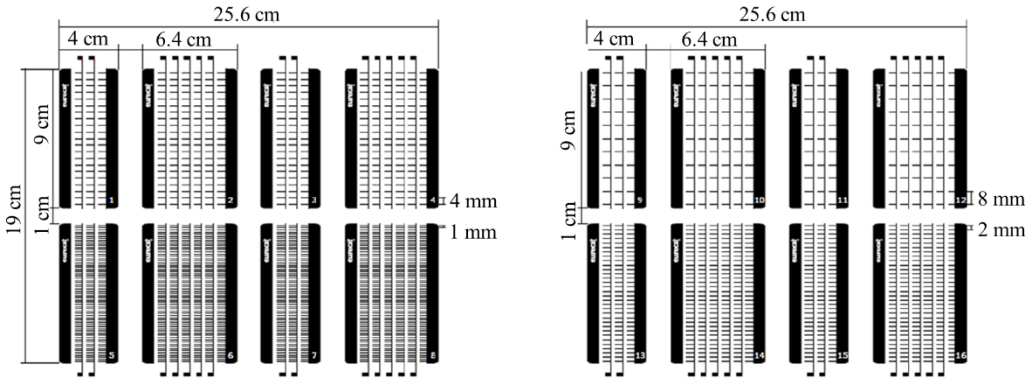

Figure 3.21 The design of the screen for the screen-printed silver electrode, which evaluates modules with either 3 or 6 cells, as well as several spacing values between the fingers, namely 1, 2, 4 and 8 mm.

First, the four considered spacings between the electrode fingers have been tested in one batch of 6-cells modules, and the J-V curves of the best devices for each spacing are shown in Figure 3.22. The photovoltaic parameters of the corresponding modules are listed in Table 3.9. The spacings that gave the best results, over 20 modules per each value, are 1 and 4 mm. For this reason, we focused on these values to compare between modules with 3 and 6 cells. In principle as the distance between the fingers increases the resistance increases which should lead to a decrease in both the FF and the J_{sc}. The parameters presented in Table 3.9 agrees with the hypothesis since both the values of the FF and the Jsc are lower in the case of modules with an electrode configuration of 8mm than in case of the modules with an electrode configuration of 1mm. However, the area beneath the electrode interprets the data from a different perspective since the PAL under the electrode finger suffers degradation that means that the lower the number of the fingers the larger the photogenerated current. Considering the proposed hypothesis, the results of 2mm and 4mm showed the optimum electrode spacing for the electrode configuration despite that the 2mm was unexpected. Second is the number of modules optimization in which the number of the connected modules is proportional to the Voc that makes the 6 cells configuration is better than the 3 cells configuration.

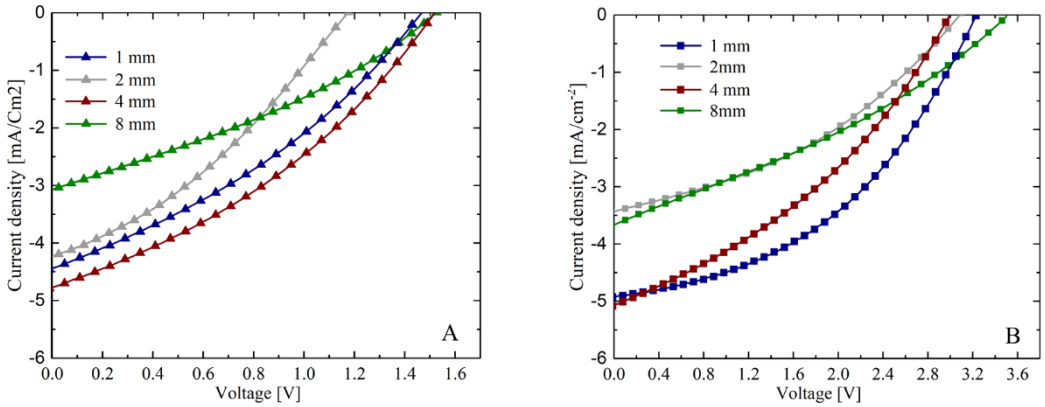

Figure 3.22 The best JV curves of 3 cells modules, triangle, (A) and 6 cells modules, square, (B) with different silver finger spacing (top electrode) 1mm (blue), 2mm (gray), 4 mm (red) and 8mm (olive).

Table 3.9 the photovoltaic parameters of the 3-cells and 6-cells modules with different spacings between the silver electrode fingers.

Finger spacing	V_{oc} (V)	J_{sc} (mA/cm^2)	FF (%)	PCE (%)
1 mm	3 cells modules			
	1.40±0.19	4.23±0.38	32.38±2.82	0.47±0.13
	6 cells modules			
	3.51±1.5	3.54±0.28	35.29±6.55	0.67±0.33
2 mm	3 cells modules			
	1.02±0.37	2.42±1.03	31.69±3.60	0.26±0.15
	6 cells modules			
	2.07±0.70	2.57±1.08	30.06±3.5	0.30±0.20
4 mm	3 cells modules			
	1.25±0.17	4.33±0.66	30.54±2.62	0.58±0.16
	6 cells modules			
	2.94±0.21	4.35±0.37	35.30±2.28	0.76±0.10
8 mm	3 cells modules			
	1.24±0.32	2.08±0.80	32.47±2.46	0.29±0.15
	6 cells modules			
	2.02±0.89	2.1±1.08	15±61	0.24±0.18

It must be said that the V_{oc} values, around a mean of 1.2 V for 3 cells and 2.9 V for 6 cells, are near to the expected ones for a P3TH:PCBM system (approximately 1.5 V and 3 V, respectively) due to their energy levels of the materials, being slightly lower. The current densities, between 3 and 5 mA·cm^{-2}, are not the best ones we could expect from these devices. The same may be said for the fill factors, between 30 and 45% considering the two groups. In terms of efficiency, the obtained values are below than 1% with very few exceptions.these observed lower values might be due to the low geometrical fill factor to connent the cells per module.

After realizing the importance of the silver paste incompatibility and seeking for the optimization of the electrode geometry, we applied different PEDOT: PSS inks as a solution of preventing the interaction between the electrode and the active layer. The photovoltaic

parameters of the 3-cells modules with different HTLs is presented in Table 3.10. Figure 3.23 shows the best JV curves of the 3-cells modules with different HTLs.

Table 3.10 The photovoltaic parameters of the 3- cells modules with different HTLs.

Electrode	V_{oc}[V]	J_{sc}[mA/cm^2]	FF[%]	PCE[%]
HYE+Ag 4mm	1.45±0.16	3.44±0.87	32.58±3.19	0.55±0.19
Best device	1.63	4.53	36.64	0.91
PEDOT+Ag 4mm	1.27±0.28	4.83±0.35	31.71±2.80	0.68±0.21
Best device	1.46	4.98	35.81	0.88
PEDOT+Ag 1mm	1.22±0.17	4.12±0.81	31.06±2.30	0.54±0.16
Best device	1.37	4.41	33.83	0.69
PEDOT+HYE+Ag 4mm	1.31±0.51	3.47±1.42	35.13±4.61	0.62±0.39
Best device	1.58	4.79	39.42	1.01

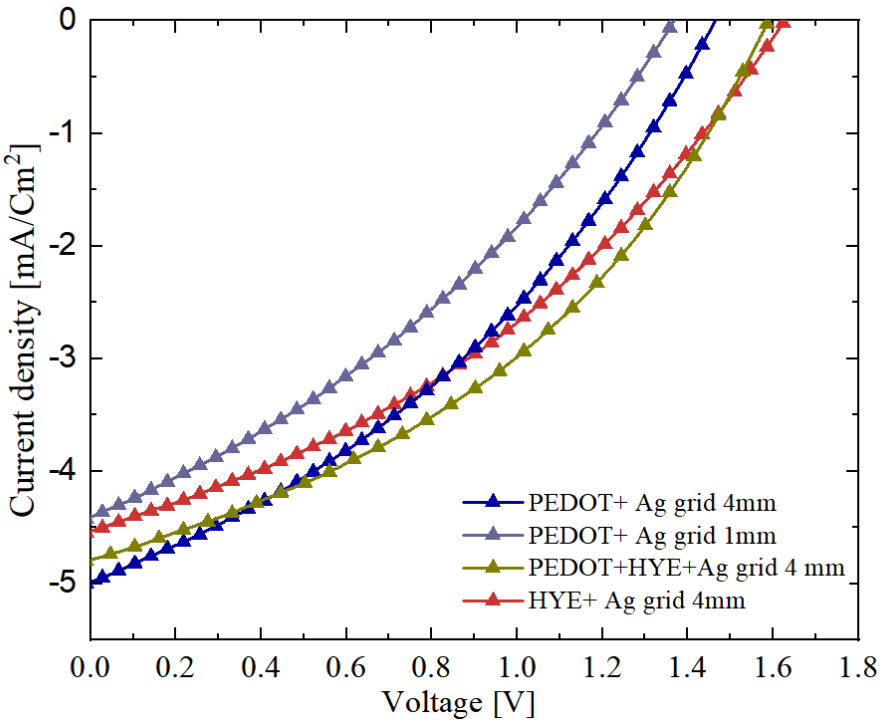

Figure 3.23 The JV curves of the best 3-cells modules with different HTLs.

Introducing the HYE as HTL did not help so much the photovoltaic parameters and the efficiency of the modules since the performance of the modules of PEDOT + Ag grid 4mm is better than the modules of HYE+Ag grid 4mm. This could be due to the less polymer content in case of HYE since the polymer works as an electrode where the electrons pass throgh to reach the silver grid. Exhibitibg two layers of PEDOT:PSS improves the photovoltaic performance of the emodules that leads the future work for implement two layers of different functioning PEDOT:PSS and apply more optimiziation for the corresponding function of each layer such as the thickness, the electrical proprties, the optical properties and their rheological properties.

3.7 CONCLUSIONS

In this chapter, silver nanowires were synthesized and optimized by Polyol method. High FOM of the prepared silver nanowires films was obtained. Application of the silver nanowires as an electrode to replace the ITO into OPV devices are crucial because of their high roughness no matter if the silver nanowires are prepared or of commercial inks. However, silver nanowires have high potentials to be applied for the transparent electrode since they have high transmittance and electrical conductivity in addition to their solution processing. Implementing silver nanowires as a top electrode had a comparable performance in doctor bladed devices, however the prepared one were not compatible for the roll-to-roll technique. Different electrode materials and geometry have been applied to optimize the photovoltaic performance of the devices. Screen printed grid geometry of silver electrode has been optimized where PEDOT:PSS plays two roles as an electrode and as a HTL. One layer of PEDOT:PSS to play two roles was not effective and for the future work two layers should be applied to implement the corresponding the functions with their optimization. Introducing the HYE as HTL did not help so much the photovoltaic parameters and the efficiency of the modules. Further optimization of the electrode geometry by investigating the fingers spacing for better charge collection. In this sense, we observe that 8 mm spacing has revealed as an excessive distance between fingers, probably for a bad charge collection and the spacing of 4 mm revealed good performance of the modules with efficiency reaches 1%.

3.8 References of Chapter 3

[1] W. Cao, J. Li, H. Chen, J. Xue, Transparent electrodes for organic optoelectronic devices,J.PhotonicsEnergy, 4(2014), https://doi.org/10.1117/1.jpe.4.040990.

[2] N.J. Jeon, J.H. Noh, Y.C. Kim, W.S. Yang, S. Ryu, S. Il Seok, Solvent engineering for high-performance inorganic-organic hybrid perovskite solar cells, Nat. Mater. 13 (2014) 897–903. https://doi.org/10.1038/nmat4014.

[3] F.C. Krebs, Solar Energy Materials & Solar Cells Fabrication and processing of polymer solar cells : A review of printing and coating techniques, 93 (2009) 394–412. https://doi.org/10.1016/j.solmat.2008.10.004.

[4] F.C. Krebs, J. Alstrup, H. Spanggaard, K. Larsen, E. Kold, Production of large-area polymer solar cells by industrial silk screen printing, lifetime considerations and lamination with polyethyleneterephthalate, Sol. Energy Mater. Sol. Cells. 83 (2004) 293–300. https://doi.org/10.1016/j.solmat.2004.02.031.

[5] H. Zhen, K. Li, C. Chen, Y. Yu, Z. Zheng, Q. Ling, Water-borne foldable polymer solar cells: one-step transferring free-standing polymer films onto woven fabric electrodes, J. Mater. Chem. A. 5 (2017) 782–788. https://doi.org/10.1039/c6ta08309a.

[6] Y. Zhou, F. Li, S. Barrau, W. Tian, O. Inganäs, F. Zhang, Inverted and transparent polymer solar cells prepared with vacuum-free processing, Sol. Energy Mater. Sol. Cells. 93 (2009) 497–500. https://doi.org/10.1016/j.solmat.2008.11.002.

[7] C.H. Lee, D.R. Kim, I.S. Cho, N. William, Q. Wang, X. Zheng, Peel-and-stick: Fabricating thin film solar cell on universal substrates, Sci. Rep. 2 (2012) 2–5. https://doi.org/10.1038/srep01000.

[8] X. Wang, T. Ishwara, W. Gong, M. Campoy-Quiles, J. Nelson, D.D.C. Bradley, High-performance metal-free solar cells using stamp transfer printed vapor phase polymerized poly(3,4-ethylenedioxythiophene) top anodes, Adv. Funct. Mater. 22 (2012) 1454–1460. https://doi.org/10.1002/adfm.201101787.

[9] T.M. Schmidt, T.T. Larsen-Olsen, J.E. Carlé, D. Angmo, F.C. Krebs, Upscaling of Perovskite Solar Cells: Fully Ambient Roll Processing of Flexible Perovskite Solar Cells with Printed Back Electrodes, Adv. Energy Mater. 5 (2015) 1–9. https://doi.org/10.1002/aenm.201500569.

[10] C. J. Mueller, E. Gann, C. R. McNeillc and M. Thelakkat, Influence of fluorination in π-extended backbone polydiketopyrrolopyrroles on charge carrier mobility and depth-dependent molecular alignment, J.Mater.Chem.C,2015, 3,8916, https://doi: 10.1039/c5tc01948f.

[11] C. Girotto, B.P. Rand, J. Genoe, P. Heremans, Solar Energy Materials & Solar Cells Exploring spray coating as a deposition technique for the fabrication of solution-processed solar cells, 93 (2009) 454–458. https://doi.org/10.1016/j.solmat.2008.11.052.

[12] E. Ramasamy, W.J. Lee, D.Y. Lee, J.S. Song, Spray coated multi-wall carbon nanotube counter electrode for tri-iodide (I3-) reduction in dye-sensitized solar cells, Electrochem. Commun. 10 (2008) 1087–1089. https://doi.org/10.1016/j.elecom.2008.05.013.

[13] S. Tang, Y. Deng, X. Zheng, Y. Bai, Y. Fang, Q. Dong, H. Wei, J. Huang, Composition Engineering in Doctor-Blading of Perovskite Solar Cells, Adv. Energy Mater. 7 (2017) 1–7. https://doi.org/10.1002/aenm.201700302.

[14] K. Hwang, Y.S. Jung, Y.J. Heo, F.H. Scholes, S.E. Watkins, J. Subbiah, D.J. Jones, D.Y. Kim, D. Vak, Toward large scale roll-to-roll production of fully printed perovskite solar cells, Adv. Mater. 27 (2015) 1241–1247. https://doi.org/10.1002/adma.201404598.

[15] P. Joshi, Y. Xie, M. Ropp, D. Galipeau, S. Bailey, Q. Qiao, Dye-sensitized solar cells based on low cost nanoscale carbon/TiO 2 composite counter electrode, Energy Environ. Sci. 2 (2009) 426–429. https://doi.org/10.1039/b815947p.

[16] Z. Wei, H. Chen, K. Yan, S. Yang, Inkjet printing and instant chemical transformation of a CH3NH3PbI3/nanocarbon electrode and interface for planar perovskite solar cells, Angew. Chemie - Int. Ed. 53 (2014) 13239–13243. https://doi.org/10.1002/anie.201408638.

[17] C.N. Hoth, S.A. Choulis, P. Schilinsky, C.J. Brabec, High photovoltaic performance of inkjet printed polymer:Fullerene blends, Adv. Mater. 19 (2007) 3973–3978. https://doi.org/10.1002/adma.200700911.

[18] V. V. Brus, J. Lee, B.R. Luginbuhl, S.J. Ko, G.C. Bazan, T.Q. Nguyen, Solution-Processed Semitransparent Organic Photovoltaics: From Molecular Design to Device Performance, Adv. Mater. 31 (2019) 1–26. https://doi.org/10.1002/adma.201900904.

[19] L. Gomez De Arco, Y. Zhang, C.W. Schlenker, K. Ryu, M.E. Thompson, C. Zhou, Continuous, highly flexible, and transparent graphene films by chemical vapor deposition for organic photovoltaics, ACS Nano. 4 (2010) 2865–2873. https://doi.org/10.1021/nn901587x.

[20] C.J.M. Emmott, A. Urbina, J. Nelson, Environmental and economic assessment of ITO-free electrodes for organic solar cells, Sol. Energy Mater. Sol. Cells. 97 (2012) 14–21. https://doi.org/10.1016/j.solmat.2011.09.024.

[21] D. Angmo, F.C. Krebs, Flexible ITO-free polymer solar cells, J. Appl. Polym. Sci. 129 (2013) 1–14. https://doi.org/10.1002/app.38854.

[22] B. Azzopardi, C.J.M. Emmott, A. Urbina, F.C. Krebs, J. Mutale, J. Nelson, Economic

assessment of solar electricity production from organic-based photovoltaic modules in a domestic environment, Energy Environ. Sci. 4 (2011) 3741–3753. https://doi.org/10.1039/c1ee01766g.

[23] F. Paquin, J. Rivnay, A. Salleo, N. Stingelin, C. Silva, Multi-phase semicrystalline microstructures drive exciton dissociation in neat plastic semiconductors, J. Mater. Chem. C. 3 (2015) 10715–10722. https://doi.org/10.1039/b000000x.

[24] D.S. Hecht, L. Hu, G. Irvin, Emerging Transparent Electrodes Based on Thin Films of Carbon Nanotubes , Graphene , and Metallic Nanostructures, (2011) 1482–1513. https://doi.org/10.1002/adma.201003188.

[25] Z. Wu, Z. Chen, X. Du, J.M. Logan, J. Sippel, M. Nikolou, K. Kamaras, J.R. Reynolds, D.B. Tanner, A.F. Hebard, A.G. Rinzler, American Association for the Advancement of Science, 305 (2016) 1273–1276.

[26] S. Bae, H. Kim, Y. Lee, X. Xu, J.S. Park, Y. Zheng, J. Balakrishnan, T. Lei, H. Ri Kim, Y. Il Song, Y.J. Kim, K.S. Kim, B. Özyilmaz, J.H. Ahn, B.H. Hong, S. Iijima, Roll-to-roll production of 30-inch graphene films for transparent electrodes, Nat. Nanotechnol. 5 (2010) 574–578. https://doi.org/10.1038/nnano.2010.132.

[27] K.S. Kim, Y. Zhao, H. Jang, S.Y. Lee, J.M. Kim, K.S. Kim, J.H. Ahn, P. Kim, J.Y. Choi, B.H. Hong, Large-scale pattern growth of graphene films for stretchable transparent electrodes, Nature. 457 (2009) 706–710. https://doi.org/10.1038/nature07719.

[28] T. Kobayashi, M. Bando, N. Kimura, K. Shimizu, K. Kadono, N. Umezu, K. Miyahara, S. Hayazaki, S. Nagai, Y. Mizuguchi, Y. Murakami, D. Hobara, Production of a 100-m-long high-quality graphene transparent conductive film by roll-to-roll chemical vapor deposition and transfer process, Appl. Phys. Lett. 102 (2013) 1–5. https://doi.org/10.1063/1.4776707.

[29] 3nm) were up to a hundred microns across and visible by the naked eye. Figure 1 shows examples of the prepared films, including single-layer graphene (see also [15]). To study their electronic properties, the films were processed into multi-terminal Hall , 22 (2004) 2–6.

[30] F. Bonaccorso, Z. Sun, T. Hasan, A.C. Ferrari, Graphene photonics and optoelectronics, Nat. Publ. Gr. 4 (2010) 611–622. https://doi.org/10.1038/nphoton.2010.186.

[31] B.N. Chandrashekar, B. Deng, A.S. Smitha, Y. Chen, C. Tan, H. Zhang, H. Peng, Z. Liu, Roll-to-Roll Green Transfer of CVD Graphene onto Plastic for a Transparent and Flexible Triboelectric Nanogenerator, Adv. Mater. 27 (2015) 5210–5216. https://doi.org/10.1002/adma.201502560.

[32] D.W. Lee, T.K. Hong, D. Kang, J. Lee, M. Heo, J.Y. Kim, B.S. Kim, H.S. Shin, Highly controllable transparent and conducting thin films using layer-by-layer assembly of oppositely charged reduced graphene oxides, J. Mater. Chem. 21 (2011) 3438–3442. https://doi.org/10.1039/c0jm02270e.

[33] S.B. Yang, B.S. Kong, D.H. Jung, Y.K. Baek, C.S. Han, S.K. Oh, H.T. Jung, Recent advances in hybrids of carbon nanotube network films and nanomaterials for their potential applications as transparent conducting films, Nanoscale. 3 (2011) 1361–1373. https://doi.org/10.1039/c0nr00855a.

[34] T. Dürkop, S.A. Getty, E. Cobas, M.S. Fuhrer, Extraordinary Mobility in Semiconducting Carbon Nanotubes, Nano Lett. 4 (2004) 35–39. https://doi.org/10.1021/nl034841q.

[35] Z. Yao, C.L. Kane, C. Dekker, High-Field Electrical Transport in Single-Wall Carbon Nanotubes, Phys. Rev. Lett. 8, (2000) 2941–2944, https://doi.org/10.1103/PhysRevLett.84.2941

[36] Y. Zhou, R. Azumi, Carbon nanotube based transparent conductive films: progress, challenges, and perspectives, Sci. Technol. Adv. Mater. 17 (2016) 493–516. https://doi.org/10.1080/14686996.2016.1214526.

[37] F. Basarir, F.S. Irani, A. Kosemen, B.T. Camic, F. Oytun, B. Tunaboylu, H.J. Shin, K.Y. Nam, H. Choi, Recent progresses on solution-processed silver nanowire based transparent conducting electrodes for organic solar cells, Mater. Today Chem. 3 (2017) 60–72. https://doi.org/10.1016/j.mtchem.2017.02.001.

[38] L. Hu, H. Wu, Y. Cui, Metal nanogrids, nanowires, and nanofibers for transparent electrodes, MRS Bulletin, Solution-processed transparent electrodes , 36 (2011) 760–765, https://doi.org/10.1557/mrs.2011.234.

[39] S. Hong, J. Yeo, G. Kim, D. Kim, H. Lee, J. Kwon, H. Lee, P. Lee, S.H. Ko, Nonvacuum , Maskless Fabrication of a Flexible Metal Grid Transparent Conductor by Low-Temperature Selective Laser Sintering of Nanoparticle Ink, (2013).

[40] Y. Xia, K. Sun, J. Ouyang, Solution-processed metallic conducting polymer films as transparent electrode of optoelectronic devices, Adv. Mater. 24 (2012) 2436–2440. https://doi.org/10.1002/adma.201104795.

[41] M.Gyu Kang, M.Su Kim, J.Kim, L. Jay Guo, advanced materials, 20(2008) 4413. https://doi.org/10.1002/adma.200800750.

[42] Y. Sun, B. Gates, B. Mayers, Y. Xia, Crystalline Silver Nanowires by Soft Solution Processing, Nano Lett. 2 (2002) 165–168. https://doi.org/10.1021/nl010093y.

[43] Y. Sun, Y. Yin, B.T. Mayers, T. Herricks, Y. Xia, Uniform silver nanowires synthesis by reducing AgNO3 with ethylene glycol in the presence of seeds and poly(vinyl pyrrolidone), Chem. Mater. 14 (2002) 4736–4745. https://doi.org/10.1021/cm020587b.

[44] N. Through, Large-Scale Synthesis of Uniform Silver, Adv. Mater. (2002) 833–837.

[45] J. Jiu, K. Murai, D. Kim, K. Kim, K. Suganuma, Preparation of Ag nanorods with high yield by polyol process, Mater. Chem. Phys. 114 (2009) 333–338. https://doi.org/10.1016/j.matchemphys.2008.09.028.

[46] J. Jiu, M. Nogi, T. Sugahara, T. Tokuno, T. Araki, N. Komoda, K. Suganuma, H. Uchida, K. Shinozaki, Strongly adhesive and flexible transparent silver nanowire conductive films fabricated with a high-intensity pulsed light technique, J. Mater. Chem. 22 (2012) 23561. https://doi.org/10.1039/c2jm35545k.

[47] P. Zhang, I. Wyman, J. Hu, S. Lin, Z. Zhong, Y. Tu, Z. Huang, Y. Wei, Silver nanowires: Synthesis technologies, growth mechanism and multifunctional applications, Mater. Sci. Eng. B Solid-State Mater. Adv. Technol. 223 (2017) 1–23. https://doi.org/10.1016/j.mseb.2017.05.002.

[48] N.M. Abbasi, H. Yu, L. Wang, Zain-Ul-Abdin, W.A. Amer, M. Akram, H. Khalid, Y. Chen, M. Saleem, R. Sun, J. Shan, Preparation of silver nanowires and their application in conducting polymer nanocomposites, Mater. Chem. Phys. 166 (2015) 1–15. https://doi.org/10.1016/j.matchemphys.2015.08.056.

[49] S.M. Bergin, Y.-H.H. Chen, A.R. Rathmell, P. Charbonneau, Z.-Y.Y. Li, B.J. Wiley, The effect of nanowire length and diameter on the properties of transparent, conducting nanowire films, Nanoscale. 4 (2012) 1996. https://doi.org/10.1039/c2nr30126a.

[50] G. Dennler, M.C. Scharber, C.J. Brabec, Polymer-fullerene bulk-heterojunction solar cells, Adv. Mater. 21 (2009) 1323–1338. https://doi.org/10.1002/adma.200801283.

[51] Y. Sun, Silver nanowires–unique templates for functional nanostructures, Nanoscale. 2 (2010) 1626–1642.

[52] D. Langley, G. Giusti, C. Mayousse, C. Celle, D. Bellet, J.P. Simonato, Flexible transparent conductive materials based on silver nanowire networks: A review, Nanotechnology. 24 (2013). https://doi.org/10.1088/0957-4484/24/45/452001.

[53] Y. Wu, T. Livneh, Y.X. Zhang, G. Cheng, J. Wang, J. Tang, M. Moskovits, G.D. Stucky, Templated synthesis of highly ordered mesostructured nanowires and nanowire arrays, Nano Lett. 4 (2004) 2337–2342. https://doi.org/10.1021/nl048653r.

[54] C.R. Martin, Nanomaterials : A Membrane-Based Synthetic Approach, 266 (1994).

[55] P.M. Ajayan, S. Lijima, Capillarity-induced filling of carbon nanotubes, Nature. 361 (1993) 333–334. https://doi.org/10.1038/361333a0.

[56] B. Muhsin, R. Roesch, G. Gobsch, H. Hoppe, Solar Energy Materials & Solar Cells Flexible ITO-free polymer solar cells based on highly conductive PEDOT : PSS and a printed silver grid, Sol. Energy Mater. Sol. Cells. 130 (2014) 551–554. https://doi.org/10.1016/j.solmat.2014.08.009.

[57] F. Xie, W.C.H. Choy, C.C.D. Wang, W.E.I. Sha, D.D.S. Fung, Improving the efficiency of polymer solar cells by incorporating gold nanoparticles into all polymer layers, 153304 (2011) 217–219. https://doi.org/10.1063/1.3650707.

[58] Y. Galagan, B. Zimmermann, E.W.C. Coenen, M. Jørgensen, D.M. Tanenbaum, F.C. Krebs, H. Gorter, S. Sabik, L.H. Slooff, S.C. Veenstra, J.M. Kroon, R. Andriessen, Current Collecting Grids for ITO-Free Solar Cells, (2012) 103–110. https://doi.org/10.1002/aenm.201100552.

[59] W. Bao, J. Wan, X. Han, X. Cai, H. Zhu, D. Kim, D. Ma, Y. Xu, J.N. Munday, H.D. Drew, M.S. Fuhrer, L. Hu, Approaching the limits of transparency and conductivity in graphitic materials through lithium intercalation, Nat. Commun. 5 (2014). https://doi.org/10.1038/ncomms5224.

[60] Y. Zhang, S.W. Ng, X. Lu, Z. Zheng, Solution-Processed Transparent Electrodes for Emerging Thin-Film Solar Cells, Chem. Rev. 120 (2020) 2049–2122. https://doi.org/10.1021/acs.chemrev.9b00483.

[61] D.B. Fraser, H.D. Cook, Highly Conductive, Transparent Films of Sputtered In2 − xSnx O 3 − y, J. Electrochem. Soc. 119 (1972) 1368. https://doi.org/10.1149/1.2403999.

[62] L. José Andrés, M. Fe Menéndez, D. Gómez, A. Luisa Martínez, N. Bristow, J. Paul Kettle, A. Menéndez, B. Ruiz, Rapid synthesis of ultra-long silver nanowires for tailor-made transparent conductive electrodes: proof of concept in organic solar cells, Nanotechnology. 26 (2015) 265201. https://doi.org/10.1088/0957-4484/26/26/265201.

[63] A. Kim, Y. Won, K. Woo, S. Jeong, J. Moon, All-Solution-Processed Indium-Free Transparent Composite Electrodes based on Ag Nanowire and Metal Oxide for Thin-Film Solar Cells, Adv. Funct. Mater. 24 (2014) 2462–2471. https://doi.org/10.1002/ADFM.201303518.

[64] M. Vosgueritchian, D.J. Lipomi, Z. Bao, Highly Conductive and Transparent PEDOT:PSS Films with a Fluorosurfactant for Stretchable and Flexible Transparent Electrodes, Adv. Funct. Mater. 22 (2012) 421–428. https://doi.org/10.1002/ADFM.201101775.

[65] X. Hu, X. Meng, L. Zhang, Y. Zhang, Z. Cai, Z. Huang, M. Su, Y. Wang, M. Li, F. Li, X. Yao, F. Wang, W. Ma, Y. Chen, Y. Song, A Mechanically Robust Conducting Polymer Network Electrode for Efficient Flexible Perovskite Solar Cells, Joule. 3 (2019) 2205–2218. https://doi.org/10.1016/J.JOULE.2019.06.011/ATTACHMENT/65D58ED8-23C2-44AF-AE76-B0F68C21C9ED/MMC1.PDF.

[66] G. Cai, P. Darmawan, M. Cui, J. Wang, J. Chen, S. Magdassi, P. See Lee, G.F. Cai, P. Darmawan, M.Q. Cui, J.X. Wang, J.W. Chen, P.S. Lee, S. Magdassi, Highly Stable Transparent Conductive Silver Grid/PEDOT:PSS Electrodes for Integrated Bifunctional Flexible Electrochromic Supercapacitors, Adv. Energy Mater. 6 (2016) 1501882. https://doi.org/10.1002/AENM.201501882.

[67] S. Jiang, P.X. Hou, M.L. Chen, B.W. Wang, D.M. Sun, D.M. Tang, Q. Jin, Q.X. Guo, D.D. Zhang, J.H. Du, K.P. Tai, J. Tan, E.I. Kauppinen, C. Liu, H.M. Cheng, Ultrahigh-performance transparent conductive films of carbon-welded isolated single-wall carbon nanotubes, Sci. Adv. 4 (2018). https://doi.org/10.1126/SCIADV.AAP9264/SUPPL_FILE/AAP9264_SM.PDF.

[68] F. Mirri, A.W.K. Ma, T.T. Hsu, N. Behabtu, S.L. Eichmann, C.C. Young, D.E. Tsentalovich, M. Pasquali, High-performance carbon nanotube transparent conductive films by scalable dip coating, ACS Nano. 6 (2012) 9737–9744. https://doi.org/10.1021/NN303201G/SUPPL_FILE/NN303201G_SI_001.PDF.

[69] L. He, S.C. Tjong, Nanostructured transparent conductive films: Fabrication, characterization and applications, Mater. Sci. Eng. R Rep. 109 (2016) 1–101. https://doi.org/10.1016/j.mser.2016.08.002.

[70] G. Haacke, New figure of merit for transparent conductors, J. Appl. Phys. 47 (1976) 4086–4089. https://doi.org/10.1063/1.323240.

[71] G. Viau, F. Fiévet-Vincent, and F. Fiévet, “Nucleation and growth of bimetallic CoNi and FeNi monodisperse particles prepared in polyols,” *Solid State Ionics*, vol. 84, no. 3–4, pp. 259–270, 1996, doi: 10.1016/0167-2738(96)00005-7.

[72] L.D. Marks, P.M. Ajayan, Quasimelting and phases of small particles, Phys. Rev. Lett. 60 (1988) 585–587.

[73] L.F. Gou, M. Chipara, J.M. Zaleski, Convenient, rapid synthesis of Ag nanowires (vol 19, pg 1755, 2007), Chem. Mater. 19 (2007) 4378.

[74] A.R. Roosen, W.C. Carter, Simulations of microstructural evolution: Anisotropic growth and coarsening, Phys. A Stat. Mech. Its Appl. 261 (1998) 232–247. https://doi.org/10.1016/S0378-4371(98)00377-X.

[75] C.J. Johnson, E. Dujardin, S.A. Davis, J. Murphy, S. Mann, Growth and form of gold nanorods prepared by seed-mediated , surfactant-directed synthesis, J. Mater. Chem. , 12(2002) 17–21. https://doi.org/10.1039/b200953f.

[76] P.L. Gai, M.A. Harmer, Surface Atomic Defect Structures and Growth of Gold Nanorods, Nano Letters 7 (2002) 2–5, https://doi.org/10.1021/nl0202556.

[77] Y. Sun, B. Mayers, T. Herricks, Y. Xia, Polyol synthesis of uniform silver nanowires: A plausible growth mechanism and the supporting evidence, Nano Lett. 3 (2003) 955–960. https://doi.org/10.1021/nl034312m.

[78] P.S. Mdluli, N.M. Sosibo, P.N. Mashazi, T. Nyokong, R.T. Tshikhudo, A. Skepu, E. Van Der Lingen, Selective adsorption of PVP on the surface of silver nanoparticles: A molecular dynamics study, J. Mol. Struct. 1004 (2011) 131–137. https://doi.org/10.1016/j.molstruc.2011.07.049.

[79] N.R. Jana, L. Gearheart, C.J. Murphy, Wet chemical synthesis of silver nanorods and nanowires of controllable aspect ratio, chemical communications 7(2001) 617–618. https://doi.org/10.1039/b100521i.

[80] C.J. Murphy, N.R. Jana, Controlling the aspect ratio of inorganic nanorods and nanowires, Adv. Mater. 14 (2002) 80–82. https://doi.org/10.1002/1521-4095(20020104)14.

[81] J.J. Zhu, X.H. Liao, X.N. Zhao, H.Y. Chen, Preparation of silver nanorods by electrochemical methods, Mater. Lett. 49 (2001) 91–95. https://doi.org/10.1016/S0167-577X(00)00349-9.

[82] S. Bhattacharrya, S.K. Saha, D. Chakravorty, Nanowire formation in a polymeric film, Appl. Phys. Lett. 76 (2000) 3896–3898. https://doi.org/10.1063/1.126813.

[83] K. Korte, Rapid Synthesis of Silver Nanowires, Science (80-.). (n.d.) 28–29.

[84] L. Yang, T. Zhang, H. Zhou, S.C. Price, B.J. Wiley, W. You, Solution-Processed Flexible Polymer Solar Cells with Silver Nanowire Electrodes, *CS Appl. Mater. Interfaces* 2011, 3, 10, 4075–4084, https://doi.org/10.1021/am2009585.

[85] S. Coskun, B. Aksoy, H.E. Unalan, Polyol Synthesis of Silver Nanowires : An Extensive Parametric Study, Cryst. Growth Des. 2011, 11, 11, 4963–4969, https://doi.org/10.1021/cg200874g.

[86] M.R. Azani, A. Hassanpour, T. Torres, Benefits, Problems, and Solutions of Silver Nanowire Transparent Conductive Electrodes in Indium Tin Oxide (ITO)-Free Flexible Solar Cells, Adv. Energy Mater. 10 (2020). https://doi.org/10.1002/aenm.202002536.

[87] C.E. Petoukhoff, D.M.O. Carroll, Plasmonic electrodes for bulk- heterojunction organic photovoltaics , Journal of Photonics for Energy 5 (2022), https://doi.org/10.1117/1.JPE.5.057002 .

[88] J.H. Yim, S. Joe, C. Pang, K.M. Lee, H. Jeong, J. Park, Y.H. Ahn, J.C. De Mello, S. Lee, Fully Solution-Processed Semitransparent Organic Solar Cells with a Silver Nanowire Cathode and a Conducting Polymer Anode, (2014) 2857–2863.

[89] W. Xiong, H. Liu, Y. Chen, M. Zheng, Y. Zhao, Highly Conductive , Air-Stable Silver Nanowire @ Iongel Composite Films toward Flexible Transparent Electrodes, advanced materials 28(2016) 7167-7172. https://doi.org/10.1002/adma.201600358.

[90] T. Sannicolo, M. Lagrange, A. Cabos, C. Celle, J. Simonato, D. Bellet, Metallic Nanowire-Based Transparent Electrodes for Next Generation Flexible Devices : a Review, (2016) 6052–6075. https://doi.org/10.1002/smll.201602581.

[91] W. Li, H. Zhang, S. Shi, J. Xu, X. Qin, Q. He, K. Yang, W. Dai, G. Liu, Q. Zhou, H. Yu, S.R.P. Silva, M. Fahlman, Recent progress in silver nanowire networks for flexible organic electronics, J. Mater. Chem. C. 8 (2020) 4636–4674. https://doi.org/10.1039/C9TC06865A.

[92] L. Hu, J. Song, X. Yin, Z. Su, Z. Li, Research Progress on Polymer Solar Cells Based on, polymers,12(2020), https://doi.org/10.3390/polym12010145.

[93] F.C. Krebs, T. Tromholt, M. Jørgensen, Upscaling of polymer solar cell fabrication using full roll-to-roll processing, Nanoscale. 2 (2010) 873–886. https://doi.org/10.1039/b9nr00430k.

[94] F.C. Krebs, S.A. Gevorgyan, J. Alstrup, A roll-to-roll process to flexible polymer solar cells: model studies, manufacture and operational stability studies, J. Mater. Chem. 19 (2009) 5442–5451. https://doi.org/10.1039/B823001C.

[95] B. Zimmermann, H.F. Schleiermacher, M. Niggemann, U. Würfel, ITO-free flexible inverted organic solar cell modules with high fill factor prepared by slot die coating, Sol. Energy Mater. Sol. Cells. 95 (2011) 1587–1589. https://doi.org/10.1016/J.SOLMAT.2010.11.025.

[96] I. Burgués-Ceballos, M. Stella, P. Lacharmoise, E. Martínez-Ferrero, Towards industrialization of polymer solar cells: material processing for upscaling, J. Mater. Chem. A. 2 (2014) 17711–17722. https://doi.org/10.1039/C4TA03780D.

[97] I. Burgués-Ceballos, N. Kehagias, C.M. Sotomayor-Torres, M. Campoy-Quiles, P.D. Lacharmoise, Embedded inkjet printed silver grids for ITO-free organic solar cells with high fill factor, Sol. Energy Mater. Sol. Cells. 127 (2014) 50–57. https://doi.org/10.1016/J.SOLMAT.2014.03.024.

Chapter 4 Photovoltaic performance of solar cells based on 3-perylene imide acceptors

Abstract

The microstructure of the photoactive layer components is quite challenging since it affects the performance of the OSC. Side chains of the molecules affect their molecular packing and hence their molecular energy levels. In this work we present three synthesized electron acceptors based on perylene imide (PI) of similar energy levels, despite their packing properties. We measure the absorption in both solution and solid-state, cyclic voltammetry and films are characterized by grazing incident wide angle X-ray scattering (GIWAXS). Then, as a following step, we compare the same characterizations of the three molecules in blends with two different donor polymers, namely PCDTBT and PBDBT, since their energy levels have a well aligning with the energy levels of PI acceptors. We show how critical is the difference between the three acceptors in blends. Finally, correlating the structural evidence to the OSCs performance prepared by the six blends is presented. We reach to the conclusion that a good pairing of donor acceptor should imply energy alignment as well as tendencies of their degree of crystallization. The results of this chapter have been published in the Rana Adel, Elena Gala, Matías J. Alonso-Navarro, Edgar Gutierrez, Jaime Martin, Marco Stella, Eugenia Martinez-Ferrero, Alejandro de la Peña, Alexandra Harbuzaru, María del Mar Ramos, Rocio Ponce Ortiz, Jose Luis Segura and Mariano Campoy-Quiles, Comparing the microstructure and photovoltaic performance of 3 perylene imide acceptors with similar energy levels but different packing tendencies, J. Mater. Chem. C, 10, 1698-1710, 2022, doi: 10.1039/D1TC05037K.''.

4.1 PDI molecules in OPV devices

OPV technology has a high potential for large-scale production by solution processing methods leading to light-weight and flexible systems.[1] The synthesis of new materials of improved properties are quite progressed.[2] Fullerene acceptors have many advantages that allow their application in the OPV devices such as being good electron conductors, high charge mobilities, efficient exciton separation and deep LUMO level.[1] Despite their poor absorption that limits light harvesting. The efficiency of OPV devices are exceeding 18%[3] due to the implementation of non-fullerene acceptors (NFAs). NFA is developing the efficiency of large-area OPV devices.[4], [5]

Yet, Rylene imides are applied in optoelectronics such as perylene imides (PI)[6] and naphthalene imide[5]–[9] that has electron withdrawing moieties of arylene imides. Indeed, the efficiencies of devices based on PI acceptors reported values of 9–10%.[2], [10]–[18] PIs are gaining the interest because of their optical absorption enhancing the light harvesting,[19] in addition to their high photostability, low cost synthesis[20] and solution-processing adaptability. In PI molecules, π−π interactions between the perylene cores leads to high aggregation tendency and resulting in a high order of column-shape structures. These aggregation has an impact on the of the optoelectronic properties[21] and considered as a charge carrier trapping source,[22] meanwhile the electrical conductivity was affected by the morphological change in solid state films.[23]

For investigating the performance of OPV devices based on PI molecules, there are three ways to control their morphology:[22] First, inheriting the phase separation by controlling the length of the nanophases in the copolymers. L.Bu reported devices of efficiency of 1.5% based on PIs with electron donors;[24] Second, tuning the molecular geometry of perylene diimides (PDIs). Rajaram and co-workers obtained PCE values of 2.77 % by combination of a nonplanar PI derivative and a hole-transporting polymer;[25] Third, by controlling the crystallization in PI-based thin films by varying donor polymers and the processing conditions willing well compatibility.

In this chapter, we synthesized three electron acceptors based on perylene imide-based of different tendencies to their molecular packing. Their molecular structure is tuned to produce PIPB, 3PIPT, and 4PIPM as shown in Figure 4.1. The solid-state optical absorption, emission, and electrochemical properties in addition to their films characterization by grazing incident wide angle X-rays (GIWAXs) is presented. Furthermore, the same characterizations are performed on the blends of the new acceptors along with the two polymer donors. The donor polymers, are poly[N-9′-heptadecanyl-2,7-carbazole-alt-5,5-(4′,7′-di-2-thienyl2′,1′,3′-benzothiadiazole) (PCDTBT) and poly[(2,6-(4,8-bis(5-(2-ethylhexyl)thiophen-2-yl)-benzo[1,2-b:4,5-b']dithiophene))-alt-(5,5-(1',3'-di-2-thienyl-5',7'-bis(2-ethylhexyl)benzo[1',2'-c:4',5'-c']dithiophene-4,8-dione)] (PBDBT) (Figure 4.1), with a well aligned energy levels to the PI acceptors unlike their structural order.[26] Characterizing the PI acceptors in blends reveals their molecular packing tendency and their effect on the performance of their photovoltaic devices. While the devices performance was not highly efficient, we revealed insights about the microstructure compatibility of the blend components.

4.2 Synthesis of new PI molecules

Novel PI molecules, PIPB, 3PIPT and 4PIPM are shown in Figure 4.1. They were synthetized by the group of Prof. Jose Luis Segura (Universidad Complutense de Madrid) by condensation of perylenimide diketone (PID) with the corresponding o-phenylenediamine to have different geometrical structure planar and 3-D structural(chapter two small molecules synthesis section).[27] The three novel molecules were purified by chromatography and presented a good solubility in chlorinated solvents such as chloroform, dichloromethane and chlorobenzene.

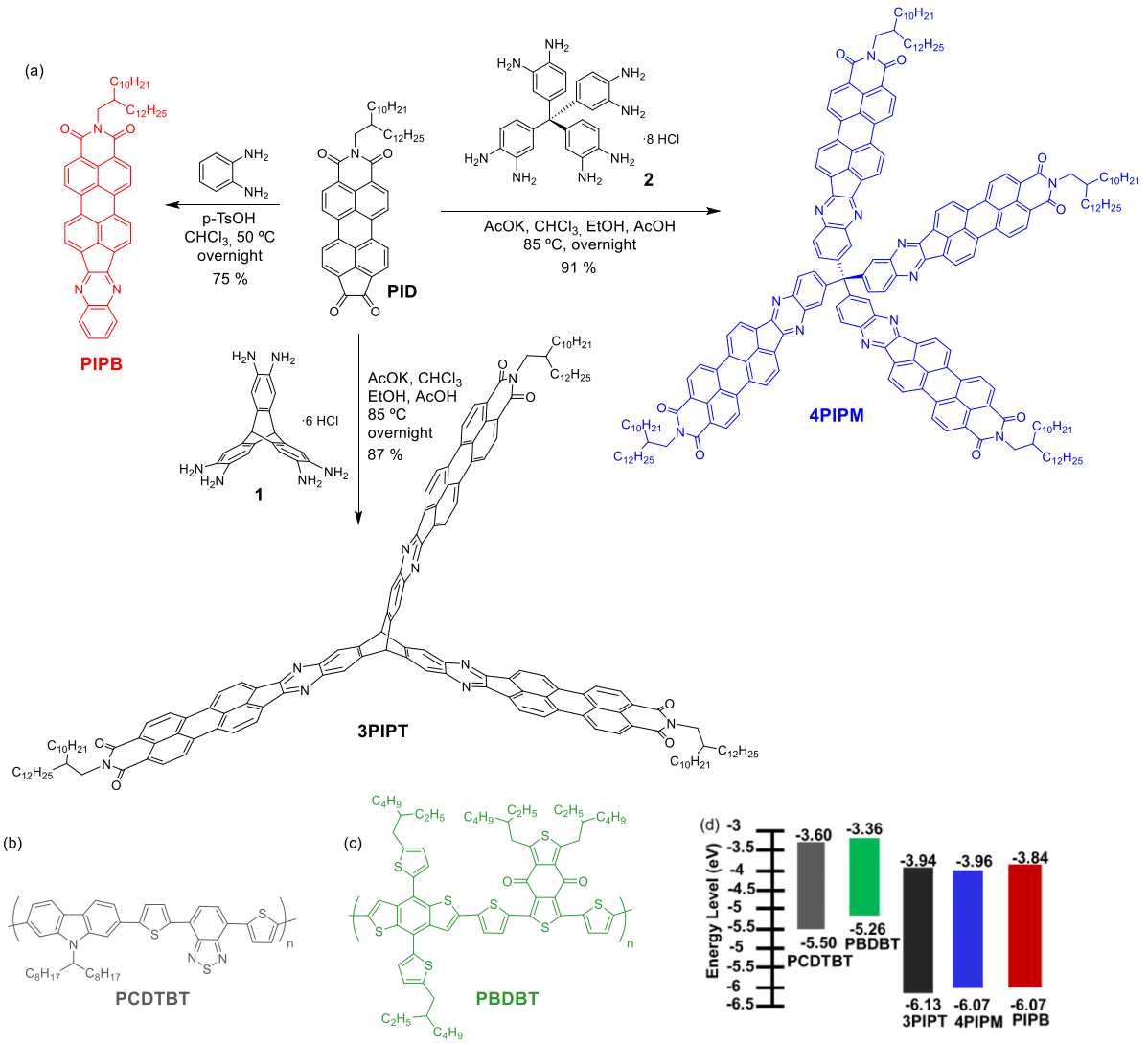

Figure 4.1. (a) The molecular structure of three PI molecules PIPB, 3PIPTand 4PIPM, (b) PCDTBT, (c) PBDBT and (d) the energetic levels of these molecules.

The molecules were theoretically investigated by the groups of María del Mar Ramos, Rocio Ponce Ortiz at the University of Malaga. Geometrical optimization was accomplished employing the DFT exchange correlation functional B3LYP/6-31(d,p) level, assuming the molecules in gas phase, and alkyl chains of imide groups were changed by methyl groups in order to simplify the calculations. For the linear PIPB, the HOMO and LUMO orbitals are all over the molecule.[28] In the case of 3PIPT, the HOMO is over the three cores of perylene resulting in combining the degenerated orbitals and shows delocalization over the three branches.[29], [30] The triptycene unit contribution is observed (Figure 4.2). For 4PIPM, it was found that the HOMO is located in two perylenimide cores whereas LUMO is situated in only one perylenimide unit.

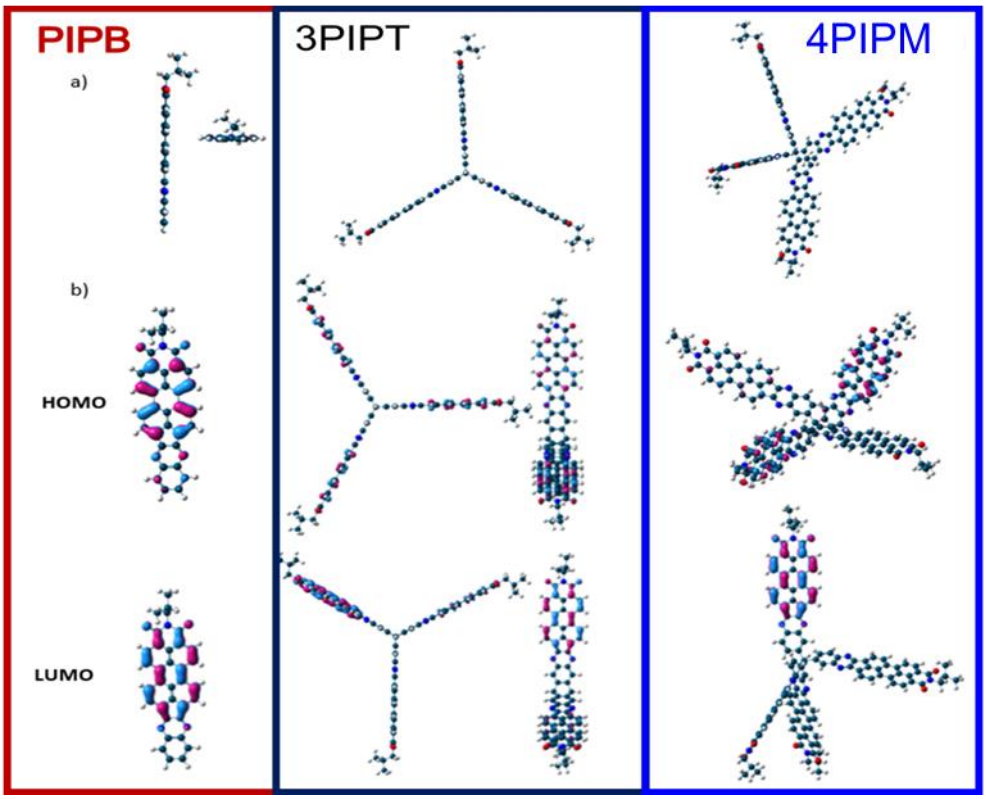

Figure 4.2. (a) Optimization of the PI molecules molecular and (b) their topologies, this Figure adopted from refrence[47].

Table 4.1. Properties of the three PI molecules in solution.

Acceptor	λ_{abs} (nm)	Molar extinction coefficient ($M^{-1}cm^{-1}$)	λ_{onset} (nm)	E_g (eV)	λ_{em} (nm)	$E^{1/2}_{redI}$ (V)	$E^{1/2}_{redII}$ (V)	E_{LUMO} (eV)	E_{HOMO} (eV)
PIPB	323, 364, 379, 463, 496, 534	1.67×10^5	555	2.23	545, 588, 637	-1.26	-1.44	-3.84	-6.07
3PIPT	337, 395, 470, 501, 540	3.26×10^5	566	2.19	548, 592, 640	-1.16	-1.38	-3.94	-6.13
4PIPM	331, 368, 388, 471, 503, 541	3.14×10^5	587	2.11	546, 590, 638	-1.14	-1.39	-3.96	-6.07

For more insights, the electrochemical and the optical properties of the PI molecules measured by UV-Visible and cyclic voltammetry and fluorescence spectroscopies was measured. The obtained data are summarized in Table 4.1. These experiments was measured by Elena Gala in the Universidad Complutense de Madrid

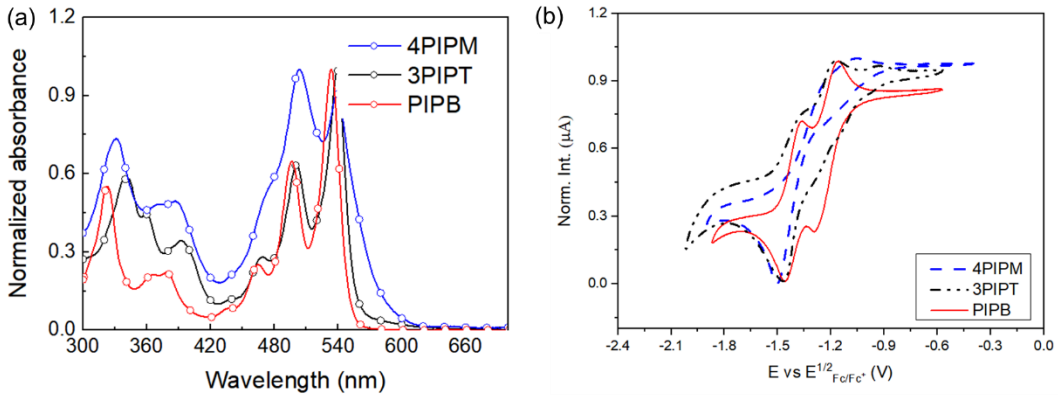

Figure 4.3. (a) The absorption spectra of the three PI molecules in solution, (b) measured cyclic voltammograms, this Figure adopted from refrence[47].

The obtained redox potentials in the middle between the forward and the reverse scans is shown in Figure 4.3b, the measurement was performed in dichloromethane solutions with platinum electrode was the working electrode, while the Ag/Ag^{+} was the reference electrode. All the three molecules PIPB, 3PIPT and 4PIPM, exhibit two successive reversible reduction processes Fig. 4.3(b) that are classically found for perylenimide derivatives. These two reduction processes are monoelectronic for PIPB. Concerning with the derivatives with higher dimensionality, 3PIPT and 4PIPM, it is worth mentioning that no splitting is observed in the two reduction processes which suggests that the coulombic interactions from the electrons in different perylenimide subunits is negligible. Thus, the two successive reversible reduction processes observed for the triptycene and tetraphenylmethane derivatives involve simultaneous reduction of all perylenimide moieties. This means that the novel non-planar derivatives accept up to six and eight electrons upon reduction for 3PIPT and 4PIPM respectively. The estimated values, by using standard approximations $E_{HOMO} = E_{gopt} + E_{LUMO}$[35],[33], and [34], of HOMO and LUMO energies for the PI molecules are listed in Table 4.1[36].

Table 4.1 shows the UV-Vis and fluorescence spectra were measured in chloroform solutions. perylenimide derivatives Characteristic were recorded for the three PI molecules. For the planar molecule, PIPB, the main peaks were observed at 497 nm and 535 nm of the S0–S1correlated to the 0–0 and 0–1 band. While the peak at 465 nm correlated to the S0–S2 transition as seen in Figure 4.3a. Similarly with a red shift trend was obtained in the UV-vis spectra with the higher dimension molecule, 3PIPT and 4PIPM.

Aggregation in three molecules were tested by measuring the absorption at different concentrations. Figures 4.4 shows a red shift as well as the (0,1) vibronic band has a relative enhance to the (0,0) transition. This behaviour is correlated to the aggregation of perylenimide unit. Aggregates lead to enhance (0,1) vibronic band in comparison to non-aggregated PI molecules. Therefore, the ratio of the (0,0) and the (0,1) transition intensities decreases, which confirms the aggregation[37]–[41] by the molecular exciton.[42]–[44] For 4PIPM **,** this behaviour is clearly observed because of the self-aggregation obtained at 10^{-7} M concentration. Table 4.1shows that PIPB has molar extinction coefficient (ε) of value

167197 $M^{-1}cm^{-1}$, which is half the value for 3PIPT and 4PIPM at 326029 $M^{-1}cm^{-1}$ and 313757 $M^{-1}cm^{-1}$, respectively.

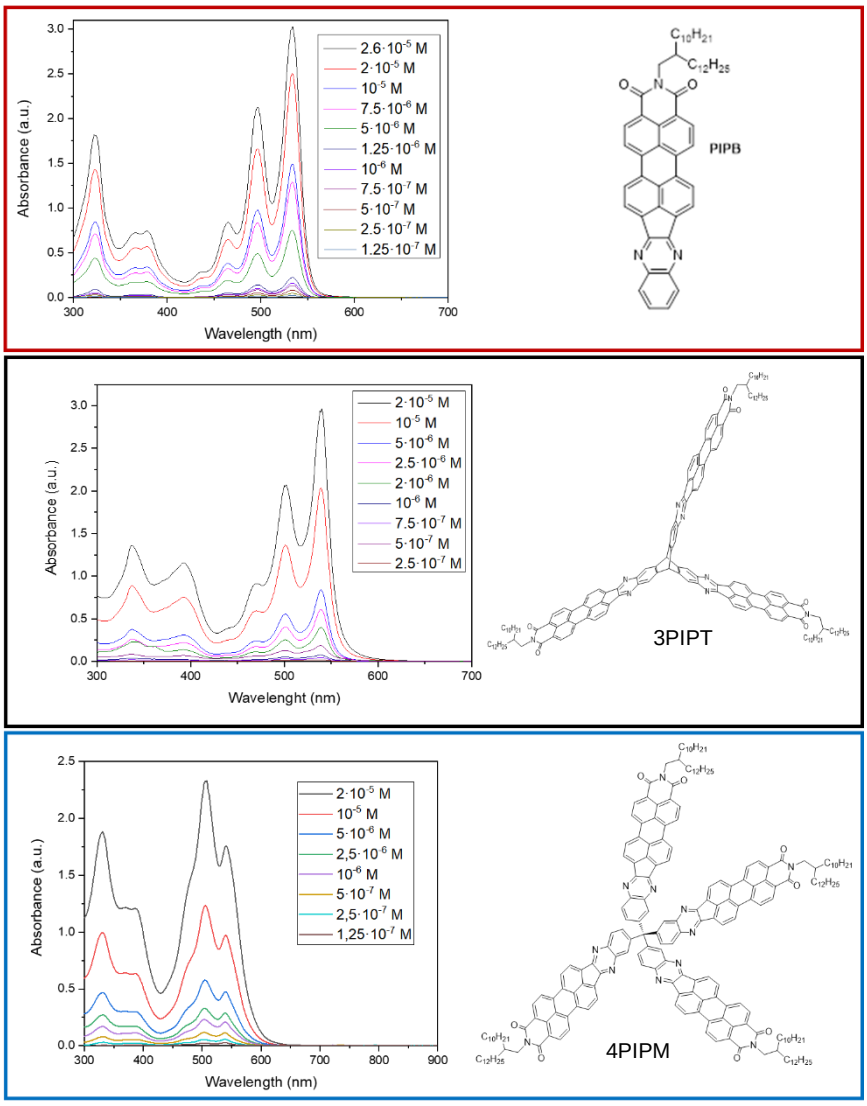

Figure 4.4 Optical absorption spectra at different concentrations of (a) PIPB, (b) 3PIPT and (c) 4PIPM in solution, this Figure adopted from refrence[47].

In solid state, the optical properties of the thin films of PIPB, 3PIPT and 4PIPM**,** obtained by UV-vis spectroscopy. The spectra obtained from the solid-state UV-Vis spectra shown in Figure 4.4 agreed the high aggregation tendency in the PI molecules´ films. As it can be seen, PIPB absorption peaks have a relative change in the intensity and a red shift of 55 nm at 590 nm in case of the solid state than in the case of solution. This shift is correlated to the strong aggregation tendency of this molecule in the solid-state forming crystals. Planar π-conjugated electron acceptors are common to their tendency to cofacial π−π stacking, favoring columnar and lamellar assemblies[9], [17], [45] which are beneficial in order to achieve good electron mobilities[46]. On the contrary, this tendency toward aggregation is responsible for severe phase separation when they are combined with donor polymers in

bulk heterojunction thin films thus producing only modest efficiencies in organic photovoltaic devices[17], [47]. For the higher dimensional molecules 3PIPT and 4PIPM the relative intensity of its absorption peaks at 497 and 535 nm changes in solid state due to its tendency to aggregation (Figure4.4). For non-aggregated solutions we should observe that the absorption at 535 nm is significantly more intense than the absorption at 497 nm, but we observe the opposite in solid state films.

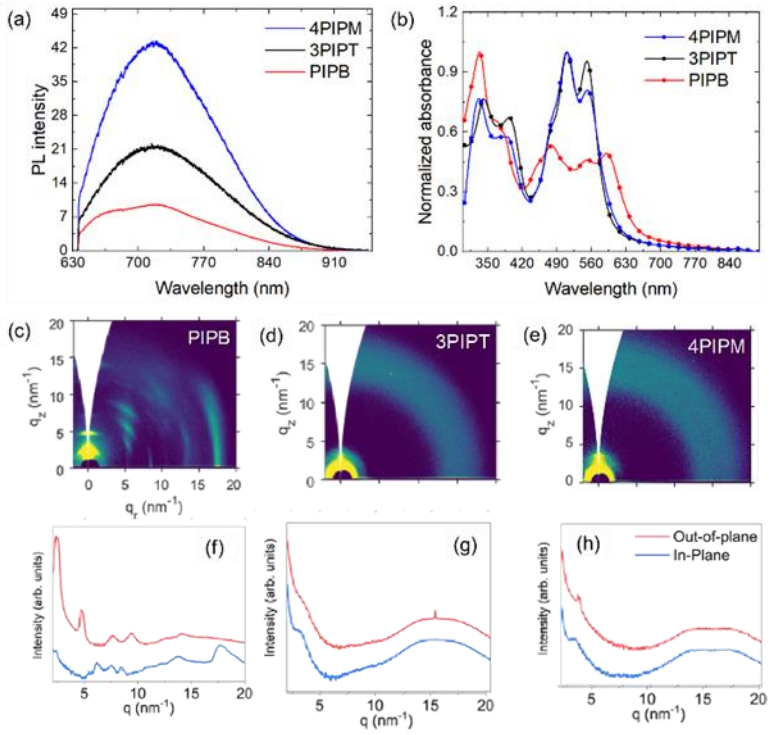

Figure 4.5. (a) The photoluminescence spectra of the three PI molecules, (b) the absorption spectra of the three PI molecules in solid state , (c-e) the two-dimensions GIWAXS and (f-h) corresponding OOP and IP profiles, this Figure adopted from refrence[47].

For further information about the molecular packing of the small molecules, films of 4PIPM, 3PIPT and PIPB are prepared by blade coating and studied by GIWAX. These measurements were carried out by Edgar and Jaime at ALBA synchrotron. The two-dimensional (2D) GIWAXS patterns of the three molecules are presented in Figure 4.4 and the corresponding out-of-plane (OOP) and in plane (IP) line cut profiles for the three molecules are showed in Figure 4.4(f-h). Interestingly, the measurements showed varying packing order of the PIPB than 3PIPT and 4PIPM. π-π intermolecular stacking appear in peaks at q_r= 2, 5, 8 and 18 nm^{-1} in PIPB revealed the highest degree of crystallinity among the three molecules in the OOP direction while in the IP direction where the intramolecular stacking showed less degree of crystallinity since the peak intensity at 2 nm^{-1} has reduces and the peak at 5 nm^{-1} disappeared. That is ascribed to the edge-on orientation to the substrate. For 4PIPM and 3PIPT both OOP and IP showed lower order packing. Peaks at q_z= 3.5 nm^{-1} and at q_z= q_r = 17.5 nm^{-1} in 4PIPM showed higher degree of crystallinity than

disordering shown from the isotropic reflections in the 3PIPT. Therefore, strong differences in the packing behaviour confirmed by GIWAXS on thin films of each NFA. While PIPB film exhibits a larger number of better resolved peaks, 3PIPT has isotropic structure. We can claim that the planar molecule PIPB form a well order film by π-π stacking while 4PIPM of four branches that form lamellar packing hindering the π-π stacking unlike the 3PIPT of three branches that are perpendicularly aligned to the molecule plane resulting in amorphous film.

4.3 Preparing heterojunctions by blending PI molecules with polymer donors

After revealing the packing order of the three PI molecules, it is interesting to further study the molecular packing of the three molecules in blend structure. PBDBT and PCDTBT of molecular structure shown in Figure 4.1 are the electron donor polymers chosen to be blended with the three PI molecules 4PIPM, 3PIPT and PIPB for their preferred energy levels aligning to the small molecules[26] as shown in Figure 4.1(d). In addition to their high molar extinction coefficients obtained from the UV-Vis absorption spectra to be 3.61.593 x 10^6 $cm^{-1}M^{-1}$ for PCDTBT and 1.990 $cm^{-1}M^{-1}$ x 10^6 for PBDBT**.** Furthermore, they have different degree of crystallinity since PCDTBT form amorphous films unlike PBDBT films gain a crystalline order[49].

First, blend films are prepared by combining the three molecules with PCDTBT of weight ration 1:1 in CF: CB (3:1 VR). The optical absorption of the prepared blends and the neat PCDTBT was measured by UV-VIS spectroscopy as shown in Figure 4.7 (a). PCDTBT have two absorption bands: short wavelength band due to the N-(1-octylnonyl)-2,7-di(thien-2-yl) carbazole unit and long wavelength band due to the intramolecular charge transfer. The blends have the optical peaks in the same bands of the small molecule and the spectrum is normalized to the film thickness as shown in Figures 4.7(a). The PCDTBT:3PIPT has stronger absorption than the PCDTBT: PIPB and PCDTBT: 4PIPM. The long wavelength absorption peak present in the polymer spectra corresponds to the internal charge transfer state is red shifted in case of PCDTBT: PIPB and PCDTBT: 3PIPT for more interaction between the polymer donor and the acceptor. Apparently, the PI molecules enhanced the absorption of the blend films in the visible spectrum for more light harvesting purpose.

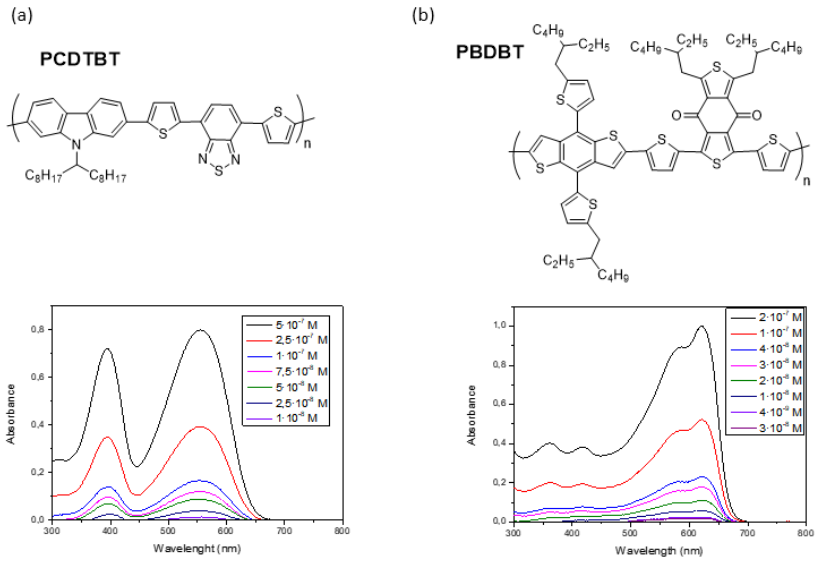

Figure 4.6. (a) Optical absorption spectra obtained in solutions for PCDTBT and for PBDBT(b)

The PL spectra of the PCDTBT and the blends were obtained by illuminating the films with HeNe laser source of power 1mW. The PL peaks shown in Figure 4.7(b) are normalized to their optical absorption at 633nm. The UV–Vis and PL spectra can probe indirectly the quality of the small molecules stacking. The PL is dominated by the emission characteristics of the intermolecular species. PCDTBT has emission peak at 697 nm. The broad shifted PL emission peaks from 715 nm for 4PIPM, 3PIPT and PIPB in the small molecules (see Fig.4.3(d)) to 720, 713, 759 and 697 nm for 4PIPM: PCDTBT, 3PIPT: PCDTBT, PIPB: PCDTBT and PCDTBT (see Fig.4.7(b)), respectively is correlated to the interaction between the PI molecules and the polymer PCDTBT. The broadening in PL spectra of the blend films indicating more intensive emissive characteristics at wavelengths longer than 700 nm. For blends of PIPB and 4PIPM, a red shifted peak is indicating the aggregation arises due to the π-π intermolecular interaction of the high crystalline PDI molecules. The above results of the three blends evidence the PI molecules aggregation and the interaction between the PI molecules and the polymer donor. The low ability of 3PIPT to aggregate helps obtained the hypochromic shift in the blend PCDTBT:3PIPT due to the good interaction between the polymer donor and the PI acceptor. While the bathochromic shift obtained in the blend PCDTBT: PIPB films is due to the PI molecules aggregation that is hindered by the polymer matrix. The red shift obtained in the blend PCDTBT:4PIPM spectrum, addressed by PL shift, is correlated to the less aggregation compared to PIPB.

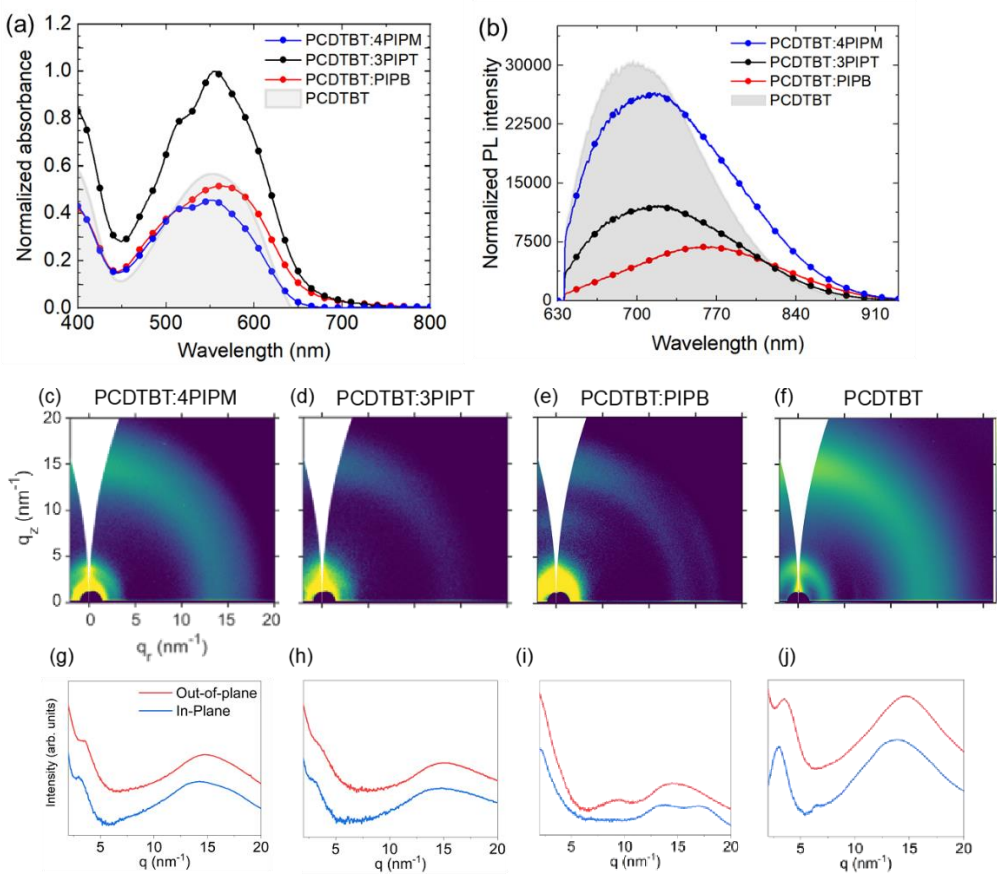

Figure 3.7. (a) optical absorption spectra of PCDTBT and its blends, (b) PI spectra of PCDTBT: PIPB, PCDTBT:3PIPT, PCDTBT:4PIPM and PCDTBT. (c-f) their corresponding GIWAXS patterns and (g-f) their OOP and IP profiles, this Figure adopted from refrence[47].

The GIWAX experiments have been performed by Edgar Gutierrez, and Jaime Martin in POLYMAT, University of the Basque Country. The two-dimensional (2D) GIWAXS patterns of 4PIPM: PCDTBT, 3PIPT: PCDTBT, PIPB: PCDTBT and PCDTBT are obtained and presented in Figure 4.7(c-f) and the corresponding OOP and IP line cut are presented in Figure 4.7(g-j). As it can be seen, for the blends of the 4PIPM: PCDTBT and 3PIPT: PCDTBT the peaks represent the less degree of crystallinity than both the polymer and the acceptor that is due to the presence of amorphous regions in the film. In general, blending the three acceptors with PCDTBT results in broadening and less resolved OOP and IP peaks than in case of the polymer and the small molecule alone, implying more aggregation. This leads to expectation of microstructure recombination if these blends are applied in OPV devices[50].

Second, films are prepared by blending the PI molecules with PBDBT with the same condition followed in the first polymer PCDTBT of weight ratio (1:1) soluble in CF: CB (3:1 VR). The optical properties of the films are shown in Figures 4.8(a-b). Each spectrum is normalized to the film thickness. The absorption spectra of the blend resemble a mixture of the spectra of the corresponding components.

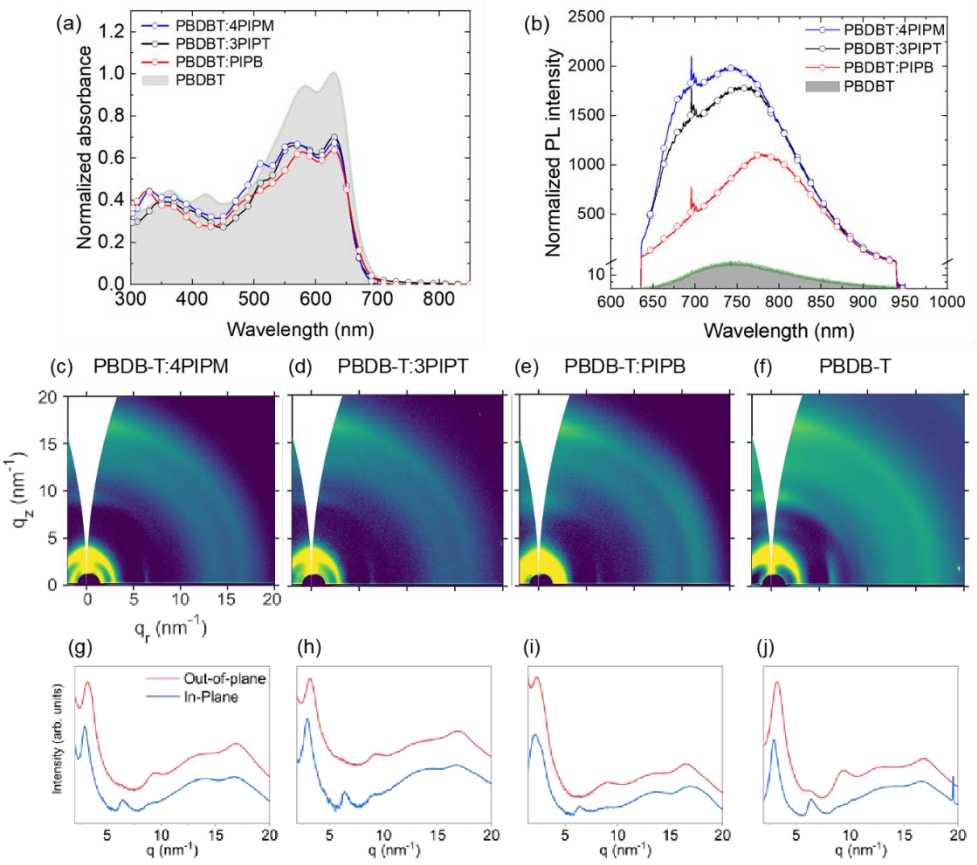

Figure 4.8. (a) The optical absorption spectra of the PBDBT and its blends in solid state, (b) their corresponding photoluminescence spectra, (c-h) GIWAXS of PBDBT and the blends, and(g-j) their corresponding (OOP) and (IP) profiles, this Figure adopted from refrence[47].

The PL spectra of the PBDBT blends are shown in Figure 4.8. The PL peaks shifted from 715 nm for 4PIPM, 3PIPT and PIPB in the small molecules (see Figure 4.5) and at 736 nm for the PBDBT polymer to 767, 772, and 773 nm for 4PIPM: PBDBT, 3PIPT: PBDBT,and PIPB: PBDBT, respectively. The PL peak of the blends are red shifted and get broaden indicated the aggregation in the blend films of PBDBT. In case of the PBDBT:4PIPM and PBDBT: PIPB both the donor polymer and the small molecule have high degree of order that increase the tendency to create microstructure islands. For the blends of PBDBT comparing to the blends of PCDTBT the PL peaks intensity are reduced due to the presence of the phase separation. PBDBT has high ordered structure that is reflected in their low intensity PL spectra due to the short π-π stacking led to non-radiative relations.[51]–[53]. These findings importance of the degree of microstructure order of both pairs in the heterojunction to avoid the phase separation and the short π-π stacking for improving the charge separation efficiency in OPV devices.

The two-dimensional (2D) GIWAXS patterns of 4PIPM: PBDBT, 3PIPT: PBDBT, PIPB: PBDBT and PBDBT with the corresponding OOP and IP line cut profiles are shown in Figure 4.8(c-f). For PBDBT:PIPB, which has peaks at q_r = 3.5 nm^{-1} and q_r = 17.5 nm^{-1}, seems to maintain the degree of crystallinity from the PI molecule. Diffraction pattern obtained is corelated to the phase separation present in the blend in addition to the PL data indicated the existence of both crystalline structures of the polymer and the PI acceptor. That indicates the presence of phase separation between the small molecule and the polymer that agrees

with the presence of the two PL peaks of the donor and the acceptor. For the PBDBT:4PIPM and PBDBT:3PIPT GIWAX results that more isotopic ordering appeared in the PI molecules domains, however the PL data assure the phase separation between the polymer and the acceptor in the blend.

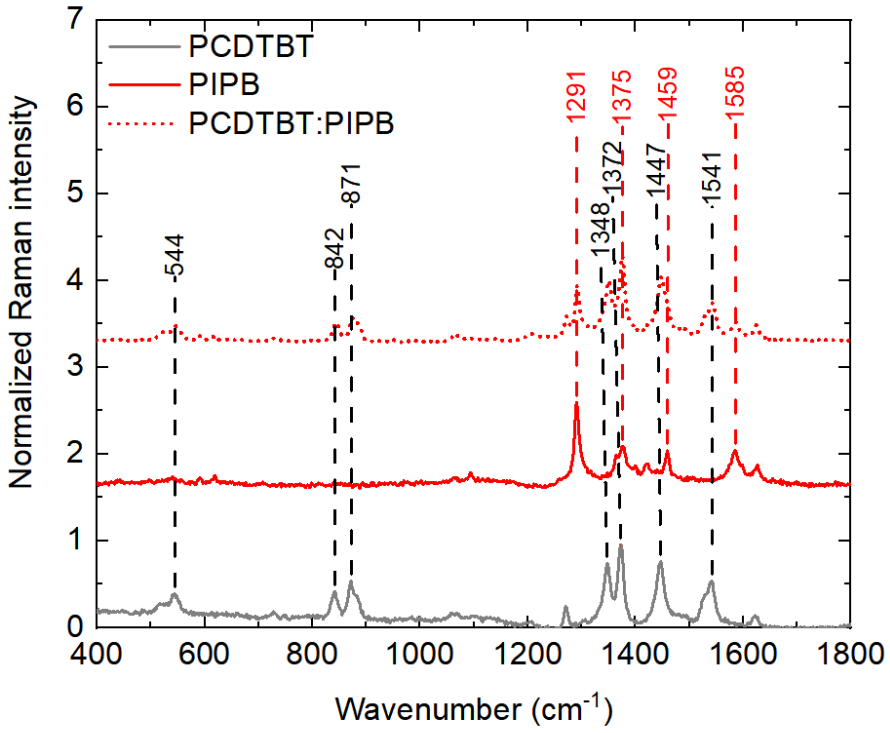

Figure 4.9. Obtained Raman spectra of PCDTBT, PIPB and their blend, this Figure adopted from refrence[47].

.

After revealing the molecular packing information by GIWAX and PL, chemical change needs to be investigated for further insights about the microstructure. Raman spectra of the blends are obtained by shining the blend film prepared by blade coating on glass with 488 nm laser source of power 1mW. Raman Spectra of the electron donor polymer, PIPB and their blend PCDTBT: PIPB are shown in Figure 4.9. For all the blends, the Raman peaks of both the donor and the small molecule are present in the blend spectra. Having the polymer peaks in the blend suggest that there is not a chemical change in the monomer. However, Table 3.2 shows the shifts observed that indicates a interaction between the donor polymer and the PI molecule which in accordance with the PL data.

For PCDTBT blends, the polymer peaks shift to higher wavenumbers when mixed with 3PIPT that is correlating to the polymer reducing its ordering [54], [55] unlike in the case of PBDBT, where the polymer peaks cannot be resolved in blends. Raman peaks of the PI molecules are more affected by blending with PBDBT than with blending with PCDTBT since their peaks are shifted to lowers wavenumbers.

Table 4.2. Raman peaks of the PI molecules and their blends.

PCDTBT (cm^{-1})	4PIPM (cm^{-1})	3PIPT (cm^{-1})	PIPB (cm^{-1})	PCDTBT: PIPB (cm^{-1})	PCDTBT: 3PIPT (cm^{-1})	PCDTBT: 4PIPM (cm^{-1})	PBDBT (cm^{-1})	PBDBT :4PIPM (cm^{-1})	PBDBT :3PIPT (cm^{-1})	PBDBT : PIPB (cm^{-1})
							379			356
544	553	**561**	540	546	547	546	527		**561**	538
							580			591
	618	**625**	591				692	618	**623**	618
	717	**717**	708					717	**713**	711
842				844	844	842				
871				874	875	874	785			
1077	1066	**1065**	1068	1068	**1066**	1063	1073	1065	1075	1065
	1096	**1095**	1093					1091	**1091**	1093
1270				1272		1208	1195			
-----	1291	**1291**	1291	1291	**1291**	1289	1296	1289	**1291**	1289
1348	-----		-----	1350	1352	1350				
1372	1376	**1379**	1375	**1376**	**1377**	**1374**		1374	**1377**	1374
1447	1460	**1460**	1459	1449	1449	1449	1430	1428	1429	1427
								1459	**1459**	1457
1541	------	-----	-----	1543	1543	1541			1489	1488
-----	1588	**1587**	1585	1587	**1587**	1587		1585	1540	
							1645		**1585**	1584
1622	1628	**1628**	1627	1625	**1627**	1625	1789	1627	**1628**	1627

4.4 PV performance of devices based on PI molecules

After studying the blends microstructures, investigating the performance of OPV devices of these microstructure and have insights of their correlation is the following step. The three electron acceptors, 4PIPM, 3PIPT and PIPB, were applied in photovoltaic devices incorporated with electron donor polymers: PCDTBT and PBDBT. The devices of glass /ITO/AZO/active layer/MoO_3/Ag were prepared.

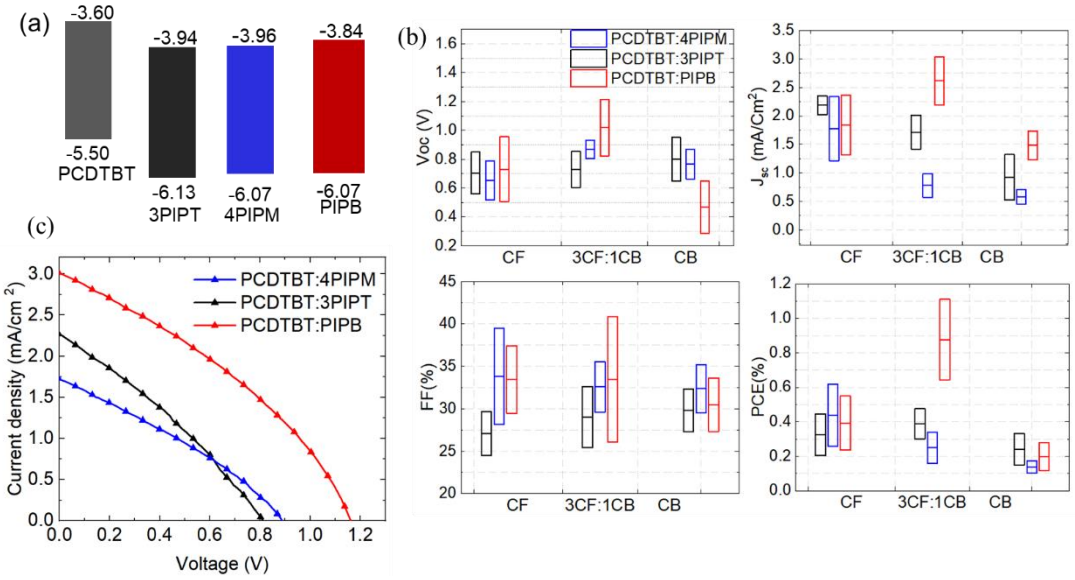

Figure 4.10.(a) the energy diagram of the hetero junction formed by blending the three PI molecules with PCDTBT (b) V_{oc}, J_{sc}, FF, PCE of devices based on PCDTBT: PIPB, PCDTBT:3PIPT and PCDTBT:4PIPM and (c) the J- V curves of the champion cells of the corresponding blends, this Figure adopted from refrence[47].

Table 4.3. Average ± standard deviation (best cell) values of PV parameters for 288 OPV devices

Heterojunctions	V_{oc} (V)	J_{sc}(mA/cm^2)	FF (%)	PCE (%)
PCDTBT:4PIPM	0.88±0.06 (0.92)	1.46±0.03 (1.44)	32±2 (33)	0.41±0.04 (0.44)
PCDTBT:3PIPT	0.7±0.2 (0.8)	2.2±0.1 (2.3)	33±3 (30)	0.49±0.11 (0.56)
PCDTBT: PIPB	1.16±0.01 (1.16)	3.02±0.01 (3.02)	32±4 (35)	1.12±0.14 (1.22)
PBDBT:4PIPM	0.75±0.01 (0.75)	2.3±0.1 (2.4)	41±1 (41)	0.73±0.01 (0.74)
PBDBT:3PIPT	0.79±0.04 (0.82)	2.45±0.08 (2.5)	40±4 (42)	0.76±0.13 (0.85)
PBDBT: PIPB	0.88±0.01 (0.87)	2.0±0.2 (2.2)	25±1 (26)	0.43±0.07 (0.48)

Two series of devices are prepared based on the donor polymer. First is applying the blends of the less crystalline donor polymer PCDTBT. Figure 4.10 and Table 4.3 shows the performance of devices based on PCDTBT. The blend of PCDTBT: PIPB showed the highest PCE values of 1.2%. The performance of the devices with 4PIPM and 3PIPT showed less efficiency of the values 0.56% and 0.47%, respectively. Unfortunately, the devices efficiency was low despite the photoactive layer thickness and the processing optimization[56]. In general, FF were low (29-33 %) which is because of the low order of packing, obtained revealed in the GIWAX data, enhancing the charge carrier trapping, microstructure recombination and restraining the charge transport. The values of the V_{oc} (see Figure 4.11) are not the values expected from the energy levels difference between the donor and the acceptor reflecting the microstructure recombination in devices. This is in agreement to the reported conclusion that the high crystalline donor needs to be blended with less crystalline acceptor to improve the charge mobility, which will enhance the FF and PCE in the device[57]. This finding indicates that PI molecules form charge trapping sites that cannot be easily missed, even by using different geometry[21]. However, in case of PCDTBT: PIPB, the ordering of PIPB enhanced the conductivity of the intermolecular π-π stacking.

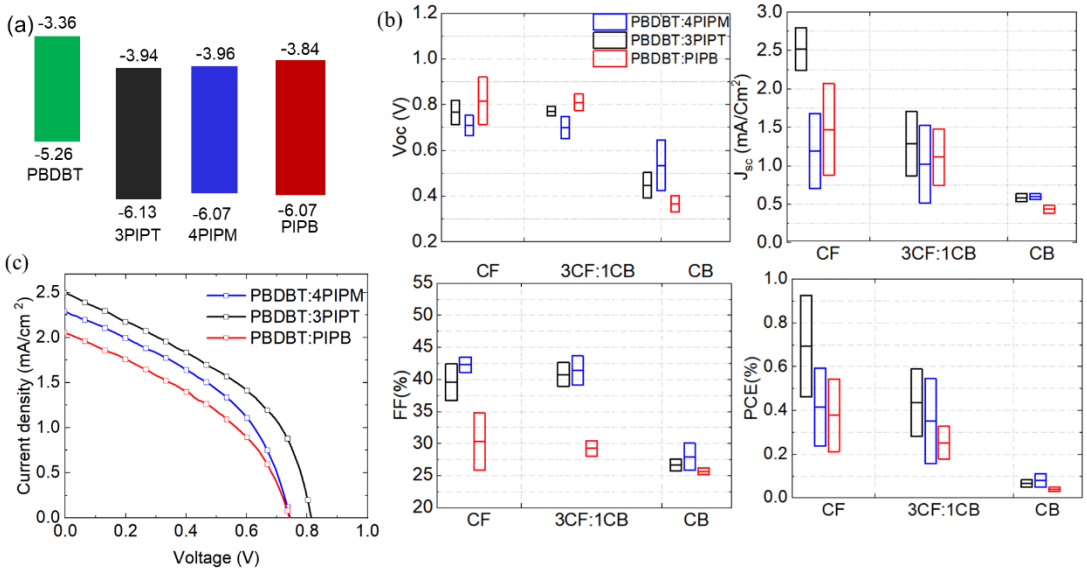

Figure 4.11. (a) the energy diagram of the hetero junction formed by blending the three PI molecules with PBDBT (b) V_{oc}, J_{sc}, FF, PCE of devices based on PBDBT: PIPB, PBDBT:3PIPT and PBDBT:4PIPM and (c) the J- V curves of the champion cells of the corresponding blends, this Figure adopted from refrence[47].

Second polymer to be implied in devices is PBDBT, which is a highly crystalline polymer. As shown in figure 4.11 and table 4.3 the devices performance has declined to lower efficiencies. PBDBT: PIPB devices exhibited the lowest efficiency among the three small molecules of value 0.48 %. While the PBDBT:4PIPM and PBDBT:3PIPT provided higher efficiency of 0.74% and 0.85%, respectively. The fill factor of the devices has been improved to 50% and 44% than in case of the blends with PCDTBT. These results interrelated to the difference in acceptors degree of crystallinity and hence their molecular packing in blends discussed by the GIWAX data. When the planar PIPB molecules blended with the high crystalline PBDBT, micro islands are formed to restrain the formation of an intermolecular

connection, hindering the charge transport and limiting the improvement of PCE[58]. The high crystallinity of PIPB tends form phase separated regions in the blend that reduce the J_{sc}. The 3D form in case of 3PIPT helps the charge transfer between polymer layers in coherence to the J_{sc} results.

4.5 Effect of PI molecule solubility on the performance of the OPV devices

As mentioned above aggregation of PI molecules is a critical issue so that three different solvents have been investigated searching for better solubility: chlorobenzene, chloroform and their combination. Figure 4.10 and Figure 4.11 shows the devices performance based on the solvent used. Despite the low efficiency, the photovoltaic performance was different depending on their degree of solubility. The chloroform: chlorobenzene co-solvent enhances the PCE of the devices than the CB. That is due to the drying time since the CF has lower boiling point temperature than CB which prevents the formation of large phase separation. Both CF and CB showed low solubility of PI molecules and the combination of both solvents works better than each solvent alone.

Even though the enormous optimization of the solvents used there was still hard to complete dissolve these molecules in solvents that drive us to investigate the devices efficiencies depend on Hansen solubility parameters by ANOVA studies which are shown in Table 4.4.[53], [59]–[64] Polarity showed F factor of 71.4 while hydrogen bonds and dispersion have similar values of 114.8. These data have a lot of dispersion that needs further analysis therefore, the surface map shown in Figure 4.12 Provided the relation between the PCE of the devices and the solubility parameters for different solvent used in the BHJ such as TCE: tetrachloroethane, DCM: dichloromethane, CB: Chlorobenzene and CF: chloroform. Chloroform enhanced the solubility of the molecules and thus the photovoltaic performance. CB, DCM and TCE showed less performance than in case of combining CF and CB (3:1) VR.

Table 4.4 ANOVA statistics of different solvents, electron donors, and solubility parameters.

F factor	Parameter
45.1	Different **solvents** for **PCDTBT: PIPB** devices
44.1	Different **solvents** for **PBDBT: PIPB** devices
54.5	Different **solvents** for **PBDBT:3PIPT**
8.2	Different **solvents** for **PCDTBT:3PIPT**
11.9	Different **solvents** for **PBDBT:4PIPM**
24.6	Different **solvents** for **PCDTBT:4PIPM**
0.78	Different **donors** for **3PIPT**
4.2	Different **donors** for **4PIPM**
120.3	Different **donors** for **PIPB**
114.8	Hydrogen bonds
71.4	Polarity
114.8	Dispersion

From the above data more insights are presented about the advantages of the π-π intermolecular stacking for improving the charge transport in heterojunctions and hence the device efficiency. Overcoming this problem can be achieved by increasing the grain boundaries of the small PI molecules can help the charge transport and extraction.[65]

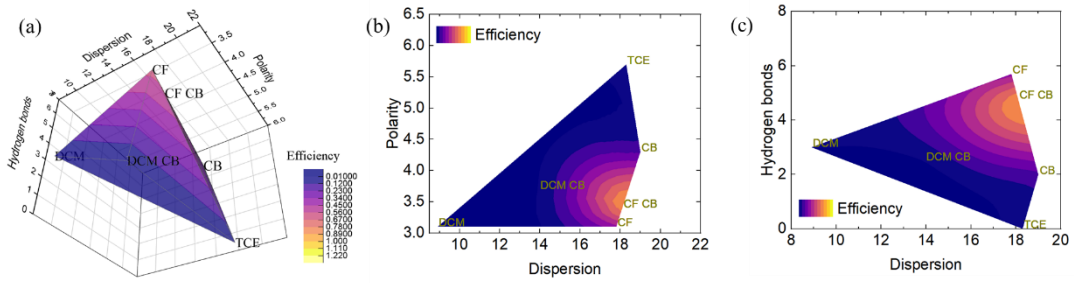

Figure 4.12 (a) Surface map for Hansen parameters and devices efficiency. (b) and (c) Side view of the surface map.

4.5 Conclusion

We conclude this investigation by shining the light on how to choose the heterojunction pair in terms of their molecular structure. Tunning the geometry of the three PI molecules as a NFA affect their molecular packing and the performance of their OPV devices. When the planar PIPB molecule with high ordering degree paired with the PCDTBT, of low order structure, the highest efficiency is recorded art 1.2%. Unlike pairing the same molecule with the PBDBT, polymer that has high ordered structure resulted in low efficient devices because of the high phase separation. The high ordered PI molecules 3PIPT and 4PIPM showed better blending with the PBDBT and hence better efficiency for the OPV devices. That reflects the importance of the ordering structure variance between the donor and the acceptor in the heterojunction of OPV device since disordering in the intermolecular structure hinder the charge trapping and enhance the charge transport.

4.6 References for Chapter 4

[1] B. C. Thompson and J. M. J. Fréchet, “Polymer-fullerene composite solar cells,” *Angew. Chemie - Int. Ed.*, vol. 47, no. 1, pp. 58–77, 2008, doi: 10.1002/anie.200702506.

[2] M. C. Scharber *et al.*, “Design rules for donors in bulk-heterojunction solar cells - Towards 10 % energy-conversion efficiency,” *Adv. Mater.*, vol. 18, no. 6, pp. 789–794, 2006, doi: 10.1002/adma.200501717.

[3] Q. Liu *et al.*, “18% Efficiency organic solar cells,” *Sci. Bull.*, vol. 65, no. 4, pp. 272–275, 2020, doi: 10.1016/j.scib.2020.01.001.

[4] M. Stolar and T. Baumgartner, “Organic n-type materials for charge transport and charge storage applications,” *Phys. Chem. Chem. Phys.*, vol. 15, no. 23, pp. 9007–9024, 2013, doi: 10.1039/c3cp51379c.

[5] Q. Liu, S. E. Bottle, and P. Sonar, “Developments of Diketopyrrolopyrrole-Dye-Based Organic Semiconductors for a Wide Range of Applications in Electronics,” *Adv. Mater.*, vol. 32, no. 4, pp. 1–46, 2020, doi: 10.1002/adma.201903882.

[6] X. Guo, A. Facchetti, and T. J. Marks, “Imide- and Amide-Functionalized Polymer Semiconductors,” *Chem. Rev.*, vol. 114, pp. 8943–9021, 2014.

[7] S. G. Higgins, B. V. O. Muir, G. Dell’Erba, A. Perinot, M. Caironi, and A. J. Campbell, “Self-aligned organic field-effect transistors on plastic with picofarad overlap capacitances and megahertz operating frequencies,” *Appl. Phys. Lett.*, vol. 108, no. 2, pp. 1–6, 2016, doi: 10.1063/1.4939045.

[8] N. L. Vaklev, J. H. G. Steinke, and A. J. Campbell, “Gravure Printed Ultrathin Dielectric for Low Voltage Flexible Organic Field-Effect Transistors,” *Adv. Mater. Interfaces*, vol. 6, no. 11, pp. 1–6, 2019, doi: 10.1002/admi.201900173.

[9] X. Guo, A. Facchetti, and T. J. Marks, Imide- and Amide-Functionalized Polymer Semiconductors, *Chem. Rev.* 2014, 114, 18, 8943−9021, https://doi.org/10.1021/cr500225d.

[10] M. Al Kobaisi, S. V. Bhosale, K. Latham, A. M. Raynor, and S. V. Bhosale, “Functional Naphthalene Diimides: Synthesis, Properties, and Applications,” *Chem. Rev.*, vol. 116, no. 19, pp. 11685–11796, 2016, doi: 10.1021/acs.chemrev.6b00160.

[11] V. Sharma, J. D. B. Koenig, and G. C. Welch, “Perylene diimide based non-fullerene acceptors: top performers and an emerging class featuring N-annulation,” *J. Mater. Chem. A*, vol. 9, no. 11, pp. 6775–6789, 2021, doi: 10.1039/d0ta11197j.

[12] F. Tintori *et al.*, “Side-chain engineering of perylene diimide dimers: Impact on morphology and photovoltaic performance,” *Nano Sel.*, vol. 1, no. 3, pp. 388–394, 2020, doi: 10.1002/nano.202000089.

[13] E. Zhou, J. Cong, Q. Wei, K. Tajima, C. Yang, and K. Hashimoto, “All-polymer solar cells from perylene diimide based copolymers: Material design and phase separation control,” *Angew. Chemie - Int. Ed.*, vol. 50, no. 12, pp. 2799–2803, 2011, doi: 10.1002/anie.201005408.

[14] X. Zhang *et al.*, “A potential perylene diimide dimer-based acceptor material for highly efficient solution-processed non-fullerene organic solar cells with 4.03% efficiency,” *Adv. Mater.*, vol. 25, no. 40, pp. 5791–5797, 2013, doi: 10.1002/adma.201300897.

[15] “cr5b00188 1..91 _ Enhanced Reader.pdf.” .

[16] M. A. Bassi, M. A. Lopez, L. Confalone, R. M. Gaudio, L. Lombardo, and D. Lauritano, “Enhanced Reader.pdf,” *Nature*, vol. 388. pp. 539–547, 2020.

[17] P. J. Brown *et al.*, “Effect of interchain interactions on the absorption and emission of poly(3-hexylthiophene),” *Phys. Rev. B - Condens. Matter Mater. Phys.*, vol. 67, no. 6, pp. 1–16, 2003, doi: 10.1103/PhysRevB.67.064203.

[18] R. K. Gupta and A. A. Sudhakar, “Perylene-Based Liquid Crystals as Materials for Organic Electronics Applications,” *Langmuir*, vol. 35, no. 7, pp. 2455–2479, 2019, doi:

10.1021/acs.langmuir.8b01081.
[19] M. A. Mattson, T. D. Green, P. T. Lake, M. McCullagh, and A. T. Krummel, “Elucidating Structural Evolution of Perylene Diimide Aggregates Using Vibrational Spectroscopy and Molecular Dynamics Simulations,” *J. Phys. Chem. B*, vol. 122, no. 18, pp. 4891–4900, 2018, doi: 10.1021/acs.jpcb.8b02355.
[20] C. B. Nielsen, S. Holliday, H. Y. Chen, S. J. Cryer, and I. McCulloch, “Non-Fullerene Electron Acceptors for Use in Organic Solar Cells,” *Acc. Chem. Res.*, vol. 48, no. 11, pp. 2803–2812, 2015, doi: 10.1021/acs.accounts.5b00199.
[21] R. Singh, E. Aluicio-Sarduy, Z. Kan, T. Ye, R. C. I. Mackenzie, and P. E. Keivanidis, “Fullerene-free organic solar cells with an efficiency of 3.7% based on a low-cost geometrically planar perylene diimide monomer,” *Journal of Materials Chemistry A*, vol. 2, no. 35. pp. 14348–14353, 2014, doi: 10.1039/c4ta02851a.
[22] L. Zang, Y. Che, and J. S. Moore, “One-dimensional self-assembly of planar π-conjugated molecules: Adaptable building blocks for organic nanodevices,” *Acc. Chem. Res.*, vol. 41, no. 12, pp. 1596–1608, 2008, doi: 10.1021/ar800030w.
[23] T. Ye, R. Singh, H. J. Butt, G. Floudas, and P. E. Keivanidis, “Effect of local and global structural order on the performance of perylene diimide excimeric solar cells,” *ACS Appl. Mater. Interfaces*, vol. 5, no. 22, pp. 11844–11857, 2013, doi: 10.1021/am4035416.
[24] B. Russ *et al.*, “Power factor enhancement in solution-processed organic n-type thermoelectrics through molecular design,” *Adv. Mater.*, vol. 26, no. 21, pp. 3473–3477, 2014, doi: 10.1002/adma.201306116.
[25] L. Bu *et al.*, “Monodisperse Co-oligomer approach toward nanostructured films with alternating donor-acceptor lamellae,” *J. Am. Chem. Soc.*, vol. 131, no. 37, pp. 13242–13243, 2009, doi: 10.1021/ja905980w.
[26] S. Rajaram, R. Shivanna, S. K. Kandappa, and K. S. Narayan, “Nonplanar perylene diimides as potential alternatives to fullerenes in organic solar cells,” *J. Phys. Chem. Lett.*, vol. 3, no. 17, pp. 2405–2408, 2012, doi: 10.1021/jz301047d.
[27] H. Fu, Z. Wang, and Y. Sun, “Polymer Donors for High-Performance Non-Fullerene Organic Solar Cells,” *Angew. Chemie - Int. Ed.*, vol. 58, no. 14, pp. 4442–4453, Mar. 2019, doi: 10.1002/anie.201806291.
[28] P. De Echegaray *et al.*, “Synthesis of Perylene Imide Diones as Platforms for the Development of Pyrazine Based Organic Semiconductors,” *J. Org. Chem.*, vol. 81, no. 22, pp. 11256–11267, 2016, doi: 10.1021/acs.joc.6b02214.
[29] H. Herrera *et al.*, “Linear and star-shaped naphthalimide-fused pyrazinacenes,” *Chem. Commun.*, vol. 49, no. 7, pp. 713–715, 2013, doi: 10.1039/c2cc36791b.
[30] M. M. Oliva *et al.*, “Extending Hexaazatriphenylene with Mono-/Bithiophenes in Acceptor-Donor Diads and Acceptor-Donor-Acceptor Triads,” *J. Phys. Chem. C*, vol. 120, no. 40, pp. 23276–23285, 2016, doi: 10.1021/acs.jpcc.6b08123.
[31] R. Juárez *et al.*, “Hexaazatriphenylene (HAT) versus tri-HAT: The bigger the better?,” *Chem. - A Eur. J.*, vol. 17, no. 37, pp. 10312–10322, 2011, doi: 10.1002/chem.201101198.
[32] G. Li *et al.*, “Chalcogen-Fused Perylene Diimides-Based Nonfullerene Acceptors for High-Performance Organic Solar Cells: Insight into the Effect of O, S, and Se,” *Sol. RRL*, vol. 4, no. 3, pp. 1–9, 2020, doi: 10.1002/solr.201900453.
[33] T. Hodsden *et al.*, “Core Fluorination Enhances Solubility and Ambient Stability of an IDT-Based n-Type Semiconductor in Transistor Devices,” *Adv. Funct. Mater.*, vol. 30, no. 17, pp. 1–12, 2020, doi: 10.1002/adfm.202000325.
[34] E. M. Espinoza, J. A. Clark, J. Soliman, J. B. Derr, M. Morales, and V. I. Vullev, “Practical Aspects of Cyclic Voltammetry: How to Estimate Reduction Potentials When Irreversibility Prevails,” *J. Electrochem. Soc.*, vol. 166, no. 5, pp. H3175–H3187, 2019, doi: 10.1149/2.0241905jes.
[35] K. Ding *et al.*, “Propeller-like acceptors with difluoride perylene diimides for organic solar cells,” *Org. Electron.*, vol. 78, no. October 2019, p. 105569, 2020, doi: 10.1016/j.orgel.2019.105569.

[36] X. Li, L. E. Sinks, B. Rybtchinski, and M. R. Wasielewski, “Ultrafast aggregate-to-aggregate energy transfer within self-assembled light-harvesting columns of zinc phthalocyanine tetrakis(perylenediimide),” *J. Am. Chem. Soc.*, vol. 126, no. 35, pp. 10810–10811, 2004, doi: 10.1021/ja047176b.

[37] M. H. Hennessy, Z. G. Soos, R. A. Pascal, and A. Girlando, “Vibronic structure of PTCDA stacks: The exciton-phonon-charge-transfer dimer,” *Chem. Phys.*, vol. 245, no. 1–3, pp. 199–212, 1999, doi: 10.1016/S0301-0104(99)00082-8.

[38] F. F. So and S. R. Forrest, “Evidence for Exciton Confinement in Crystalline Organic Multiple Quantum Wells,” *Phys. Rev. Lett.*, vol. 66, no. 20, pp. 2649–2652, 1991, doi: 10.1103/PhysRevLett.66.2649.

[39] F. Würthner, C. Thalacker, A. Sautter, W. Schärtl, W. Ibach, and O. Hollricher, “Hierarchical Self-Organization of Perylene Bisimide - Melamine Assemblies to Fluorescent Mesoscopic Superstructures,” *Chem. - A Eur. J.*, vol. 6, no. 21, pp. 3871–3886, 2000, doi: 10.1002/1521-3765(20001103)6:21<3871::AID-CHEM3871>3.3.CO;2-W.

[40] A. D. Q. Li, W. Wang, and L. Q. Wang, “Folding versus self-assembling,” *Chem. - A Eur. J.*, vol. 9, no. 19, pp. 4594–4601, 2003, doi: 10.1002/chem.200305025.

[41] W. Wang, L. S. Li, G. Helms, H. H. Zhou, and A. D. Q. Li, “To fold or to assemble?,” *J. Am. Chem. Soc.*, vol. 125, no. 5, pp. 1120–1121, 2003, doi: 10.1021/ja027186h.

[42] H. Langhals and R. Ismael, “Cyclophanes as model compounds for permanent, dynamic aggregates-induced chirality with strong CD effects,” *European J. Org. Chem.*, no. 9, pp. 1915–1917, 1998, doi: 10.1002/(sici)1099-0690(199809)1998:9<1915::aid-ejoc1915>3.0.co;2-1.

[43] T. Van der Boom, R. T. Hayes, Y. Zhao, P. J. Bushard, E. A. Weiss, and M. R. Wasielewski, “Charge transport in photofunctional nanoparticles self-assembled from zinc 5,10,15,20-tetrakis(perylenediimide)porphyrin building blocks,” *J. Am. Chem. Soc.*, vol. 124, no. 32, pp. 9582–9590, 2002, doi: 10.1021/ja026286k.

[44] N. Sakai, J. Mareda, E. Vauthey, and S. Matile, “Core-substituted naphthalenediimides,” *Chem. Commun.*, vol. 46, no. 24, pp. 4225–4237, 2010, doi: 10.1039/c0cc00078g.

[45] Z. Liu *et al.*, “New organic semiconductors with imide/amide-containing molecular systems,” *Adv. Mater.*, vol. 26, no. 40, pp. 6965–6977, 2014, doi: 10.1002/adma.201305718.

[46] F. Würthner, C. R. Saha-Möller, B. Fimmel, S. Ogi, P. Leowanawat, and D. Schmidt, “Perylene Bisimide Dye Assemblies as Archetype Functional Supramolecular Materials,” *Chem. Rev.*, vol. 116, no. 3, pp. 962–1052, 2016, doi: 10.1021/acs.chemrev.5b00188.

[47] R. Adel *et al.*, “Comparing the microstructure and photovoltaic performance of 3 perylene imide acceptors with similar energy levels but different packing tendencies,” *J. Mater. Chem. C*, vol. 10, no. 5, pp. 1698–1710, Feb. 2022, doi: 10.1039/D1TC05037K.

[48] S. Marina *et al.*, “Common high-performance semiconducting polymers are not amorphous but semi-para-crystalline,” pp. 1–24, 2021, [Online]. Available: http://arxiv.org/abs/2103.15650.

[49] J. Min *et al.*, “Nano Energy High ef fi ciency and stability small molecule solar cells developed by bulk microstructure fi ne-tuning,” *Nano Energy*, vol. 28, pp. 241–249, 2016, doi: 10.1016/j.nanoen.2016.08.047.

[50] L. Le Bras, K. Chaitou, S. Aloïse, C. Adamo, and A. Perrier, “Aggregation-caused quenching: Versus crystallization induced emission in thiazolo[5,4-b] thieno[3,2-e] pyridine (TTP) derivatives: Theoretical insights,” *Phys. Chem. Chem. Phys.*, vol. 21, no. 1, pp. 46–56, 2019, doi: 10.1039/c8cp04730h.

[51] W. Z. Yuan *et al.*, “Changing the behavior of chromophores from aggregation-caused quenching to aggregation-induced emission: Development of highly efficient light emitters in the solid state,” *Adv. Mater.*, vol. 22, no. 19, pp. 2159–2163, 2010, doi: 10.1002/adma.200904056.

[52] M. Pope and C. E. Swenberg, “Electronic Processes in Organic Crystals and Polymers,” *Oxford Univ. Press USA 2nd Ed.*, p. 1328, 1999, https://books.google.com/books/about/Electronic_Processes_in_Organic_Crystals.html?id=AZVUAAAAMAAJ.

[53] W. C. Tsoi *et al.*, “The nature of in-plane skeleton Raman modes of P3HT and their correlation to the degree of molecular order in P3HT:PCBM blend thin films,” *J. Am. Chem. Soc.*, vol. 133, no. 25, pp. 9834–9843, 2011, doi: 10.1021/ja2013104.

[54] X. Rodríguez-Martínez, E. Pascual-San-José, Z. Fei, M. Heeney, R. Guimerà, and M. Campoy-Quiles, “Predicting the photocurrent-composition dependence in organic solar cells,” *Energy Environ. Sci.*, vol. 14, no. 2, pp. 986–994, 2021, doi: 10.1039/d0ee02958k.

[55] M. Stella and E. Mart, “Blade coated P3HT : non-fullerene acceptor solar cells : a high-throughput parameter study with a focus on up-scalability †,” pp. 20369–20382, 2019, doi: 10.1039/c9ta07361b.

[56] Y. Wang *et al.*, “Tailoring the molecular geometry of polyfluoride perylene diimide acceptors towards efficient organic solar cells,” *Journal of Materials Chemistry C*, vol. 8, no. 24. pp. 8224–8233, 2020, doi: 10.1039/d0tc01707h.

[57] S. Marina *et al.*, “The Importance of Quantifying the Composition of the Amorphous Intermixed Phase in Organic Solar Cells,” *Adv. Mater.*, vol. 32, no. 47, pp. 1–7, 2020, doi: 10.1002/adma.202005241.

[58] W. C. O. Ribeiro, V. Lobosco, and P. F. M. Martinez, “Solubility parameters analysis of Eucalyptus urograndis kraft lignin,” *BioResources*, vol. 15, no. 4, pp. 8577–8600, 2020, doi: 10.15376/biores.15.4.8577-8600.

[59] F. A. Ogliari *et al.*, “Influence of chain extender length of aromatic dimethacrylates on polymer network development,” *Dent. Mater.*, vol. 24, no. 2, pp. 165–171, 2008, doi: 10.1016/j.dental.2007.03.007.

[60] D. Fairhurst, R. Sharma, S. ichi Takeda, T. Cosgrove, and S. W. Prescott, “Fast NMR relaxation, powder wettability and Hansen Solubility Parameter analyses applied to particle dispersibility,” *Powder Technol.*, vol. 377, pp. 545–552, 2021, doi: 10.1016/j.powtec.2020.09.002.

[61] M. Hosseini, M. S. Roberts, R. Aboofazeli, and H. R. Moghimi, “Measurement of Hansen Solubility Parameters of third-degree burn eschar,” *Burns*, pp. 1–12, 2021, doi: 10.1016/j.burns.2021.07.017.

[62] M. S. Hossain, N. A. Rahim, M. M. Aman, and J. Selvaraj, “Application of ANOVA method to study solar energy for hydrogen production,” *Int. J. Hydrogen Energy*, vol. 44, no. 29, pp. 14571–14579, 2019, doi: 10.1016/j.ijhydene.2019.04.028.

[63] M. M. Crowley *et al.*, “The influence of guaifenesin and ketoprofen on the properties of hot-melt extruded polyethylene oxide films,” *Eur. J. Pharm. Sci.*, vol. 22, no. 5, pp. 409–418, 2004, doi: 10.1016/j.ejps.2004.04.005.

[64] P. E. Keivanidis, I. A. Howard, and R. H. Friend, “Intermolecular interactions of perylene diimides in photovoltaic blends of fluorene copolymers: Disorder effects on photophysical properties, film morphology and device efficiency,” *Adv. Funct. Mater.*, vol. 18, no. 20, pp. 3189–3202, 2008, doi: 10.1002/adfm.200800356.

Chapter 5 Challenges for upscaling OPV devices from blade coating to slot die roll-to-roll

Abstract

The successful printing of high throughput solution processed OPV modules will boost their wide industrial implementation. It is of crucial importance to understand where the efficiency losses experimented by large-scale processed modules come from. Questioning the efficiency gap between the lab-scale cells and the large-scale modules motivates us to implement a methodology that understand and tackle the process of upscaling step by step. Therefore, we examined the efficiency losses associated to all the steps during the upscaling of lab-scale. In this chapter we have developed a methodology for tracking the efficiency losses along the upscaling process from lab- to devices prepared by roll-to-roll coating. This methodology has allowed a close inspection of the impact of each printing phase in the final efficiency of the device through a step-by-step process. In this chapter we showed that the performance does not critically depend on the thickness/microstructure changes of the photoactive material, the efficiency losses are due to the blocking layers and the absorption of the electrodes.

5.1 Introduction: why is it challenging to up-scale OPV devices?

Organic solar cells have high potential for the large-scale production due to its low cost, flexibility and architecture perspectives for buildings. The photoactive materials' printing-ability in large area using roll-to-roll (R2R) processing techniques is a major advantage of the organic photovoltaic technology. Nowadays, the innovation of the photoactive materials have resulted in an enormous development in devices efficiency that is considered interesting for commercialization. The highest reported power conversion efficiencies (PCE) is 18.22% so far [1],[2], [3]. Despite these very good results, the upscaling from the lab to fab is still lacking this high efficiency. The closure of the gap between lab scale devices and industrial scale modules is not straightforward[4]. In fact, different parameters are running in the large-scale processing such as slot die roll-to-roll coating than in lab processing such as spin coating. Among these parameters, the long exposure to air while roll-to-roll processing on contrary to the lab-scale devices prepared in inert atmosphere that affect the devices lifetime and stability[5]–[8]. In addition, and related to this, there are morphological changes that consequently affect the structure- performance nexus of the solution processed organic films such as phase separation and/or different orientation of the donor and the acceptor. These changes affect the charge carrier transport and hence the photovoltaic parameters[9]–[12].
More parameters are changing at the same time that need to be analysed one by one. The first step changing in the roll-to-roll processing is the substrate. Replacing rigid glass substrates with flexible polymeric films is an extremely attractive possibility for roll-to-roll processing with the advantages of weight reduction and the flexibility. Semicrystalline polyethylene terephthalate (PET), due to their high mechanical properties, optical transparency and solvent resistance properties, are the most applied plastic substrates for flexible optoelectronic devices[13][14], [15]. When coated with Indium Tin Oxide (ITO) exhibits high transparency 85%-90% and good electrical conductivity with a sheet resistance as low as 8–12 Ω sq-1[16]. Furthermore, ITO-Metal-ITO (IMI) coated PET is more favourable because of its better electrical conductivity (sheet resistance ca 1- 8 Ω sq−1)[17].

Another parameter to consider while upscaling processing is the thickness variation in the printed stripes by slot die roll-to-roll, thick at the edges and thinner in the middle of the stripes forming wavy shapes along the printed stripes. In OPV devices the thickness of the layers plays an important role in many roles such as light absorption[18] and the ability to extract charge carriers[19]. Varying the thickness of the layers might add parallel resistance in the cell that might reduce the fill factor of the whole device since the thick layers are reported to reduce the driving field in the active layer, and thus, the charge carrier collection [20]. This thickness variations is responsible for variation in the performance in different batches[21]–[23]. This problem could be overcome mechanically by reverse gravure (RG) coating that is able to produce uniform thin film as reported[22], [24]. Another considered way is applying materials that have tolerant performance to thickness variations in the photoactive layer[25], [26] and in the blocking layers[27], [28].

Interfacial layers have a great impact on the performance of the solar cells, through their contribution to charge carriers extraction to the corresponding electrodes [29]–[34]. The common solution-processed materials for electron transport layers (ETLs) are titanium oxide (TiOx)[35], zinc oxide (ZnO)[36], and less common systems such as cesium carbonate (Cs_2CO_3)[37]. Zinc oxide (ZnO) has many favorable advantages such as high electron mobility, non-toxicity and optical transparency[38]. From energy bands perspectives, the Fermi energy of ZnO match most applied electron acceptor materials LUMO levels. In addition, Al doped ZnO (AZO) offers more favorable property to the roll-to-roll processing by

functioning efficiently in thick layers (>50nm)[39] in addition to its better stability and in comparison to the ZnO it does not need light soaking for enhancing the efficiency [40]

For the hole transporting materials, the most applied materials in solution processing are molybdenum oxide (MoOx)[41], vanadium oxide (V_2Ox)[42], and poly(3,4-ethylenedioxythiophene):polystyrene sulfonate (PEDOT:PSS). PEDOT:PSS has the advantage of high transmittance in the visible region, as well as high work function matching most photoactive materials' energy levels [31], [32], [34], [43]–[47]. Despite the fact that PEDOT:PSS forms a colloidal dispersion in water with high surface tension that stands against the flow of coating process. This requires more effort to ease the coating processing such as adding materials to enhance the wettability, however the additives might hinder the device efficiency[48], [49]. In addition to the fact of adding water into organic solar cells could seriously reduce their stability [50].

All the up mentioned issues have a direct impact in the performance of the devices prepared by high throughput techniques. Therefore, defining and quantifying the energy losses through the up-scaling processing would help to identify the challenging factors in solution processed OPV devices. Thus, in this work we have followed a step-by-step approach based on combining different printing techniques from blade coating to slot die roll-to-roll with the aim of assessing the causes of performance losses that affect industrialization of the printed devices.

5.2 Step-by-step methodology tackling the upscaling processing

Figure 5.1 shows the experimental steps through which our strategy is deployed. According to this experimental design, all the cells are of the inverted structure substrate/electrode/ETL/PAL/HTL/electrode. Blade coated on top of glass substrate/ITO is considered as a reference cell sown in Figure 5.1 structure i. The first step consists in replacing the glass substrate to the flexible IMI coated PET and comparing the differences arising from this change as shown in Figure 5.1 structure ii. This step is followed by introducing the roll-to-roll coating in the first layer instead of blade coating the ETL as shown in Figure 5.1 structure iii, following by slot die roll-to-roll coating of the PAL as shown in Figure 5.1 structure iv and end with slot die roll-to-roll coating for the HTL as shown in Figure 5.1 structure v. The silver electrode is kept evaporated through all the steps due to its high electrical conductivity. This methodology implies the efficiency loss tracking through the upscaling of the solar cell processing. All the devices were printed and measured under ambient environment. Clearly, other aspects such as top electrode, cell size, and cell interconnections in modules also affect the performance and should be the topic of future step-by step studies.

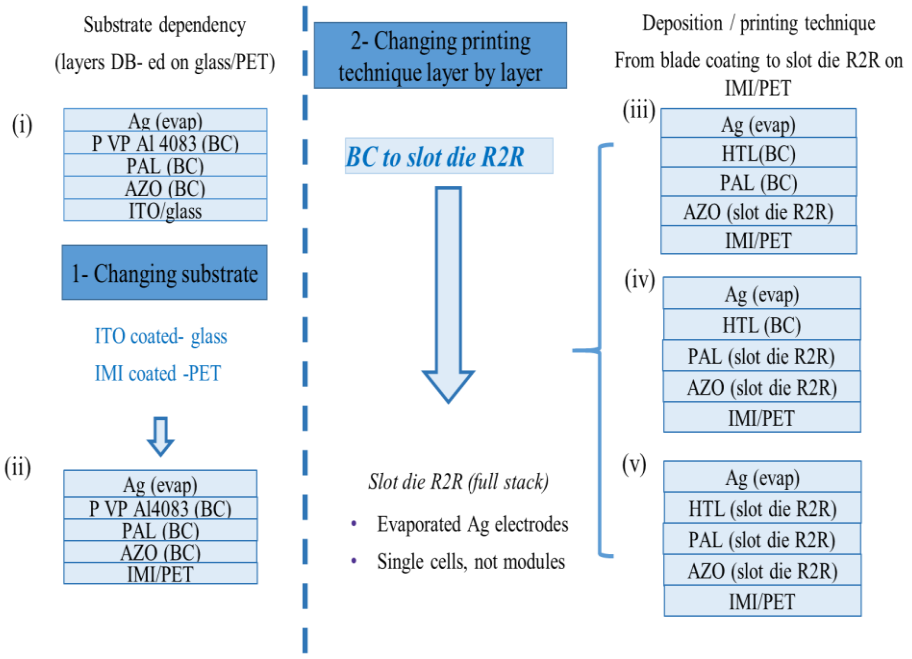

Figure 5.1 Step-by-step methodology for the upscaling processing from blade coating (BC) to slot die roll-to-roll (R2R).

5.3 Preparing the reference device

As mentioned above preparing and optimizing reference device of structure glass/ITO/AZO/PAL/Clevios P VP Al 4083/Ag is the starting point for the experimental methodology. Blade coating conditions listed in Table 5.1 are followed for the rest of the layers except the silver that is evaporated on the whole stack. All the layers have been deposited by dr blade technique with the printing conditions showed in

Table , with the exception of the top electrode that was thermally evaporated. Two steps are followed to optimize the reference device: first optimizing the thickness of PAL and second optimizing the annealing conditions of the PAL.

Table 5.1 The printing conditions for the reference device.

Ink	**Doctor blade printing parameters**			
	Ink volume [µl]	blade speed [mm/s]	Blade gap [µm]	plate temperature [ºC]
AZO	50	5	50	40
Blue ink	80	6	100	60
P VP AL 4083	180	5	575	65

The optimization of the thickness of the PAL has been done by instant control of the active layer thickness during the printing process. Therefore, the optical density of the photoactive layer is monitored by the UV-VIS spectroscopy, by processing different blade speeds. The relation held out between the active layer thickness, the optical density and the blade speed is shown in figure 5.2. Figure 5.3 shows the box plot with the mean values of the photovoltaic parameters of the prepared devices over different blade speeds while the whisker represents the maximum and the minimum values of the parameters.

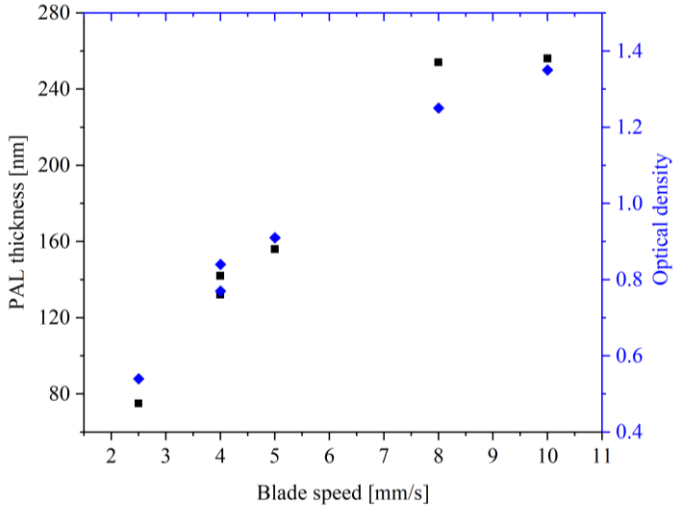

Figure 5.2 Relationship between the PAL thickness, blade speed and optical density.

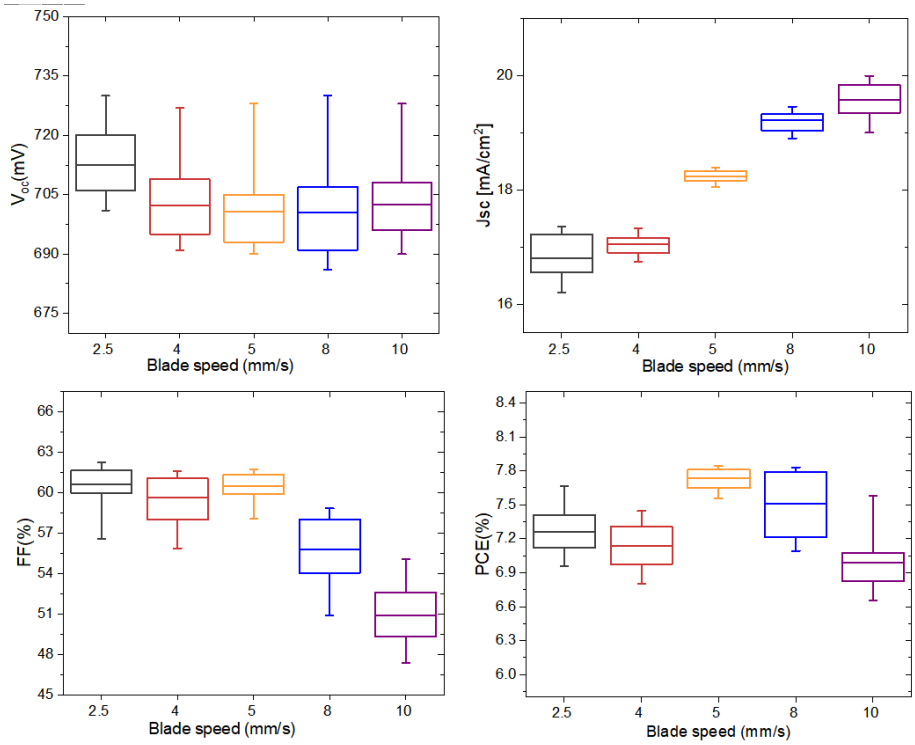

Figure 5.3 The photovoltaic parameters of the devices prepared at different blade speeds for the photoactive layer.

The thickness of PAL corresponding to the highest efficiency obtained of value 7.8% ~8%, is 150 nm, which corresponds to an optical density of 0.9. As it can be seen, there is no much change in the efficiencies of the devices (6.5-7.7%) over the range of thicknesses obtained, 80-260 nm, by varying the blade speed over the range of 2.5-10 mm/s. This is an important advantage of these materials that have a great potential in the up-scaled OPV technology.

The second step in optimizing the reference process is the thermal annealing. The thermal annealing is reported [51]–[53] to affect the degree of crystallinity of the heterojunction and hence the charge carrier transport in the photoactive layer of the devices. Therefore, different annealing conditions are carried out to the devices inside the glove box between 120 ºC and 140 ºC. Figure 5.4 shows the absorption spectra of the different annealed PAL films. All the films are blade coated on glass with the following annealing conditions; without annealing, annealed at 120ºC for 10 minutes, annealed at 130ºC for 3 minutes, annealed at 120ºC for 5 minutes + at 130ºC for 3 minutes and annealed at 120ºC for 5 minutes + at 140ºC for 3 minutes.

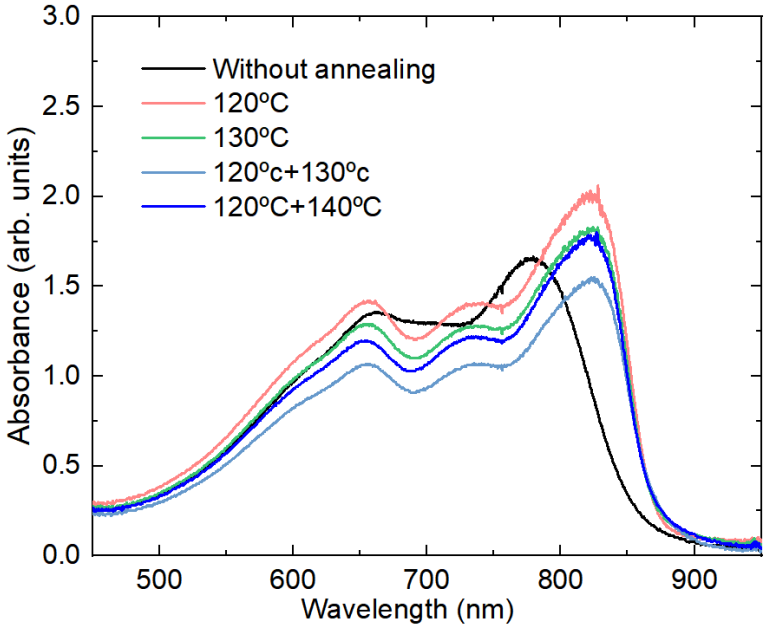

Figure 5.4 The absorption spectra of the PAL annealed at the following conditions: without annealing in black, annealed at 120ºC for 10 minutes in Cimon, annealed at 130ºC for 3 minutes in green, annealed at 120ºC for 5 minutes + at 130ºC for 3 minutes in baby blue and annealed at 120ºC for 5 minutes+ at 140ºC for 3minutes in blue.

The main peak of the PAL film at 830 nm in the non-annealed film is shifted by annealing independently on the temperature of the annealing process indicating the change in the degree of crystallinity of the annealed films. As a following step, these annealing conditions are carried out to the reference device to obtain the best photovoltaic performance. Figure 5.5 shows the J-V curves of the champion cells for each batch of devices annealed at different conditions and Table 5.2 lists their corresponding photovoltaic parameters.

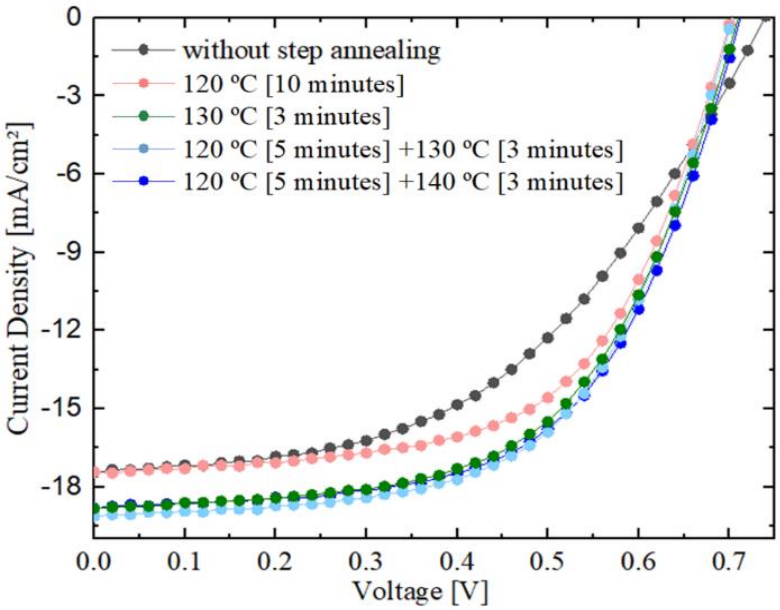

Figure 5.5 The J-V curves of the champion cells prepared at different annealing conditions.

Table 5.2 The average values± the standard deviation of the photovoltaic performance of 26 devices prepared with different annealing conditions along with their corresponding champion cells.

Annealing conditions	V_{oc} (mV)	J_{sc} (mA/cm²)	FF (%)	PCE (%)
Without step annealing	713±13	17.8±0.3	49±4	6.5±0.4
Champion cell	715	17.9	49	6.9
120 ºC (10 min)	702±12	18.3±1.1	54±5	6.8±0.4
Champion cell	702	17.4	59	7.2
130 ºC (3 min)	708±12	18.5±0.4	57±2	7.5±0.2
Champion cell	710	18.8	58	7.7
120 ºC (10 min) +130 ºC (3 min)	708±10	18.6±0.5	56±3	7.4±0.4
Champion cell	708	19.1	58	7.8
120 ºC (10 min) + 140 ºC(3 min)	716±11	18.5±0.4	57±3	7.5±0.3
Champion cell	712	18.8	59	7.8

The best performance is obtained after annealing for 5 minutes at 120ºC + 3 minutes at 130ºC condition, of device parameters PCE =7.9%, FF=58%, J_{sc}=19 mA/cm^2 and V_{oc}=0.71 V that reached us to the start point of our proposed methodology in Figure 5.1 structure *i*. Therefore, we start tracking the efficiency losses layer-by-layer through the upscaling.

5.4 Efficiency losses due to the substrate change

In the first step, substituting the glass substrate with the IMI coated PET substrate. Following the same device structure, the whole stack are blade coated on the new substrate except the evaporated Ag electrode Figure 5.1 structure *ii*. However, temperature above 120 ºC degrades the PET, this temperature limits the annealing processing of the device that is why we annealed this batch at 110 ºC. At this step, we tested two different materials for the HTL: Clevios P VP AL 4083 and Clevios solar 388. Despite the high electrical conductivity of the P VP AL 4083, this ink is not easy to be coated by roll-to-roll, so that Clevios 388 that has good electrical conductivity (for more reasons on selecting this material see section' Losses arising in the HTL'), is applied. Figure 5.6 shows the champion cells of each device batch with the two different substrates. All the photovoltaic parameters of both device batches comparing the devices performance with two difference substrates are listed in Table 5.4.

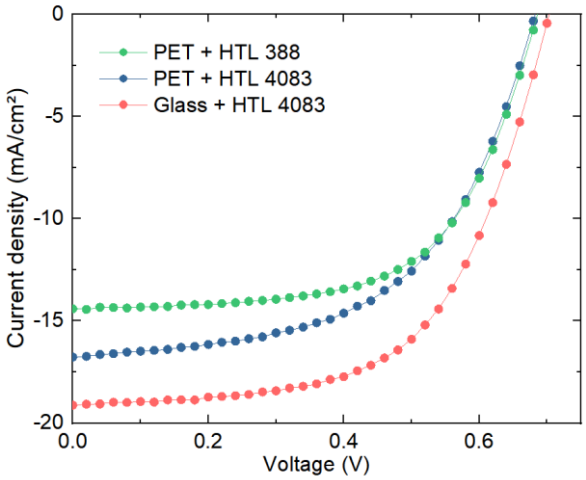

Figure 5.6 The. J-V curves of the champion cells prepared with different substrates and two HTLs.

Table 5.3 The average values ± standard deviation of photovoltaic parameters out of 53 devices prepared with different substrates and two HTLs.

Substrate (HTL)	V_{oc} (mV)	J_{sc} (mA/cm²)	FF (%)	PCE (%)
PET/IMI (HTL 4083)	671± 17	15.4± 1.2	47 ± 7	4.9 ± 1.2
PET/IMI (HTL 388)	685 ±17	13.8± 1.1	56 ±5	5.3 ±0.5
Glass/ITO (HTL 4083)	708 ± 10	18.6 ± 0.5	56 ±3	7.4 ± 0.4

The best performance of devices with glass substrate of efficiency of 7.7% while the best performance of devices with PET substrate has the value of 5.3% independently on the HTL applied. Devices with glass substrates have higher J_{sc}, V_{oc} compared to the devices with PET substrates. In case of devices with PET and HTL 4083 have higher J_{sc} compared to devices with PET substrate and HTL 388 unlike the FF and V_{oc}.

In order to get an insight of the reasons of the efficiency loss, we have analyzed the applied substrates properties. First, we analyze the electrical properties in which the two substrate

have slightly similar values of resistance PET/IMI and glass/ITO substrates are 6.5 ± 0.6 and 4.2 ± 0.2 Ω sq^{-1}, respectively. For comparison, the standard PET/ITO substrates typically exhibit sheet resistance values in the range of 6-500 Ω sq^{-1} depending on the thickness. Second, the optical properties, we measured the optical spectra of both substrates shown in Figure 5.7 and the PAL film from the PV-F formulated ink labeled as blue ink. The PET/IMI substrate shows higher absorption in the range where the blue ink absorbs, below 500 nm and above 700 nm. That is resulting in less light to enter the cell with PET substrate than the light that enter the devices with glass substrate and hence decreasing the J_{sc} of the devices with PET substrate. The optical loss exhibited by the two substrates is calculated by the equation below:

$$loss = \frac{A_P - A_G}{A_G} * 100 \qquad \text{Equation 3.1}$$

Where, A_G indicates the absorption of glass/ITO and A_P the one of PET/IMI.

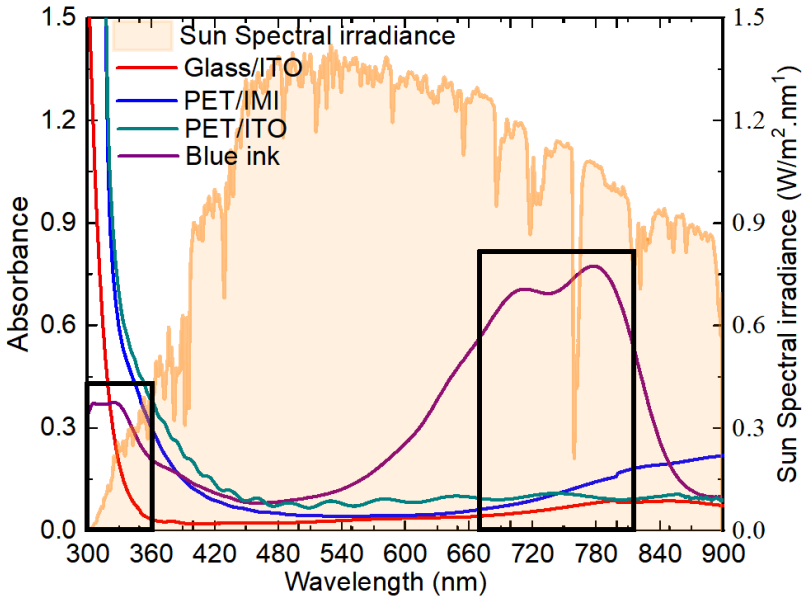

Figure 5.7 The absorption spectra of glass/ITO, PET/IMI and blue ink and sun spectral irradiance.

Considering the PCE values, a light loss value of 11.4% in the region where the blue ink absorbs (650-850 nm region) calculated when introducing PET/IMI substrate instead of the glass/ITO substrate. Besides the loss of extra 4.3% of light enters the cell with glass substrate while PET/IMI absorb all the light in the region 300 to 380 nm. To sum up these 16% loss in the J_{sc} is interrelated to the optical loss between the two substrates. Additional loss is considered because of the annealing limiting temperature for devices with PET/IMI lower than the optimized annealing condition with devices prepared with glass substrates. The observed lower values of the open circuit voltage of the device with PET/IMI with the two HTLs and the FF for the flexible devices with HTL 4083 is correlated to the cracks induced by the thermal treatment in the PET/IMI/AZO layer, which cause device leakage and possibly increase in charge carrier recombination.

5.5 Efficiency losses arising in the ETL

The following step is to compare between the performance of devices of the same structure prepared by depositing the AZO as ETL by blade coating and by slot die roll-to-roll as shown in Figure 5.1 structure iii. In addition, two different materials for the HTL mention in the previous step, Clevios P VP AL 4083 and Clevios solar 388, will be applied for the HTL.

The J-V curves of the champion cells for each batch of devices are shown in Figure 5.8 and Table 5.4 lists the average values of the photovoltaic parameters of the devices.

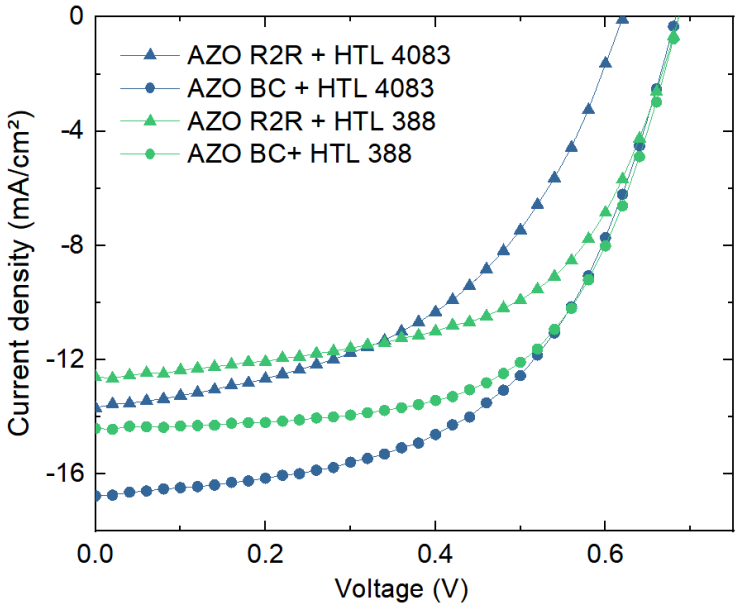

Figure. 5.8 The J-V curves of the champion cells with AZO blade coating (circles) or slot die R2R coated (triangles), in combination with HTL 4083 (blue color) or HTL 388(green line) layer.

Table 5. 4 The average values of the photovoltaic parameters of devices with blade coated and slot die R2R AZO and HTLs P VPAL 4083 (blue) and Clevios 388(green)

Samples	V_{oc} (mV)	J_{sc} (mA/cm²)	FF (%)	PCE (%)
AZO R2R 4083	592±49	13.9 ± 0.4	43 ± 4	3.6 ±0.6
AZO BC 4083	671± 17	15.4± 1.2	47 ± 7	4.9 ± 1.2
AZO R2R 388	673 ± 17	12.3 ± 0.9	52 ±5	4.3 ±0.4
AZO BC 388	685 ±17	13.9 ±1.1	56 ±5	5.3 ± 0.5

Devices with P VP AL 4083 and R2R-AZO shows efficiencies around 4%, while with P VP AL 4083 and BC- AZO shows efficiencies closer to 5%. Devices with Clevios 388 and R2R-AZO showed efficiency of 4%, while devices with Clevios 388 and BC- AZO have efficiencies of 5%. Regardless of the applied HTL, the devices with BC-AZO showed higher parameters J_{sc}, V_{oc} and FF than the devices of R2R-ed AZO layer.

That is reflecting the same loss independently on the applied HTL. To understand this loss, we analyzed the AZO layers by stylus profilometry. The measured thickness for slot die coated AZO is 32 ± 16 nm and for the blade coated AZO is 22 ± 1 nm. The change in layer thickness is addressed by the deposition techniques that are limited by the required

rheological properties for the corresponding technique. Slot die R2R coated film exhibit higher root means square (RMS) surface roughness of values RMS of 22 ± 9 nm than the blade coated film of values 4 ± 2 nm.

ZnO film roughness is reported to affect the photovoltaic performance of OPV devices by different mechanisms[54]–[56]. By comparing blade coated films to spin coated films, roughness in blade coated films is reported due to the different liquid spreading mechanisms and drying kinetics and hindering the devices performance and stability as a consequence[57]. The roughness in R2R-AZO layer result in enlarging the interfacial area at ETL/PAL interface, leading to higher trap density that is the source of the trap assisted recombination[57]–[60], and the reason for the reduction of the FF and V_{oc} in those devices[61]. Furthermore, the surface energy of the electron transport layer is affected by the roughness present in the AZO layer and as a consequence influence the wetting of the following ink on top. In addition, the interfacial area at the donor/acceptor interface is decreased because of the high roughness in the ETL printed by roll-to-roll resulting in less dissociation of the charge carriers and hence hindering the photogenerated current[58]. Therefore, we corelated the observed reduction in V_{oc} and FF for the devices with R2R-AZO to the large RMS roughness obtained in comparing to the values obtained by the devices with BC-AZO.

In this step the different materials for the HTLs did not affect the efficiency of the devices, however, better FF and V_{oc}, are observed in case of Clevios 388 than in case of Al 4083. Therefore, we have focused on the HTL 388 in the following experiment. The comparison of the device's performance based on different HTLs, and discussion of their properties are followed in "Efficiency losses due to the HTL" section.

5.6 Efficiency losses arising in the PAL

The following step is to deposit the photoactive layer by slot die R2R as shown in Figure 5.1 structure iv. The J-V curves of the champion cells of both sets with PAL coated by slot die R2R and PAL blade coated are shown in Figure 5.9. Quite similar parameters V_{oc}, FF and J_{sc} were observed for both batches, as listed in Table 5.5.

Slot die roll-to-rolled photoactive layer did not exhibit a significant difference in efficiency compared to the blade coated. That is interrelated to the hypothesis that the microstructure of the investigated material is resilient to changes resulted from the deposition method. This property gets along with the upscaling processing overcoming the coating inhomogeneities or roughness.

Table 5.5 The average value ± the standard deviation of the photovoltaic parameters of 79 devices prepared by blade coated and slot die R2R.

Samples	V_{oc} (mV)	J_{sc} (mA/cm²)	FF (%)	PCE (%)
PAL R2R	684±33	12±2	49±5	4.0±0.5
PAL BC	673±17	12.3±0.9	52±5	4.3±0.4

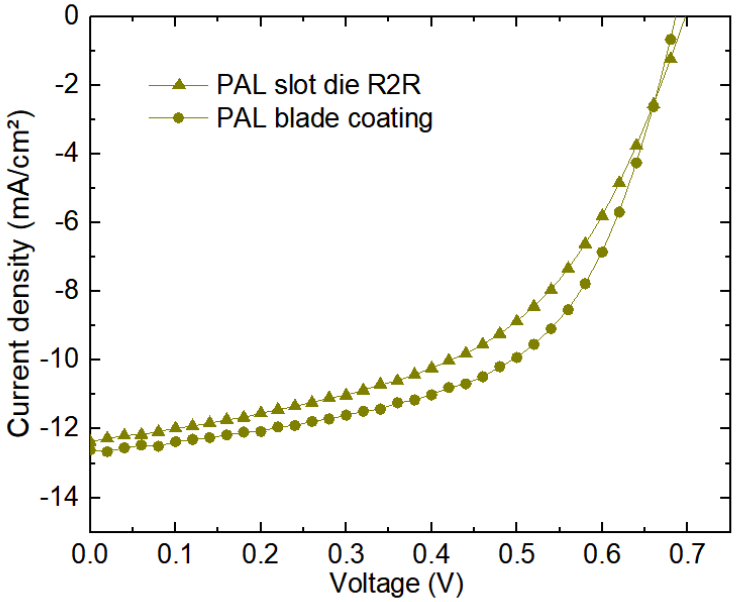

Figure 5. 9 The champion cells of the device based on blade coated PAL (circle) and slot die coated R2R (triangle).

5.7 Efficiency losses arising in the HTLs

This is the last stage of our methodology in which we investigate the effect of printing technique on the hole transport layer and correlate it to the device performance.

Different commercial PEDOT: PSS inks were applied in the common experiment: P VP Al 4083 is widely applied because of its high electrical conductivity and transparency. Despite, its high surface tension resulting in the de-wetting on the hydrophobic surface of the active layer.

These de-wetting problems can be treated by the addition of isopropanol (IPA) to the ink, however addition of too much IPA caused leakage out of the print- head ruining the printing process. It is reported that among different solvents, IPA is the solvent of choice to solve the PEDOT agglomerate that helps the PEDOT: PSS to form a uniform layer. The phase separation formed by the PEDOT-rich agglomerates create an interfacial energy barrier between PEDOT: PSS and the photoactive layer that increase the recombination rate and contributes to observed s-shape in the JV curves of the devices. The IPA hydrophobicity preferentially solve the PEDOT-rich agglomerates in an aqueous PEDOT:PSS solution [46]. Therefore, in order to avoid this problem, we have focused on two other HTLs: Clevios 388 and Clevios 434.

The devices shown in Figure 5.1 of structure v are prepared. The J-V curves of the champion cells of each set of devices are shown in Figure 5.10. Table 5.6 shows the average values of the photovoltaic parameters of the prepared devices. The best efficiency of devices with BC-HTL 388 is 4%, while for the case of BC-HTL 434 is 3.7%. Changing the printing technique to R2R dropped the efficiency to 3.2 % and 2.4%, respectively. Lower photovoltaic parameters J_{sc} and V_{oc} obtained by devices prepared by slot die R2R than the prepared devices by blade coating. Clearly, the reduction in the FF of the R2Red HTLs is the main reason for the efficiency drop. In addition, an S shape present in the J-V curves of the R2R coated HTL devices, is related to the low surface recombination at the electrode[62], [63]

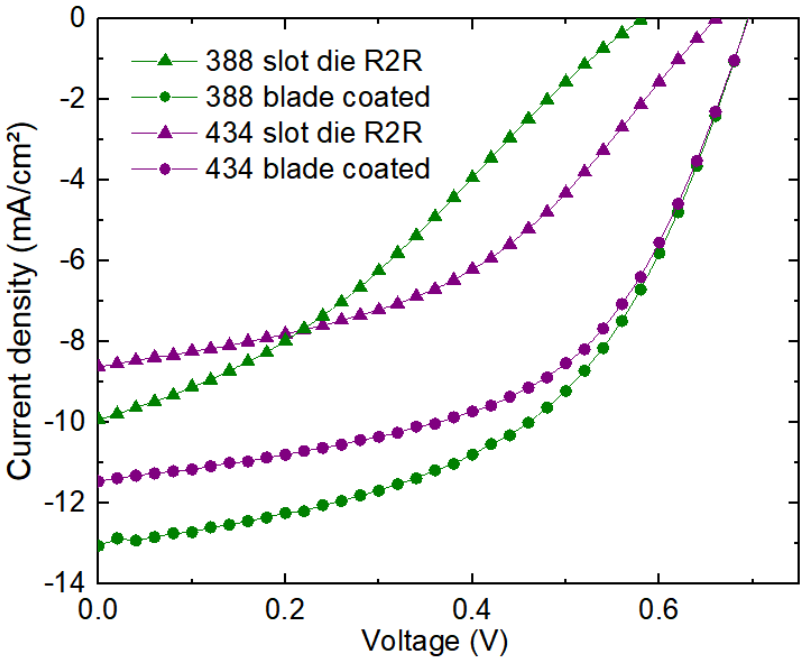

Figure 5.10 The J-V curves of the champion solar cells with HTLs 388 (green) and 434 (purple), deposited by blade coating (circle) and by slot die R2R coating(triangle).

Table 5.6 The average values ± standard deviation of photovoltaic parameters of 189 solar cells prepared by slot die roll-to-roll and blade coating.

HTL	V_{oc} (mV)	J_{sc} (mA/cm²)	FF (%)	PCE (%)
HTL 388 (BC)	684±33	12.1±1.6	49±5	4.0±0.5
HTL 388 (R2R)	620±58	11.2±0.7	34±6	2.4±0.4
HTL 434 (BC)	673±26	11.3±2.1	49±4	3.7±0.6
HTL 434 (R2R)	625±60	8.9±0.3	37±3	2.1±0.3

To further understand this result, we have analyzed other parameters for the HTLs such as the contact angle, electrical conductivity, optical properties, work functions and the topography. The contact angle was measured for the different hole transport layers on top of PAL/AZO/IMI/PET layers deposited by R2R to simulate the same results from the devices. Table 5.8 lists all the measured data.

Both HTL 388 and HTL434 gave lower contact angle than HTL 4083 which facilitates the coating of the former materials on top of the PAL. Therefore, we discarded HTL 4083 in this experiment.

Table 5.7 Measured parameters of the different HTLs applied in this experiment.

Parameter	HTL 4083	HTL 388	HTL 434
Contact angle (º)	95 ±2	25±8	23 ±4
Work function (eV)	5.0±0.1	5.0±0.1	4.8±0.1
Sheet resistance before annealing (Ω/sq^{-1})	0.2 ± 0.6	1.3 ± 0.3	26.2 ± 3.1
Sheet resistance after annealing (Ω/ sq^{-1}))	0.3 ± 0.4	0.4 ± 0.1	17.4 ± 3.2

The sheet resistance results, see Table 5.7, showed higher conductivity of HTL 4083 while HTL 434 showed the lowest conductivity. The thermal annealing improved the electrical conductivity of these materials, which is due to the moisture evaporation [64] or microstructural changes.

The work function (ϕ) of the three HTL materials was determined by Kelvin Probe Force Microscopy (KPFM) at room temperature under ambient conditions (for more details see the experimental chapter). The HTL 434 showed lower work function by 0.2 eV than HTL 4083 and HTL 388 which explains the higher V_{oc} and J_{sc} obtained for devices based on HTL 388 and HTL 4083, with respect to the devices based on HTL 434. PEDOT:PSS as an electron blocking layer has a limit duet to its mismatch to the energy level of PAL (PBTZT-stat-BDTT-8 at 5.2 eV[65]) resulting in reduction of V_{oc} [66]. The increase in the work function of the HTL, enhance the charge extraction and result in increasing the V_{oc} and improving the J_{sc} and FF[67], [69–72].

The absorption spectra of the three HTLs are shown in Figure 5.11. Due to the backward illumination in OSC, the HTL transparency led to an increase in the J_{sc}. This is because of allowing lighter to be reflected by the silver electrode into the active layer for multiple illumination. The absorption curves were normalized to the layers' thicknesses and reflect the high transmittance of the P VP Al 4083 in comparison with the other two samples. On the other hand, the comparison of the two Clevios inks shows that 434 absorbs more than 388 which explains why the J_{sc} is lower when 434 is employed in the devices.

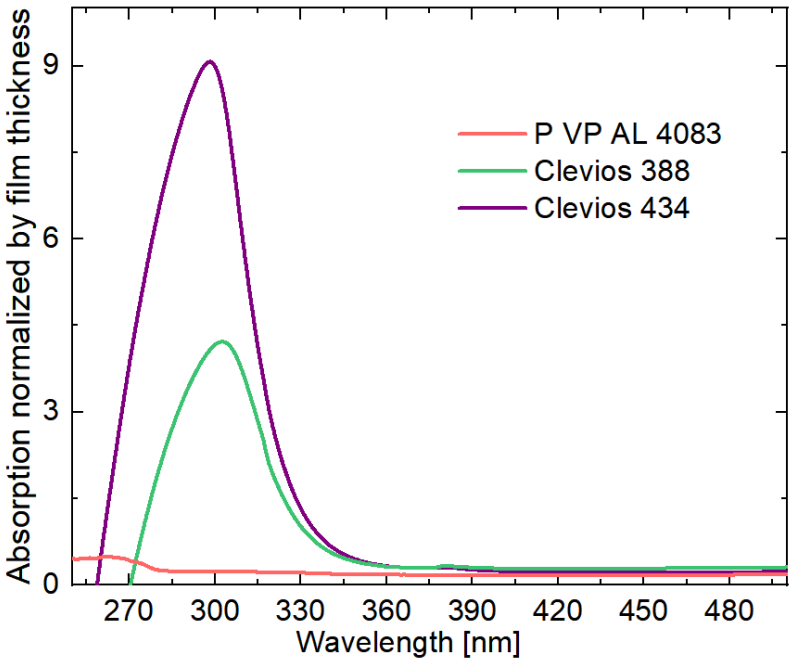

Figure 5.11 The absorption spectra of the different HTLs.

The morphology of the three HTL films blade coated on glass was investigated by atomic force microscopy (AFM). These images were taken by Francesco Silvestri of the AFM service in ICMAB. Figure 5.12 shows that pores are present in the HTL 388 (thickness of 257 nm) and HTL 434 films (thickness of 255 nm), with depths of up to 20 nm. This porous morphology could lead to direct contact between the top contact and the PAL, unlike the smooth topography of HTL 4083 (thickness of 530 nm). That elaborates partially the lower performance for HTL 388 devices, compared to devices with HTL 4083.

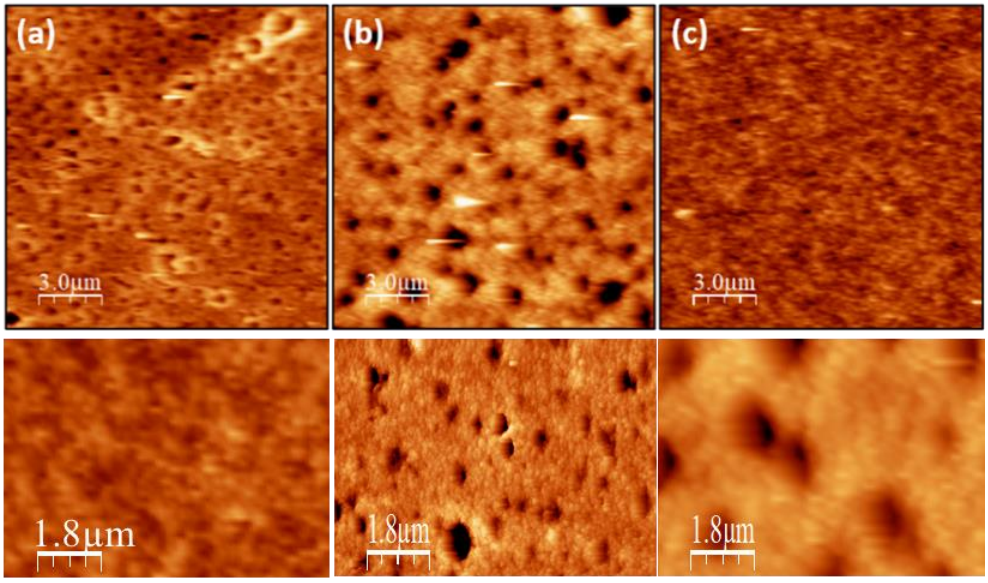

Figure 5.12 AFM topography images of the different HTLs: a) HTL 4083, b) HTL 388 and c) HTL 434. The scale in the upper row is of 3 microns, the scale in the down row is of 1.8 microns

These findings showed the main source of efficiency loss is assigned to the HTL printing by slot die roll-to-roll coating technique. First, their coating by the slot die roll-to-roll is limited by their rheological properties. Second, PET limits the thermal annealing of the devices and, resulting in less conductive HTL in slot die roll-to-roll coated devices than in the case of blade coated devices on glass substrates. Third, the reduction in the FF caused by both the rough ETL, and the porous HTL, deposited by slot die roll-to-roll. Finally, shunts created due to the porosity in the slot die R2R coated HTL, decrease FF, J_{sc} and, hence, the total efficiency.

Figure 5.13 summarizes the efficiency loss sources examined in this work through the up scaling from blade coating to slot die R2R coating.

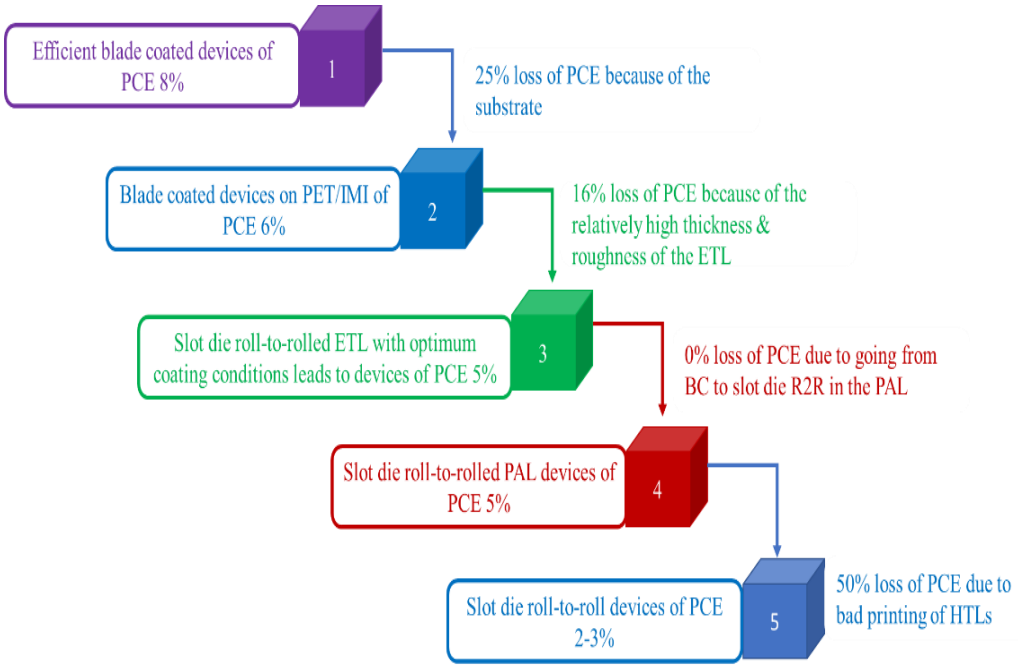

Figure 5.13 Efficiency losses through the upscaling process of organic solar cells.

Flexible TCE based on PET resulted in 25% reduction in the device efficiency due to the increased optical absorption and the limiting of the annealing temperature of the devices. Slot die R2R coating resulted in rough ETL that negatively influenced the device performance and considered as the third efficiency loss source. A photoactive system with thickness-independent performances helped to overcome the upscaling processing, being in favor to the roll-to-roll coating, keeping the same performance of the devices without additional loss. Low surface tension, highly transparent and highly conductive HTL inks are the key parameters for upscaling solution processed organic solar cells. HTLs considered the main efficiency loss by the reduction of 50% efficiency through the upscaling processing due to their electrical properties and their roughness.

5.8 Conclusion

A step-by-step methodology was experimented to evaluate each stage in the upscaling processing from blade coating to slot die R2R coating of OPV devices. Flexible substrates limited the thermal annealing of the devices and provided strong parasitic optical absorption, influencing the photogenerated current of the devices. The coating technique change for depositing the ETL result in introducing roughness that hinder the device performance. For the specific PAL material with performance insensitivity to film thickness properties applied in this experiment, no efficiency loss was experimented by changing the coating technique. Finally, HTL, whose printing is considered a challenge in the upscaling, reduced the FF of the devices due to the film quality induced by its wetting properties. These findings will help bolding the main challenges for the industrialization of solution processed organic photovoltaic devices.

5.9 References for Chapter 5

[1] Q. Liu et al., “18% Efficiency organic solar cells,” Sci. Bull., vol. 65, no. 4, pp. 272–275, 2020, doi: 10.1016/j.scib.2020.01.001.

[2] L. Meng et al., “Organic and solution-processed tandem solar cells with 17.3% efficiency,” Science (80-.)., vol. 361, no. 6407, pp. 1094–1098, Sep. 2018, doi: 10.1126/science.aat2612.

[3] G. Yu, J. Gao, J. C. Hummelen, F. Wudl, and A. J. Heeger, “Polymer photovoltaic cells: Enhanced efficiencies via a network of internal donor-acceptor heterojunctions,” Science (80-.)., vol. 270, no. 5243, p. 1789, 1995, doi: 10.1126/science.270.5243.1789.

[4] I. Burgués-Ceballos, M. Stella, P. Lacharmoise, and E. Martínez-Ferrero, “Towards industrialization of polymer solar cells: material processing for upscaling,” J. Mater. Chem. A, vol. 2, no. 42, pp. 17711–17722, Oct. 2014, doi: 10.1039/C4TA03780D.

[5] J. E. Carlé et al., “Overcoming the Scaling Lag for Polymer Solar Cells,” Joule, vol. 1, no. 2, pp. 274–289, 2017, doi: 10.1016/j.joule.2017.08.002.

[6] M. Helgesen et al., “Environmental Science,” 2014, doi: 10.1039/c4ee01223b.

[7] M. Hösel et al., “High-volume processed, ITO-free superstrates and substrates for roll-to-roll development of organic electronics,” Adv. Sci., vol. 1, no. 1, pp. 1–12, 2014, doi: 10.1002/advs.201400002.

[8] F. C. Krebs, T. Tromholt, and M. Jørgensen, “Upscaling of polymer solar cell fabrication using full roll-to-roll processing,” Nanoscale, vol. 2, no. 6, p. 873, 2010, doi: 10.1039/b9nr00430k.

[9] D. Chen, A. Nakahara, D. Wei, D. Nordlund, and T. P. Russell, “P3HT/PCBM Bulk Heterojunction Organic Photovoltaics: Correlating Efficiency and Morphology,” pp. 561–567, 2011.

[10] C. Mcdowell, M. Abdelsamie, M. F. Toney, and G. C. Bazan, “Solvent Additives : Key Morphology-Directing Agents for Solution-Processed Organic Solar Cells,” vol. 1707114, pp. 1–30, 2018, doi: 10.1002/adma.201707114.

[11] P. K. Shin, P. Kumar, A. Kumar, S. Kannappan, and S. Ochiai, “Effects of organic solvents for composite active layer of PCDTBT/PC 71BM on characteristics of organic solar cell devices,” Int. J. Photoenergy, vol. 2014, 2014, doi: 10.1155/2014/786468.

[12] Y. Huang, E. J. Kramer, A. J. Heeger, and G. C. Bazan, “Bulk heterojunction solar cells: Morphology and performance relationships,” Chem. Rev., vol. 114, no. 14, pp. 7006–7043, 2014, doi: 10.1021/cr400353v.

[13] Q. H. Lu and F. Zheng, “Polyimides for electronic applications,” in Advanced Polyimide Materials: Synthesis, Characterization, and Applications, Elsevier, 2018, pp. 195–255.

[14] V. Zardetto, T. M. Brown, A. Reale, and A. Di Carlo, “Substrates for flexible electronics: A practical investigation on the electrical, film flexibility, optical, temperature, and solvent resistance properties,” J. Polym. Sci. Part B Polym. Phys., vol. 49, no. 9, pp. 638–648, 2011, doi: 10.1002/polb.22227.

[15] B. Qu and S. R. Forrest, “Continuous roll-to-roll fabrication of organic photovoltaic cells via interconnected high-vacuum and low-pressure organic vapor phase

deposition systems," Appl. Phys. Lett., vol. 113, no. 5, pp. 1–5, 2018, doi: 10.1063/1.5039701.

[16] I. Burgú Es-Ceballos et al., "Towards industrialization of polymer solar cells: Material processing for upscaling," J. Mater. Chem. A, vol. 2, no. 42, pp. 17711–17722, 2014, doi: 10.1039/c4ta03780d.

[17] L. Lucera et al., "Highly efficient, large area, roll coated flexible and rigid OPV modules with geometric fill factors up to 98.5% processed with commercially available materials," Energy Environ. Sci., vol. 9, no. 1, pp. 89–94, Jan. 2016, doi: 10.1039/c5ee03315b.

[18] L. A. A. Pettersson, L. S. Roman, and O. Inganäs, "Modeling photocurrent action spectra of photovoltaic devices based on organic thin films," J. Appl. Phys., vol. 86, no. 1, pp. 487–496, 1999, doi: 10.1063/1.370757.

[19] F. Deledalle et al., "Understanding the effect of unintentional doping on transport optimization and analysis in efficient organic bulk-heterojunction solar cells," Phys. Rev. X, vol. 5, no. 1, pp. 1–13, 2015, doi: 10.1103/PhysRevX.5.011032.

[20] T. Kirchartz, T. Agostinelli, M. Campoy-Quiles, W. Gong, and J. Nelson, "Understanding the thickness-dependent performance of organic bulk heterojunction solar cells: The influence of mobility, lifetime, and space charge," J. Phys. Chem. Lett., vol. 3, no. 23, pp. 3470–3475, 2012, doi: 10.1021/jz301639y.

[21] J. Park, K. Shin, and C. Lee, "Mechanical aspects of the chemical mechanical polishing process: A review," Int. J. Precis. Eng. Manuf., vol. 17, no. 4, pp. 537–550, 2016, doi: 10.1007/s12541-016-0067-z.

[22] D. Vak, H. Weerasinghe, J. Ramamurthy, J. Subbiah, M. Brown, and D. J. Jones, "Reverse gravure coating for roll-to-roll production of organic photovoltaics," Sol. Energy Mater. Sol. Cells, vol. 149, pp. 154–161, 2016, doi: 10.1016/j.solmat.2016.01.015.

[23] J. Park, K. Shin, and C. Lee, "Improvement of cross-machine directional thickness deviation for uniform pressure-sensitive adhesive layer in roll-to-roll slot-die coating process," Int. J. Precis. Eng. Manuf., vol. 16, no. 5, pp. 937–943, 2015, doi: 10.1007/s12541-015-0122-1.

[24] D. Tobjork, H. Aarnio, T. Mäkelä, and R. Österbacka, "Roll-to-roll fabrication of bulk heterojunction plastic solar cells using the reverse gravure coating technique," Mater. Res. Soc. Symp. Proc., vol. 1091, pp. 62–67, 2008, doi: 10.1557/proc-1091-aa05-45.

[25] T. Wang et al., "High-Efficiency Thickness-Insensitive Organic Solar Cells with an Insulating Polymer," ACS Appl. Mater. Interfaces, vol. 13, no. 9, pp. 11134–11143, 2021, doi: 10.1021/acsami.0c22452.

[26] G. Zhang et al., "Overcoming Space-Charge Effect for Efficient Thick-Film Non-Fullerene Organic Solar Cells," Adv. Energy Mater., vol. 8, no. 25, pp. 1–8, 2018, doi: 10.1002/aenm.201801609.

[27] T. Stubhan, H. Oh, L. Pinna, J. Krantz, I. Litzov, and C. J. Brabec, "Inverted organic solar cells using a solution processed aluminum-doped zinc oxide buffer layer," Org. Electron., vol. 12, no. 9, pp. 1539–1543, 2011, doi: 10.1016/j.orgel.2011.05.027.

[28] J. Wei et al., "Roll-to-roll printed stable and thickness-independent ZnO:PEI composite electron transport layer for inverted organic solar cells," Sol. Energy, vol. 193, no. September, pp. 102–110, 2019, doi: 10.1016/j.solener.2019.09.037.

[29] B. Walker, H. Choi, and J. Y. Kim, "Interfacial engineering for highly efficient organic

solar cells," Curr. Appl. Phys., vol. 17, no. 3, pp. 370–391, Mar. 2017, doi: 10.1016/j.cap.2016.12.007.

[30] S. Lattante, "Electron and Hole Transport Layers: Their Use in Inverted Bulk Heterojunction Polymer Solar Cells," Electronics, vol. 3, no. 1, pp. 132–164, Mar. 2014, doi: 10.3390/electronics3010132.

[31] M. Hilal and J. I. Han, "Interface engineering of G-PEDOT: PSS hole transport layer via interlayer chemical functionalization for enhanced efficiency of large-area hybrid solar cells and their charge transport investigation," Sol. Energy, vol. 174, no. September, pp. 743–756, Nov. 2018, doi: 10.1016/j.solener.2018.09.031.

[32] J. Y. Kim et al., "Fabricated by All-Solution Processing," Science (80-.)., vol. 317, no. July, pp. 222–225, 2007, [Online]. Available: http://www.sciencemag.org/content/317/5835/222.short.

[33] S. Züfle, R. Hansson, E. A. Katz, and E. Moons, "Initial photo-degradation of PCDTBT:PC 70 BM solar cells studied under various illumination conditions: Role of the hole transport layer," Sol. Energy, vol. 183, no. March, pp. 234–239, May 2019, doi: 10.1016/j.solener.2019.03.020.

[34] A. Rana, A. Kumar, S. Chand, and R. K. Singh, "Hole transport layer influencing the charge carrier dynamics during the degradation of organic solar cells," J. Appl. Phys., vol. 125, no. 5, 2019, doi: 10.1063/1.5059555.

[35] A. Hadipour, R. Müller, and P. Heremans, "Room temperature solution-processed electron transport layer for organic solar cells," Org. Electron., vol. 14, no. 10, pp. 2379–2386, 2013.

[36] A. K. K. Kyaw et al., "Improved light harvesting and improved efficiency by insertion of an optical spacer (ZnO) in solution-processed small-molecule solar cells," Nano Lett., vol. 13, no. 8, pp. 3796–3801, 2013, doi: 10.1021/nl401758g.

[37] M.-F. Xu et al., "Work-function tuneable and aqueous solution-processed Cs 2 CO 3 for high-performance polymer solar cells," J. Mater. Chem. A, vol. 2, no. 24, pp. 9400–9404, 2014.

[38] W. C. H. Choy and D. Zhang, "Solution-Processed Metal Oxides as Efficient Carrier Transport Layers for Organic Photovoltaics," Small, vol. 12, no. 4, pp. 416–431, 2016.

[39] L. K. Jagadamma et al., "Polymer Solar Cells with Efficiency >10% Enabled via a Facile Solution-Processed Al-Doped ZnO Electron Transporting Layer," Adv. Energy Mater., vol. 5, no. 12, pp. 1–12, 2015, doi: 10.1002/aenm.201500204.

[40] Z. Jiang, S. Soltanian, B. Gholamkhass, A. Aljaafari, and P. Servati, "Light-soaking free organic photovoltaic devices with sol-gel deposited ZnO and AZO electron transport layers," RSC Adv., vol. 8, no. 64, pp. 36542–36548, 2018, doi: 10.1039/C8RA07071G.

[41] C. Girotto, E. Voroshazi, D. Cheyns, P. Heremans, and B. P. Rand, "Solution-processed MoO3 thin films as a hole-injection layer for organic solar cells," ACS Appl. Mater. Interfaces, vol. 3, no. 9, pp. 3244–3247, 2011.

[42] Z. Tan et al., "Solution-processed vanadium oxide as a hole collection layer on an ITO electrode for high-performance polymer solar cells," Phys. Chem. Chem. Phys., vol. 14, no. 42, pp. 14589–14595, 2012.

[43] M. Goumri, B. Lucas, B. Ratier, and M. Baitoul, "Inverted Polymer Solar Cells with a Reduced Graphene Oxide/Poly (3,4-Ethylene Dioxythiophene):Poly(4-Styrene Sulfonate) (PEDOT:PSS) Hole Transport Layer," J. Electron. Mater., vol. 48, no. 2,

pp. 1097–1105, 2019, doi: 10.1007/s11664-018-06841-9.

[44] Z. Xie et al., “The modified PEDOT:PSS as cathode interfacial layer for scalable organic solar cells,” Org. Electron. physics, Mater. Appl., vol. 71, no. March, pp. 143–149, Aug. 2019, doi: 10.1016/j.orgel.2019.05.012.

[45] S. Rafique et al., “UV- ozone treated graphene oxide/ PEDOT:PSS bilayer as a novel hole transport layer in highly efficient and stable organic solar cells,” Org. Electron. physics, Mater. Appl., vol. 66, no. December 2018, pp. 32–42, Mar. 2019, doi: 10.1016/j.orgel.2018.12.005.

[46] G. Namkoong, E. M. Younes, T. M. Abdel-Fattah, E. M. El-Maghraby, A. H. Elsayed, and A. H. Abo Elazm, “Aging process of PEDOT:PSS dispersion and robust recovery of aged PEDOT:PSS as a hole transport layer for organic solar cells,” Org. Electron. physics, Mater. Appl., vol. 25, pp. 237–244, Oct. 2015, doi: 10.1016/j.orgel.2015.06.049.

[47] Y. Dang et al., “Solution processed hybrid Graphene-MoO 3 hole transport layers for improved performance of organic solar cells,” Org. Electron. physics, Mater. Appl., vol. 67, no. September 2018, pp. 95–100, Apr. 2019, doi: 10.1016/j.orgel.2019.01.013.

[48] D. Wang et al., “Ultrathin anode buffer layer for enhancing performance of polymer solar cells,” Int. J. Photoenergy, vol. 2014, 2014.

[49] M. Petrosino and A. Rubino, “The effect of the PEDOT: PSS surface energy on the interface potential barrier,” Synth. Met., vol. 161, no. 23–24, pp. 2714–2717, 2012.

[50] B. Arredondo et al., “Analysing impact of oxygen and water exposure on roll-coated organic solar cell performance using impedance spectroscopy,” Sol. Energy Mater. Sol. Cells, vol. 176, no. November 2017, pp. 397–404, 2018, doi: 10.1016/j.solmat.2017.10.028.

[51] M. Gerhard, A. P. Arndt, I. A. Howard, A. Rahimi-Iman, U. Lemmer, and M. Koch, “Temperature- and Energy-Dependent Separation of Charge-Transfer States in PTB7-Based Organic Solar Cells,” J. Phys. Chem. C, vol. 119, no. 51, pp. 28309–28318, Dec. 2015, doi: 10.1021/acs.jpcc.5b09842.

[52] S. Ben Dkhil et al., “Toward High-Temperature Stability of PTB7-Based Bulk Heterojunction Solar Cells: Impact of Fullerene Size and Solvent Additive,” Adv. Energy Mater., vol. 7, no. 4, pp. 1–11, 2017, doi: 10.1002/aenm.201601486.

[53] G. Juška, I. D. W. Samuel, B. Ebenhoch, S. A. J. Thomson, and K. Genevic, “Charge carrier mobility of the organic photovoltaic materials PTB7 and PC 71 BM and its influence on device performance,” vol. 22, pp. 62–68, 2015, doi: 10.1016/j.orgel.2015.03.013.

[54] F. C. Krebs, T. Tromholt, and M. Jørgensen, “Upscaling of polymer solar cell fabrication using full roll-to-roll processing,” Nanoscale, vol. 2, no. 6, pp. 873–886, Jun. 2010, doi: 10.1039/B9NR00430K.

[55] M. Hösel et al., “High-Volume Processed, ITO-Free Superstrates and Substrates for Roll-to-Roll Development of Organic Electronics,” Adv. Sci., vol. 1, no. 1, p. 1400002, Dec. 2014, doi: 10.1002/ADVS.201400002.

[56] T. R. Andersen et al., “Scalable, ambient atmosphere roll-to-roll manufacture of encapsulated large area, flexible organic tandem solar cell modules,” Energy Environ. Sci., vol. 7, no. 9, pp. 2925–2933, 2014, doi: 10.1039/C4EE01223B.

[57] G. Ji et al., “12.88% efficiency in doctor-blade coated organic solar cells through

optimizing the surface morphology of a ZnO cathode buffer layer," J. Mater. Chem. A, vol. 7, no. 1, pp. 212–220, 2019, doi: 10.1039/c8ta08873j.

[58] Z. Ma, Z. Tang, E. Wang, M. R. Andersson, O. Inganäs, and F. Zhang, "Influences of surface roughness of ZnO electron transport layer on the photovoltaic performance of organic inverted solar cells," J. Phys. Chem. C, vol. 116, no. 46, pp. 24462–24468, 2012, doi: 10.1021/jp308480u.

[59] J. Wei et al., "Silane-Capped ZnO Nanoparticles for Use as the Electron Transport Layer in Inverted Organic Solar Cells," ACS Nano, vol. 12, no. 6, pp. 5518–5529, 2018, doi: 10.1021/acsnano.8b01178.

[60] C. A. Polyzoidis et al., "Improvement of Inverted OPV Performance by Enhancement of ZnO Layer Properties as an Electron Transfer Layer," in Materials Today: Proceedings, Jan. 2016, vol. 3, no. 3, pp. 758–771, doi: 10.1016/j.matpr.2016.02.007.

[61] Z. Liang, Q. Zhang, L. Jiang, and G. Cao, "ZnO cathode buffer layers for inverted polymer solar cells," Energy Environ. Sci., vol. 8, no. 12, pp. 3442–3476, 2015, doi: 10.1039/c5ee02510a.

[62] A. Khalf, J. Gojanović, N. Ćirović, and S. Živanović, "Two different types of S-shaped J-V characteristics in organic solar cells," Opt. Quantum Electron., vol. 52, no. 2, pp. 1–10, 2020, doi: 10.1007/s11082-020-2236-7.

[63] A. Wagenpfahl, D. Rauh, M. Binder, C. Deibel, and V. Dyakonov, "S-shaped current-voltage characteristics of organic solar devices," Phys. Rev. B - Condens. Matter Mater. Phys., vol. 82, no. 11, pp. 1–8, 2010, doi: 10.1103/PhysRevB.82.115306.

[64] B. Friedel et al., "Effects of layer thickness and annealing of PEDOT:PSS layers in organic photodetectors," Macromolecules, vol. 42, no. 17, pp. 6741–6747, 2009, doi: 10.1021/ma901182u.

[65] "Engineering high-performance and air-stable PBTZT-stat-BDTT-8_PC61BM_PC71BM organic solar cells _ Enhanced Reader.pdf." .

[66] P. Lin et al., "Surface Modification of PEDOT:PSS for Enhanced Performance of Inverted Perovskite Solar Cells," ACS Appl. Energy Mater., vol. 4, no. 5, pp. 4408–4415, 2021, doi: 10.1021/acsaem.0c03249.

[67] S. Im et al., "Improved Stability of Interfacial Energy-Level Alignment in Inverted Planar Perovskite Solar Cells," ACS Appl. Mater. Interfaces, vol. 10, no. 22, pp. 18964–18973, 2018, doi: 10.1021/acsami.8b03543.

[68] B. Xu et al., "Functional solid additive modified PEDOT:PSS as an anode buffer layer for enhanced photovoltaic performance and stability in polymer solar cells," Sci. Rep., vol. 7, no. October 2016, pp. 1–13, 2017, doi: 10.1038/srep45079.

[69] I. Gelmetti *et al.*, "Energy alignment and recombination in perovskite solar cells: Weighted influence on the open circuit voltage," *Energy Environ. Sci.*, vol. 12, no. 4, pp. 1309–1316, 2019, doi: 10.1039/c9ee00528e.

Chapter 6 Degradation study of OPV modules

Abstract

The degradation of solution processed photovoltaic modules is still a dominant issue that hinders the commercialization. Since the degradation of the modules is strongly correlated to the active layer components, we have compared the degradation of roll-to-roll modules based on fullerene acceptors (FA) (P3HT: PCBM) and non-fullerene acceptors (NFA) (P3HT:o-IDTBR) heterojunctions to have more insights in the lifetime of the OPV modules for the industrial scale application. Two types of encapsulation systems (PET only and barrier foil) are used to isolate the modules from the environmental conditions, such as (the diffusion of) oxygen and humidity. The degradation of the roll-to-roll modules has been carried out in a climatic chamber with controlled conditions (temperature and humidity) for hundreds of hours in air following ISOS-L-1 protocol. We have investigated the degradation by several characterization techniques, such as electrical characterization, photoluminescence, Raman spectroscopy in addition to the EPR spectroscopy. Imaging techniques have been used as well for comparing fresh and degraded modules using the laser beam induced current (LBIC) technique, in order to reveal information about the photodegradation mechanisms. It has been found that the FA stabilizes the donor polymer more than the NFA. Modules based on P3HT: PCBM and P3HT:o-IDTBR encapsulated with barrier foil were active up to 522 and 249 hours, respectively, while modules encapsulated with PET foil showed activity only for 21 hours. In addition, not only the photoactive layer components were found to be the origin of the degradation process but also the HTL is affected by the oxygen diffusion.

6.1 Degradation challenges in OPV devices

Organic photovoltaic modules prepared by high throughput techniques, such as roll-to-roll, are cutting the edge towards industrialization due to their capacity for a fast solution processing on flexible substrates and low-cost production [1,2]. The device efficiency is rapidly improving, with current high records exceeding 18%, by synthesizing and combining new materials. The lack of device stability is, however, still an obstacle to meet the market needs [3–10][11]. Therefore, research on device stability is increasingly gaining attention. Undoubtedly, OPV devices suffer from degradation when different layers are exposed to environmental conditions, such as light, oxygen, temperature and humidity, that deteriorate the lifetime of the devices if they are not protected [12]. The concept of device degradation refers to a decrease of the performance over time due to the reduction of the cell parameters J_{sc}, V_{oc}, FF and resulting PCE, and the performance in general[13]. Degradation mechanisms, as reported in literature[13–16], are classified as extrinsic, when caused by external factors, including chemical reactions with the water and oxygen coming from the environment or cracks due to repeated bending; and intrinsic, when the process occurs in the dark and without other external stimuli. Extrinsic degradation includes the diffusion of external oxygen and water into the device, the degradation of the photoactive materials by light, morphological evolution by applying high temperatures, diffusion of the materials from the electrode and interfacial layer and the subsequent reaction with the organic materials and morphological changes in the photoactive layer. Organic solar cells reported to have the low oxygen transmission rate (OTR) 10^{-5} cm^3/m^2d bar and water vapour transmission rate(WVTR) of 10^{-5} g/m^2 d [17]. In addition, the OPV device undergoes degradation under dark due to the molecular rearrangement in the photoactive layer and at the interfaces, that affects the charge extraction such as the phase separation between the donor and the acceptor.

In addition, illuminating the OPV devices induces additional degradation that leads to an exponential decay in the efficiency of the device and loss of the short-circuit current due to different types of photodegradation avenues, some requiring the presence of oxygen and some not. As an example, for fullerene based OPVs, photodegradation has been found to be related to the photodimerization of the fullerene molecule of C_{60} and PCBM[18,19].

Several strategies investigated to increase the modules stability have been reported[11],[25],[26],[22–24],[25–27]. A proper encapsulation is required to provide extrinsic stability to the OPV devices through the reduction of oxygen and water diffusion into the devices. Furthermore, it improves the mechanical stability of the devices such as bending and scratches. In addition, encapsulation can act as a UV filter with the aim of eliminating the UV part of the solar radiation that degrades the photoactive materials [28]. Different types of encapsulation strategies are reported for OPV devices [29,30], indicating that both flexible and rigid options are able to enhance their lifetime by an amount of many thousand hours [31,32]. Even if glass encapsulation offers the best performances in terms of water and oxygen permeation rates, it is not compatible with OPV devices for flexible applications[33]. Therefore, different research papers have reported encapsulation methods that combines the advantages of high device protection with transparency, flexibility and low-cost.

Amongst the different materials that have been used for encapsulation are the metal oxides such as TiO_2 and Al_2O_3 [34]. Al_2O_3 layers deposited by atomic layer deposition have demonstrated to preserve the efficiency of pentacene based solar cells for 6000 hours with an efficiency loss of 6% [35]. Al_2O_3 has also showed superior encapsulation for P3HT:PCBM based solar cell to retain 80% of their efficiency after 500 h in air [36]. Other types of

materials, such as MgF_2 [37] and graphene oxide GO [38], have been shown to improve the lifetime of OPV device by several hundred hours. On the other hand, encapsulation based on organic materials have also been reported to protect OPV devices [31,39,40]. Bisphenol based epoxy has been applied as an encapsulation material [41]. UV curable glue has been reported as a top encapsulation for achieving high stability in OPV devices based on PCDTBT:PC_{71}BM [42]. Multilayer combinations such as polyethylene (42mm)/ethylene vinyl alcohol copolymer (6mm)/polyethylene (42mm) (PE/EVOH/PE) or polypropylene/polyvinyl alcohol/inorganic layer/polyethylene (PP/PVA/In/ PE) have resulted in water transmission rates of 10^{-3}g $m^{-2}day^{-1}$, allowing to reach lifetimes of several years[43,44].

In this chapter, we aim to evaluate the influence of the encapsulating layer on OPV modules prepared by roll-to-roll slot die printing technique in air. For that, we have studied the photo and thermal degradation. we have fabricated 25 modules by slot die coating, each with 3 cells connected in series. Samples were fabricated on ITO coated PET, the active layers,were P3HT:PCBM and P·HT:o-IDTBR, ZnO and PEDOT:PSS were deposited by slot die, and then as top electrode by screen printing with the geometry shown in Figure XX. We compare the encapsulation with thin PET (brand/provider) and barrier foil (brand/provider). Further details in the Experimental Chapter. All the experimental details are described in the experimental chapter. We followed ISOS-L-1 protocol adjusting the environmental conditions for the modules in a climatic chamber[45]. From the results in the chapter, it seems that the barrier foil of thickness 80 µ and 86% transmittance has been designed to block UV, and to minimize the transmission of both oxygen and water to <0,01 g/sqm.day and 0,005 g/sqm.day, respectively. PET foils are used to assure a minimum stability during characterization and an easy access to the material, without spending expensive material just for tests. The interesting devices were than encapsulated with barrier foil. Moreover, we have done a direct comparison between fullerene and non-fullerene acceptors combined with the workhorse donor P3HT to detect changes in their behaviour upon degradation.

6.2 Degradation induced by light exposure

The degradation of OPV modules under light exposure has been investigated by measuring the J-V characteristics of the modules for different light exposure time intervals as shown in Fig. 6.1. The main photovoltaic parameters are summarized in table 6.1. From the measured values, we calculated the normalised values at different degradation time intervals that are presented in Figure 6.2 for the four sets of modules. The modules encapsulated with barrier foil based on P3HT: PCBM and P3HT:o-IDTBR showed active performance for more than 522 and 291 hours, respectively, while the same type of modules encapsulated with only PET foil were active for slightly more than 21 hours. The T_{80} values, defined as the time to which the modules retain 80% of their initial efficiency, for the four sets of modules are tabulated in Table 6.2 showing that the modules based on P3HT: PCBM are more stable than the modules based on P3HT:o-IDTBR.

These results revealed that the modules encapsulated with barrier foil resist the degradation for longer periods of time (as one may expect considering that they have been designed to prevent at least in part, gas transmission). Interestingly, we notice that the efficiency of modules based on P3HT: PCBM encapsulated with the barrier foil increased in the first hours after exposing to illumination. This increase in the efficiency is accompanied by the increase of the photo generated current and slight decrease in the V_{oc}. This change has been reported to correlate to the change in the degree of crystallinity of the photo active layer which is similar to the effect of thermal annealing [46].

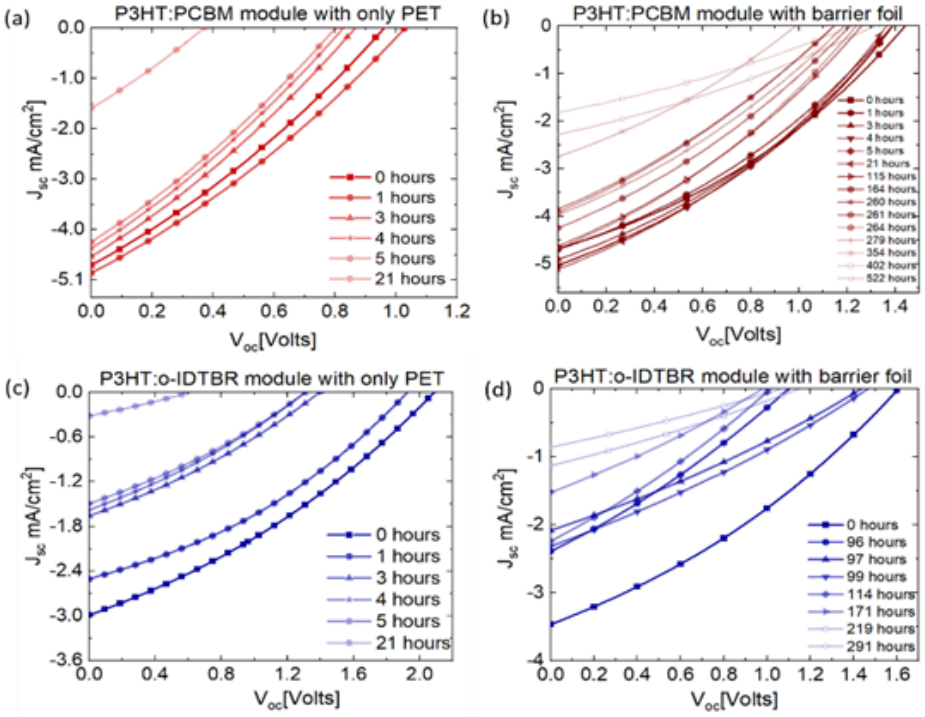

Fig. 6.1 The J-V curves before and during the degradation process under 1 sun of (a) module based on P3HT: PCBM encapsulated only with PET, (b) module based on P3HT: PCBM encapsulated with barrier foil, (c) module based on P3HT:o-IDTBR encapsulated only with PET and (d) module based on P3HT:o-IDTBR encapsulated with barrier foil.

Table 6.1. Evolution with time of the Photovoltaic parameters of the P3HT: PCBM and P3HT:o-IDTBR based modules with different encapsulation conditions.

Modules	Encapsulation	Exposure time (hours)	V_{oc} (V)	J_{sc} ($mA \cdot cm^{-2}$)	FF (%)	PCE (%)
P3HT:O-IDTBR	PET	0	1.44	-3	59.5	0.60
		1	1.38	-2.01	31.7	0.36
		3	1.38	-1.62	29.1	0.19
		4	1.38	-1.53	30.1	0.18
		5	1.38	-1.5	30	0.18
		21	1.36	-0.33	28.8	0.02
	Barrier	0	1.6	-3.45	32.2	0.60
		96	1.11	-2.4	28.7	0.25
		97	1.19	-2.43	29.3	0.28
		99	1.23	-2.55	29.2	0.30
		114	1.01	-2.25	28.6	0.22
		219	0.84	-1.29	28.1	0.03
		291	0.79	-0.99	27.6	0.02
P3HT: PCBM	PET	0	0.91	-4.41	29.2	0.39
		1	0.97	-4.56	29	0.43
		3	0.83	-4.29	29	0.34
		4	0.79	-4.14	28.7	0.31
		5	0.8	-4.32	28.3	0.33
		21	0.36	-1.62	26.9	0.05
	Barrier	0	1.44	-4.68	33.9	0.76
		1	1.39	-4.68	33.4	0.72
		3	1.39	-4.89	33.9	0.77
		4	1.39	-5.01	33.8	0.78
		5	1.39	-5.04	33.8	0.79
		21	1.36	-5.1	33.6	0.78
		115	1.25	-4.62	32	0.62
		164	1.21	-4.23	31	0.53
		260	1.15	-3.84	30.3	0.45
		261	1.15	-3.9	30.1	0.45
		279	1.19	-3.96	30.8	0.48
		354	0.91	-2.97	30.8	0.09
		402	0.95	-2.49	30.9	0.08
		522	0.9	-2.01	30.8	0.06

Table 6.2 Estimated T_{80} of the four sets of modules.

Modules	T_{80} (hours)
P3HT:PCBM (PET)	3
P3HT:PCBM (barrier)	120
P3HT:o-IDTBR (PET)	1
P3HT:o-IDTBR (barrier)	31

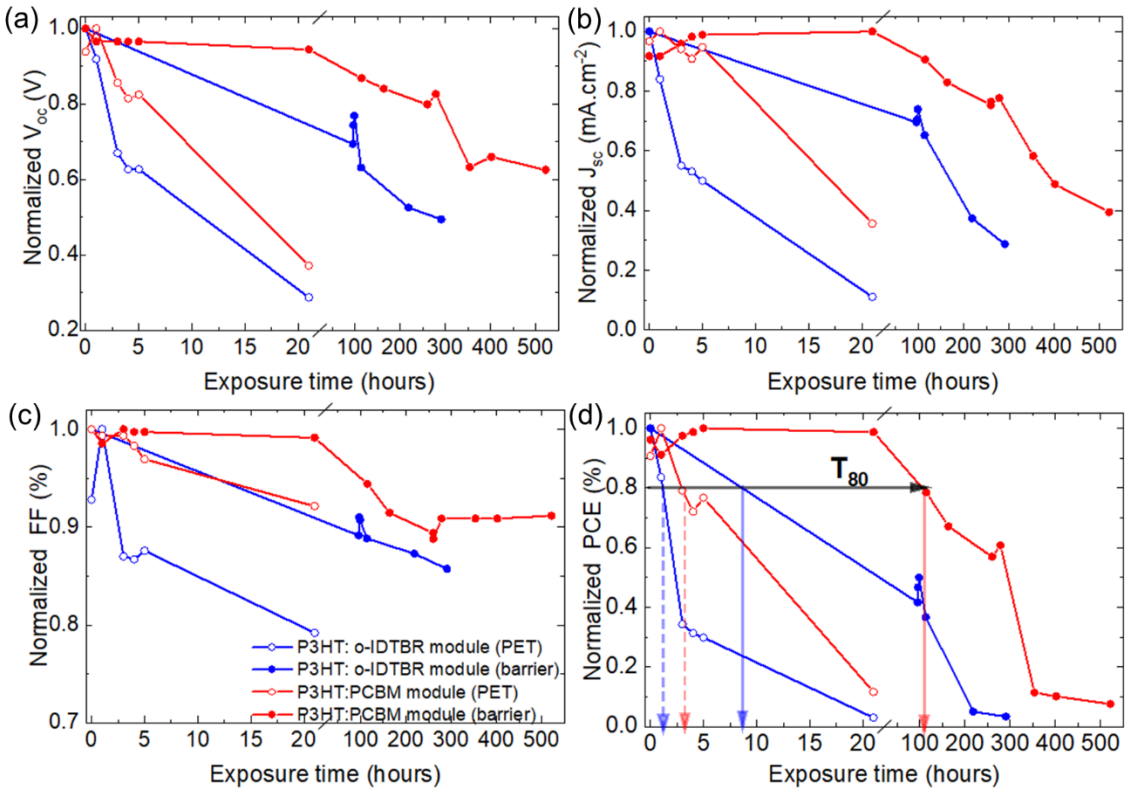

Fig. 6.2 The normalized evolution with time of the photovoltaic parameters of the degraded P3HT:o-IDTBR modules in blue and P3HT: PCBM modules in red with PET and with barrier foil.

As shown in Figure 6.2, the degraded modules suffered from the reduction of J_{sc} and V_{oc}. The reduction of J_{sc} can be caused by several factors, such as low charge extraction and the increase in the trap states. The fill factor of the modules is also reduced after exposing the modules to light, being the decrease of the FF of modules encapsulated with PET faster than in the modules encapsulated with barrier foil.

These findings ascribed the importance of encapsulation for the OPV modules. Indeed, the encapsulated solar cell with barrier foil took 120 and 31 hours to degrade by more than 20% for P3HT: PCBM and P3HT:o-IDTBR modules, respectively, under continuous illumination. The PET encapsulated modules exhibited T_{80} of less than 3 hours, and got totally degraded after 21 hours.

This observation correlates the role of external ambient conditions in the degradation process of OPV modules such as oxygen or water. While in PET encapsulated modules both extrinsic and intrinsic factors have been observed, in modules encapsulated with barrier foil

could be dominated by intrinsic or photoinduced related factors. That opens the question of what is the source of degradation? Since both modules were degraded but in different rates, it is plausible that the combination of oxygen and light result in photooxidation and the subsequent degradation. In fact, these two agents induce the photo oxidation of the photoactive layer materials. Oxygen can react with either the donor or the acceptor to create trap states that hinder the photogenerated current [47]. For the case of fullerenes, PCBM has been reported to play a role to stabilize polymers in the PAL in the OPV device [48,49]. This stabilization is based on two aspects: exciton quenching and radical scavenging. The exciton quenching hinders the excited singlet state and the triplet states lifetime by transferring the electron to PCBM. The triplet states have longer lifetime, which is in favour to the reaction with the singlet oxygen that is the first step in the photo-oxidation of P3HT films [50]. However, PCBM has high intersystem crossing that could lead the degradation of other polymers. It is also reported that fullerenes can scavenge oxygen-cantered radicals[51,52] that are produced by UV-exposure in the surface of the ZnO ETL.

To deepen our understanding of the mechanisms behind the photo degradation, we have measured the EQE of the modules before and after different time intervals of light exposure. The normalized EQE measurements of the modules are shown in Figure 6.3. For reference, the main absorption bands of PCBM, P3HT and o-IDTBR are marked as shadows of colours green, pink and purple, respectively. For P3HT: PCBM modules, encapsulated with PET, degradation causes a decrease in the spectrum intensity right from the first hours, but with no change in the shape. Starting from that moment, donor and acceptor-related peaks decrease in intensity. For the modules based on P3HT:o-IDTBR encapsulated with PET foil both peaks of P3HT and o-IDTBR are hindered after three hours of illumination, while in case of modules based on P3HT:o-IDTBR encapsulated with barrier foil the shape of the spectrum does not significantly change during the exposure time, but the integrated current does. The EQE trends are in good agreement with the solar cell efficient trends (Fig. 6.2), namely the modules encapsulated by barrier foils were active for longer time than the modules encapsulated with only PET foils. This is mainly due to the lower amount of oxygen and water penetrating to the modules that slows the degradation of the photoactive layer. In addition, the EQE spectrum showed lower intensity upon degradation, but the shape remains the same. Therefore, the absorption capacity of both donor and acceptor is affected at the same rate. From EQE we can tell that the absorption is not significantly changing, but the charge generation/collection decreases significantly upon degradation.

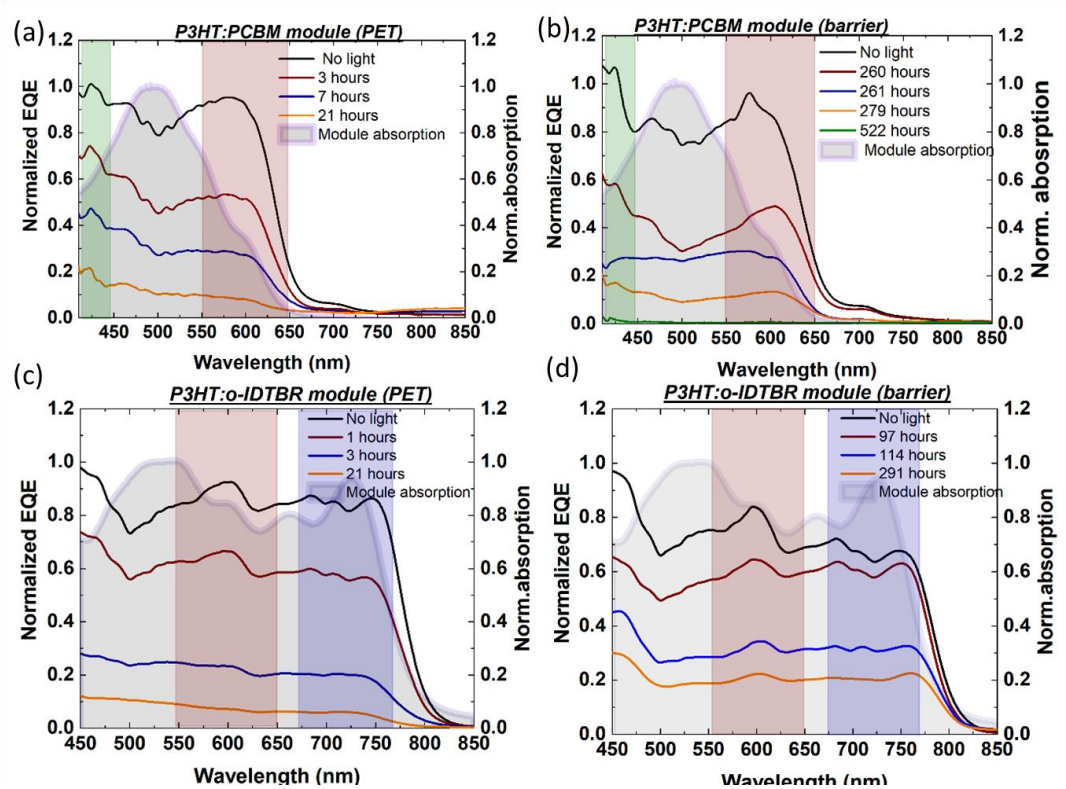

Figure 6.3 The normalized EQE before (black) and after exposing the modules to light for different periods in the climatic chamber (a) P3HT: PCBM (PET), (b) P3HT: PCBM (barrier), (c) P3HT:o-IDTBR (PET) and (d) P3HT:o-IDTBR(barrier), pink square marks the spectral region where the P3HT have strong absorption peaks, green square marks the corresponding for PCBM and the purple square marks the interesting area for o-IDTBR.

6.3 Degradation induced by thermal treatment

Aside to the light induced factors, thermally induced changes could also play a role in the module degradation process. Since modules were exposed to both light irradiation and temperature during the degradation experiment in the climatic chamber, we considered interesting to verify whether the temperature was having any effects on the performance of the modules. To study this possibility, the temperature inside the climatic chamber was set to 24ºC and a thermocouple was fixed directly above the module to monitor the temperature during the light exposure time. We observed that the temperature was slightly above 30 ºC. This measurement could, however, have issues with the thermal contact resistance and thus we designed a different experiment to double check.

Indeed, in order to determine the real temperature of the module exposed to the solar simulator, an infrared camera was used to measure the temperature of the module while illuminating the modules and the corresponding efficiency was recorded[53]. The relation between module efficiency and its temperature is shown in Figure 6.4.

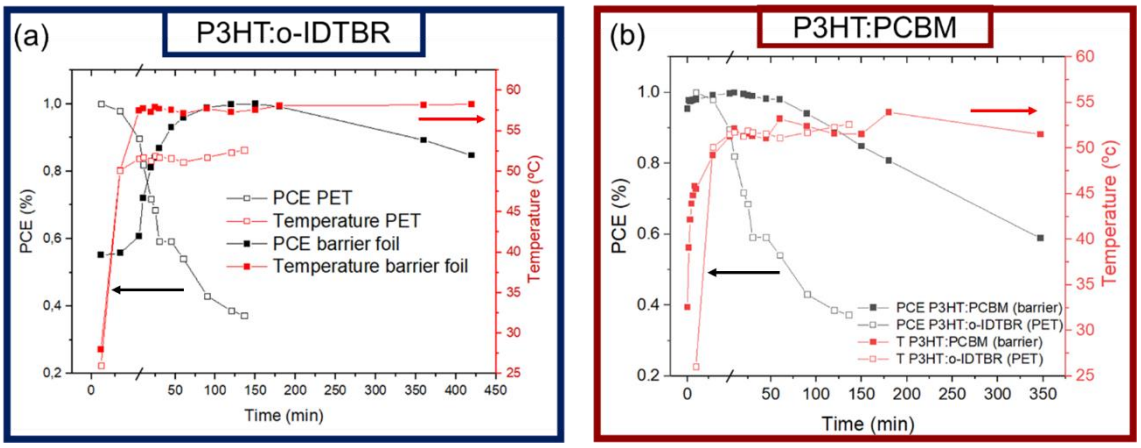

Figure 6.4 (a) Relationship between efficiency and temperature of P3HT:o-IDTBR modules encapsulated with PET and barrier foil and (b) relationship between efficiency and temperature of P3HT: PCBM modules encapsulated with PET and barrier foil.

The first observation is that, upon illumination, the modules rise their temperature up to 50-55 ºC. This is consistent with previous publications[53]. On the other hand, we observe the same behaviour for modules based on the two different active layer materials and encapsulated with PET, in which the efficiency strongly decreases by increasing the temperature. On the other hand, the modules encapsulated with barrier foil exhibit an efficiency raise after the temperature increases and a later decrease while the exposure is maintained. The initial increase in the efficiency is probably associated to an enhancement of the charge transport and carrier extraction[43] due to an increase in the crystallization, although we cannot rule out the activation of the ZnO with UV illumination. It can also be related to the fact that hot OPV tend to exhibit higher efficiencies compared to measurements performed at room temperature due to the thermally induced hopping transport[53]. Further experiments on the reversibility of the different effects would clarify this.

In general terms, the fact that the outcome of the experiment above depends on the encapsulation material, suggest that the external factors are the major source of degradation. We hypothesize that charge traps are originated by the presence of oxygen and water in the environment and their formation is accelerated either by the illumination or by the increase in the temperature which is responsible for deteriorating the performance of the modules. According to the literature, electron trapping affects the charge transport that in accordance decrease the photogenerated current and FF, and is also associated with non-radiative recombination that is responsible for decreasing the V_{oc} and hence the whole performance of the devices[46][54] [55]. Therefore, in our case, we can tentatively assign the decrease in the PCE to the formation of charge traps induced by the diffusion of oxygen towards the active layer and to the degradation of the interfacial contacts that is accelerated by the temperature increase. We note that we cannot fully discard phase separation in the photoactive layer (vide infra).

To further characterize and understand the cause and effect of degradation in the modules, we have undertaken spectroscopic characterization of the samples. Up to now, most of the studies in the literature have been related to the P3HT, so that further studies are needed to understand the role of PCBM and o-IDTBR, interlayers and electrodes in device degradation.

6.4 LBIC and PL characterization

To further elucidate the effect of photo degradation on local change of OPV device performance, non-destructive imaging characterizations like LBIC and PL measurements are done to determine the defects induced by the process of degradation and correlate the loss in device performance with local changes in device behaviour.

The LBIC technique allows mapping the charge collection resulting from the photovoltaic effect since it locally scans the modules and reveals information about the extracted current when the module is scanned by the laser beam [56,57]. Such technique is used for investigating several parameters, such as processing parameters [58], electrode materials [59], and moisture diffusion inside the devices during degradation [60].

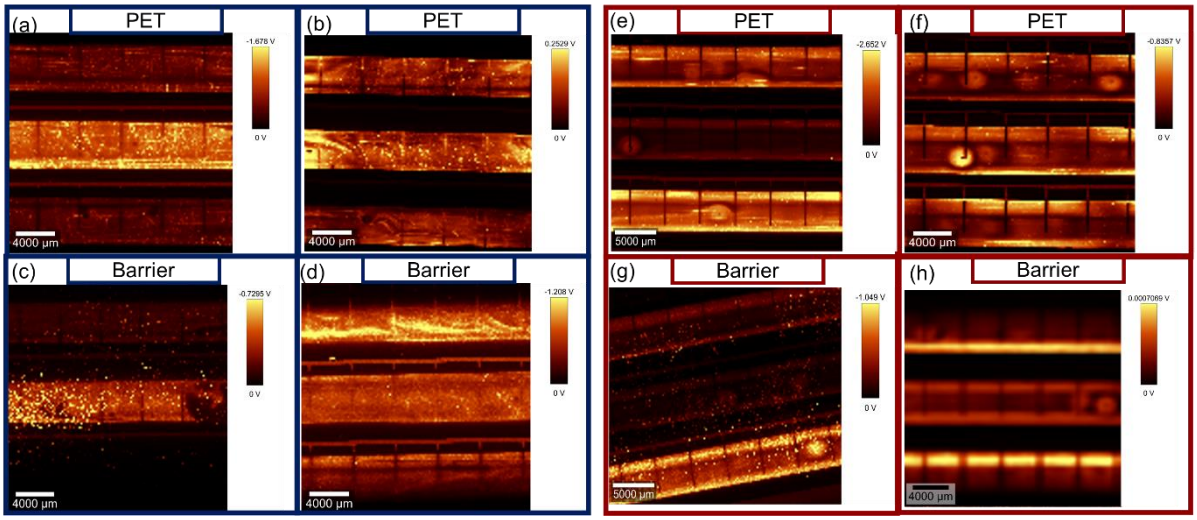

Figure 6.5 LBIC photocurrent mapping of (a) fresh P3HT:o-IDTBR module (PET), (b) degraded P3HT:o-IDTBR module (PET) after exposing to light for 21 hours in climatic chamber, c) fresh P3HT:o-IDTBR module (barrier), (d) degraded P3HT:o-IDTBR module (barrier) after exposing to light for 339 hours in climatic chamber, (e) fresh P3HT:PCBM module(PET), (f) degraded P3HT:PCBM module (PET) after exposing to light for 21 hours in climatic chamber, (g) fresh P3HT:PCBM module (barrier) and (h) degraded P3HT:PCBM module (barrier) after exposing to light for 522 hours in climatic chamber. Note that scale bars are different in each image.

Figure 6.5 shows the LBIC mapping of the modules based on both fullerene and non-fullerene hetero-junctions encapsulated by barrier foil and only PET, before and after light exposure of 21 hours for PET modules, 291 hours for modules based on P3HT:o-IDTBR with barrier foil and 522 hours for modules based on P3HT: PCBM with barrier foil. One of the advantages of this non-destructive characterization technique is that it allows the evaluation of the printing defects of the whole module, which are difficult to detect by the performance measurements. Indeed, the variation of the current mapping of the three devices in fresh modules are ascribed to the printing quality of the module. This variation can be attributed to the inhomogeneity of the thickness of the active layer or to the different distancing of the meniscus guides to the main source of the ink injection in the slot die head. One appreciation is that each cell contributes unequally to the charge generation in the module. Another observation is that, in general, the areas below the silver electrode suffered a complete loss of current.

In general trend is: for the as deposited materials, we see that some of the cells are “dark”, i.e. they don´t contribute significantly to the photocurrent of the module, due to, likely, shunts. Degraded samples are, however, homogeneously degraded, i.e. all cells are degraded for each module producing the same small current each, but also the degradation

covers the whole area, so the gas uptake fully penetrates into the cell leading to degradation of the whole film or across the whole interface. On the other hand, the comparison of the fresh modules permits to observe that samples encapsulated with PET suffer more current losses than those protected by barrier foils. That is in agreement with the previous results confirming the higher degradation rate in the modules with PET encapsulation. In the case of the modules exposed to light for 21 hours and only protected with PET, the current loss was homogenously distributed along the different cells within the modules. In the case of the modules encapsulated with barrier foil, the P3HT:o-IDTBR heterojunction have a homogenous current loss along the whole device while in the case of degraded modules based on P3HT: PCBM hetero-junction the current loss was higher at the centre of each device. It is possible that the differentiation between the centre and the edges are due to the inhomogeneity of the thickness of the active layer and the presence of other layers like the HTL and ETL. Due to the series connection between the devices in one module, HTL does not cover the whole stripe (one device) and the regions where the HTL is coated might absorb the photons emitted by the active layer.

In addition, PEDOT: PSS is significant as highly acidic and hygroscopic lead to the corrosion to the ITO electrode. Indium is diffusing of to the PAL and therefore traps charge carriers[61–63]. Water diffusion to the device layers hinder the device stability [64]. Furthermore, water entry to the device from the edges via absorption by the PEDOT: PSS leading to the cathode oxidation, and J_{sc} reduction[65–67][68] [69].

The photoluminescence (PL) of the OPV modules has been investigated to help to elucidate the effects of light exposure in the degradation of the modules. PL spectra in the literature have been used to investigate the charge transfer rate to the electrode [70] and the degradation mechanism in OPV modules [58,71–73]. Macro PL characterization has been performed to the modules with the position for the corresponding LBIC measurement and Raman spectra in the following section.

The PL spectrum of the studied module based on P3HT: PCBM has a dominant peak at 724 nm and a secondary peak at 801nm. Both maxima are in correlation to the PL emission of the donor polymer reported in the literature [74]. In the case of module based on P3HT:o-IDTBR, there is one peak at 786 nm and a shoulder at 854 nm that suggest the overlapping of the signals from P3HT and o-IDTBR. All the measured PL peaks are listed in Table 6.3. As shown in Figure 6.6, after the degradation, the ratio in intensity between peaks changes, which is ascribed to the change in the molecular conformation [75]. The 0–0, 0–1 and 0-2 emission correspond to singlet emissions after inter-chain vibrational relaxation. This vibronic structure is an indicator of the delocalized excitons from interchain π-π stacking of the polymer chain, known as H-aggregates. Commonly, aggregation affect the interface between the donor and acceptor in the active layer, which hinder the exciton dissociation and enhance the non-radiative recombination in the device [76,77]. Thus, the induced aggregation in the polymer might be correlated to the change in the polymer crystallinity, and the subsequent reduction of exciton dissociation process in the degraded modules. This is in accordance with the voltage loss obtained in the photodegradation experiments.

It is observed that the degraded modules based on both P3HT:o-IDTBR and P3HT: PCBM show a large increase in the PL intensity compared to the fresh modules. The degraded modules encapsulated with barrier foil have less intensity variation than in case of modules encapsulated with PET. The PL intensity could be interrelated to the excitons generated in the active layer providing high PL intensity [78], while the low PL intensity indicate that the excitons are efficiently dissociated into charge carriers in the active layer or effective charge extraction by the charge transport layers or that excitons have a nonradiative recombination [55]. Therefore, the observed increase in PL intensity suggests a decrease in the exciton dissociation ability in the degraded modules, probably due to the increase in the phase separation between the donor and the acceptor. This can result in reduced photogenerated current, which is considered one of the main reasons for the initial photodegradation results from air-induced photodegradation process [79] [80]. The increase

in the PL intensity for modules-based on P3HT:o-IDTBR encapsulated with PET is due to the degradation of the o-IDTBR because of the generation of radicals in the surface of ZnO that are mitigated by the PCBM, unlike the case in modules based on P3HT: PCBM encapsulated with PET. The barrier foil contains UV filters; thus, the concentration of radicals is lower, and the PL intensity less than with PET.

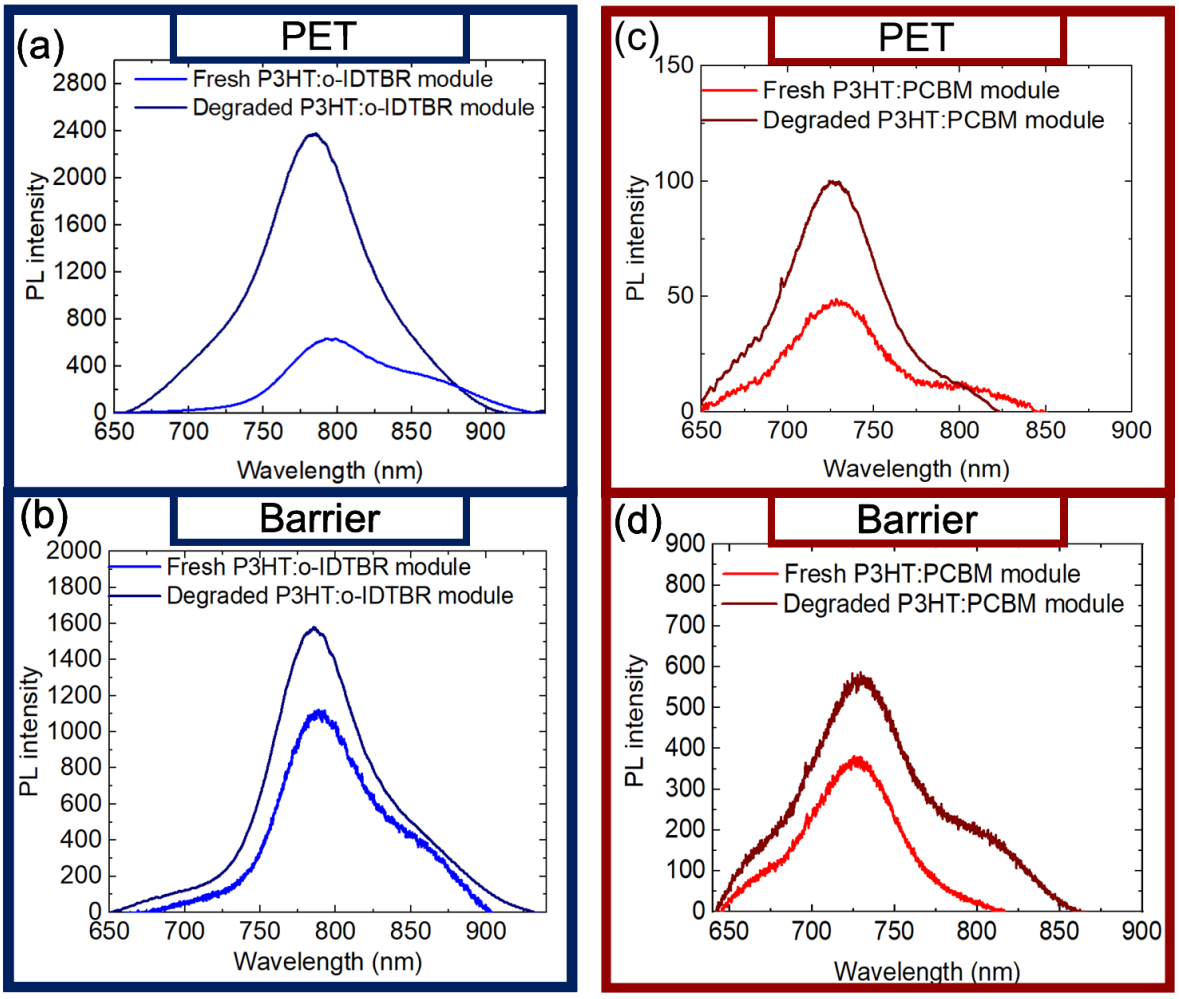

Figure 6.6 A) PL of both, the fresh P3HT:o-IDTBR module in blue and the degraded, exposed to light for 21 hours in climatic chamber, P3HT:o-IDTBR module in dark blue, encapsulated with PET,(B) PL of both, the fresh P3HT:o-IDTBR module in blue and the degraded, exposed to light for 339 hours in climatic chamber, P3HT:o-IDTBR module in dark blue, encapsulated with barrier, (C) the PL of the fresh P3HT:PCBM module in red and the degraded P3HT:PCBM module, exposed to light for 21 hours in climatic chamber, in dark red both encapsulated with PET and D) the PL of the fresh P3HT:PCBM module in red and the degraded P3HT:PCBM module, exposed to light for 522 hours in climatic chamber, in dark red both encapsulated with barrier foil.

Table 6.3 Photoluminescence peaks (in nm) measured for the modules.

Fresh P3HT: PCBM module (barrier)	Degraded P3HT: PCBM module (barrier)	Fresh P3HT: PCBM module (PET)	Degraded P3HT: PCBM module (PET)	Fresh P3HT: o-IDTBR module (barrier)	Degraded P3HT: o-IDTBR module (barrier)	Fresh P3HT: o-IDTBR module (PET)	Degraded P3HT: o-IDTBR module (PET)
725.3	724.8	725.5	724.4	786.3	787.8	786.1	787.4
801.8	801.3	801.3	800.2			854.0	859.7

6.5 Raman characterization

Raman technique is sensitive to the vibrations in the conjugated systems of C–C and C=C bonds and can detect the change in the conformational twisting and in the aggregation of the polymer chain [81–84]. When air diffuses into the active layer and the modules are exposed to light, the oxygen doping of the active layer induces a decrease in the performance of the module. Trap states are formed by oxygen interaction in the active layer that increases the hole concentration [85,86], in addition to polymer aggregation [80]. Therefore, for further understanding how the polymer reacts with oxygen atoms, a comparison of the Raman spectra between the fresh and the degraded modules has been performed. Average Raman spectra were obtained for the fresh and degraded modules based on both P3HT:o-IDTBR and P3HT: PCBM hetero junctions by exciting the modules with a laser source with a wavelength of 488 nm, a power of 10 mW, a grating of 1200 g/mm and excitation area 576 mm^2. Exciting at this wavelength, we are performing resonant experiments mainly for the donor.

Figure 6.7 shows the obtained Raman spectra with the stretching mode of C=C at 1450 cm^{-1}, the C–C one at 1379 cm^{-1} and other features located at 1202 cm^{-1} assigned to C–C stretch mode, 1183 cm^{-1} assigned to C–C stretch with the C–H bending mode, and 726 cm^{-1} assigned to the C–S–C deformation mode. The main changes observed between the fresh and the degraded modules are: (1) shift of thiophene C-C stretch peak at 1450 cm^{-1} (see Table 6.4) in fresh modules toward higher wavenumbers in the degraded modules that is characteristic of the oxidised state of P3HT, (2) reduction in the main peak intensity and (3) the intensity reduction of the degraded modules based on P3HT:o-IDTBR heterojunction that are higher than the intensity reduction in case of the degraded modules based on P3HT:PCBM heterojunction, suggesting that the PCBM stabilizes the polymer more than o-IDTBR.

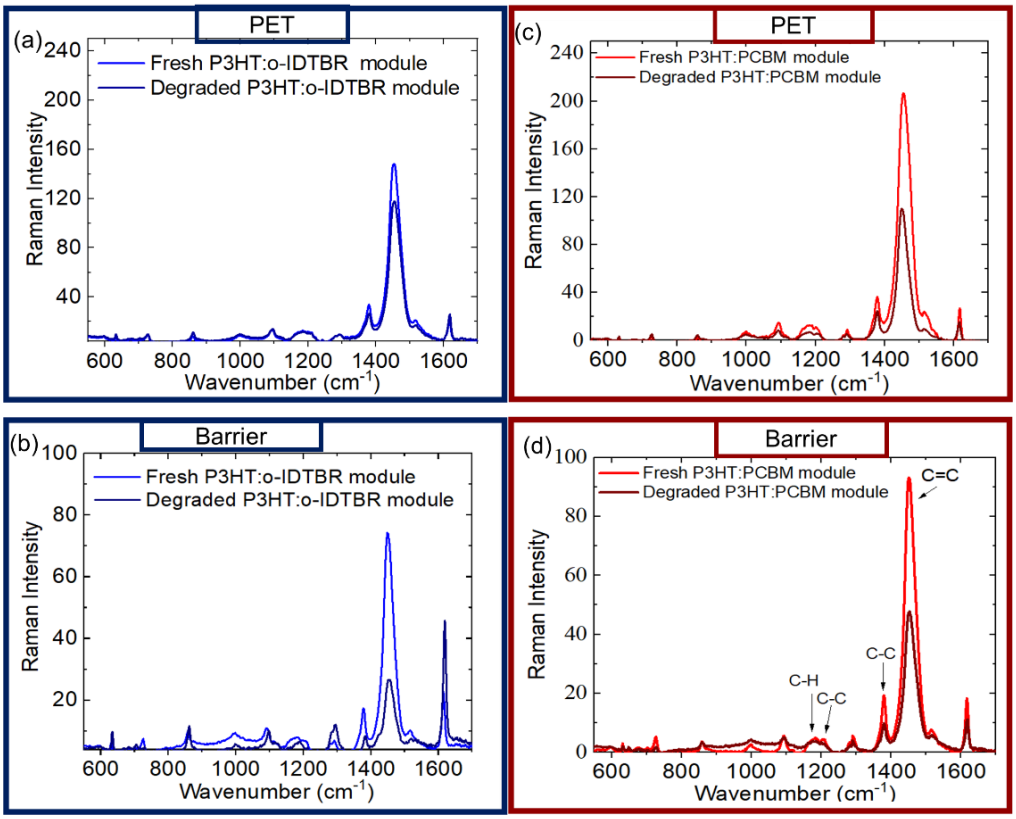

Figure 6.7 The average Raman spectra of the whole (a) P3HT:o-IDTBR module (PET) in blue and degraded P3HT:o-IDTBR module (PET) in dark blue after exposing to light for 21 hours in climatic chamber (b) P3HT:o-IDTBR module (barrier) in blue and degraded P3HT:o-IDTBR module (barrier) in dark blue after exposing to light for 339 hours in climatic chamber, (c) P3HT:PCBM module (barrier) in red and degraded P3HT:PCBM module (barrier) in dark red after exposing to light for 21 hours in climatic chamber and (d) P3HT:PCBM module (barrier) in red and degraded P3HT:PCBM module (barrier) in dark red after exposing to light for 522 hours in climatic chambe, peaks for reference materials were considered from the reported literature[87–89].

The up shift of the peaks indicates that the C-C bonds of the thiophene unit are vibrating at higher frequencies during the degradation. This change could be a result of the crystallization process induced by heating[90]. The formation of oxygen-related defect states in P3HT during the photooxidation process of the polymer donor that has been identified as a source of photocurrent loss [91]. Photodegradation leads to the oxidation of the thiophene backbone, breaking the polymer conjugation which results in the loss of the polymer crystallinity and hence the reduction of the absorption ability of the polymer [92]. This process is called bleaching of the active layer and results in the reduction in the photogenerated current of the degraded modules. Furthermore, the appearance of this shift is also observed when comparing the fresh modules encapsulated with barrier and the fresh modules encapsulated with PET. In the case of the modules encapsulated with PET foil, air diffusion is easily achieved and there is a certain degree of degradation that is not observed in the modules protected with a barrier foil.

These findings revealed that the photodegradation has two steps; first is the initial step of degradation, which is followed by reductions in absorption[93]. [94,95]. The diffusion of oxygen and water accompanied with light exposure enhances chemical degradation of the organic layers and interfaces, which deteriorate the photovoltaic performance[96]. The photooxidation of the PAL results in bleaching, change in the energy levels, reduction in charge carrier mobilities and aggregation of fullerene domains [85]. In addition, the oxidation

of PAL leads to an increase in the electronic traps that reduces the FF and V_{oc} of a device[97,98]. Not only the active layer but also the cathode oxidized due to presence of oxygen caused in S shaped I-V curve. The ease diffusion of oxygen and water assets via pinholes and voids in the metal layer to the module layers[66].

Table 6.4 Raman peaks (in cm^{-1}) measured for the modules.

Fresh P3HT: PCBM module (barrier)	Degraded P3HT: PCBM module (barrier)	Fresh P3HT: PCBM module (PET)	Degraded P3HT: PCBM module (PET)	Fresh P3HT: o-IDTBR module (barrier)	Degraded P3HT: o-IDTBR module (barrier)	Fresh P3HT: o-IDTBR module (PET)	Degraded P3HT: o-IDTBR module (PET)
631	631	631	631	631	634	632	632
727	727	727	727	726	729	725	727
859	857	859	857	858	862	860	862
1093	1093	1093	1092	998	997	997	997
1183	1187	1182	1182	1090	1097	1094	1096
1203	1201	1201	1203	1184	1189	1184	1184
1290	1290	1291	1290	1292	1292	1292	1293
1379	1379	1379	1379	1378	1383	1379	1381
1451	1452	1454	1449	1449	1453	1454	1456
1515	1517	1515	1513	1517	1518	1517	1518
1617	1618	1619	1617	1615	1619	1617	1619
1660	1658	1655	1656	1679	1680	1680	1680
1729	1730	1729	1729	1729	1730	1730	1730
1842	1842	1842	1842				

6.6 EPR spectroscopy

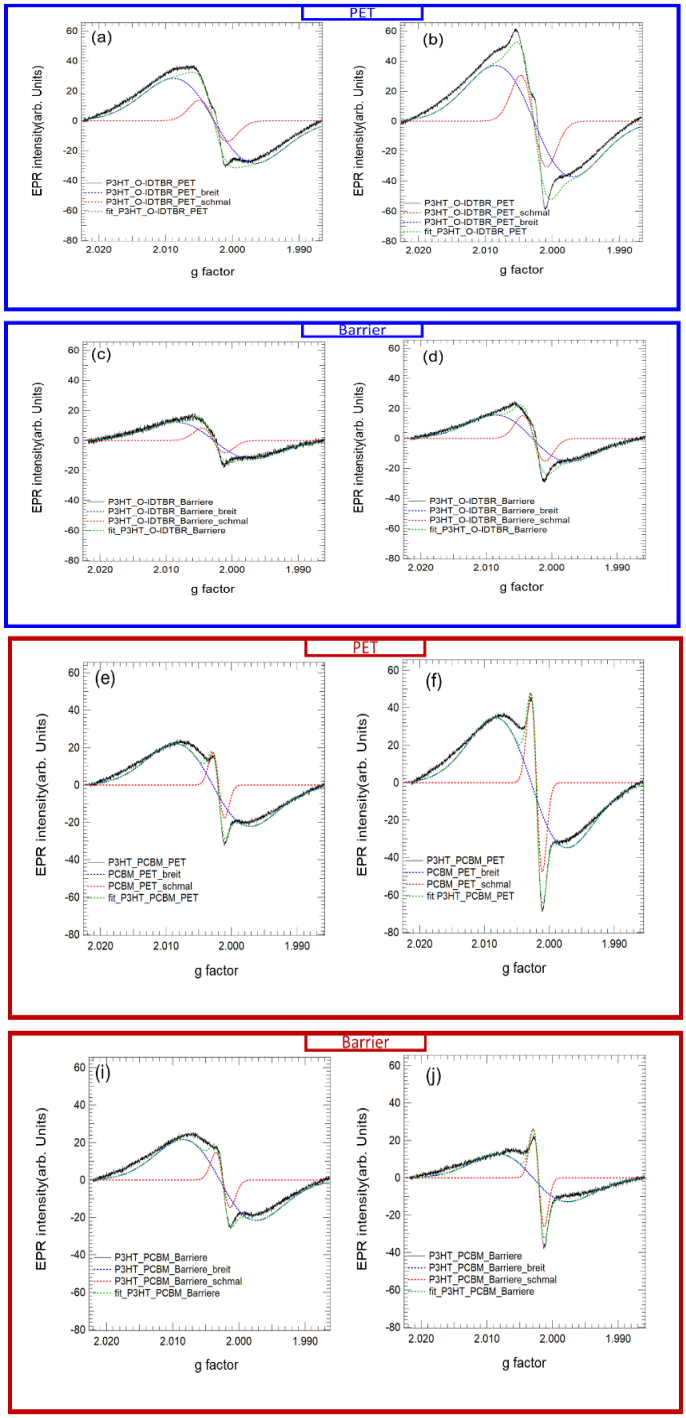

Figure 6.8 EPR results for OPV modules, degraded in a climate chamber under constant illumination. The spectrum consists of the whole signal in black and its fit in green that consist of broad peak in blue and narrow peak in red of (a) fresh module based on P3HT:o-IDTBR encapsulated with PET,(b) degraded modules based on P3HT:o-IDTBR encapsulated with PET, (c) fresh module based on P3HT:o-IDTBR encapsulated with barrier foil, (d) degraded modules based on P3HT:o-IDTBR encapsulated with barrier foil, (e) fresh module based on P3HT:PCBM encapsulated with PET, (f) degraded modules based on P3HT:PCBM encapsulated with PET, (i) fresh module based on P3HT:PCBM encapsulated with barrier foil and (j) degraded module based on P3HT:PCBM encapsulated with barrier.

The EPR spectra of all the modules, fresh and degraded, are shown in Figure 6.8. This measurement has been carried out by Yannis in the university of Wurzburg. As it can be seen from the figure, the obtained spectrum consists of two overlapping signals, which can be fitted by first-derivative Gaussians to two signals; The narrow signal (red lines) is attributed to $P3HT^{+}/P3HT{:}O_2^{-}$ complex, as supported by literature [86,99,100]. P3HT is known to form $P3HT^{+}/P3HT{:}O_2^{-}$ complexes that are also referred to as environmental p-doping. By $P3HT^{+}$-we refer to the polaron, a quasiparticle that is mobile at ambient temperatures, while the $P3HT{:}O_2^{-}$-complex is a charge trap and recombination centre. To clarify the origin of the broad peak, reference measurements on modules without active layer (structure PET/ITO/AZO/HTL) and furthermore without HTL (structure PET/ITO/AZO) were measured and shown in Figure 6.9.

The small EPR peak seen in the PET/ITO/AZO structure was assigned to the O^{*} oxygen vacancy of the ZnO, and the intensity of this peak is known to increase by doping with aluminium[101,102]. The measurement of the PET/ITO/AZO/HTL sample shows a broad signal that can be assigned to PEDOT: PSS by comparing with the PET/ITO/AZO sample.. EPR signals for PEDOT:PSS are known in literature and are assigned to positive charges on the PEDOT chain [103,104]. Interestly, it has been reported that the number of positive charges on the PEDOT: PSS polymer chain increases by increasing temperature[103].

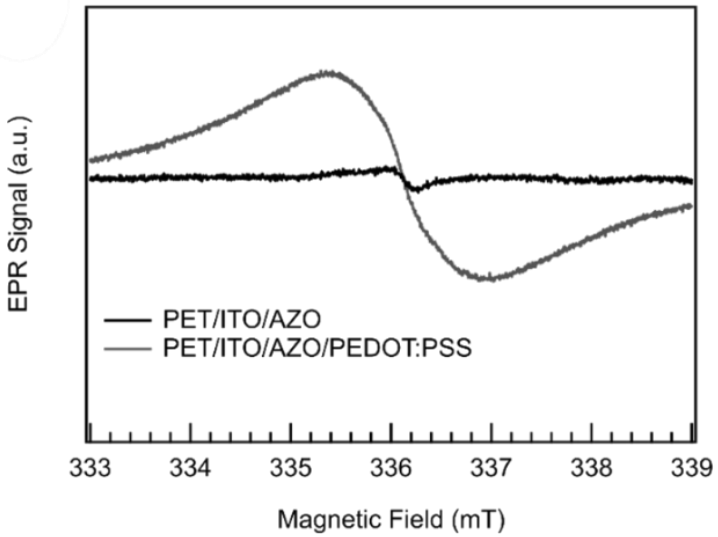

Figure 6.9 EPR results for devices without the active layer. a) EPR signal for modules with PET/ITO/AZO (black) and PET/ITO/AZO/HTL (grey), revealing the HTL PEDOT: PSS as origin of the broad EPR signal.

The signal intensities and thus the spin concentrations of the narrow signal ascribed to P3HT increase considerably with extended time of module light exposure in the climatic chamber (Figure 6.10) indicating an enhancement in the concentration of P3HT radicals. Herby, the encapsulation with barrier foil is far more effective than standard PET-foil as can be concluded from the observed spin concentrations in the active layer and in agreement with the device data. However, modules with the acceptor o-IDTBR showed a higher spin count (integrated area under the red curve) for pristine and degraded modules than those with PCBM. This observation is consistent with other NFA-based blends, since photoexcitation or charge transfer produce mobile electrons on the NFA that are energetically able to transfer to O_2 to form $O_2^{\cdot-}$ radicals [99] that contribute to the degradation of the donor polymer. On the other hand, as mentioned earlier, the PCBM has been reported to stabilize many conjugated polymers in the photoactive layer in the OPV device[48,49].

Variation in signal intensity or spin concentration of the hole transport layer PEDOT: PSS upon extended time in the climatic chamber does not show a clear trend (Figure 6.10(b)), beside the fact that the modules encapsulated by PET show higher spin concentration than those protected with barrier foils, supporting again the fact that the barrier foil acts as a better protective layer. The hygroscopic PEDOT: PSS enhance the absorption of water to diffuse through the whole device. The phase separation in PEDOT:PSS is reported to increase the interfacial degradation via oxygen and water [105]. The oxidized metal layer and the phase separated photoactive layer cause less interface between the electron donor and the electron acceptor that affect the charge dissociation negatively and therefore the module performance [85].

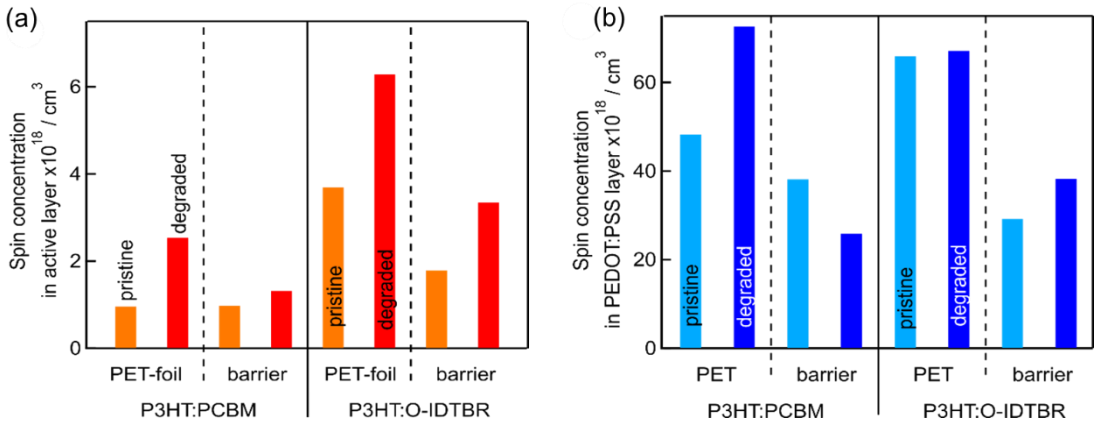

Figure 6.10. (a) Spin concentration in the active layer of OPV modules based on P3HT: PCBM and P3HT:o-IDTBR, pristine (orange) and after degradation (red). The spin count in the degraded modules is increased, while it is also higher in modules with PET-foil as encapsulation and with O-IDTBR as acceptor, (b) Spin concentration in PEDOT: PSS layer, pristine (light blue) and after degradation (dark blue). Upon degradation, there is no visible trend in radical buildup.

6.7 Conclusion

In this chapter, we presented a complete investigation of the degradation sources in solar modules, with the aim of deepening our understanding on the process in order to improve their lifetime. We have presented spectroscopic and imaging characterization of fresh and degraded modules based on FA and NFA heterojunctions prepared by roll-to-roll processing technique. It has been demonstrated that the barrier foil increased the lifetime of the modules in comparison to the PET encapsulation presumably due to the slower diffusion of the oxygen and water, as well as UV protection. PCBM showed more stabilization when it is blended to the polymer P3HT than in case of blending to the o-IDTBR. Devices data showed T80 of 120h,3h ,31h, and 1h for the P3HT: PCBM modules encapsulated with barrier, PET, P3HT:o-IDTBR modules encapsulated with barrier and PET, respectively. EQE experiments showed a homogeneous decrease in photocurrent without much spectral change, suggesting not significant change in absorption upon degradation. Thermal experiments indicated that samples get 30-35ºC hotter upon illumination, which results in an initial increase in efficiency for the barrier encapsulated devices followed by degradation caused from the morphological change. Raman spectra showed that there is some degree of chemical degradation of the active layer. Raman shifts suggest increased crystallinity, which

might be associated to phase separation. PL data strongly agreed with this. LBIC showed that degradation is homogeneous in all the devices, and throughout the whole device area (rather than pinhole like). EPR spectrum shows the role of the PEDOT: PSS and the active layer in the chemical degradation process.

In general conclusion, barrier foil much better than PET encapsulation, and P3HT: PCBM more stable than o-IDTBR based modules. We have also seen that PCBM plays a protective role of the P3HT that extends the lifetime of the encapsulated modules 200 hours more than with the popular NFA o-IDTBR.

6.8 References for Chapter 6

[1] M.C. Scharber, N.S. Sariciftci, Efficiency of bulk-heterojunction organic solar cells, Prog. Polym. Sci. 38 (2013) 1929–1940. https://doi.org/10.1016/j.progpolymsci.2013.05.001.

[2] R. Shivanna, S. Shoaee, S. Dimitrov, S.K. Kandappa, S. Rajaram, J.R. Durrant, K.S. Narayan, Charge generation and transport in efficient organic bulk heterojunction solar cells with a perylene acceptor, Energy Environ. Sci. 7 (2014) 435–441. https://doi.org/10.1039/c3ee42484g.

[3] Y. Liu, J. Zhao, Z. Li, C. Mu, W. Ma, H. Hu, K. Jiang, H. Lin, H. Ade, H. Yan, Aggregation and morphology control enables multiple cases of high-efficiency polymer solar cells, Nat. Commun. 5 (2014). https://doi.org/10.1038/ncomms6293.

[4] M.A. Green, E.D. Dunlop, J. Hohl-Ebinger, M. Yoshita, N. Kopidakis, X. Hao, Solar cell efficiency tables (Version 58), Prog. Photovoltaics Res. Appl. (2021) 657–667. https://doi.org/10.1002/pip.3444.

[5] H. Zhou, Y. Zhang, C.K. Mai, S.D. Collins, G.C. Bazan, T.Q. Nguyen, A.J. Heeger, Polymer homo-tandem solar cells with best efficiency of 11.3%, Adv. Mater. 27 (2015) 1767–1773. https://doi.org/10.1002/adma.201404220.

[6] J. You, L. Dou, K. Yoshimura, T. Kato, K. Ohya, T. Moriarty, K. Emery, C.C. Chen, J. Gao, G. Li, Y. Yang, A polymer tandem solar cell with 10.6% power conversion efficiency, Nat. Commun. 4 (2013) 1410–1446. http://dx.doi.org/10.1038/ncomms2411.

[7] X. Ma, W. Gao, J. Yu, Q. An, M. Zhang, Z. Hu, J. Wang, W. Tang, C. Yang, F. Zhang, Ternary nonfullerene polymer solar cells with efficiency >13.7% by integrating the advantages of the materials and two binary cells, Energy Environ. Sci. 11 (2018) 2134–2141. https://doi.org/10.1039/c8ee01107a.

[8] R.A.J. Janssen, J. Nelson, Factors limiting device efficiency in organic photovoltaics, Adv. Mater. 25 (2013) 1847–1858. https://doi.org/10.1002/adma.201202873.

[9] Y. Cai, Y. Li, R. Wang, H. Wu, Z. Chen, J. Zhang, Z. Ma, X. Hao, Y. Zhao, C. Zhang, F. Huang, Y. Sun, A Well-Mixed Phase Formed by Two Compatible Non-Fullerene Acceptors Enables Ternary Organic Solar Cells with Efficiency over 18.6%, Adv. Mater. 33 (2021) 1–9. https://doi.org/10.1002/adma.202101733.

[10] V. Turkovic, S. Engmann, N. Tsierkezos, H. Hoppe, M. Madsen, H.G. Rubahn, U. Ritter, G. Gobsch, Long-term stabilization of organic solar cells using hydroperoxide decomposers as additives, Appl. Phys. A Mater. Sci. Process. 122 (2016). https://doi.org/10.1007/s00339-016-9758-7.

[11] J. You, L. Dou, K. Yoshimura, T. Kato, K. Ohya, T. Moriarty, K. Emery, C.C. Chen, J. Gao, G. Li, Y. Yang, A polymer tandem solar cell with 10.6% power conversion efficiency, Nat. Commun. 4 (2013) 1–10. https://doi.org/10.1038/ncomms2411.

[12] N.F. Chalabi, A. Guen-Bouazza, Polymer/fullerene bulk heterojunction solar cells, EEA - Electroteh. Electron. Autom. 67 (2019) 5–12.

[13] M. Azzouzi, A study of the degradation of organic solar cells, 2016.

[14] S. Rafique, S.M. Abdullah, K. Sulaiman, M. Iwamoto, Fundamentals of bulk

heterojunction organic solar cells: An overview of stability/degradation issues and strategies for improvement, Renew. Sustain. Energy Rev. 84 (2018) 43–53. https://doi.org/10.1016/j.rser.2017.12.008.
[15] N. Grossiord, J.M. Kroon, R. Andriessen, P.W.M. Blom, Degradation mechanisms in organic photovoltaic devices, Org. Electron. 13 (2012) 432–456. https://doi.org/10.1016/j.orgel.2011.11.027.
[16] E.M. Speller, A.J. Clarke, N. Aristidou, M.F. Wyatt, L. Francàs, G. Fish, H. Cha, H.K.H. Lee, J. Luke, A. Wadsworth, A.D. Evans, I. McCulloch, J.S. Kim, S.A. Haque, J.R. Durrant, S.D. Dimitrov, W.C. Tsoi, Z. Li, Toward improved environmental stability of polymer: Fullerene and polymer:Nonfullerene organic solar cells: A common energetic origin of light- A nd oxygen-induced degradation, ACS Energy Lett. 4 (2019) 846–852. https://doi.org/10.1021/acsenergylett.9b00109.
[17] D. Georgiou, S. Logothetidis, High-barrier films for flexible organic electronic devices, in: Handb. Flex. Org. Electron. Mater. Manuf. Appl., Woodhead Publishing, 2015: pp. 123–142. https://doi.org/10.1016/B978-1-78242-035-4.00005-1.
[18] W.R. Mateker, M.D. McGehee, Progress in Understanding Degradation Mechanisms and Improving Stability in Organic Photovoltaics, Adv. Mater. 29 (2017). https://doi.org/10.1002/adma.201603940.
[19] S. Pont, S. Osella, A. Smith, A. V. Marsh, Z. Li, D. Beljonne, J.T. Cabral, J.R. Durrant, Evidence for Strong and Weak Phenyl-C61-Butyric Acid Methyl Ester Photodimer Populations in Organic Solar Cells, Chem. Mater. 31 (2019) 6076–6083. https://doi.org/10.1021/acs.chemmater.8b05194.
[20] T. Yang, M. Wang, C. Duan, X. Hu, L. Huang, J. Peng, F. Huang, X. Gong, Inverted polymer solar cells with 8.4% efficiency by conjugated polyelectrolyte, Energy Environ. Sci. 5 (2012) 8208–8214. https://doi.org/10.1039/c2ee22296e.
[21] Z. He, B. Xiao, F. Liu, H. Wu, Y. Yang, S. Xiao, C. Wang, T.P. Russell, Y. Cao, Single-junction polymer solar cells with high efficiency and photovoltage, Nat. Photonics. 9 (2015) 174–179. https://doi.org/10.1038/nphoton.2015.6.
[22] P. Cheng, J. Hou, Y. Li, X. Zhan, Layer-by-layer solution-processed low-bandgap polymer-PC61BM solar cells with high efficiency, Adv. Energy Mater. 4 (2014). https://doi.org/10.1002/aenm.201301349.
[23] W. Ma, J.R. Tumbleston, L. Ye, C. Wang, J. Hou, H. Ade, Quantification of nano- and mesoscale phase separation and relation to donor and acceptor quantum efficiency, Jsc, and FF in polymer:Fullerene solar cells, Adv. Mater. 26 (2014) 4234–4241. https://doi.org/10.1002/adma.201400216.
[24] Y. Sun, G.C. Welch, W.L. Leong, C.J. Takacs, G.C. Bazan, A.J. Heeger, Solution-processed small-molecule solar cells with 6.7% efficiency, Nat. Mater. 11 (2012) 44–48. https://doi.org/10.1038/nmat3160.
[25] W. Chen, Y. Wu, J. Liu, C. Qin, X. Yang, A. Islam, Y.B. Cheng, L. Han, Hybrid interfacial layer leads to solid performance improvement of inverted perovskite solar cells, Energy Environ. Sci. 8 (2015) 629–640. https://doi.org/10.1039/c4ee02833c.
[26] T.E. Zachariah A. Page,* Yao Liu,* Volodimyr V. Duzhko,† Thomas P. Russell, Fulleropyrrolidine interlayers:Tailoring electrictrodes to raise organic solar cell efficiency, Science (80-.). 346 (2014) 441–444. https://doi.org/10.1126/science.1255826.
[27] Z. Yin, J. Wei, Q. Zheng, Interfacial Materials for Organic Solar Cells: Recent Advances and Perspectives, Adv. Sci. 3 (2016) 1–37. https://doi.org/10.1002/advs.201500362.
[28] M. Sun Ryu, H. Jin Cha, J. Jang, Improvement of operation lifetime for conjugated polymer:fullerene organic solar cells by introducing a UV absorbing film, Sol. Energy Mater. Sol. Cells. 94 (2010) 152–156. https://doi.org/10.1016/j.solmat.2009.08.011.
[29] P. Cheng, X. Zhan, Stability of organic solar cells: Challenges and strategies, Chem. Soc. Rev. 45 (2016) 2544–2582. https://doi.org/10.1039/c5cs00593k.
[30] M. Jørgensen, K. Norrman, S.A. Gevorgyan, T. Tromholt, B. Andreasen, F.C. Krebs, Stability of polymer solar cells, Adv. Mater. 24 (2012) 580–612.

https://doi.org/10.1002/adma.201104187.
[31] F.C. Krebs, Encapsulation of polymer photovoltaic prototypes, Sol. Energy Mater. Sol. Cells. 90 (2006) 3633–3643. https://doi.org/10.1016/j.solmat.2006.06.055.
[32] C. Lungenschmied, G. Dennler, H. Neugebauer, S.N. Sariciftci, M. Glatthaar, T. Meyer, A. Meyer, Flexible, long-lived, large-area, organic solar cells, Sol. Energy Mater. Sol. Cells. 91 (2007) 379–384. https://doi.org/10.1016/j.solmat.2006.10.013.
[33] S. Schuller, P. Schilinsky, J. Hauch, C.J. Brabec, Determination of the degradation constant of bulk heterojunction solar cells by accelerated lifetime measurements, Appl. Phys. A Mater. Sci. Process. 79 (2004) 37–40. https://doi.org/10.1007/s00339-003-2499-4.
[34] G. Dennler, C. Lungenschmied, H. Neugebauer, N.S. Sariciftci, A. Labouret, Flexible, conjugated polymer-fullerene-based bulk-heterojunction solar cells: Basics, encapsulation, and integration, J. Mater. Res. 20 (2005) 3224–3233. https://doi.org/10.1557/jmr.2005.0399.
[35] W.J. Potscavage, S. Yoo, B. Domercq, B. Kippelen, Encapsulation of pentacene/C 60 organic solar cells with Al 2O 3 deposited by atomic layer deposition, Appl. Phys. Lett. 90 (2007) 2005–2008. https://doi.org/10.1063/1.2751108.
[36] B. Ray, M.A. Alam, A compact physical model for morphology induced intrinsic degradation of organic bulk heterojunction solar cell, Appl. Phys. Lett. 99 (2011) 1–4. https://doi.org/10.1063/1.3610460.
[37] P. Romero-Gomez, R. Betancur, A. Martinez-Otero, X. Elias, M. Mariano, B. Romero, B. Arredondo, R. Vergaz, J. Martorell, Enhanced stability in semi-transparent PTB7/PC71BM photovoltaic cells, Sol. Energy Mater. Sol. Cells. 137 (2015) 44–49. https://doi.org/10.1016/j.solmat.2015.01.026.
[38] T. Kim, J.H. Kang, S.J. Yang, S.J. Sung, Y.S. Kim, C.R. Park, Facile preparation of reduced graphene oxide-based gas barrier films for organic photovoltaic devices, Energy Environ. Sci. 7 (2014) 3403–3411. https://doi.org/10.1039/c4ee02310b.
[39] S.B. Sapkota, A. Spies, B. Zimmermann, I. Dürr, U. Würfel, Promising long-term stability of encapsulated ITO-free bulk-heterojunction organic solar cells under different aging conditions, Sol. Energy Mater. Sol. Cells. 130 (2014) 144–150. https://doi.org/10.1016/j.solmat.2014.07.004.
[40] D.M. Tanenbaum, H.F. Dam, R. Rösch, M. Jørgensen, H. Hoppe, F.C. Krebs, Edge sealing for low cost stability enhancement of roll-to-roll processed flexible polymer solar cell modules, Sol. Energy Mater. Sol. Cells. 97 (2012) 157–163. https://doi.org/10.1016/j.solmat.2011.09.064.
[41] D. Elkington, N. Cooling, X.J. Zhou, W.J. Belcher, P.C. Dastoor, Single-step annealing and encapsulation for organic photovoltaics using an exothermically-setting encapsulant material, Sol. Energy Mater. Sol. Cells. 124 (2014) 75–78. https://doi.org/10.1016/j.solmat.2014.01.039.
[42] C.H. Peters, I.T. Sachs-Quintana, J.P. Kastrop, S. Beaupré, M. Leclerc, M.D. McGehee, High efficiency polymer solar cells with long operating lifetimes, Adv. Energy Mater. 1 (2011) 491–494. https://doi.org/10.1002/aenm.201100138.
[43] V. Chawla, M. Ruoho, M. Weber, A.A. Chaaya, A.A. Taylor, C. Charmette, P. Miele, M. Bechelany, J. Michler, I. Utke, Fracture mechanics and oxygen gas barrier properties of Al2O3/ZnO nanolaminates on PET deposited by atomic layer deposition, Nanomaterials. 9 (2019). https://doi.org/10.3390/nano9010088.
[44] S. Cros, R. De Bettignies, S. Berson, S. Bailly, P. Maisse, N. Lemaitre, S. Guillerez, Definition of encapsulation barrier requirements: A method applied to organic solar cells, Sol. Energy Mater. Sol. Cells. 95 (2011) S65–S69. https://doi.org/10.1016/j.solmat.2011.01.035.
[45] M. V. Khenkin, E.A. Katz, A. Abate, G. Bardizza, J.J. Berry, C. Brabec, F. Brunetti, V. Bulović, Q. Burlingame, A. Di Carlo, R. Cheacharoen, Y.B. Cheng, A. Colsmann, S. Cros, K. Domanski, M. Dusza, C.J. Fell, S.R. Forrest, Y. Galagan, D. Di Girolamo, M. Grätzel, A. Hagfeldt, E. von Hauff, H. Hoppe, J. Kettle, H. Köbler, M.S. Leite, S. (Frank) Liu, Y.L. Loo, J.M. Luther, C.Q. Ma, M. Madsen, M. Manceau, M. Matheron,

M. McGehee, R. Meitzner, M.K. Nazeeruddin, A.F. Nogueira, Ç. Odabaşı, A. Osherov, N.G. Park, M.O. Reese, F. De Rossi, M. Saliba, U.S. Schubert, H.J. Snaith, S.D. Stranks, W. Tress, P.A. Troshin, V. Turkovic, S. Veenstra, I. Visoly-Fisher, A. Walsh, T. Watson, H. Xie, R. Yıldırım, S.M. Zakeeruddin, K. Zhu, M. Lira-Cantu, Consensus statement for stability assessment and reporting for perovskite photovoltaics based on ISOS procedures, Nat. Energy. 5 (2020) 35–49. https://doi.org/10.1038/s41560-019-0529-5.

[46] J.M. Chem, O. Zapata-arteaga, A.R. Gon, Comparing different geometries for photovoltaic- thermoelectric hybrid devices based on organics †, (2021) 2123–2132. https://doi.org/10.1039/D0TC05067A.

[47] V.I. Madogni, B. Kounouhéwa, A. Akpo, M. Agbomahéna, S.A. Hounkpatin, C.N. Awanou, Comparison of degradation mechanisms in organic photovoltaic devices upon exposure to a temperate and a subequatorial climate, Chem. Phys. Lett. 640 (2015) 201–214. https://doi.org/10.1016/j.cplett.2015.09.023.

[48] P.E. Burrows, G.L. Graff, M.E. Gross, P.M. Martin, M. Hall, E. Mast, C.C. Bonham, W.D. Bennett, L.A. Michalski, M.S. Weaver, J.J. Brown, D. Fogarty, L.S. Sapochak, Gas permeation and lifetime tests on polymer-based barrier coatings, in: Org. Light. Mater. Devices IV, SPIE, 2001: p. 75. https://doi.org/10.1117/12.416878.

[49] A.G. Erlat, B.M. Henry, C.R.M. Grovenor, A.G.D. Briggs, R.J. Chater, Y. Tsukahara, Mechanism of Water Vapor Transport through PET/AlOxNy Gas Barrier Films, J. Phys. Chem. B. 108 (2003) 883–890. https://doi.org/10.1021/JP036244Y.

[50] J. Ahmad, K. Bazaka, L.J. Anderson, R.D. White, M. V. Jacob, Materials and methods for encapsulation of OPV: A review, Renew. Sustain. Energy Rev. 27 (2013) 104–117. https://doi.org/10.1016/J.RSER.2013.06.027.

[51] S. Shoaee, M.P. Eng, E. Espíldora, J.L. Delgado, B. Campo, N. Martín, D. Vanderzande, J.R. Durrant, Influence of nanoscale phase separation on geminate versus bimolecular recombination in P3HT: fullerene blend films, Energy Environ. Sci. 3 (2010) 971–976. https://doi.org/10.1039/C003394D.

[52] S. Chambon, A. Rivaton, J.L. Gardette, M. Firon, Photo- and thermal degradation of MDMO-PPV:PCBM blends, Sol. Energy Mater. Sol. Cells. 91 (2007) 394–398. https://doi.org/10.1016/J.SOLMAT.2006.10.015.

[53] J.P. Jurado, B. Dörling, O. Zapata-Arteaga, A.R. Goñi, M. Campoy-Quiles, Comparing different geometries for photovoltaic-thermoelectric hybrid devices based on organics, J. Mater. Chem. C. 9 (2021) 2123–2132. https://doi.org/10.1039/d0tc05067a.

[54] H. Lee, J. Sohn, P. Tyagi, C. Lee, Crystallinity dependent thermal degradation in organic solar cell, Appl. Phys. Lett. 110 (2017) 1–6. https://doi.org/10.1063/1.4975140.

[55] L. Duan, H. Yi, Y. Zhang, F. Haque, C. Xu, A. Uddin, Comparative study of light- and thermal-induced degradation for both fullerene and non-fullerene-based organic solar cells, Sustain. Energy Fuels. 3 (2019) 723–735. https://doi.org/10.1039/c8se00567b.

[56] J. Bergqvist, E.A. Tholén, O. Inganäs, LED array scanner for inline characterization of thin film photovoltaic modules, Sol. Energy Mater. Sol. Cells. 157 (2016) 1057–1064. https://doi.org/10.1016/j.solmat.2016.08.010.

[57] H.C. Weerasinghe, S.E. Watkins, N. Duffy, D.J. Jones, A.D. Scully, Influence of moisture out-gassing from encapsulant materials on the lifetime of organic solar cells, Sol. Energy Mater. Sol. Cells. 132 (2015) 485–491. https://doi.org/10.1016/j.solmat.2014.09.030.

[58] A. Savva, I. Burgue, G. Papazoglou, S.A. Choulis, High-Performance Inverted Organic Photovoltaics Without Hole-Selective Contact, (2015). https://doi.org/10.1021/acsami.5b06578.

[59] F.C. Krebs, T. Tromholt, M. Jørgensen, Upscaling of polymer solar cell fabrication using full roll-to-roll processing, Nanoscale. 2 (2010) 873–886. https://doi.org/10.1039/b9nr00430k.

[60] M. Corazza, F.C. Krebs, S.A. Gevorgyan, Lifetime of organic photovoltaics: Linking outdoor and indoor tests, Sol. Energy Mater. Sol. Cells. 143 (2015) 467–472.

https://doi.org/10.1016/j.solmat.2015.07.037.
[61] A. Sharma, S.E. Watkins, D.A. Lewis, G. Andersson, Effect of indium and tin contamination on the efficiency and electronic properties of organic bulk hetero-junction solar cells, Sol. Energy Mater. Sol. Cells. 95 (2011) 3251–3255. https://doi.org/10.1016/J.SOLMAT.2011.07.012.
[62] M.P. De Jong, L.J. Van Ijzendoorn, M.J.A. De Voigt, Stability of the interface between indium-tin-oxide and poly(3,4-ethylenedioxythiophene)/poly(styrenesulfonate) in polymer light-emitting diodes, Appl. Phys. Lett. 77 (2000) 2255. https://doi.org/10.1063/1.1315344.
[63] A. Sharma, G. Andersson, D.A. Lewis, Role of humidity on indium and tin migration in organic photovoltaic devices, Phys. Chem. Chem. Phys. 13 (2011) 4381–4387. https://doi.org/10.1039/C0CP02203A.
[64] S. Rafique, S.M. Abdullah, K. Sulaiman, M. Iwamoto, Layer by layer characterisation of the degradation process in PCDTBT:PC71BM based normal architecture polymer solar cells, Org. Electron. C (2017) 65–74. https://doi.org/10.1016/J.ORGEL.2016.10.029.
[65] E. Voroshazi, B. Verreet, A. Buri, R. Müller, D. Di Nuzzo, P. Heremans, Influence of cathode oxidation via the hole extraction layer in polymer:fullerene solar cells, Org. Electron. 12 (2011) 736–744. https://doi.org/10.1016/J.ORGEL.2011.01.025.
[66] K. Feron, T.J. Nagle, L.J. Rozanski, B.B. Gong, C.J. Fell, Spatially resolved photocurrent measurements of organic solar cells: tracking water ingress at edges and pinholes, Sol. Energy Mater. Sol. Cells. 109 (2013) 169–177. https://doi.org/10.1016/J.SOLMAT.2012.10.027.
[67] T.S. Glen, N.W. Scarratt, H. Yi, A. Iraqi, T. Wang, J. Kingsley, A.R. Buckley, D.G. Lidzey, A.M. Donald, Grain size dependence of degradation of aluminium/calcium cathodes in organic solar cells following exposure to humid air, Sol. Energy Mater. Sol. Cells. 140 (2015) 25–32. https://doi.org/10.1016/J.SOLMAT.2015.03.015.
[68] P. Cheng, X. Zhan, Stability of organic solar cells: challenges and strategies, Chem. Soc. Rev. 45 (2016) 2544–2582. https://doi.org/10.1039/C5CS00593K.
[69] S.N. Habisreutinger, T. Leijtens, G.E. Eperon, S.D. Stranks, R.J. Nicholas, H.J. Snaith, Carbon nanotube/polymer composites as a highly stable hole collection layer in perovskite solar cells, Nano Lett. 14 (2014) 5561–5568. https://doi.org/10.1021/NL501982B/SUPPL_FILE/NL501982B_SI_001.PDF.
[70] E. Planes, M. Spalla, S. Juillard, L. Perrin, L. Flandin, Absolute Quantification of Photo-/Electroluminescence Imaging for Solar Cells: Definition and Application to Organic and Perovskite Devices, ACS Appl. Electron. Mater. 1 (2019) 2489–2501. https://doi.org/10.1021/acsaelm.9b00450.
[71] M. Seeland, D.A.M. Egbe, H. Hoppe, Locally resolved large scale phase separation in polymer : fullerene blends, (2016) 1244–1250. https://doi.org/10.1039/c5ta07004j.
[72] J. Adams, M. Salvador, L. Lucera, S. Langner, G.D. Spyropoulos, F.W. Fecher, M.M. Voigt, S.A. Dowland, A. Osvet, H. Egelhaaf, C.J. Brabec, Water Ingress in Encapsulated Inverted Organic Solar Cells : Correlating Infrared Imaging and Photovoltaic Performance, (2015) 1–11. https://doi.org/10.1002/aenm.201501065.
[73] J.A. Phys, H. Hoppe, J. Bachmann, B. Muhsin, K. Drüe, I. Riedel, G. Gobsch, C. Buerhop-, C.J. Brabec, V. Dyakonov, H. Hoppe, J. Bachmann, B. Muhsin, K. Drüe, I. Riedel, V. Dyakonov, Quality control of polymer solar modules by lock-in thermography, 014505 (2012) 1–5. https://doi.org/10.1063/1.3272709.
[74] N. Banerji, S. Cowan, E. Vauthey, A.J. Heeger, Ultrafast relaxation of the poly(3-hexylthiophene) emission spectrum, J. Phys. Chem. C. 115 (2011) 9726–9739. https://doi.org/10.1021/jp1119348.
[75] M.J. Newman, E.M. Speller, J. Barbé, J. Luke, M. Li, Z. Li, Z.K. Wang, S.M. Jain, J.S. Kim, H.K.H. Lee, W.C. Tsoi, Photo-stability study of a solution-processed small molecule solar cell system: correlation between molecular conformation and degradation, Sci. Technol. Adv. Mater. 19 (2018) 194–202. https://doi.org/10.1080/14686996.2018.1433948.

[76] Q. An, F. Zhang, L. Li, J. Wang, J. Zhang, L. Zhou, W. Tang, Improved efficiency of bulk heterojunction polymer solar cells by doping low-bandgap small molecules, ACS Appl. Mater. Interfaces. 6 (2014) 6537–6544. https://doi.org/10.1021/am500074s.
[77] J. Wan, X. Xu, G. Zhang, Y. Li, K. Feng, Q. Peng, Highly efficient halogen-free solvent processed small-molecule organic solar cells enabled by material design and device engineering, Energy Environ. Sci. 10 (2017) 1739–1745. https://doi.org/10.1039/c7ee00805h.
[78] S. Holliday, R.S. Ashraf, A. Wadsworth, D. Baran, S.A. Yousaf, C.B. Nielsen, C.H. Tan, S.D. Dimitrov, Z. Shang, N. Gasparini, M. Alamoudi, F. Laquai, C.J. Brabec, A. Salleo, J.R. Durrant, I. McCulloch, High-efficiency and air-stable P3HT-based polymer solar cells with a new non-fullerene acceptor, Nat. Commun. 7 (2016) 1–11. https://doi.org/10.1038/ncomms11585.
[79] L. Duan, X. Meng, Y. Zhang, H. Yi, K. Jin, F. Haque, C. Xu, Z. Xiao, L. Ding, A. Uddin, Comparative analysis of burn-in photo-degradation in non-fullerene COi8DFIC acceptor based high-efficiency ternary organic solar cells, Mater. Chem. Front. 3 (2019) 1085–1096. https://doi.org/10.1039/c9qm00130a.
[80] L. Duan, M. Guli, Y. Zhang, H. Yi, F. Haque, A. Uddin, The Air Effect in the Burn-In Thermal Degradation of Nonfullerene Organic Solar Cells, 1901401 (2020) 1–10. https://doi.org/10.1002/ente.201901401.
[81] W.C. Tsoi, W. Zhang, J. Razzell Hollis, M. Suh, M. Heeney, I. McCulloch, J.S. Kim, In-situ monitoring of molecular vibrations of two organic semiconductors in photovoltaic blends and their impact on thin film morphology, Appl. Phys. Lett. 102 (2013) 1–5. https://doi.org/10.1063/1.4803912.
[82] J. Razzell-Hollis, W.C. Tsoi, J.S. Kim, Directly probing the molecular order of conjugated polymer in OPV blends induced by different film thicknesses, substrates and additives, J. Mater. Chem. C. 1 (2013) 6235–6243. https://doi.org/10.1039/c3tc31245c.
[83] W.C. Tsoi, D.T. James, J.S. Kim, P.G. Nicholson, C.E. Murphy, D.D.C. Bradley, J. Nelson, J.S. Kim, The nature of in-plane skeleton Raman modes of P3HT and their correlation to the degree of molecular order in P3HT:PCBM blend thin films, J. Am. Chem. Soc. 133 (2011) 9834–9843. https://doi.org/10.1021/ja2013104.
[84] W.C. Tsoi, D.T. James, E.B. Domingo, J.S. Kim, M. Al-Hashimi, C.E. Murphy, N. Stingelin, M. Heeney, J.S. Kim, Effects of a heavy atom on molecular order and morphology in conjugated polymer:fullerene photovoltaic blend thin films and devices, ACS Nano. 6 (2012) 9646–9656. https://doi.org/10.1021/nn304024g.
[85] A.J. Parnell, A.J. Cadby, A.D.F. Dunbar, G.L. Roberts, A. Plumridge, R.M. Dalgliesh, M.W.A. Skoda, R.A.L. Jones, Physical mechanisms responsible for the water-induced degradation of PC61BM P3HT photovoltaic thin films, J. Polym. Sci. Part B Polym. Phys. 54 (2016) 141–146. https://doi.org/10.1002/polb.23902.
[86] A. Seemann, T. Sauermann, C. Lungenschmied, O. Armbruster, S. Bauer, H.J. Egelhaaf, J. Hauch, Reversible and irreversible degradation of organic solar cell performance by oxygen, Sol. Energy. 85 (2011) 1238–1249. https://doi.org/10.1016/j.solener.2010.09.007.
[87] O. Rodríguez-Romeu, M. Constenla, M. Carrassón, M. Campoy-Quiles, A. Soler-Membrives, Are anthropogenic fibres a real problem for red mullets (Mullus barbatus) from the NW Mediterranean?, Sci. Total Environ. 733 (2020) 139336. https://doi.org/10.1016/J.SCITOTENV.2020.139336.
[88] W.C. Tsoi, D.T. James, J.S. Kim, P.G. Nicholson, C.E. Murphy, D.D.C. Bradley, J. Nelson, J.S. Kim, The nature of in-plane skeleton Raman modes of P3HT and their correlation to the degree of molecular order in P3HT:PCBM blend thin films, J. Am. Chem. Soc. 133 (2011) 9834–9843. https://doi.org/10.1021/JA2013104/SUPPL_FILE/JA2013104_SI_001.PDF.
[89] E. Rezasoltani, A.A.Y. Guilbert, J. Yan, X. Rodríguez-Martínez, M. Azzouzi, F. Eisner, S.M. Tuladhar, Z. Hamid, A. Wadsworth, I. McCulloch, M. Campoy-Quiles, J. Nelson, Correlating the Phase Behavior with the Device Performance in Binary Poly-3-

hexylthiophene: Nonfullerene Acceptor Blend Using Optical Probes of the Microstructure, Chem. Mater. 32 (2020) 8294–8305. https://doi.org/10.1021/acs.chemmater.0c02093.
[90] W.C. Tsoi, D.T. James, J.S. Kim, P.G. Nicholson, C.E. Murphy, D.D.C. Bradley, J. Nelson, J.S. Kim, The nature of in-plane skeleton Raman modes of P3HT and their correlation to the degree of molecular order in P3HT:PCBM blend thin films, J. Am. Chem. Soc. 133 (2011) 9834–9843. https://doi.org/10.1021/ja2013104.
[91] M. Kaiser, V. Nádaždy, P. Šiffalovič, J. Ivančo, E. Majková, Correlation between electrical parameters and defect states of polythiophene:fullerene based solar cell, Thin Solid Films. 614 (2016) 16–24. https://doi.org/10.1016/j.tsf.2016.02.001.
[92] P. Šiffalovic, J. Müllerová, M. Kaiser, V. Nádaz, Optical absorption study of P3HT : PCBM blend photo-oxidation for bulk heterojunction solar cells, 134 (2016) 294–301. https://doi.org/10.1016/j.solener.2016.05.009.
[93] J. Razzell-hollis, J. Wade, W.C. Tsoi, Y. Soon, J. Durrant, J.S. Kim, Photochemical stability of high efficiency PTB7:PC70BM solar cell blends, J. Mater. Chem. A. 2 (2014) 20189–20195. https://doi.org/10.1039/c4ta05641h.
[94] S. Alem, S. Wakim, J. Lu, G. Robertson, J. Ding, Y. Tao, Degradation mechanism of benzodithiophene-based conjugated polymers when exposed to light in air, ACS Appl. Mater. Interfaces. 4 (2012) 2993–2998. https://doi.org/10.1021/am300362b.
[95] M.O. Reese, A.J. Morfa, M.S. White, N. Kopidakis, S.E. Shaheen, G. Rumbles, D.S. Ginley, Pathways for the degradation of organic photovoltaic P3HT:PCBM based devices, Sol. Energy Mater. Sol. Cells. 92 (2008) 746–752. https://doi.org/10.1016/j.solmat.2008.01.020.
[96] T. Liu, L. Huo, X. Sun, B. Fan, Y. Cai, T. Kim, J.Y. Kim, H. Choi, Y. Sun, Ternary Organic Solar Cells Based on Two Highly Efficient Polymer Donors with Enhanced Power Conversion Efficiency, Adv. Energy Mater. 6 (2016) 1502109. https://doi.org/10.1002/AENM.201502109.
[97] J. Schafferhans, A. Baumann, A. Wagenpfahl, C. Deibel, V. Dyakonov, Oxygen doping of P3HT:PCBM blends: Influence on trap states, charge carrier mobility and solar cell performance, Org. Electron. 11 (2010) 1693–1700. https://doi.org/10.1016/J.ORGEL.2010.07.016.
[98] A. Seemann, T. Sauermann, C. Lungenschmied, O. Armbruster, S. Bauer, H.J. Egelhaaf, J. Hauch, Reversible and irreversible degradation of organic solar cell performance by oxygen, Sol. Energy. 85 (2011) 1238–1249. https://doi.org/10.1016/J.SOLENER.2010.09.007.
[99] I. Sudakov, M. Van Landeghem, R. Lenaerts, W. Maes, S. Van Doorslaer, E. Goovaerts, The Interplay of Stability between Donor and Acceptor Materials in a Fullerene-Free Bulk Heterojunction Solar Cell Blend, 2002095 (2020) 1–13. https://doi.org/10.1002/aenm.202002095.
[100] A. Aguirre, S.C.J.J. Meskers, R.A.J.J. Janssen, H.J. Egelhaaf, Formation of metastable charges as a first step in photoinduced degradation in π-conjugated polymer:fullerene blends for photovoltaic applications, Org. Electron. 12 (2011) 1657–1662. https://doi.org/10.1016/j.orgel.2011.06.020.
[101] A. Roy, A.A. Science, Significant Enhancement in the Conductivity of Al-Doped Zinc Oxide thin Films for TCO Application Signi ¯ cant Enhancement in the Conductivity of Al-Doped Zinc Oxide thin Films for TCO Application, Int. J. Nanosci. 15 (2016) 1650011–1650018. https://doi.org/10.1142/S0219581X16500113.
[102] C. Drouilly, J. Kra, S. Casale, D. Bazer-bachi, V. Lecocq, H. Vezin, ZnO Oxygen Vacancies Formation and Filling Followed by in Situ Photoluminescence and in Situ EPR, J. Phys. Chem. C. 116 (2012), https://doi.org/10.1021/jp307693y.
[103] J.K. Lee, J.M. Cho, W.S. Shin, S.J. Moon, N.T. Kemp, H. Zhang, R. Lamb, The stability of PEDOT:PSS films monitored by electron spin resonance, J. Korean Phys. Soc. 52 (2008) 621–626. https://doi.org/10.3938/jkps.52.621.
[104] J. Ouyang, Q. Xu, C.W. Chu, Y. Yang, G. Li, J. Shinar, On the mechanism of conductivity enhancement in poly(3,4- ethylenedioxythiophene):poly(styrene

sulfonate) film through solvent treatment, Polymer (Guildf). 45 (2004) 8443–8450. https://doi.org/10.1016/j.polymer.2004.10.001.
[105] K. Norrman, M. V. Madsen, S.A. Gevorgyan, F.C. Krebs, Degradation patterns in water and oxygen of an inverted polymer solar cell, J. Am. Chem. Soc. 132 (2010) 16883–16892. https://doi.org/10.1021/JA106299G/SUPPL_FILE/JA106299G_SI_001.

Chapter 7 outcomes and perspectives

In this thesis we investigated some of the main challenges OPV devices exhibited through the upscaling processing. On the one hand, we correlated the performance of the OPV devices to the microstructure of the photoactive layer applied in the devices for a particular example. Specifically, different PI molecules were applied as electron acceptors and the effect of the corresponding molecular packing on the performance of the devices was studied. Moreover, different electrode designs and materials were optimized in order to maintain efficient modules. Finally, degradation studies of the OPV modules were accomplished to investigate their stability. The major outcomes of experiments carried out through the thesis are summarized as followed. In general, Table 7.1 summarize the reported requirements for encapsulating materials.

Table 7.1 the encapsulating materials requirements.

Characteristics	Requirement
water vapour transmission rate	10^{-3}–10^{-6} g·m^{-2}·day^{-1}
Oxygen transmission rate	10^{-3}–10^{-5} cm3·m^{-2}·day^{-1}·atm^{-1}
Glass transition temperature	<−40 °C
Light transmission	>90%
Water absorption	<0.5 wt % (20 °C/100% RH)
Tensile modulus	<20.7 mPa (>3000 psi) at 25 °C

7.1 Conclusion

In the first experimental chapter (i.e. Chapter 3), we studied the synthesis of silver nanowires by the solution processed polyol method. We optimized the nanowires' dimension through controlling different parameters such as stirring speed, reaction temperature, and the molar ratio between PVP: $AgNO_3$. The optimized AgNWs were of diameter 76 nm and more than 100 µm meters long, and were selected by its electrical properties. Their films had a promising FOM (7.86 x$10^{-2}\Omega^{-1}$) compared to the TCE films such as ITO (1.76 x$10^{-2}\Omega^{-1}$).

The good FOM revealed the potential of AgNWs for their application in solar cell to replace ITO. However, the resulting high roughness did not help their implementation. Devices based on silver nanowires showed low performance regardless of the inks being commercially provided or synthesized by us. PEDOT: PSS was used to overcome the nanowires roughness, and resulted in devices with higher photocurrent. Although blending the PEDOT: PSS with the silver nanowires improves the devices efficiency, the obtained efficiency was still half of the value obtained by the reference devices based on ITO electrodes.

On the other hand, providing AgNWs as a top electrode in the inverted structure solar cell to obtain semi-transparent solar cell has the obstacle of low adhesion of the AgNWs to the beneath layer, resulting in low device performance.

This motivated us to shift our attention to screen printed silver grids based on commercial inks, and optimize their design for roll-to-rolled OPV modules. There, PEDOT:PSS plays two roles, namely, an electrode and a HTL. Introducing the HYE as HTL did not help so much the photovoltaic parameters and the efficiency of the modules. Further optimization of the electrode geometry was carried out by investigating the fingers spacing, for better charge collection. In this sense, we observe that 8 mm spacing has revealed as an excessive distance between fingers -probably for a bad charge collection- and the spacing of 4 mm revealed good performance of the modules with efficiency reaches 1% with an active area of 14.85 cm^2.

In Chapter four we emphasized the difficulty of designing NFAs with a desired microstructure in the blend. NFAs are privileged for tunning their energy levels to match the electron donor materials. However, their microstructure still plays a crucial challenge which determines their potential application in solar cells. Three PI molecules, (PIPB,3PIPT, and 4PIPM), were designed to explore who their molecular packing in heterojunctions correlates to the performance of the solar cells. This investigation was carried out by using GIWAX, UV-VIS and Raman spectroscopy. Pristine films of PIPB showed the highest ordering structure unlike the higher dimension molecules, 3PIPT and 4PIPM. These Studies provided the importance of the degree of crystallinity variance between the donor and the acceptor in the heterojunction. Therefore, when a planar molecule PIPB paired with the PCDTBT that has a moderate degree of ordering, devices showed efficiency of 1.2%, while devices based on the same molecule PIPB blend with the PBDBT, a polymer that exhibits a higher degree of crystallinity than PCDTBT, showed efficiency of 0.48 %.

The low efficiency of the devices highlighted the challenges associated to microstructure. These are not only based on the molecular ordering tendency of the molecules but also on the PI molecules solubility and ability to aggregate, as well as their miscibility. Aggregation tendency of the PI molecules observed by GIWAXS and in the red shift in their absorption spectra in solid state through π−π stacking. Despite π−π stacking being favorable for good electron mobility, this strong packing tendency resulted in phase separation in the bulk heterojunction.

In chapter five we revealed the challenges of upscaling processing in OPV devices. We provided a step-by-step methodology to show the limitations of each step through the upscaling from blade coating to the roll-to-roll coating. First, a reference device of inverted structure was optimized by blade coating all the layers on glass substrate, except the silver electrode that was evaporated. Annealing conditions applied to enhance the photovoltaic performance resulted in a efficiency value of 8%. Moving from blade coating to roll-to-roll coating implies changes step by step.

The first change was for the rigid glass substrate coated with ITO to be replaced by the flexible PET substrate coated with IMI. This change resulted in 25% reduction in the device efficiency limiting the efficiency to a value of 6%.

Second step was to change the deposition technique of the ETL(AZO) from blade coating to roll-to-roll on top of the flexible PET/IMI. This change exhibited another efficiency loss of

16% to end the devices with efficiency value of 5% due to the roughness of the slot die R2R coated layer. Roughness in ETL influenced the photovoltaic performance by different means. First, by enlarging the interfacial area at ETL/PAL interface resulting in high trap density and hence reduction of the FF and V_{oc} of the devices. second, by changing the ETL surface energy and, therefore, influence the wetting of the deposited ink on top. Third, by decreasing the interfacial area at the donor/acceptor interface led to less charge dissociation.

Third step was to coat the PAL by slot die R2R on top of the R2R-ed ETL/IMI/PET. The implementation of a material has thickness/microstructure insensitive performance enabled the roll-to-roll processing remaining the same performance to the devices.

Last step was to coat the HTL during roll-to-roll to detect an additional efficiency reduction of 50%, yielding devices with efficiency of 2-3%. Therefore, HTLs can be considered the main efficiency loss during the upscaling processing due to their rheological and electrical properties reducing the FF of the devices. The optical absorption of the HTL resulted in reduction in the photogenerated current and the porosity revealed by AFM figures was responsible for shunts possibilities in the devices.

Finally, the stability of OPV modules prepared by roll-to-roll coating technique has been analyzed. In order to study the extrinsic degradation mechanisms of modules based on FA and NFAs, a spectroscopic investigation was carried out that combined EPR, LBIC and Raman, and revealed the role of fullerene in stabilizing the OPV modules. The EPR spectrum confirms the p-doping of the polymer with oxygen and revealed that the HTL is also a source of degradation of the module by building up radicals. PCBM protected P3HT to extend the lifetime of the encapsulated modules up to 200 hours. Fullerene based modules lasted more than the encapsulated modules based on P3HT:o-IDTBR.

7.2 Future work

ITO has a high conductivity (10–50 ohms /□) and a high transparency (more than 80%) in the visible range, despite its brittleness that limits the application in the large-scale production and stands against the flexibility as a major advantage of the OPV.

Electrode materials to replace ITO, exhibiting optimum transparency, conductivity, stability, low cost and compatibility with roll-to-roll deposition have been reported[1] such as PEDOT: PSS[2] metallic nanowires[3], carbon nanotubes[4], and thin metal layers[5].Table 7.2 shows a comparison between different materials reported as TCE. Metal nanowires represent the highest potential material for the application of electrodes in organic solar cells. AgNWs promise a high potential in organic solar cells because of their optical and electrical characteristics in addition to their flexibility and their stability. Their ability to be produced in low-cost solution processing imply their integration at large scale industry. They are the most promising candidate to replace ITO and to produce semi-transparent flexible organic solar cells when applied as top electrode[6]. Table 7.3 showed the reported efficient devices with AgNWs combined with different PEDOT: PSS or embedded in the flexible substrate as a replacement for the ITO electrode.

Table 7.2 Comparison of TCE materials[7].

Materials	Sheet resistance	Optical transmittance	Flexibility	Fabrication	cost
Carbon nanotubes	High	Low	High	Solution processing	Low
CVD Graphene	Low	High	High	Vapour deposition	High
Reduced Graphene Oxide	High	Low	High	Solution processing	Low
Conductive polymers	High	Low/medium	High	Solution processing	Low
Metallic nanowires	low	High	High	Solution processing	Low

Table 7.3 The performance of the reported flexible organic solar cells[7].

Device structure	V_{oc} (V)	J_{sc} (mA/cm^2)	FF (%)	PCE (%)	Reference
PET/AgNWs/PH1000/PEDOT:PSS 4083/PAL/PFN-Br/Al	0.83	19.17	65.1	10.30	[8]
AgNWs@PI/ZnO/Active Layer/MoO3/Ag	0.82	19.6	72	11.6	[9]
PET/Embedded-AgNWs/AZO-SG/Active Layer/MoO3/Al	0.83	25.05	73.0	15.50	[10]
PET/PSSNa:AgNWs/ZnO NPs/PFN-Br/PAL/MoO3/Ag	0.7	26.99	69.7	13.15	[11]
PET/AgNWs/ZnO/active layer/MoO3/Ag	0.84	22.26	64.66	12.02	[12]

The main drawback of silver nanowires is the resulting high roughness, Optimizing the nanowires dimensions is aimed to be less 30 nm for haze and roughness reduction[13]. solutions reported are by annealing the AgNWs, or by embedding the AgNW into the substrate (either by contact transfer method or by applied pressure method), or by flattening the AgNWs surface by applying an extra layer [7]. Silver nano rings showed better optical and electrical characteristics than the silver nanowires due to their circular shape enhancing the electrical properties and optical properties having higher transparency and less haze than the silver nanowires.

Inorganic and nanocarbon HTLs are desired in OPV due to their transparency in the visible range, electrical properties, and high stability. Different materials have been reported with

high potential as HTLs, such as MoO_3[14] , WO_3[15], GO[16], and CNTs[17]. Mo and Ni doped with V and Cu were reported to enhance the V_{oc}, FF, and J_{sc} due to tunning the WF. Functionalizing CNTs with amino improved FF and J_{sc}. Compositing PEDOT: PSS with other materials was a good way to improve the device performance[18], [19]. Adding metal oxides such as MoO_3, V_2O_5 graphene oxide enhanced the electron blocking and the device stability and hindered the recombination in devices. Adding metal nanoparticles increased the electrical conductivity and the optical absorption leading to an increase in the photogenerated current of the devices[20]. Small molecule solution processed HTLs is favored in large scales organic solar cells due to the high stability, low costs, and ease preparation. Small molecules are promising not only as HTLs but also as electron acceptor materials. However, PI based molecules are promising as NFAs, their structure has aggregation through the stacking that led to trap assist recombination. More investigation is required for designing NFA with higher solubility and a packing tendency that match the electron donor material. Not only their energy level aligning to the donor materials but also their microstructure that needs to be optimized to avoid phase separation and forming microcrystals in the heterojunction.

OPV could reach a lifetime of more than 20 years by good encapsulation and blocking the UV radiation [21]. Two sources of degradation in OSC are identified, namely extrinsic and intrinsic sources. Extrinsic degradation results from the reaction of the organic materials with oxygen and water that leads to bleaching of the active layer[22] and reduction of the conductivity of the photoactive and charge transport layers[23]. UV radiation leads to intrinsic degradation in OSC by breaking the carbon bonds in the organic materials. Encapsulation has been reported to remove the extrinsic degradation and to block the UV radiation [24]. Encapsulation materials should have requirements such as high dielectric constant, light transmission, mechanical strength, and resistance to ultraviolet (UV) degradation and thermal oxidation. Glass encapsulation has been reported the best life time for OSC resulting in water vapour transmission, as a measure of general gas permeation, of less than 10^{-6}g (m^2 day)$^{-1}$[25]. Thin, transparent and inexpensive efficient barrier encapsulation are required for the protection of OSC achieved by lamination or direct deposition of thin film encapsulation[26]. Best results are in both cases obtained with multilayer structures[27]. Polyvinyl butyral (PVB), ethylene vinyl acetate (EVA), and thermoplastic polyurethane (TPU) were reported to encapsulate OPV devices[28].

7.3 References fot Chapter 7

[1] Y. Zhang, S. W. Ng, X. Lu, and Z. Zheng, “Solution-Processed Transparent Electrodes for Emerging Thin-Film Solar Cells,” *Chem. Rev.*, vol. 120, no. 4, pp. 2049–2122, Feb. 2020, doi: 10.1021/acs.chemrev.9b00483.

[2] H. Shi, C. Liu, Q. Jiang, and J. Xu, “Effective Approaches to Improve the Electrical Conductivity of PEDOT:PSS: A Review,” *Adv. Electron. Mater.*, vol. 1, no. 4, p. 1500017, Apr. 2015, doi: 10.1002/aelm.201500017.

[3] J. Y. Lee, S. T. Connor, Y. Cui, and P. Peumans, “Solution-processed metal nanowire mesh transparent electrodes,” *Nano Lett.*, vol. 8, no. 2, pp. 689–692, Feb. 2008, doi: 10.1021/nl073296g.

[4] G. Mazzotta *et al.*, “Solubilization of Carbon Nanotubes with Ethylene-Vinyl Acetate for Solution-Processed Conductive Films and Charge Extraction Layers in Perovskite Solar

Cells," *ACS Appl. Mater. Interfaces*, vol. 11, no. 1, pp. 1185–1191, Jan. 2019, doi: 10.1021/acsami.8b15396.

[5] A. T. Barrows, R. Masters, A. J. Pearson, C. Rodenburg, and D. G. Lidzey, "Indium-free multilayer semi-transparent electrodes for polymer solar cells," *Sol. Energy Mater. Sol. Cells*, vol. 144, pp. 600–607, Jan. 2016, doi: 10.1016/j.solmat.2015.10.010.

[6] W. Li *et al.*, "Recent progress in silver nanowire networks for flexible organic electronics," *J. Mater. Chem. C*, vol. 8, no. 14, pp. 4636–4674, Apr. 2020, doi: 10.1039/C9TC06865A.

[7] M. R. Azani, A. Hassanpour, and T. Torres, "Benefits, Problems, and Solutions of Silver Nanowire Transparent Conductive Electrodes in Indium Tin Oxide (ITO)-Free Flexible Solar Cells," *Adv. Energy Mater.*, vol. 10, no. 48, 2020, doi: 10.1002/aenm.202002536.

[8] T. Lei *et al.*, "Bendable and foldable flexible organic solar cells based on Ag nanowire films with 10.30% efficiency," *J. Mater. Chem. A*, vol. 7, no. 8, pp. 3737–3744, Feb. 2019, doi: 10.1039/c8ta11293b.

[9] J. H. Seo *et al.*, "Cold Isostatic-Pressured Silver Nanowire Electrodes for Flexible Organic Solar Cells via Room-Temperature Processes," *Adv. Mater.*, vol. 29, no. 30, p. 1701479, Aug. 2017, doi: 10.1002/adma.201701479.

[10] Y. Cui *et al.*, "Single-Junction Organic Photovoltaic Cells with Approaching 18% Efficiency," *Adv. Mater.*, vol. 32, no. 19, p. 1908205, May 2020, doi: 10.1002/ADMA.201908205.

[11] Y. Sun *et al.*, "Flexible organic photovoltaics based on water-processed silver nanowire electrodes," *Nat. Electron. 2019 211*, vol. 2, no. 11, pp. 513–520, Nov. 2019, doi: 10.1038/s41928-019-0315-1.

[12] Y. X. Zhang *et al.*, "Synergetic Transparent Electrode Architecture for Efficient Non-Fullerene Flexible Organic Solar Cells with >12% Efficiency," *ACS Nano*, vol. 13, no. 4, pp. 4686–4694, Apr. 2019, doi: 10.1021/ACSNANO.9B00970/SUPPL_FILE/NN9B00970_SI_001.PDF.

[13] S. A. Gevorgyan *et al.*, "Improving, characterizing and predicting the lifetime of organic photovoltaics," *Journal of Physics D: Applied Physics*, vol. 50, no. 10. IOP Publishing, p. 103001, Feb. 07, 2017, doi: 10.1088/1361-6463/50/10/103001.

[14] G. Ji *et al.*, "Fully Coated Semitransparent Organic Solar Cells with a Doctor-Blade-Coated Composite Anode Buffer Layer of Phosphomolybdic Acid and PEDOT:PSS and a Spray-Coated Silver Nanowire Top Electrode," *ACS Appl. Mater. Interfaces*, vol. 10, no. 1, pp. 943–954, Jan. 2018, doi: 10.1021/ACSAMI.7B13346/SUPPL_FILE/AM7B13346_SI_001.PDF.

[15] R. Remya, P. T. G. Gayathri, and B. Deb, "Studies on solution-processed tungsten oxide nanostructures for efficient hole transport in the inverted polymer solar cells," *Mater. Chem. Phys.*, vol. 255, Nov. 2020, doi: 10.1016/J.MATCHEMPHYS.2020.123584.

[16] Z. Liu, S. Niu, and N. Wang, "Oleylamine-functionalized graphene oxide as an electron block layer towards high-performance and photostable fullerene-free polymer solar cells," *Nanoscale*, vol. 9, no. 42, pp. 16293–16304, Nov. 2017, doi: 10.1039/C7NR05939F.

[17] X. Zhang, S. Sun, and X. Liu, “Amino functionalized carbon nanotubes as hole transport layer for high performance polymer solar cells,” *Inorg. Chem. Commun.*, vol. 103, pp. 142–148, May 2019, doi: 10.1016/J.INOCHE.2019.03.008.

[18] C. Hou and H. Yu, “Modifying the nanostructures of PEDOT:PSS/Ti3C2TX composite hole transport layers for highly efficient polymer solar cells,” *J. Mater. Chem. C*, vol. 8, no. 12, pp. 4169–4180, Mar. 2020, doi: 10.1039/D0TC00075B.

[19] Q. Yang *et al.*, “Boosting Performance of Non-Fullerene Organic Solar Cells by 2D g-C3N4 Doped PEDOT:PSS,” *Adv. Funct. Mater.*, vol. 30, no. 15, p. 1910205, Apr. 2020, doi: 10.1002/ADFM.201910205.

[20] C. Anrango-Camacho, K. Pavón-Ipiales, B. A. Frontana-Uribe, and A. Palma-Cando, “Recent Advances in Hole-Transporting Layers for Organic Solar Cells,” *Nanomaterials*, vol. 12, no. 3, pp. 1–54, 2022, doi: 10.3390/nano12030443.

[21] M. Hermenau, M. Riede, K. Leo, S. A. Gevorgyan, F. C. Krebs, and K. Norrman, “Water and oxygen induced degradation of small molecule organic solar cells,” *Sol. Energy Mater. Sol. Cells*, vol. 95, no. 5, pp. 1268–1277, May 2011, doi: 10.1016/j.solmat.2011.01.001.

[22] A. Rivaton, A. Tournebize, J. Gaume, P. O. Bussière, J. L. Gardette, and S. Therias, “Photostability of organic materials used in polymer solar cells,” *Polymer International*, vol. 63, no. 8. John Wiley & Sons, Ltd, pp. 1335–1345, Aug. 01, 2014, doi: 10.1002/pi.4656.

[23] M. Riede, D. Spoltore, and K. Leo, “Organic Solar Cells—The Path to Commercial Success,” *Adv. Energy Mater.*, vol. 11, no. 1, 2021, doi: 10.1002/aenm.202002653.

[24] F. C. Krebs, “Encapsulation of polymer photovoltaic prototypes,” *Sol. Energy Mater. Sol. Cells*, vol. 90, no. 20, pp. 3633–3643, Dec. 2006, doi: 10.1016/j.solmat.2006.06.055.

[25] Q. Burlingame, X. Huang, X. Liu, C. Jeong, C. Coburn, and S. R. Forrest, “Intrinsically stable organic solar cells under high-intensity illumination,” *Nature*, vol. 573, no. 7774, pp. 394–397, Sep. 2019, doi: 10.1038/s41586-019-1544-1.

[26] P. Boldrighini, A. Fauveau, S. Thérias, J. L. Gardette, M. Hidalgo, and S. Cros, “Optical calcium test for measurement of multiple permeation pathways in flexible organic optoelectronic encapsulation,” *Rev. Sci. Instrum.*, vol. 90, no. 1, p. 014710, Jan. 2019, doi: 10.1063/1.5021182.

[27] E. G. Jeong, J. H. Kwon, K. S. Kang, S. Y. Jeong, and K. C. Choi, “A review of highly reliable flexible encapsulation technologies towards rollable and foldable OLEDs,” *J. Inf. Disp.*, 2019, doi: 10.1080/15980316.2019.1688694.

[28] A. Uddin, M. B. Upama, H. Yi, and L. Duan, “Encapsulation of organic and perovskite solar cells: A review,” *Coatings*, vol. 9, no. 2, 2019, doi: 10.3390/coatings9020065.